UNIVERSITÀ DEGLI STUDI DI TRIESTE

XXIX CICLO DEL DOTTORATO DI RICERCA IN

NANOTECNOLOGIE

Synthesis of fluorescent carbon nanoparticles (CNPs) and their applications in drug delivery

Settore scientifico-disciplinare: **BIO/14**

DOTTORANDO
SAMER BAYDA

COORDINATORE
PROF. LUCIA PASQUATO

SUPERVISORE DI TESI
DR. GIUSEPPE TOFFOLI

CO-SUPERVISORE DI TESI
DR. FLAVIO RIZZOLIO

ANNO ACCADEMICO 2015/2016

UNIVERSITÀ DEGLI STUDI DI TRIESTE

XXIX CICLO DEL DOTTORATO DI RICERCA IN

NANOTECNOLOGIE

Synthesis of fluorescent carbon nanoparticles (CNPs) and their applications in drug delivery

Settore scientifico-disciplinare: **BIO/14**

DOTTORANDO
SAMER BAYDA

COORDINATORE
PROF. LUCIA PASQUATO

SUPERVISORE DI TESI
DR. GIUSEPPE TOFFOLI

CO-SUPERVISORE DI TESI
DR. FLAVIO RIZZOLIO

ANNO ACCADEMICO 2015/2016

"The role of the infinitely small in nature is infinitely large."

"Louis Pasteur"

TABLE OF CONTENTS

Acknowledgments

*I would like to express my sincere gratitude to **Dr. Giuseppe Toffoli**, the director of the Clinical and Experimental Pharmacology division (FSC) at National Cancer Institute (CRO-Aviano-Italy) for offering me the opportunity to pursue my PhD degree in the division (Nanomedicine Lab) and for allowing me to grow as a research scientist.*

*A special thanks to my co-supervisor, **Dr. Flavio Rizzolio** for the continuous support of my PhD study and related research, for his patience, motivation, and immense knowledge. His guidance helped me in all the time of research and writing of this thesis.*

*I would like to thank **Prof. Lucia Pasquato**, the coordinator of the doctoral school of Nanotechnology at University of Trieste-Italy for her strong support, excellent advice, and her effort make for the school of Nanotechnology during the three years of PhD.*

*I would like to thank **Dr. Giuseppe Corona** for his encouragement and meaningful discussions and his expert guidance in those years.*

*I really thank **Prof. Pietro Riello** and **Prof. Alvise Benedetti** for offering me the opportunity to join their team for 4 months in the Department of Molecular Sciences and Nanosystems at University Ca'Foscari Venice and who gave access to the laboratory and research facilities. My sincere thanks to **Enrico Pontoglio** and **Emmanuele Ambrosi** for their help during my stay in Venice.*

*I am highly obliged to **Dr. Eric Manoury** (LCC-Toulouse-France) and **Mr. Walid Koussa** for their immense support, never ending encouragement and technical discussions.*

*My huge appreciation goes to my colleagues at the FSC unit and Nanomedicine Lab (**Vinit Kumar**, **Stefano Palazzolo**, **Mohamad Hadla**, **Concetta Russo Spena**, **Lucia De Stefano**, **Eva Dreussi**, and **Sara Gagno**) for the enjoyable moments during the three years.*

*A special thanks to my family. Words cannot express how grateful I am to my mother, my father, my brother and my sister for all of the sacrifices that they have made on my behalf. Their prayers for me was what sustained me thus far. At the end I would like to express my special appreciation to my beloved wife **Alaa** who spent sleepless nights with me and was always my support in the moments when there was no one to answer my queries.*

Samer Bayda
(21 December 2016)

Abstract *(English)*

Nanomedicine requires intelligent and non-toxic nanomaterials for real clinical applications. Carbon materials possess interesting properties but with some limitations due to toxic effects. Interest in carbon nanoparticles (CNPs) is increasing because they are considered green materials with tunable optical properties, overcoming the problem of toxicity associated with quantum dots or nanocrystals, and can be utilized as smart drug delivery systems. Using black tea as a raw material, we synthesized CNPs with a narrow size distribution, tunable optical properties covering visible to deep red absorption, non-toxicity and easy synthesis for large-scale production. We utilized these CNPs to label subcellular structures such as exosomes. More importantly, these new CNPs can escape lysosomal sequestration and rapidly distribute themselves in the cytoplasm to release doxorubicin (doxo) with better efficacy than the free drug. The release of doxo from CNPs was optimal at low pH, similar to the tumour microenvironment. These CNPs were non-toxic in mice and reduced the tumour burden when loaded with doxo due to an improved pharmacokinetics profile. In summary, we created a new delivery system that is potentially useful for improving cancer treatments and opening a new window for tagging microvesicles utilized in liquid biopsies.

Abstract *(Italian)*

La traslazione della nanomedicina in ambito clinico richiede l'identificazione di nanomateriali che consentano un approccio intelligente alla malattia senza causare tossicità. In tale ambito può essere iscritta la ricerca sul carbonio, che presenta proprietà interessanti ma anche alcuni limiti dovuti all'insorgenza di effetti avversi. A tal proposito, tanti sforzi si stanno concentrando sulle nanoparticelle di carbonio (CNPs) in quanto hanno origine naturale, presentano proprietà ottiche modulabili e possono essere usati per la messa a punto di sistemi di delivery del farmaco intelligenti. Tali caratteristiche le rendono migliori rispetto ai quantum dots e ai nanocristalli, le cui tossicità son ben note.

Utilizzando tè nero come materiale grezzo, abbiamo prodotto CNPs caratterizzate da una distribuzione molto stretta di dimensioni, proprietà ottiche modulabili (con assorbimento dalla luce visibile al profondo rosso), non tossiche. Il protocollo di sintesi è semplice e applicabile anche su larga scala. Queste CNPs sono state utilizzate per marcare strutture subcellulari come gli esosomi. Abbiamo anche dimostrato che queste tali strutture non vengono sequestrate dai lisosomi e possono rapidamente distribuirsi nel citoplasma rilasciando la doxorubicina (doxo) con miglior efficacia rispetto al farmaco libero. Il rilascio della doxo dalle CNPs risulta ottimale in condizioni di basso pH, simile a quello che accade nel microambiente tumorale. Gli studi *in vivo* hanno dimostrato che le CNPs non sono tossiche e riducono lo sviluppo del tumore quando caricate con doxo, grazie a un miglior profilo farmacocinetico.

In conclusione, abbiamo creato un nuovo sistema di trasporto del farmaco con grandi potenzialità in ambito oncologico nel miglioramento della terapia, aprendo la strada per l'utilizzo di microvescicole funzionalizzate nelle biopsie liquide.

Chapter 1:

Introduction

1. INTRODUCTION

1.1. The history of Nanoscience and Nanotechnology

The prefix *nano* is referred to a Greek prefix meaning *dwarf* or something very small and depicts one billionth of a meter (10^{-9} m). Nanomaterials, refer to the class of materials with at least one of the dimensions in the nanometric range. Nanoscience deals with the study of atoms, molecules and nanoscale particles at scales ranging between 1-100 nm [1]. As a comparison, one must realize that a single human hair has 80 000 nm thickness and that the DNA double helix has 2 nm diameter (**Figure 1**) [2]. The development of nanoscience can be traced to the time of the Greeks and Democritus in 5th century B.C., when people thought that matter could be broken down to an indestructible basic component of matter, which scientists now call *atoms*.

Nanotechnology is one of the most promising technologies of the 21st century. These applications are increasing exponentially because of the extremely small size of a large surface area per unit of volume. According to the National Nanotechnology Initiative (NNI) in the United States, Nanotechnology is defined as the understanding and control of matter at dimensions of 1-100 nm where unique phenomena enable novel applications [3]. This definition suggests two necessary conditions for nanotechnology. The first is an issue of *scale*: nanotechnology is concerned with things of a certain nano size. The second issue has to do with that of *novelty*: nanotechnology does not just deal with small things, but rather must deal with them in a way that takes advantage of some properties that are manifest because of the nanoscale [4].

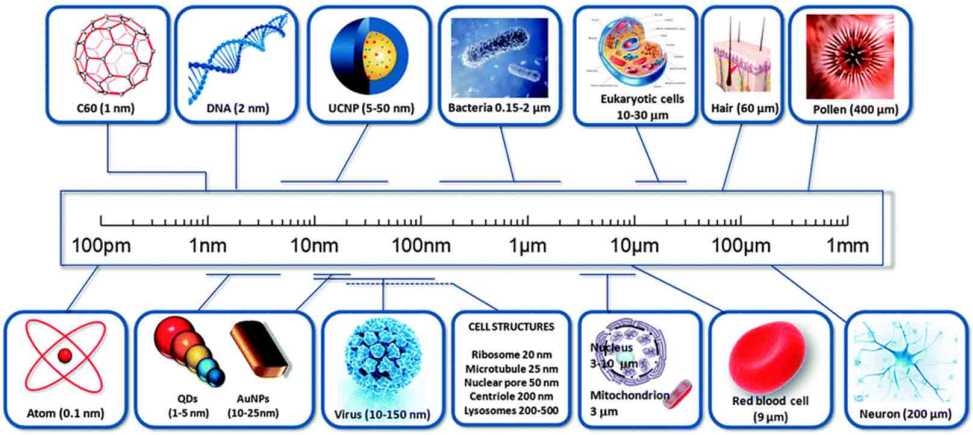

Figure 1: A comparison of Nanomaterials sizes [2]**.**

The concept of nanotechnology is credited to the American physicist and Nobel Prize laureate Richard Feynman. In 1959, during the annual meeting of the American Physical

Society, Feynman presented a lecture entitled "*There's Plenty of Room at the Bottom*" at the California Institute of Technology (Caltech). In this lecture, Feynman make the hypothesis "*Why can't we write the entire 24 volumes of the Encyclopædia Britannica on the head of a pin?*", and described a vision of using machines to construct smaller machines which would, in turn make even smaller machines, and so on down to the molecular level [5]. This novel idea demonstrated new ways of thinking and Feynman's hypotheses have since been proven correct. For these reasons, he is considered the father of modern nanotechnology. Fifteen years after Feynman's lecture, a Japanese scientist, Norio Taniguchi was the first to use the term "nanotechnology" in 1974, and its definition is still valid even today: *"nanotechnology mainly consists of the processing of separation, consolidation and deformation of materials by one atom or one molecule"* [6].

After Feynman staked out the new field of research and awakened the interest of many scientists, two directions of thought arose describing the various possibilities for producing nanostructures. The top-down approach largely corresponds to Feynman's comment on stepwise reduction in the size of already existing machines and instruments. The bottom-up approach revolves around the construction of nanostructures atom for atom by physical and chemical methods and by using and controlled manipulation of the self-organizing forces of atoms and molecules. This theory of "molecular engineering" became popular in 1986 when "*Engines of Creation: The Coming Era of Nanotechnology"* was published [7], the first and controversially discussed book on nanotechnology in which the author K. Eric Drexler described the construction of complex machines from individual atoms, which can independently manipulate molecules and atoms and thereby produce things and self-replicate. The possible uses of such "nanobots" or "assemblers" in medicine are described by K. Eric Drexler, Chris Peterson and Gayle Pergamit in their book "*Unbounding the Future: the Nanotechnology Revolution"* published in 1991 [8], in which the term "nanomedicine" was supposedly used for the first time.

Nanoparticles and structures have been used by humans for quite a long time. For example, an extraordinary work with glass made by the Roman in the fourth century AD demonstrates one of the greatest examples of nanotechnology in the ancient world. The Lycurgus cup, which is part of the collection of the British Museum, represents one of the most outstanding achievements in ancient glass industry. It is probably the oldest and most famous example of dichroic glass. Dichroic glass is the term used to describe two completely different types of glass, which undergo a color change in certain lighting conditions. This means that the

Cup have two different colors: the glass appears green in direct light, and red-purple when light shines through the glass (**Figure 2**) [9].

Figure 2: The Lycurgus cup. The glass appears green in reflected light (A) and red-purple in transmitted light (B) [9]**.**

The explanation for this phenomenon was obtained in 1990 after scientists analyzed the cup using a transmission electron microscopy (TEM) [10]. It was found that the dichroism (two colors) is observed due to the presence of nanoparticles with 50-100 nm in diameter. X-ray analysis showed that these nanoparticles are silver-gold (Ag-Au) alloy, with a ratio of Ag:Au of about 7:3, containing in addition about 10% copper (Cu) dispersed in a glass matrix [11,12]. The red color observed is a result of absorption of light (~ 520 nm) by gold nanoparticles. The red-purple color results due to the absorption by the larger particles while the green color is attributed to the light scattering by colloidal dispersions of silver nanoparticles with size > 40 nm. The Lycurgus cup is recognized as one of the oldest synthetic nanocomposites [1]. A similar effect is seen in some late medieval church windows, which shine a luminous red and yellow because nanoparticles of gold and silver have been fused into the glass. **Figure 3** shows an example of how these nanoparticles of different sizes were applied to stained glass windows [13].

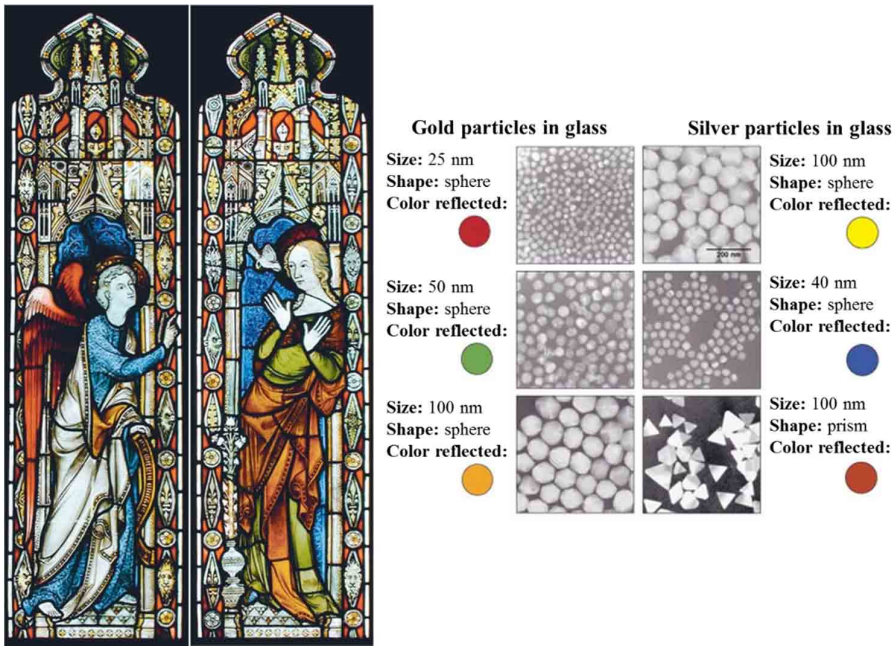

Figure 3*:* Effect of nanoparticles on the colors of the stained glass windows [13]**.**

During the 9th-17th centuries, glowing, glittering "luster" ceramic glazes used in the Islamic world, and later in Europe, contained silver or copper or other nanoparticles [14]. The Italians also employed nanoparticles in creating Renaissance pottery during 16th century [15]. They were influenced by Ottoman techniques: during the 13th-18th centuries, in the making of "Damascus" saber blades, carbon nanotubes and cementite nanowires were used to provide strength, resilience, and the ability to hold a keen edge [16]. These special properties of the colors and materials were already being produced intentionally many hundreds of years ago. Medieval artists and forgers, however, did not know the cause of these surprising effects.

In 1857, Michael Faraday was the first to study the preparation and properties of colloidal suspensions of "Ruby" gold. Those particles are known for their unique optical and electronic properties, which makes them one of the most interesting nanoparticles. It demonstrated how gold nanostructures under certain lighting conditions produces different-colored solutions [17]. Since Feynman's early visionary ideas on nanotechnology, there was progress until in 1981 when a new type of microscope, the Scanning Tunneling Microscope (STM), was invented by the physicists Gerd Binnig and Heinrich Rohrer at IBM Zurich Research Laboratory [18,19]. The STM uses a sharp tip that moves so close to a conductive surface that the electron wave functions of the atoms in the tip overlap with the surface atom

wave functions. When a voltage is applied, electrons "tunnel" through the vacuum gap from the foremost atom of the tip into the surface (or *vice versa*). In 1983, the group published the first STM image of the Si(111)-7x7 reconstructed surface, which nowadays can be routinely imaged as shown in **Figure 4** [20,21].

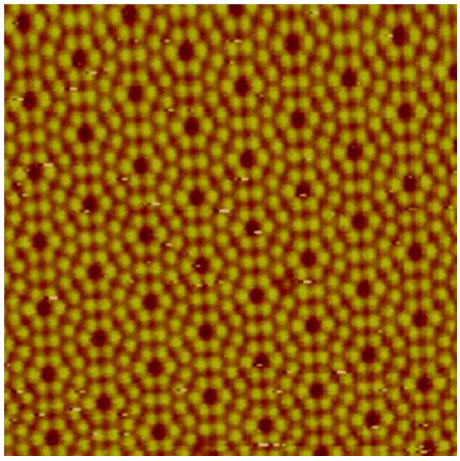

Figure 4: STM image of the Si(111)-7x7 reconstructed surface showing atomic scale resolution of the top-most layer of silicon atoms [21]**.**

A few years later, in 1990, Don Eigler of IBM Almaden and his colleagues used a STM to manipulate 35 individual xenon atoms on a nickel surface and formed the letters of IBM logo **(Figure 5**) [22]. The STM was invented to image surfaces at the atomic scale, but has been used as a tool with which atoms and molecules can be manipulated to create structures. The tunneling current can be used to selectively break chemical bonds or to induce chemical associations.

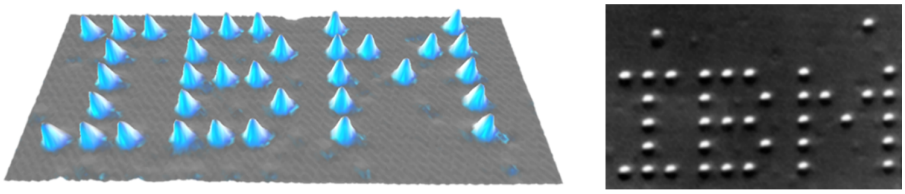

Figure 5: 35 Xenon atoms positioned on a nickel (110) substrate using a STM to form IBM logo [22]**.**

In 1986, Gerd Binnig and Heinrich Rohrer shared the Nobel Prize in Physics "for their design of the scanning tunneling microscope". This invention led to the development of the Atomic Force Microscope (AFM) and a whole range of related Scanning Probe Microscopes (SPM), which are the instruments of choice for nanotechnology researchers today [23,24]. At around the same time, in 1985, Robert Curl, Harold Kroto and Richard Smalley

discovered that carbon can also exist in the form of very stable spheres, which they named fullerenes or buckyballs [25]. The carbon balls with chemical formula C60 or C70 are formed when graphite is evaporated in an inert atmosphere. A new carbon chemistry has developed from this discovery, and it's now possible to enclose metal atoms in them, and to create new organic compounds. Few years later, in 1991, Iijima *et al.* reported Transmission Electron Microscopy (TEM) observations of hollow graphitic tubes or carbon nanotubes, which form another member of the fullerene structural family (**Figure 6**) [26]. The strength and flexibility of carbon nanotubes makes them potentially useful in many nanotechnological applications. Carbon nanotubes are now used as composite fibers in polymers and concrete to improve the mechanical, thermal and electrical properties of the bulk product. They also have potential applications as field emitters, energy storage materials, catalysis and molecular electronics components.

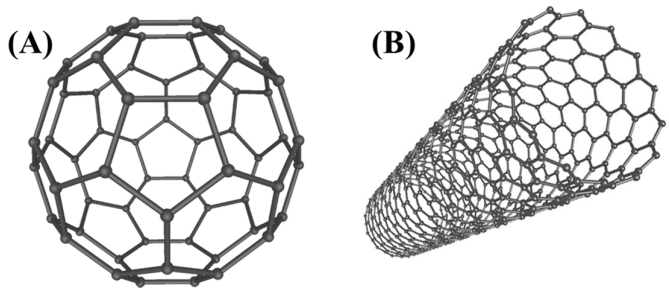

Figure 6: Schematic of a C_{60} buckyball (Fullerene) (A) and carbon nanotube (B).

In 2004, a new class of carbon nanomaterials called carbon dots (C-dots) with size below 10 nm was discovered accidentally by Xu *et al.* during the purification of single-walled carbon nanotubes [27]. C-dots with fascinating properties have gradually become a rising star as a new nanocarbon member due to their benign, abundant and inexpensive nature [28]. Possessing such superior properties as low toxicity and good biocompatibility renders C-dots favorable materials for applications in bioimaging, biosensor and drug delivery [29–33]. Based on their excellent optical and electronic properties, C-dots can also offer exciting opportunities for catalysis, light energy conversion, photovoltaic devices and nanoprobes for sensitive ion detection [34–37].

In 2006, Paul Rothemund at the California Institute of Technology introduced the term "scaffolded DNA origami", which has revolutionized the field of structural DNA nanotechnology by enhancing the complexity and size of self-assembled DNA

nanostructures in a simple "one-pot" reaction [38]. The conceptual foundation for DNA nanotechnology was first laid out by Nadrian Seeman in 1982: *"It is possible to generate sequences of oligomeric nucleic acids which will preferentially associate to form migrationally immobile junctions, rather than linear duplexes, as they usually do"* [39]. DNA nanotechnology has already become an interdisciplinary research area, with researchers from physics, chemistry, materials science, computer science, and medicine coming together to find solutions for future challenges in nanotechnology.

The beginning of 21st century saw an increased interest in the emerging fields of nanoscience and nanotechnology. In the United States, Feynman's concept of manipulation of matter at the atomic level played an important role in shaping national science priorities. President Bill Clinton advocated for funding of research in this emerging technology during a speech at Caltech on 21 January 2000. Three years later, President George W. Bush signed into law the 21st century Nanotechnology Research and Development Act. The legislation made nanotechnology research a national priority and created the National Technology Initiative (NNI).

In this context, **Table 1** presents some important events in the historical development of nanoscience and nanotechnology.

Table 1: Evolution Timeline of Nanoscience and Nanotechnology.

Year	Event	References
4th Century	Lycurgus Cup (Colored glass).	[11]
500-1450	Cathedrals (Stained glasses windows).	[40]
1450-1600	Deruta Pottery (Iridescent/metallic clusters).	[40]
1857	Michael Faraday (Synthesis of colloidal ruby gold nanoparticles).	[17]
1908	Gustav Mie (Light scattering nanoparticles).	[41]
1928	Edward Synge (Near-field optical microscope).	[42]
1931	Max Knoll and Ernst Ruska (Invention of Transmission Electron Microscope (TEM)).	[43,44]
1936	Erwin Müller (Invention of field electron microscope).	[45]

1947	William Shockley, Walter Brattain and John Bardeen (Discovery of the semiconductor transistor).	[46]
1951	Erwin Müller (Invention of field-ion microscope, first to see atoms on the surface).	[47,48]
1953	Watson and Crick (Discovery of DNA).	[49]
1956	Arthur Von Hippel (Molecular Engineering).	[50]
1958	Leo Esaki (Electron tunneling).	[51]
1959	Richard Feynman (There's Plenty of Room at the Bottom).	[5]
1960	Charles Plank and Edward Rosinski (Zeolites and catalysis).	[52]
1963	Stephen Papell (Invention of Ferrofluids).	[53]
1965	Gordon E. Moore (Moore's Law).	[54]
1970	Eiji Osawa (Predicted the existence of C_{60} in the form of icosahedron).	[55]
1974	Norio Taniguchi (First use of the term "Nanotechnology").	[6]
1974	Mark A. Ratner and Arieh Aviram (Molecular electronics).	[56]
1977	Richard P. Van Duyne (Discovery of Surface Enhanced Raman Spectroscopy (SERS)).	[57]
1980	Jacop Sagiv (Discovery of Self-Assembly Monolayers (SAMs)).	[58]
1981	Gerd Binnig and Heinrich Rohrer (Invention of Scanning Tunneling Microscope (STM)).	[59]
1981	Alexey Ekimov (Discovery of nanocrystalline Quantum Dots in a glass matrix).	[60]
1981	Eric Drexler (Molecular Engineering).	[61]
1982	Nadrian Seeman (Development of the concept of DNA Nanotechnology).	[39,62]
1983	Louis Brus (Discovery of colloidal Quantum Dots).	[63,64]

1985	Richard Smalley, Robert Curl and Harold Kroto (Discovery of Buckminsterfullerenes C60).	[25]
1986	Gerd Binnig, Christoph Gerber and Calvin F. Quate (Invention of Atomic Force Microscope (AFM).	[23]
1987	Dimitri Averin and Konstantin Likharev (Single-Electron Tunneling (SET) transistor).	[65]
1990	Donald Eigler and Erhard Schweizer (Arranged of individual Xenon atoms to form the letters IBM).	[22]
1991	Sumio Iijima (Discovery of Multi-wall Carbon nanotubes).	[26]
1992	C.T. Kresge (Discovery of mesoporous silica MCM-41).	[66,67]
1993	Sumio Iijima and Donald Bethune (Discovery of Single-wall Carbon nanotubes).	[68,69]
1996	Chad Mirkin and Robert Letsinger (SAM of DNA+gold colloids).	[70]
1997	Zyvex (First nanotechnology company founded).	[71]
1998	Cees Dekker (Creation of a Transistor using carbon nanotubes).	[72]
1999	Chad Mirkin (Development of Dip-pen Nanolithography (DPN)).	[73]
2000	Mark Hersam and Joseph Lyding (Feedback-Controlled Lithography (FCL).	[74]
2000	President Bill Clinton announces US National Nanotechnology Initiative (NNI).	[75]
2001	Carlo Montemagno (Molecular nanomachines).	[76]
2002	Cees Dekker (Carbon nanotubes functionalized with DNA).	[77]
2003	President George W. Bush signed into law the 21st Century Nanotechnology Research and Development Act.	[78]
2003	Naomi Halas (Development of gold nanoshells).	[79,80]

2004	Andre Geim and Konstantin Novoselov (Discovery of graphene).	[81]
2004	Xu *et al.* (Discovery of Fluorescent Carbon dots).	[27]
2005	James Tour (Nanocar with turning buckyball wheels).	[82,83]
2006	Paul Rothemund (DNA origami).	[38]
2010	IBM (Development of an ultra-fast lithography to create 3D nanoscale textured surface).	[84]

1.2. Nanomedicine

The application of nanotechnology in the medical field is called nanomedicine. Nanomedicine as new branch of science, is a point of interest for many investigators due to the important advances, in particular for cancer treatment. Early diagnosis and effective cancer therapy are required to treat cancer, with approximately 14.1 million new cases and 8.2 million deaths in a year worldwide [85]. Nanomedicine has been defined by the European Science Foundation's (ESF) Forward Look Nanomedicine as follows: *"Nanomedicine uses nano-sized tools for the diagnosis, prevention and treatment of disease and to gain increased understanding of the complex underlying pathophysiology of disease. The ultimate goal is improved quality of life"* [86]. It involves the three main nanotechnology areas of diagnosis, imaging agents and drug delivery with nanoparticles in the 1-1000 nm range, biochips and polymer therapeutics [87,88]. Nanotechnology could overcome many limitations of conventional approaches by reducing side effects, increase tumour accumulation and improve the efficacy of drugs [89–93]. Early pioneers in the modern era of nanomedicine can be traced back to Ilya Metchnikov and Paul Ehrlich, who jointly received the Nobel Prize for medicine in 1908, for their work on phagocytosis [94] and cell-specific diagnostics and cell-targeted therapies [95]. The work on nanoparticles for nanomedicine were increasingly developed in the last 30 years of the 20th century and included liposomes [96–98], DNA-drug complexes [99], polymer-drug conjugates [100–102], antibody-drug conjugates [103], polymer nanocapsules [104–106], polymer-protein conjugates [107], albumin-drug conjugates [108] and block-copolymer micelles [109–111]. Nanotechnology was rapidly developed allowing the incorporation of multiple therapeutics, sensing and targeting agents into nanoparticles in order to set up new devices able to detect, prevent and treat complex disease such as cancer. Nanotechnology represents a

complementary strategy to be integrated with the information derived from the genetic and epigenetic characteristics of the tumours [112,113]. It is well known that chemotherapeutic agents present severe side effects including bone marrow suppression, cardiac and kidney toxicity, hair loss and mucositis. In addition, these drugs are poorly soluble in biological fluids, quickly recognized by the mononuclear phagocyte system (MPS) and cleared from the body [114]. The important properties for a drug delivery system with nanoparticles are biocompatibility and biodegradability of nanoparticles (reduce drug toxicity by encapsulating the free drug), prevention of degradation and clearance of the drug by minimizing protein binding and escaping the immune system, and increasing the tumour accumulation by passive or active targeting [115].

With the advancements in nanotechnology, size, shape, composition, and surface properties of nanomaterials can be precisely controlled during synthesis. More importantly, these properties have been found to play important roles in the design of nanoparticles-based drug carriers with high efficacy (**Figure 7**) [116–119]. Among them, surface functionalization has been considered as the most important factor. For example, inorganic nanoparticles, such as gold or silver nanoparticles, can easily aggregate together in water, as they are hydrophobic. More importantly, when they are injected into the blood flow, the surfaces of inorganic nanoparticles are usually attached with serum proteins due to electrostatic interactions. Thus, these particles will be visible to the immune cells and eventually scavenged through phagocytosis. To overcome these issues, the biocompatible and hydrophilic polyethylene glycol (PEG) polymers have been widely used to decorate the surface of inorganic nanoparticles. With a high grafting density, tethered PEG polymers form a brush on the surface of these nanoparticles, and thus, they can be well-dispersed in water [120,121], reduce the absorption of serum proteins [122,123], increase the circulation time and the accumulation in tumour sites *in vivo* due to the enhanced permeability and retention (EPR) effect [120,124–126].

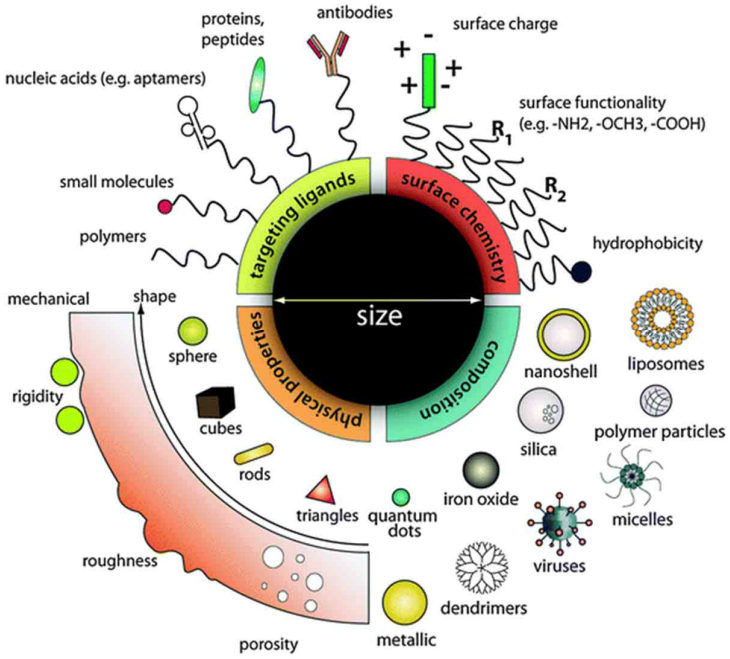

Figure 7: Design of nanoparticles-based drug delivery platform, according to the size, shape, composition and surface properties of nanoparticles [116].

Drug delivery system and more generally nanovectors can be divided into three generations based on their purpose and intended function (**Figure 8**) [127,128]. First-generation nanovectors are composed of a nanoparticle (e.g. liposomes, gold, micelles, etc.) incorporating the agent (e.g. DNA, RNA, chemotherapeutics, etc.). The first generation nanovectors were the first nanoparticles developed and were approved for clinical use more than 20 years ago (e.g. liposomes). They passively accumulate at target lesions due to microenvironment abnormalities (e.g. fenestrations in the vessel walls of tumours). In comparison, the second-generation nanovectors are usually functionalized with biocompatible polymers such as PEG. Under the protection of the tethered polymer layer, these particles could be able to exhibit a prolonged blood half-life time, which in turn helps these nanoparticles to accumulate at the tumour site through the EPR effect [129,130]. Third-generation nanovectors consist of multiple components optimized to fulfill all the tasks required by a drug delivery vector. These tasks include bypassing sequential biological barriers, protecting the drug payload, and releasing the drug payload at the pathological site in a time-dependent manner [131].

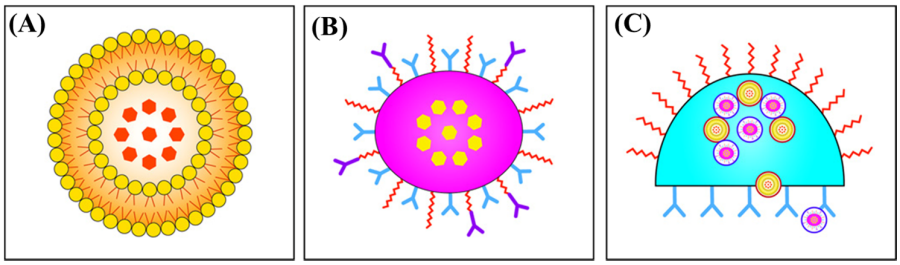

Figure 8: Hierarchy of Nanovectors. (A) First-generation; (B) Second-generation and (C) Third-generation nanovectors [127]**.**

Chapter 2:

Different types of nanostructures for drug delivery

2. DIFFERENT TYPES OF NANOSTRUCTURES FOR DRUG DELIVERY

Over the last few decades, the development of different range of nanoparticles with the ability to tune size, composition and functionality has provided an excellent resource for nanomedicine and can be categorized as organic (liposomes, polymers, micelles and dendrimers) and inorganic nanoparticles (mesoporous silica, gold, silver, quantum dots, magnetic iron oxide and carbon-based nanostructures). These nanoparticles provide great opportunity as drug carriers, due to the easy modification of targeting molecules, controlling drug release by different stimuli, and effective delivery to target sites, resulting in improved of therapeutic efficacy and reduced side effects [132]. Organic nanoparticles differ from inorganic nanoparticles in terms of the principles of fabrication. Inorganic nanoparticles are normally formed by the precipitation of inorganic salts, which are linked in a matrix. The nature of the binding among atoms can be different: covalent, metallic, etc., and the inorganic structure forms a three-dimensional arrangement with linked atoms. In this regard, the closet organic nanoparticles to an inorganic one would be a dendrimer, which is a single-molecule nanoparticle. Most of the organic nanoparticles are formed by several organic molecules, which are driven together by self-organization or chemical binding. For the organic nanoparticles, with the exception of dendrimers, we first need organic molecules that can arrange themselves three-dimensionally. Interactions among the molecules are sometimes not strong like for micelles and vesicles. Self-assembly and the presence of zwitterionic molecules, with polar and nonpolar regions, as the main components of nanoparticles or the means to encapsulate other organic molecules are key elements for the fabrication of many of the organic nanoparticles. Another important difference from inorganic nanoparticles is that many of organic nanoparticles, due to the weak nature of the interactions holding them together, have a dynamic character. Micelles and vesicles can fuse and generate larger particles. The continuous addition of surfactant to a micellar solution can increase the size of the micelles and even force it to change shape from spherical to cylindrical over the second critical micellar concentration (CMC). Sizes can also not always be truly nano for organic nanoparticles as in the case for inorganic nanoparticles. The formation of inorganic nanoparticles sometimes needs only the clustering of a few atoms. In the case of organic nanoparticles, the size and geometry of the organic molecules impose in many cases the limits to going nano. In micelles, which are among the smallest organic nanoparticles, the size is controlled by the length of the surfactant and the smallest sizes to

be achieved are that of a sphere with a radius equal to the length of the surfactant in the micellar phase, typically around 15–20 Å. The lipids forming a vesicle assemble into bilayers because of the relation of their hydrophilic and hydrophobic volume. The bilayers must close in on themselves to make the vesicle, which not only results in an internal volume that can be used for encapsulation but also establishes limits for the smallest reachable size. In this section, various organic and inorganic nanoparticles fabricated by different materials and their applications in drug delivery are illustrated and discussed below. The carbon-based nanostructures will be discussed in details in **Chapter 3**.

2.1. Liposomes

Liposomes are synthetic lipid vesicles with a hydrophilic cavity surrounded by a bilayer of amphiphilic phospholipids such as phosphatidylglycerol, phosphatidylserine, and phosphatidylcholine [133,134]. A phospholipid molecule has a phosphate group on one end, called the "head," and two side-by-side chains of fatty acids that make up the lipid "tails". The phosphate group is negatively charged, making the head polar and hydrophilic. The lipid tails are uncharged, nonpolar, and hydrophobic. Some lipid tails consist of saturated fatty acids and some contain unsaturated fatty acids. The liposomes became an important choice for many drug formulations since their discovery by Alec Bangham and colleagues in 1961 [135]. Liposomes have both a hydrophilic and hydrophobic region, permitting the encapsulation and transport of both therapeutic and diagnostic agents via a variety of methods [136]. Hydrophobic drugs can be enclosed within the phospholipid bilayers, while hydrophilic drugs can be entrapped in the cavity [137]. To avoid the recognition by reticuloendothelial system (RES) and long circulation in bloodstream, PEG molecules (e.g. PEG-DSPE) could be inserted into the liposomes (stealth liposomes) to form a hydrated layer on the liposome surface [138]. Liposome can be classified according to their lamellarity (uni- and multilamellar), size (small ≤ 100 nm, Intermediate 100-250 nm, and large ≥ 250 nm), and surface charge (anionic, cationic, or neutral) (**Figure 9)** [139–141]. The ability to synthetize liposomes with a specific size range makes them important targets for their natural phagocytosis by macrophages, which lead to the release of the encapsulated

drug. The liposomes surface can also be managed with opsonins and ligands to activate the endocytosis in different cell types.

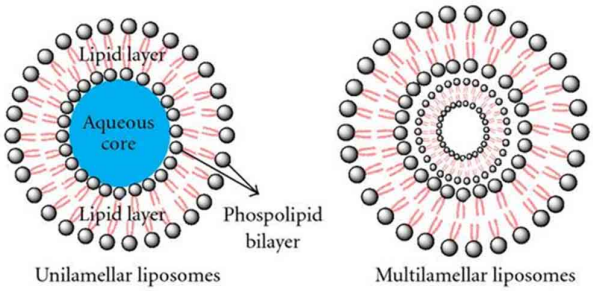

Figure 9: Schematic representation of basic structures of liposomes [139]**.**

Liposomes were the first platform in nanomedicine and represent a versatile system for drug delivery with lots of compound effective at a preclinical stage and more than 200 are under clinical evaluation [120]. The liposome was described by Bangham in 1961 [142], and demonstrate as potential drug delivery system (DDS) in the early 1970s [143–145]. Two decades later in 1990, Ambisome® (liposomal amphotericin B), the first liposomal drug formulation, was approved by FDA and in 1995 was approved the first anticancer liposome formulation (Doxil®). Liposomal nanoparticles are synthesized in order to possess several advantages: they are able to deliver both hydrophilic and hydrophobic molecules [146], their formulation protect therapeutic cargo from the *in vivo* environment and increase circulation half-life, permeability, biodistribution and targeting specificity [147]. These principles were the base on which Barenholz developed the formulation of liposomal doxorubicin (Doxil®) [148]. Doxorubicin is an anthracycline antibiotic that intercalates in DNA helix preventing replication [149,150] and it is used for various type of cancers: breast, lung, gastric, ovarian, sarcoma, myeloma, leukemia and lymphomas [151]. Unfortunately, its poor selectivity toward cancer cells induces severe systemic side effects. In particular, the patients treated with doxorubicin have been experienced severe cardiotoxicity, bone marrow toxicity with consequent myelosuppression [152]. The development of Doxil® and its approval reduces drastically doxorubicin side effects. The first clinical study carried out on Doxil® demonstrated that the new doxorubicin formulation holds a completely different

pharmacokinetic profile, which enhances the circulation time of the drug changing the biodistribution and increasing tumoural accumulation due to the EPR effect [153].
Two key changes in the history of Doxil® were considered real breakthroughs. Firstly, the inclusion of PEG in liposome surface to create a "stealth" particle, which can escape the recognition by the RES. The second major improvement was the remote loading driven by ammonium sulfate gradient to increase doxorubicin loading within each liposome [148].

2.2. Polymeric Nanoparticles

Polymeric nanoparticles have widely studied for their physical and chemical properties and used to encapsulate drugs. They are prepared from biocompatible polymers and can transport drugs in a controlled and targeted way through the surface modification [154]. Polymeric nanoparticles can be synthesized from natural polymers, such as albumin [155], hyaluronic acid [156], dextran [157] and chitosan [158], and from synthetic polymers, such as, poly acrylic acid (PAA), poly glycolic acid (PGA), poly(lactide-co-glycolide) (PLGA), poly lactic acid (PLA), and hyperbranched polymers [159]. Different methods of synthesis of polymeric nanoparticles are investigated depending on the application and drug type. These methods include solvent evaporation, nanoprecipitation, emulsion diffusion and salting out method [160–163].
Albumin is the most abundant protein in plasma and is used widely for the preparation of nanoparticles due to its biodegradability, non-toxicity, availability, hydrophilicity, and easy to prepare [164]. The major advantage of albumin is its high binding capacity for different drugs due to multiple drug binding sites [165]. The drugs can be loaded by electrostatic interaction on the surface of nanoparticles, incorporated into the nanoparticles matrix, or linked covalently to the protein due to the presence of surface reactive groups such as

amines, thiols, and carboxylic acids [166], and released through hydrolysis, diffusion, or enzymatic degradation of nanoparticles (**Figure 10**) [167].

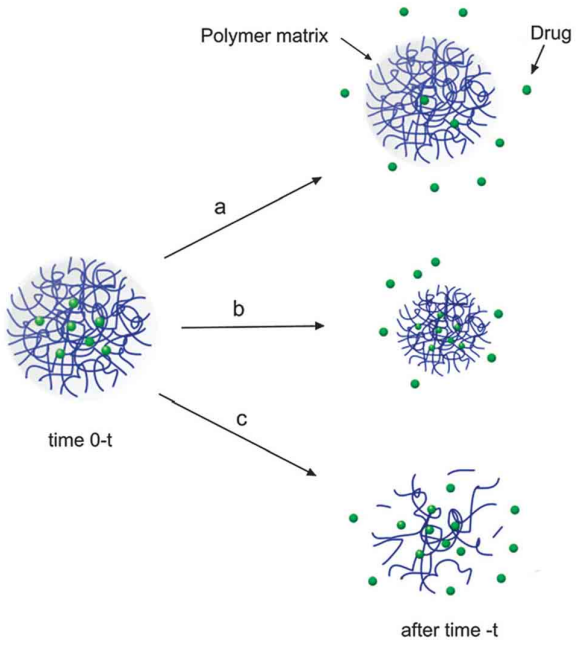

Figure 10: Drug release mechanism from polymeric nanoparticles: (a) diffusion from polymer matrix, (b) degradation of polymer matrix, and (c) biodegradation of polymer matrix due to the hydrolytic degradation [167]**.**

Among the synthetic polymers, PLA and PLGA are polyester and commonly used in drug delivery due to their biocompatibility and controlled release through the hydrolysis of ester bonds [159,168]. PLA is a polyester homopolymer and synthesized by polycondensation of lactic acid or by ring-opening polymerization (ROP) of lactide (**Figure 11A**) [169]. PLA nanoparticles have been used in drug delivery to encapsulate hydrophobic compounds and improve solubility limitations [170]. Due to its high crystallinity and low degradation rate, PLA nanoparticles have slow drug release [171]. To overcome this limitation, researchers synthesized co-polymers of lactides, PLGA and PEG-PLA [162]. PLGA is one of the most widely used biodegradable polymers for the development of nanomedicine because it can be degraded by hydrolysis of ester bonds and break down into their monomers, lactic acid (LA) and glycolic acid (GA) which are excreted from the body (**Figure 11B**) [172]. The ratio of PLA to PGA can be tuned to influence the degradation of PLGA and release the drug molecule, due to the difference in hydrophobicity of PLA and PGA from the presence

of methyl group in PLA [173]. The release rate of drugs can be adjusted from a scale of days to months [174–176].

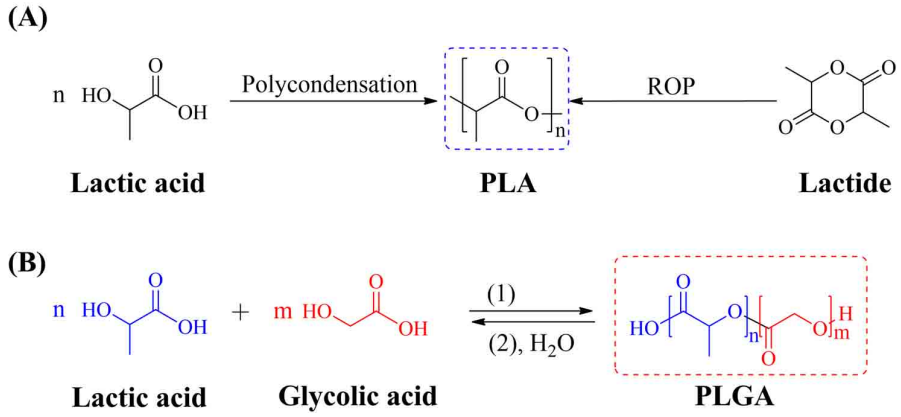

Figure 11: (A) Synthesis of PLA by polycondensation of lactic acid or by ring-opening polymerization (ROP) of lactide. (B) (1) Synthesis of PLGA by polycondensation of lactic acid and glycolic acid, and (2) hydrolysis of PLGA.

In order to enhance the solubility and drug loading capacity of PLGA (or PLA), PEG has been copolymerized with PLGA (or PLA) to form PEG-PLGA (or PEG-PLA). The modification of the surface of nanoparticles by PEG (PEGylation), make them sterically stable, enables the nanoparticles evasion of the reticuloendothelial system (RES) and improve blood circulation time [177–179].

Abraxane was the first drug formulation of this category approved by FDA in 2005. Abraxane is an albumin-bound (Nab) paclitaxel formulation. Paclitaxel, discovered in 1962, is a natural compound extracted from the bark of western yew (*Taxus brevifolia*) [180] and is widely used for the treatment of breast, lung and advanced ovarian cancer [181]. The high hydrophobicity of paclitaxel limits its clinical application. To overcome poor water solubility, a formulation of a nonionic surfactant Cremophor EL (polyethoxylated castor oil) and ethanol (1:1, v/v) is used to dissolve paclitaxel for clinical use [182]. However, the presence of Cremophor EL causes allergic, hypersensitivity and anaphylaxis reactions in animals and humans [181]. To overcome these side effects and deliver paclitaxel safely, a new paclitaxel formulation was needed. Paál *et al.* develop a formulation which is Cremophor EL free [183]. This formulation is non-covalent binding of paclitaxel to albumin, known as Abraxane™. Albumin is the major component of plasma protein and is a natural carrier of hydrophobic molecules such as vitamins, hormones, and other water-insoluble plasma substances [184,185]. In addition, albumin is involved in endothelial transcytosis through the binding of a cell surface receptor glycoprotein (gp60) called albondin [186] and

is also demonstrated that albumin is recognized by SPARC, a secreted acidic protein rich in cysteine, that appears to be up-regulated in many malignancies (breast, lung and prostate cancer), which can interact with albumin and increase the accumulation of albumin-bound drugs in the tumour [184]. Albumin stabilizes the paclitaxel particles at an average size of 130 nm, which prevents any risk of capillary obstruction and does not necessitate any particular infusion systems or steroid/antihistamine premedication before the infusion [187]. Abraxane possesses a reduced treatment volume and time required for administration. Antitumour activity and mortality were assessed in nude mice bearing human tumour xenografts (lung (H522), breast (MX-1), ovarian (SK-OV-3), prostate (PC-3), and colon (HT29)) treated with Nab or cremophor-based paclitaxel. In tumours, Abraxane had a significantly increased efficacy compared with cremophor-based paclitaxel, the difference was higher in breast (MX-1) and in ovarian (SK-OV-3) xenografts. There were more tumour free survivors (100 vs 20% for breast, 24% vs 0% for ovarian), with a significantly longer time to recurrence (103 vs 22 days for breast, 63 vs 26 days for ovarian) in the Nab-paclitaxel treated mice. This evidence was also highlighted in prostate (PC-3; 48 vs 26 days) and in colon (HT-29; 36 vs 26 days). The area under the curve (AUC) of drug concentration in tumour was 33% higher for Abraxane versus Cremophor-based paclitaxel, indicating more effective intratumoural accumulation of Nab-paclitaxel.

2.3. Micelles

In 1913, J.W. McBain introduced the term “micelle” into surface and colloidal chemistry in the context of the association of surfactant molecules in aqueous solution. Micelles are colloidal particles formed by amphiphilic molecules (block copolymers or surfactants). Amphiphilic molecules are prone to self-assemble into various nanostructures driven by hydrophobic effect. Therefore, amphiphilic polymers containing both hydrophilic and hydrophobic blocks have been extensively studied for use in drug delivery. Micelles contain polar head groups that usually form the outside as the surface of micelles. The head groups could be cationic, anionic or neutral groups. They face to the water because they are polar and hydrophilic. The hydrophobic tails are inside and away from the water since they are nonpolar and suitable for hydrophobic cargo. Depending on the type of amphiphilic molecules, micelles can be divided into lipid micelles, and polymeric micelles. Different from the lipid bilayer structure of liposomes, the lipid micelle is a monolayer structure with hydrophilic heads facing the outside aqueous medium and lipophilic tails forming the inner

core. Depending on the composition, concentration of surfactants, temperature and pH, the shape of micelles can be spherical, ellipsoidal, rode-shaped, reversed micelles, or lamellar [188,189]. By controlling the hydrophilic/hydrophobic balance, various nanostructures, such as spherical micelles, cylindrical micelles, and vesicles, can be formed from amphiphilic polymers. According to Won *et al.*, the weight fraction of the hydrophilic block (f_{Phil}) can play a vital role in controlling the shapes of nanostructures from amphiphilic polymers in a pure water medium [190]. At f_{Phil} = 55–70%, spherical micelles are predominantly formed; at f_{Phil} = 45–55%, cylindrical micelles tend to form; at f_{Phil} = 20–40%, vesicles are favored. Both polymeric micelles and vesicles are the most common and stable morphological structures of amphiphiles in water [191]. Polymeric micelles consist of a core and shell structure; the inner core is the hydrophobic part of the block copolymer, which encapsulates the poorly water-soluble drug, whereas the outer shell or corona of the hydrophilic block of the copolymer protects the drug from the aqueous environment and stabilizes the polymeric micelles against recognition *in vivo* by the reticuloendothelial system (RES). Meanwhile, polymeric vesicles possess bilayer structures with an aqueous interior core, isolating the core from the external medium (**Figure 12**) [191,192]. Polymeric vesicles can encapsulate hydrophilic molecules within the aqueous interior and also integrate hydrophobic molecules within the membrane. Therefore, polymeric vesicles have the capability to deliver hydrophilic as well as hydrophobic drugs such as anticancer drugs, genes, and proteins.

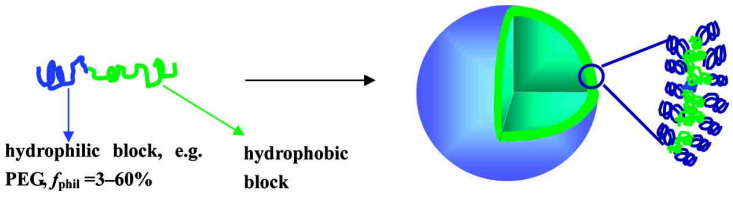

Figure 12: Polymeric vesicles derived from asymmetric block copolymers [191].

At low concentration, the amphiphilic molecules align at the interface (liquid/air or liquid/oil), their hydrophilic head oriented toward the aqueous phase and the hydrophobic tail to the other, and reduce the surface tension between them. When the concentration increases, the whole surface will be covered of amphiphilic molecules. At that moment, they start to assemble to a micellar structure. The lowest concentration at which micelles are formed is called the critical micelle concentration (CMC). The concentration of free amphiphilic molecules is constant as the micelle concentration increases, and they exist in

dynamic equilibrium (**Figure 13**). Below CMC, they will dissociate into single polymer chains and thus lose the function as drug carriers. In order to avoid the dissociation of the self-assembled nanostructures, linking the polymers to obtain nanogels which are more stable in different conditions has become a common and effective approach. In recent years, nanogels have drawn increasing attention because of their high loading capacity and good stability [193]. However, the lipid micelles have two limitations: the low drug loading capacity due to the small hydrophobic core, and the dissociation upon dilution *in vitro* and *in vivo* [194]. Polymeric micelles are prepared by a self-assembly process using hydrophilic and hydrophobic block copolymers to form a hydrophilic shell and a hydrophobic core [195,196]. These cores are generally spherical and nano-sized (10–100 nm) and can be used as nano-containers for the efficient loading of hydrophobic drugs or agents [197–199]. Thus, hydrophobic drugs that incorporate the micelles are effective drug delivery systems.

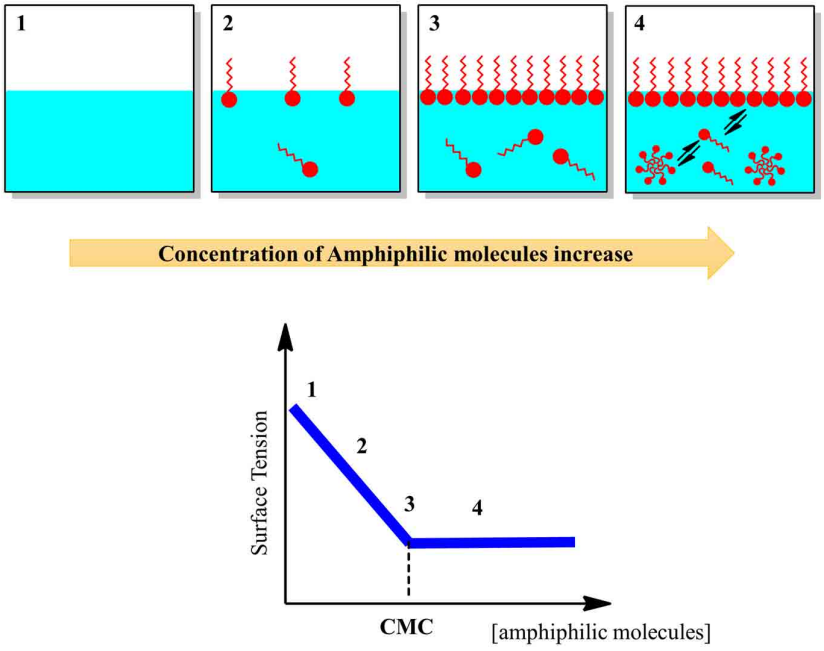

Figure 13: Formation of Micelles.

PLGA is one of the most popular hydrophobic polymers used as a core for drug encapsulation and break down the ester bonds in the body, resulting in the release of the drug [200]. Poly(ethylene-glycol) (PEG) polymers are usually adopted as the hydrophilic

segments of micelles [197,201,202] because they provide a brush-like stability corona that increases the circulatory half-time of micelles in the blood stream [130,203].

There are two routes to load drug using the amphiphilic micelle structure by chemical conjugation [204] or physical entrapment [205], and the respective drug release processes are dependent on the type of encapsulation. In the chemically conjugated drug, a non-water soluble drug as a hydrophobic core of the micelle, is conjugated to the hydrophilic polymer backbone [206] and the release occurs by bulk degradation of polymer matrix or surface erosion, whereas the physically entrapped drug is formed by the encapsulation of hydrophobic drugs into the core of a core-shell nanostructures during the self-assembly process via hydrophobic interactions [207]. Other factors that affect drug release are partition coefficient, amount of drug loaded, length of the core-forming part of the polymer, and presence and extent of cross-linking in the core.

Recent research has focused on stimulus-sensitive (smart) nanostructures for drug delivery because it is a superior approach for delivering and releasing drugs to specific site at the desired time. Many kinds of stimuli, including chemical (e.g., redox, pH), physical (e.g., temperature, light), and biological (e.g., enzymes), have been exploited in the design of smart drug delivery systems [193]. For example, a cholesterol modified amphiphilic copolymers poly((hydroxyethyl methylacrylate)-*co*-(2-(diethylamino)ethyl methacrylate))-*b*-poly(poly(ethylene glycol) methyl ether methacrylate) (Chol-*g*-P(HEMA-*co*-DEAEMA)-*b*-PPEGMA) is used with specific pH-sensitive/hydrophilic/hydrophobic structures containing different ratios of pH-sensitive PDEAEMA segments and synthesized via the combination of activators regenerated by electron transfer atom transfer radical polymerization (ARGET ATRP) and alcoholysis reaction. During the process of micellization, cholesterol formed the core of the polymeric micelle, random pH-sensitive PDEAEMA/hydrophilic PHEMA comprised the middle layer, and the PPEGEMA distributed and stretched dendritically on the surface of the polymeric micelles. Their three-layered self-assembled micelles were used as doxorubicin (DOX) delivery carriers (**Figure 14**) [208]. Currently, several micellar formulations for cancer therapy are under clinical

evaluation, but only Genexol-PM has been approved by FDA in 2007 for the treatment of breast cancer.

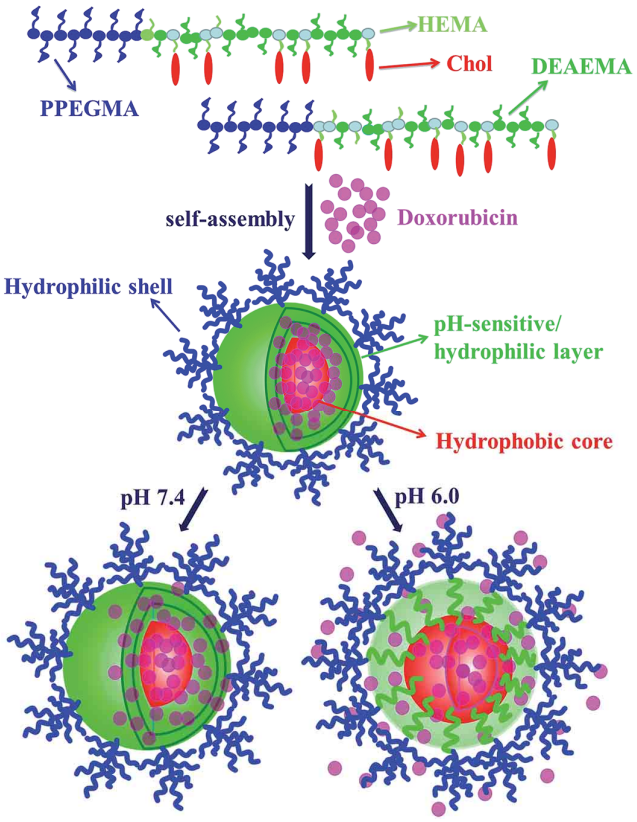

Figure 14: Scheme of drug entrapping and pH-dependent release from the polymeric micelles [208]**.**

Genexol-PM is based on the development of polymeric micelles formulation of paclitaxel. The formulation of micelles is based on biodegradable amphiphilic di-block copolymer comprised of monomethoxy poly(ethylene-glycole)-block-poly (D,L-lactide) (mPEG-PDLLA). Like Abraxane, this formulation avoiding the employment of lipid-based solvent (Cremophor EL). The first preclinical study compared the *in vivo* efficacy, toxicity and biodistribution of Genexol-PM to cremophor-EL based paclitaxel [209]. The increasing of MTD and the lethal dose 50 (LD_{50}) of Genexol-PM compared to classical paclitaxel formulation demonstrated that is a less toxic formulation. Administered in animals at the same dose of lipid-based paclitaxel, Genexol-PM resulted with the same concentration in

plasma with an increased accumulation (2-3 fold higher) in heart, lungs, kidneys and spleen. Importantly, Genexol-PM also resulted in 2-fold higher levels of paclitaxel in tumours.

2.4. Dendrimers

Apart from these nanostructures, dendrimers with three-dimensional, hyperbranched globular nanopolymeric architectures have been the research focus of many scientists these years. The term dendrimer, first proposed by Tomalia in 1985, was chosen due to its structural shape, with highly branched, three-dimensional features that resemble the architecture of a tree [210]. A typical dendrimer consists of three main structural components: (a) a focal core, (b) building blocks with several interior layers composed of repeating units, and (c) multiple peripheral functional groups (**Figure 15**). The branched units are organized in layers called ‘‘generations’’, and represent the repeating monomer unit of these macromolecules [211].

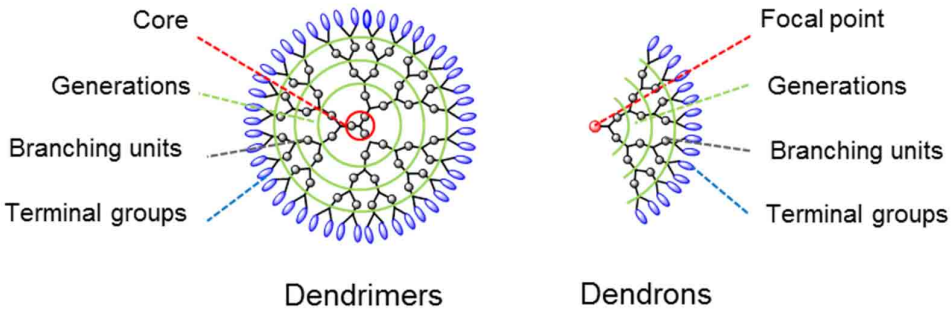

Figure 15: Typical architecture of a fourth generation (G4) dendrimer.

Two major synthetic strategies are used for the synthesis of dendrimers, namely, the divergent (core to periphery) and convergent (periphery to core) approach. Both synthetic strategies possess relative advantages and disadvantages and the appropriate route depends mainly on the kind of monomer employed and the target polymer structure [212–214]. Due to their attractive features like nanoscale size, narrow polydispersity index, excellent control over molecular structures, and availability of multiple functional groups at the periphery and cavities in the interior [215], dendrimers have been explored to be used in the delivery of different bioactive agents such as drugs [216], oligonucleotides [217], enzymes [218], vaccines [219], and genes [220].

In the last two decades, the development of dendrimers as potential drug vehicles is one of the most active areas of biomedical and pharmaceutical sciences. Dendrimers offer several featured advantages as drug carrier candidates. These advantages include: (1) high density

and reactivity of functional groups on the periphery of dendrimers that make multifarious bioactive molecules to be easily modified onto the surface [221,222] (2) well-defined globular structure, predictable molecule weight and monodispersity of dendrimers ensure reproductive pharmacokinetics [223], (3) controllable size (generation-dependent) of dendrimers satisfies various biomedical applications [224], (4) high penetration abilities of dendritic structures through the cell membrane cause increased cellular uptake level of the drugs complexed or conjugated to them [225], (5) the lack of immunogenicity of dendrimers makes them much safer choices than synthesized peptide carriers and natural protein carriers [225], (6) enhanced penetration and retention (EPR) effect of dendrimers offers preferential uptake of the materials by cancer tissues [226], (7) well-established methodologies proposed to construct nanodevices with various functional moieties based on dendrimers provide miscellaneous biomedical applications of these promising materials, such as cancer targeting therapy, magnetic response imaging, photodynamic therapy, and neutron capture therapy [227], (8) Perfectly programmed release of drugs molecules or other bioactive agents from dendrimers leads to reduced toxicity, increased bioavailability and a simplified dosing schedule [227,228]. Prolonged residence time of the drug in the blood and protection of the bioactives from their environment with increased stability are other potential advantages of dendrimeric architecture [229]. Different types of dendrimers, include polyamidoamine (PAMAM), polypropylene imine (PPI), polylysine dendrimers have been used as host for both hydrophilic and hydrophobic drugs. The ideal dendrimer carrier should exhibit high aqueous solubility and drug-loading capacity, biodegradability, low toxicity, favorable retention and biodistribution characteristics, specificity, and appropriate bioavailability [230]. Two strategies are used for the application of dendrimers to drug delivery: drug conjugation to dendrimers and drug encapsulation by dendritic structure (**Figure 16**). Firstly, the drug molecules can be covalently attached onto the surface or other functionalities to afford dendrimer–drug conjugates; secondly, the drug molecules can be physically entrapped inside the dendrimers.

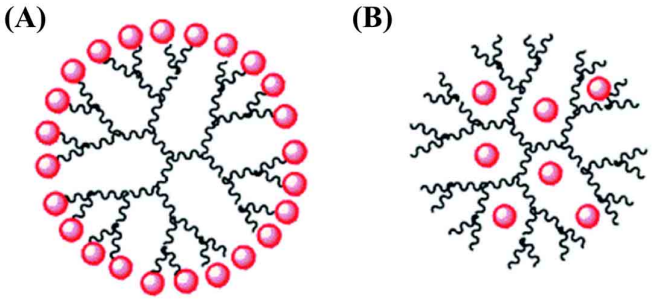

Figure 16: Types of Interactions using dendrimers. (A) Drugs covalently linked to dendrimers, and (B) Drugs entrapped inside the dendrimers.

Dendrimer-drug conjugates

Dendrimer-drug conjugates generally consist of an anti-neoplastic agent covalently attached to the peripheral groups of the dendrimer. This method offers distinct advantages over drug-encapsulated systems. Multiple drug molecules can be attached to each dendrimer molecule and the release of these therapeutic molecules is partially controlled by the nature of the linkages. The grafting of drugs to dendrimers has also been proposed to overcome resistances induced by monomeric drugs. For instance, *trans*-diaminochloroplatinum moieties have been linked to a small poly(propyleneimine) (PPI) dendrimer (**Figure 17**). It was shown that this dendrimer is equally toxic towards cisplatin-sensitive and cisplatin-resistant leukemia cell lines, but less toxic in both cases than cisplatin. This unexpected result was ascribed to difficulties to cross the cell barrier [231].

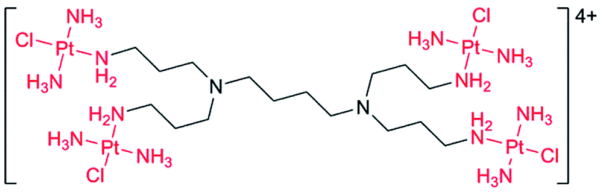

Figure 17: First generation poly(propyleneimine) (PPI) dendrimer ended by platinum, in order to overcome cisplatin resistance [231]**.**

Gurdag *et al.* reported the synthesis of polyamido amine (PAMAM)-methotrexate (MTX) conjugates from carboxylic acid-terminated G2.5 PAMAM (conjugate A) or amine-terminated G3 PAMAM (conjugate B) in order to assess the activity of dendrimer-delivered methotrexate to sensitive and resistant human acute lymphoblastoid leukemia (CCRF-CEM) and Chinese hamster ovary (CHO) cell lines [222]. Although both polymers were conjugated to the drug by the formation of amide bonds, the carboxylic acid-conjugated G2.5 PAMAM system showed increased sensitivities of 8- and 24-fold towards the MTX-resistant cell lines

CEM/MTX and RII, while amine-conjugated G3 PAMAM showed no such increases compared to free methotrexate. The differences in cytotoxicity of these amide-bonded conjugates may be indicative of differences in the intracellular drug release from the cationic dendrimer (conjugate B) versus the anionic dendrimer (conjugate A), perhaps due to the differences in lysosomal residence times dictated by the surface functionality. The results indicate the potential of dendrimer-drug conjugates for the treatment of cancer cells, particularly those that have demonstrated resistance to chemotherapeutics.

Another example of stochastic functionalization concerns methotrexate (MTX) and the TAMRA (tetramethylrhodamine) fluorophore conjugated to PAMAM dendrimers by copper-free click chemistry. Such a reaction produces serum stable linkages (**Figure 18**). The binding avidity of the dendrimer-MTX to the folic acid receptor is enhanced by a factor of 857 relative to a free MTX molecule, but the conjugate was comparatively less toxic than free MTX towards B16–F10 (melanoma) cells [232].

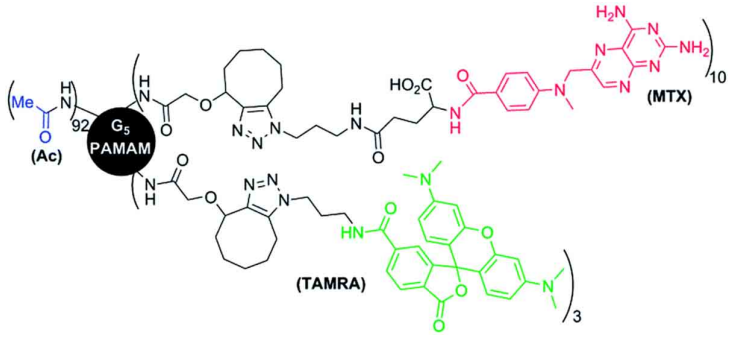

Figure 18: Stochastic grafting of methotrexate (MTX) by a stable bond to PAMAM G5 dendrimers [232]**.**

In a comparative study, doxorubicin (DOX) was conjugated to G4 PAMAM dendrimers either through a non-cleavable amide group (a PEG-PAMAM-succinic-DOX (PPSD) conjugate) or an amide group cleavable under acidic conditions (a PEG-PAMAM-cis-aconityl-DOX (PPCD) conjugate) (**Figure 19**). PEG derivative was utilized to enhance the conjugate water solubility, reduce toxicity for healthy cells, induce longer half-life in serum and enhanced tumour uptake. Both types of conjugates (PPSD and PPCD) were internalized by Skov-3 cells (ovarian carcinoma), and delivered to acidic lysosomes. However DOX was released only from the cleavable PPCD conjugates, and diffused into the nuclei, inducing cell death. The non-cleavable PPSD conjugates were found non-toxic to these cells [233].

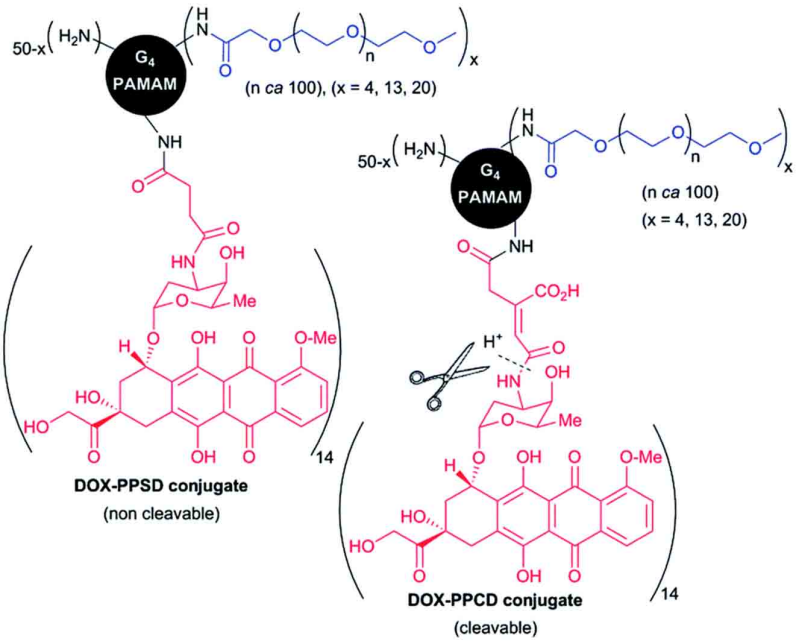

Figure 19: Fourth generation PAMAM dendrimers stochastically modified with DOX through a non-cleavable or cleavable bond [233]**.**

Paclitaxel, a poorly soluble anticancer drug, was covalently conjugated with PEG or G4-PAMAM to compare the anti-cancer activity of the drug delivered by a linear or dendritic carrier [234]. Both PEG and PAMAM increased the aqueous solubility of paclitaxel (0.3 µg/mL) dramatically to 2.5 mg/mL and 3.2 mg/mL respectively. Upon exposure to human ovarian carcinoma A2780 cells, free paclitaxel accumulated in the cytoplasm near the plasma membrane. The polymer conjugates tended to distribute intracellularly in a more homogenous fashion compared to free drug. PEG-paclitaxel conjugates reduced the efficacy of the drug 25-fold, but the PAMAM-paclitaxel conjugates decreased the IC50 more than 10-fold when compared against free drug, leading to the conclusion that the availability of a drug is dramatically influenced by the architecture of its polymer conjugate.

Drug-encapsulated dendrimers

The covalent linkage of drugs to dendrimers generally necessitates the chemical modification of both the drug and the dendrimer. In order to simplify the molecular design, the simple encapsulation of an unmodified drug inside a dendrimer has been proposed (**Figure 16B**), in particular for low water-soluble drugs [235]. Poly(glycerol succinic acid) dendrimers, or PGLSA dendrimers, were investigated as delivery vehicles for camptothecins, a group of naturally-derived hydrophobic compounds with anti-cancer activity. In a preliminary study reported by Morgan *et al.*, G4-PGLSA dendrimers with

hydroxyl (G4-PGLSA-OH) or carboxylate (G4-PGLSA-COONa) peripheral groups were used to encapsulate 10-hydroxycamptothecin (10-HCPT) for delivery to cancer cells [236]. Upon exposure to MCF-7 human breast cancer cells, unloaded dendrimer showed no cytotoxic effects, while 10-HCPT-encapsulated dendrimers led to significant cytotoxicity with less than 5% of viable cells at higher concentrations (20 μM). An alternative triblock structure was explored by introducing a 3400 molecular weight PEG core to the G4-PGLSA dendrimer to afford $(G4\text{-}PGLSA\text{-}OH)_2\text{-}PEG_{3400}$ [237]. A 20-fold increase in 10-HCPT water solubility was observed following encapsulation. The anti-cancer activity of the macromolecule/drug complex was examined using HT-29 human colon cancer cells and similar cytotoxicities were reported for encapsulated and free 10-HCPT. The conclusions drawn from these two studies led to the selection of G4-PGLSA-COONa dendrimer as a delivery vehicle for 10-HCPT and 7-butyl-10-aminocamptothecin (BACPT), a highly potent lipophilic camptothecin derivative. Anti-cancer activity was investigated for a human cancer cell line panel including breast adenocarcinoma (MCF-7), colorectal adenocarcinoma (HT-29), non-small cell lung carcinoma (NCI-H460), and glioblastoma (SF-268). The most potent formulation is with the dendrimer encapsulating 7-butyl-10-aminocamptothecin (BACPT), used towards lung cancer cells (**Figure 20**). This formulation increases aqueous solubility, induces more BACPT uptake, and increases retention, providing a rationale for the increased cytotoxicity observed [238].

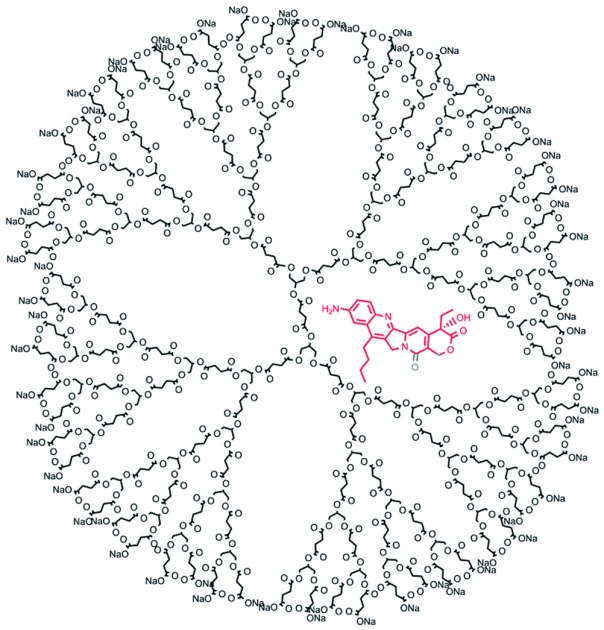

Figure 20: PGLSA dendrimer for the encapsulation of the camptothecin derivative BACPT [238]**.**

Dendrimers based on melamine have been used also to dissolve MTX and 6-mercaptopurine (anti-cancer agents) that are known as hepatotoxins (**Figure 21**). C3H mice received subchronic doses of drug-encapsulated dendrimers and alanine transaminase (ALT) levels were evaluated to determine hepatotoxicity. A significant reduction in hepatotoxicity has been observed *in vivo* for mice with the drugs entrapped in the dendrimer [239].

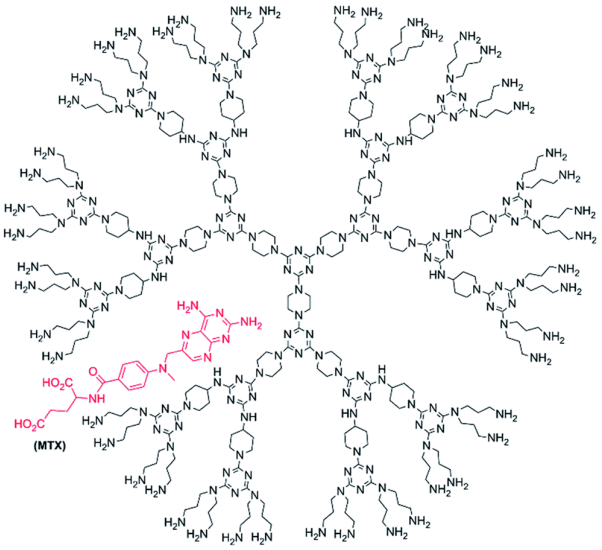

Figure 21: Melamine dendrimer for the encapsulation of MTX [239]**.**

Doxorubicin-G4-PAMAM complexes have been encapsulated into liposomal formulations for potential local delivery to locations such as skin metastasis from breast cancer [240]. The dendrimer-drug complex was incorporated into one of two formulations to modulate release compared to doxorubicin-liposomal systems. The first formulation was comprised of egg phosphatidylcholine, stearylamine, and the anti-tumour ether lipid hexadecylphosphocholine (HePC), while the second formulation did not include HePC. Incorporation efficiencies were above 90% and slow release was achieved with less than 20% released over 48 h for both systems. Cytotoxicity was assessed based on doxorubicin (DOX) activity on several cancer cell lines DMS114 and NCI-H460 (small cell lung cancer and non-small cell lung cancer, respectively), HT29 and HCT116 (colon), MDA-MB435 and MCF7 (breast), DU145 (prostate), and SF268 (central nervous system). The doxorubicin-PAMAM liposome formulation with HePC showed the highest activity against most of the cell lines, with enhanced activity towards MDA-MB435 breast cells compared to the dendrimers conjugate alone, and high sensitivity towards DMS114 and NCI-H460 lung cancer cells.

Therefore, the complexation of drugs to dendrimers via hydrophobic encapsulations or electrostatic interactions usually preserves the chemical integrity and pharmacological properties of drugs, while covalent attachment of drugs to the surface groups of dendrimers through chemical bonds is more suitable for a better control over drug release than can be achieved by simple encapsulation/electrostatic complexation of drugs into/with the dendrimers [241,242]. For this reason, drug-encapsulated dendrimer systems may best be utilized via direct intratumoural injection.

2.5. Mesoporous Silica Nanoparticles

Mesoporous silica nanoparticles (MSN) discovered in 1992 by the Mobile Oil Corporation have received intensive attention due to their monodispersity, high specific surface area, tunable pore size and diameter, and versatile functionalization [243,244]. MSN are synthesized in the presence of assembled cationic surfactant micelle templates, which serve as structure-directing agents for polymerizing silica component by electrostatic interaction (**Figure 22**) [245].

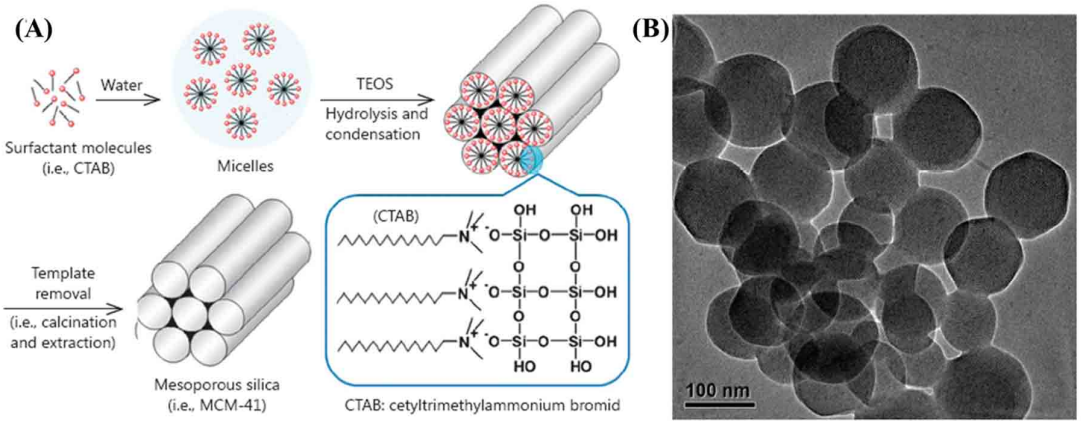

Figure 22: Synthesis scheme for the preparation of MSNs (A) and transmission electron microscopy (TEM) images of MCM-41 (B) [245]**.**

In 1968, Stöber *et al.* first discovered an effective method for the synthesis of monodispersed silica particles, which involves the hydrolysis of tetraalkyl silicates in a mixture of alcohol and water using ammonia as a catalyst [246]. The ‘‘Stöber method’’ has since been investigated widely, and subsequently particles with diameters ranging from tens of nanometers to a few microns have been obtained. With the Stöber method, excellent control can be obtained not only in the synthesis of silica particles but also in that of non-silica ones [247,248]. Based on a Stöber-like approach, it is possible to synthesize mesoporous silica

nanoparticles of a uniform size by modifying the reaction compositions. Grun *et al.* first modified the Stöber synthetic compositions by adding a cationic surfactant to the reaction mixture and obtained the submicrometer-scaled MCM-41 spherical particles [249]. Since then, mixtures of alcohol, water and ammonia have been widely used with different template systems to prepare uniform MSNs with different pore sizes and mesostructures. Later, Nooney *et al.* used both cationic surfactants (cetyltrimethylammonium bromide (CTAB)) and neutral surfactants (n dodecylamine) as templates, and showed that MSNs with a wide range of diameters from 65 to 740 nm can be obtained by simply varying the Tetraethyl orthosilicate (TEOS)–surfactant ratio under dilute conditions [250]. It is noted that when an aprotic cosolvent was used to create a homogeneous condition, spherical MSNs with smooth surfaces were formed. Mou and co-workers developed a strategy for synthesizing mono-disperse MSNs by separating the nuclei formation and particle growth into two steps [251], and subsequently modulated the size of the MSNs by controlling the pH (10.86–11.52) of the reaction solution [252]. Qiao *et al.* found that the size of MSNs increases from 30 nm to 85 nm with the decrease in pH from 10.0 to 6.0 presumably due to an decreased condensation rate [253]. It is worth noting that Chiang *et al.* systematically investigated the effects of the key reaction conditions (e.g., amount of TEOS, pH value, and reaction time) on the resulting MSNs, and concluded that the pH value is the dominant parameter influencing particle size [254].

MCM-41 as one of the importantly synthesized mesoporous materials [66], has been firstly employed as a drug delivery matrix. MCM-41 has been widely studied due to its attractive features, such as stable honeycomb mesoporous structure, large surface area (>1000 m^2/g), narrow tunable pore size (2–10 nm), and well-defined surface properties. Other groups of mesoporous materials with larger pore size such as SBA including SBA-15, SBA-16, SBA-1, SBA-3, HMS, and MSU were also used for drug delivery. For drug delivery based on mesoporous materials, several investigations using organic modified mesoporous silica have been reported [255]. MSN were designed for diagnostic (fluorescence imaging [251,256] and/or MRI [257–259]), and for therapy (drug delivery [260,261] or photodynamic therapy [262–268]). Many different drugs have been successfully loaded in MSN or covalently grafted at MSN, such as camptothecin [244], paclitaxel [269,270], doxorubicin [271,272], methotrexate [273], cysteine [274], telmisartan [275], and chlorambucil [276].

The particle size of MSN can be tuned from 50 to 300 nm allowing facile endocytosis without any significant cytotoxicity. MSN is more stable to heat, pH, mechanical stress, and

hydrolysis-induced degradations, compared to other polymer-based drug carriers. The uniform pore size distribution of MSN is very narrow and the pore diameter can be tuned between 2 and 6 nm. These features allow one to adjust the loading of different drug molecules and to study the kinetics of drug release with high precision. The high surface area (>900 m^2/g) and large pore volume (>0.9 cm^3/g) of MSN, allow high loadings of drug molecules [277]. The internal surface (i.e., cylindrical pores) and the external surface (i.e. exterior particle surface) of MSN allow the selective functionalization of the internal and/or external surfaces of MSN with different moieties. To further improve the efficiency of MSN, targeting of cancer cells with biomolecules [263,278–281] or antibodies [282] anchored on the MSN surface has been carried out. For example, mannose or galactose functionalized MSN have been reported to induce a higher cytotoxicity of cancer cells than unfunctionalized MSN and target to cancer cells more efficiently [278,279]. Folate, a targeting ligand, has been covalently attached to amino-functionalized silica nanoparticles loaded with a hydrophobic small molecule anticancer drug. Folate-functionalized nanoparticles turned out to be significantly cytotoxic to tumour cells, whereas normal cells were much less affected by the presence of these structures [283]. Lee *et al.* synthesized multifunctional nanoparticles by assembling Fe_3O_4 nanocrystals on uniform dye-doped MSN (designated as Fe_3O_4-MSN) as well as their applications to simultaneous magnetic resonance (MR) imaging, fluorescence imaging, and as a drug delivery vehicle (**Figure 23**). The superparamagnetic property of the magnetite nanocrystals enabled the nanoparticles to be used as a contrast agent in MR imaging, and the dye molecule in the silica framework imparted optical imaging modality. Integrating a multitude of magnetite nanocrystals on the silica surface resulted in remarkable enhancement of MR signal due to the synergistic magnetism. An anticancer drug, doxorubicin (DOX), could be loaded in the pores and induced efficient cell death. They demonstrated *in vivo* passive targeting and accumulation of the nanoparticles at the tumour sites by both T2 MR and fluorescence imaging. Furthermore, apoptotic morphology was clearly detected in tumour tissues of mice treated with DOX loaded nanocomposite nanoparticles, demonstrating that DOX was successfully delivered to the tumour sites and its anticancer activity was retained [271].

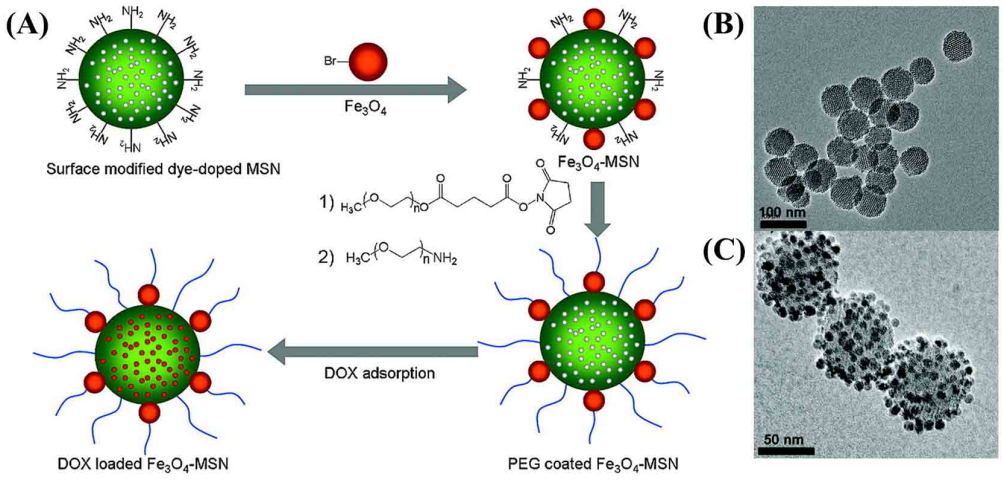

Figure 23: (A) Schematic illustration of the synthetic procedure for Fe_3O_4-MSN, and TEM images of (B) as synthesized MSN, (C) Fe_3O_4-MSN [271]**.**

Controlled and targeted release of cytotoxic agents can also be achieved by surface functionalization of MSNs. Li *et al.* established a core MSN cross-linked with a poly(acrylic acid) (PAA) through disulphide linkage, which acted as a drug release switcher (**Figure 24**) [284].

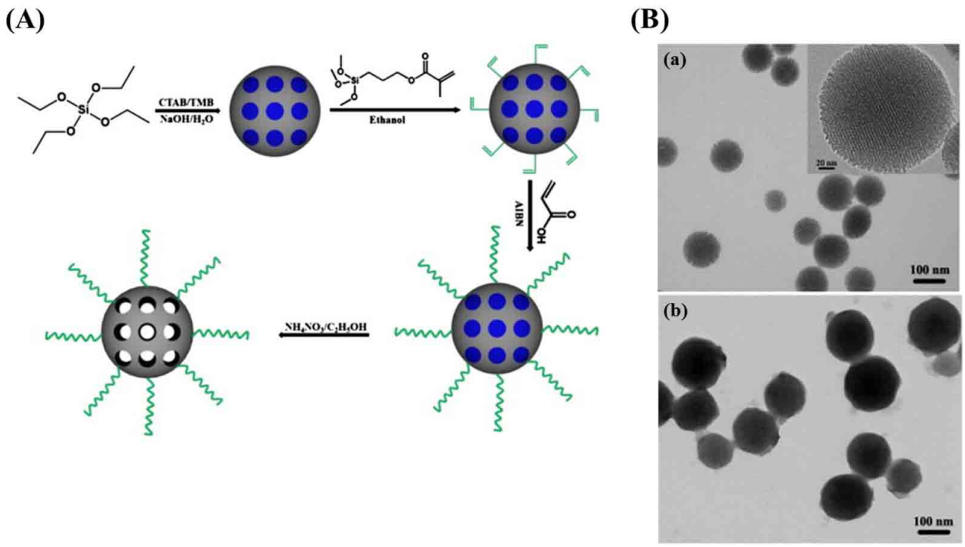

Figure 24: (A) Schematic preparation process of PAA–MSN. (B) TEM images of (a) MSN and (b) MSN–PAA [284] **.**

DOX loaded into MSN-PAA (DOX@MSN-PAA), released to the medium by the dissociation of disulphide linkage achieved by a reduction-responsive reaction. The loading content and the entrapment efficiency of DOX could reach up to 40.2% and 80.4%,

respectively. Additionally, controlled release was achieved by varying the concentration of the reductant. This study analyzed DOX release in two different mediums (phosphate-buffered saline (PBS) of pH 7.4), one with 2 mM of glutathione, simulating environment of cancer cells, and one without glutathione, corresponding to normal human cells. The release rate was 49.4% after 24h with the existence of 2 mM glutathione (simulated environment of cancer cells), about three times higher than that of without glutathione (corresponding to normal human cells), which was only 16.9%. (**Figure 25A**). Through *in vitro* assays, this study showed that DOX@MSN-PAA cross-linked produced remarkable cytotoxicity to HeLa cells (human cancer cells), and relatively lower cytotoxicity to 293 cells (human normal cells) (**Figure 25B,C**).

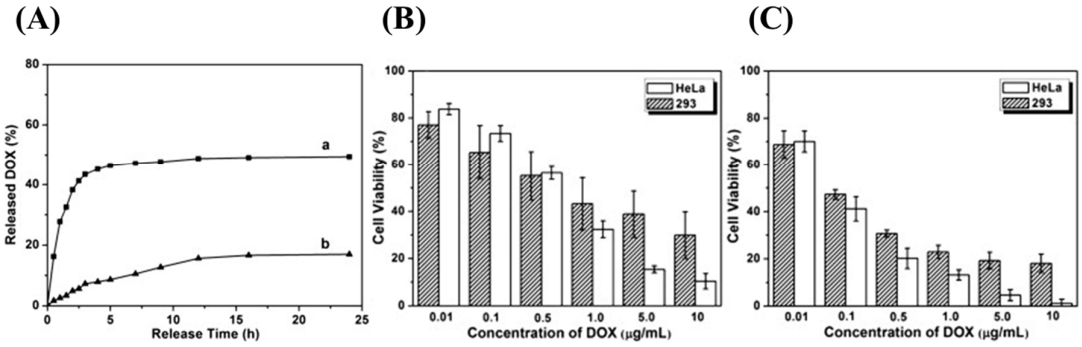

Figure 25: (A) The drug release curves of DOX@MSN–PAA (a) with and (b) without adding 2 mM of glutathione in PBS of pH = 7.4; and relative viabilities of HeLa and 293 cells incubated with DOX@MSN–PAA for (B) 24 h and (C) 48 h at different concentrations [284]**.**

2.6. Gold Nanoparticles

Gold nanoparticles (AuNPs or colloidal gold) are a suspension of nanometric particles of gold. The history of AuNPs dates back to the 4th century when they were used in stained-glass windows of medieval churches [285]. However, the scientific research of colloidal gold begin with Michael Faraday in the 1850's, when he observed a difference between the properties of colloidal gold solutions and bulk gold [17,286]. Moreover, the unique optical properties of AuNPs, depend on its shape and size, due to their interaction with light. The enhancement in the optical and photothermal properties arises from the localized surface plasmon resonance (LSPR) which cause the color of a colloidal AuNPs solution and is influenced by size and shape of AuNPs [287]. For example, spherical AuNPs with particle size of 10-20 nm show a LSPR absorption around 520 nm with red color solution [288]. Changing the size of the particles, or its length to form nanorods, the LSPR wavelength can

be increased to the near infrared (NIR) region due to the electromagnetic retardation in larger particles [289]. Moreover, gold nanorods present two LSPR bands: one is a weak band with a wavelength similar to spherical AuNPs (absorption arround 520 nm) due to the plasmon oscillation along the short axis, referred to transverse bands which is insensitive to the size changes. The second is a strong band in NIR region due to the plasmon oscillation along the long axis, referred to longitudinal band, which depends on the nanorod aspect ratio (Length/Width) (**Figure 26**) [289].

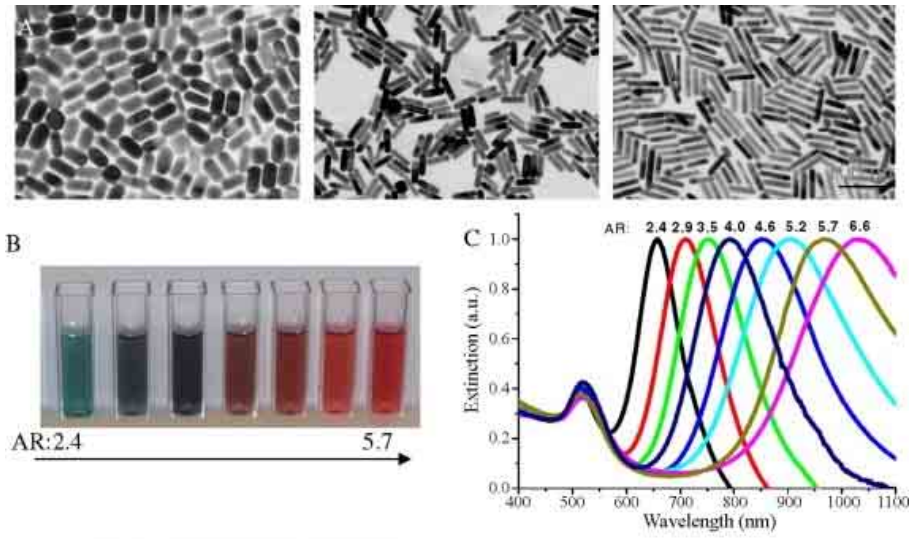

Figure 26: Tunable optical properties of gold nanorods by changing the aspect ratios. Gold nanorods of different aspect ratios exhibit different dimensions as seen by TEM (A), in different color (B) and different SPR wavelength (C) [289]**.**

This property of AuNPs is advantageous for the optical imaging and the photothermal therapy, make them suitable for medical applications aiming to kill cancer cells through the selective localized photothermal heating [290]. There are several methods for the preparation of AuNPs such as chemical [291–295], physical [296–298] and biological methods [299,300]. Chemical methods are widely used for the synthesis of AuNPs. The method pioneered by Turkevich *et al.* in 1951 and refined by Frens *et al.* in 1973 was the most commonly method for the synthesis of spherical AuNPs [291,292,301,302]. The principle of this method involves a reduction of gold salts as metal precursor to form gold atoms (Au^0) in the presence of reducing agent such as sodium citrate, sodium borohydrate, or phosphorous which produces a monodisperse AuNPs in the size range of 10-20 nm (**Figure 27A**) [291]. Citrate can act as a reducing agent and as a stabilizer of AuNPs [295].

In 1973, Frens found that the size could be controlled by changing the gold/stabilizer ratio [295,302].

Other method discovered by Brust and Schiffrin in 1994 for the synthesis of AuNPs in organic solvents that are not miscible in water with size range of 1.5-5.2 nm was inspired from Faraday's two phase system [17,293,294]. This method involved the transfer of an aqueous solution of $HAuCl_4$ to an organic solvent (e.g. toluene, chloroform, or benzene) using tetraoctylammonium bromide (TOAB) as phase transfer agent. The gold is then reduced by sodium borohydride ($NaBH_4$) in the presence of alkanethiol (e.g. dodecanethiol) which stabilized the AuNPs (**Figure 27B**) [303], resulting in a color change from orange to brown upon addition of $NaBH_4$ [293].

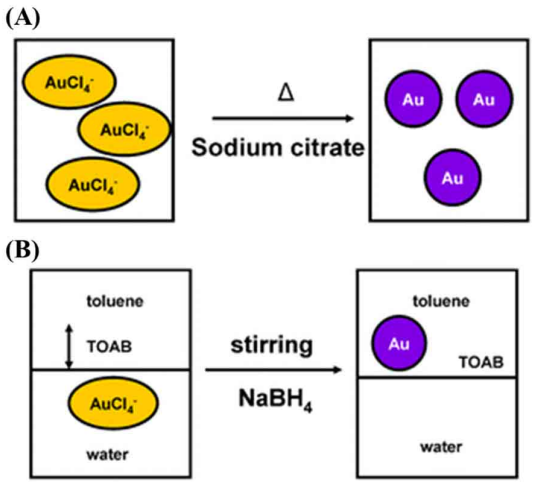

Figure 27: Two general procedures to prepare colloidal gold suspensions of small nanometre size: (A) Turkevich method and (B) Brust method [304]**.**

Another common approach to controlling the morphology of AuNPs and produce larger NPs, resulting in the formation of nanorods [305,306], nanocubes/nanocages [307–309], and nanotubes [310] is the seeding growth method (**Figure 28**). Typically, this method consists of three independent steps: (1) the preparation of surfactant-capped gold nanoparticle seeds (generally ranging in diameter from 1.5 to 5 nm) by reducing $HAuCl_4$ using $NaBH_4$, (2) the preparation of a growth solution via the reduction of $HAuCl_4$ using a milder reducing agent such as ascorbic acid (both steps in the presence of cetyltrimethylammonium bromide (CTAB) as a stabilizing surfactant, and finally (3) an addition of the gold nanoparticle seeds prepared in the first step to the growth solution (**Figure 28**) [305,311–313]. Cetyltrimethylammonium bromide (CTAB), a cationic surfactant which forms a rodlike micelles in water [314], is widely used in the gold nanorod synthesis [306,315]. It serve as

a soft template that adsorb along the long-axis crystal faces, forming a bilayer around the side wall of the nanorods, and causes a longitudinal growth of the nanostructure [315].

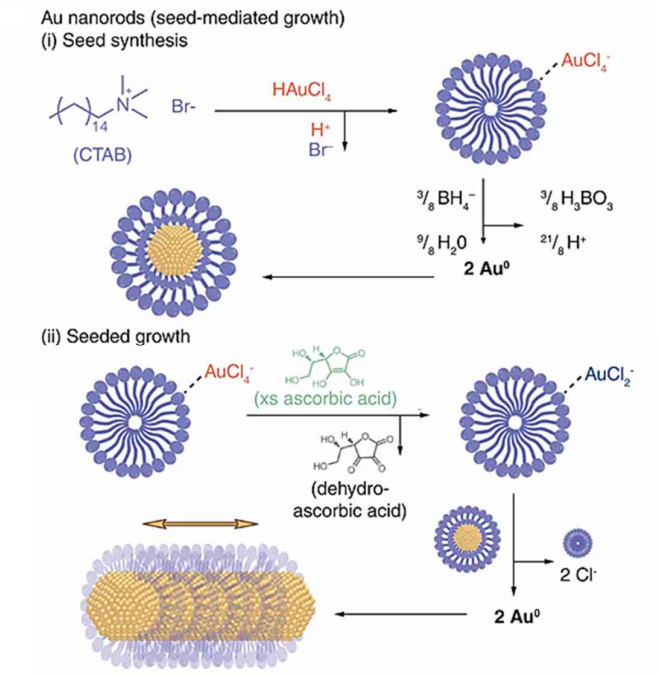

Figure 28: Seed-mediated growth of gold nanorods.

Moreover, the spherical AuNPs absorptions have not been optimal for *in vivo* application, because their absorption peak was limited to 520 nm. This limitation was overcome by the invention of gold nanorods by Murphy *et al.*, which are able to tune the optical properties from 520 nm up to 1000 nm by changing the aspect ratio of nanorods, which have been used as photothermal agents [289,290,315,316]. However, their incompatibility with other high-resolution imaging techniques (e.g. MRI) and irreproducibility in shapes led to the invention of other structures such as nanoshells and nanocages, which tune the optical properties in NIR regions to maximize the penetration depth. Gold nanoshells (AuNSs), developed by Halas and coworkers, are composed of a silica core around 60 nm and a thin shell of gold about few nanometers [317]. AuNSs are plasmonic materials with intense absorbing and scattering properties. The LSPR wavelength of AuNSs can be controlled by changing the shell thickness. Decreasing the gold shell thickness from 20 nm to 5 nm leads to LSPR red shift from 700 nm to 1000 nm. This red shift can be attributed to the hybridization of the inner and outer shell surface plasmons for thinner shell particles [318]. AuNSs possess highly favorable optical and chemical properties for photothermal cancer therapy [316,319,320], and imaging, such as optical coherence tomography (OCT) [321,322],

photoacoustic tomography (PAT) [323], and surface enhanced raman scattering (SERS) [320,324]. Similar to AuNSs, gold nanocages that are hollow and porous gold nanostructures invented by Xia and coworkers in 2002 [325] represent a class of nanostructures with tunable LSPR peaks in the NIR region. AuNSs are prepared by a galvanic replacement reaction between silver nanocubes and aqueous solution of $HAuCl_4$ [307]. By controlling the thickness, the porosity of the walls, and the amount of $HAuCl_4$ added to reaction, the LSPR of gold nanocages can be tuned to NIR region (600-1200 nm), making them suitable for photothermal therapy [326].

Owing to their large scattering and absorption, gold nanocages are used as contrast agents for imaging modalities such as dark-field microscopy [327], optical coherence tomography (OCT) [308], photoacoustic tomography (PAT) [328], and multi-photon luminescence-based detection [329,330]. Furthermore, the hollow interiors, porous walls, and tunable LSPR properties of gold nanocages can be used to construct multifunctional hybrid nanostructures interesting for theranostic applications as smart carriers for controlled release with a NIR laser [331–333]. Moreover, the drugs can be loaded into the AuNPs through a covalent or non-covalent conjugation, based on the strong affinity of different functional groups such as thiol, amines, and phosphines for gold surfaces [334]. Gibson *et al.* conjugated covalently 2 nm of AuNPs functionalized with mercaptophenol to a chemotherapeutic drug, paclitaxel, through a flexible hexaethylene glycol spacer anchored at the C-7 position of paclitaxel using carbodiimide-based esterification chemistry (**Figure 29**) [335]. Hwu *et al.* synthesized paclitaxel-polyethylenglycol-thiol (PTX-PEG-thiol) using a phosphodiester spacer attached to the surface of AuNPs, and the release of paclitaxel is triggered by phosphodiesterases in cancer cells [336]. These methods provide a simple and versatile method to use AuNPs to deliver other types of drugs using the same strategy.

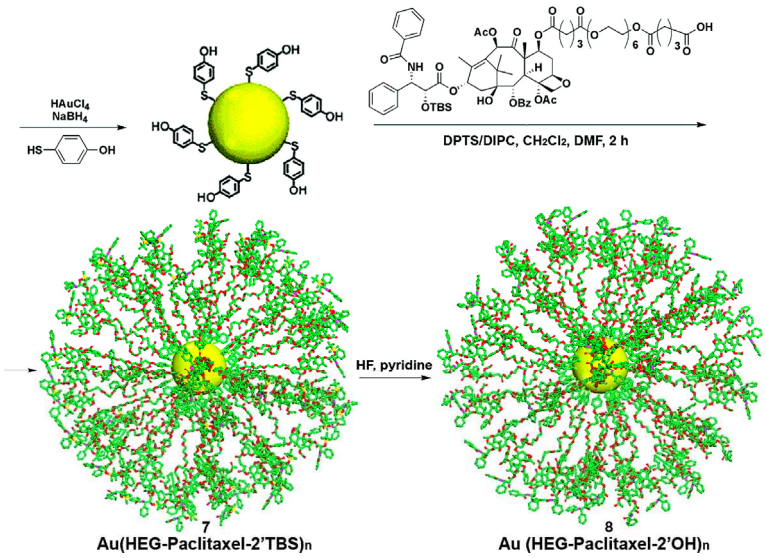

Figure 29: Covalent Coupling of Paclitaxel to 4-Mercaptophenol-Modified 2 nm AuNPs [335]**.**

The cytotoxicity of oxaliplatin-conjugated AuNPs has been also investigated. Oxaliplatin is an analog of cisplatin and is readily used in colorectal cancer chemotherapy. Its mechanism of action is to intercalate into DNA and inhibit DNA synthesis in cancer cells. Although it is very effective, oxaliplatin does not specifically target cancer cells and, therefore, can attack other rapidly dividing healthy cells. In order to improve this form of chemotherapy, enhanced drug delivery must be achieved, Brown *et al.* demonstrated increased potency of oxaliplatin when conjugated to the surfaces of AuNPs through thiolated PEG linkers [337]. Their reported fivefold increase in *in vitro* cytotoxicity after conjugation was again attributed to the efficient uptake of the particle conjugates through endocytosis into cancer cells. Dreaden *et al.* utilized AuNPs conjugated to thiol-PEGylated tamoxifen derivatives that can be used to selectively target and deliver plasmonic AuNPs to estrogen receptor (ER) positive breast cancer cells with up to 2.7-fold enhanced drug potency *in vitro* [338]. The PEG linker allowed for increased particle stability in the cell culture media as well as reduced the nonspecific binding of serum proteins to the surface of the conjugated particle.

One treatment area that has the potential to greatly benefit from coupling to AuNPs is photodynamic therapy (PDT). PDT is a form of cancer treatment that utilizes light, photosensitizers and tissue oxygen [339]. Most photosensitizing agents, such as porphyrins and phthalocyanines (Pc's), are hydrophobic and locate preferentially in apolar sites such as the lipid bilayer membranes of cells. After photosensitizer accumulation, diseased tissues are excited by specific wavelengths of light, causing energy transfer from the photosensitizer to molecular oxygen in the surrounding tissue, generate highly reactive oxygen species and

induce cell death through apoptosis. The lack of solubility of the photosensitizer's in physiological environments, which inhibits its uptake/accumulation into the diseased tissues is a significant drawback to this form of chemotherapy. To improve PDT, Cheng *et al.* conjugated Pc4, a photosensitizer, to 5-nm AuNPs and studied the coupled particles uptake and delivery **(Figure 30A)** [340]. Unlike free Pc4, the conjugated form was soluble in aqueous environments. Silicon phthalocyanine 4 (Pc4) is a hydrophobic PDT drug currently under phase I clinical trials [341]. When Pc4 is injected for *in vivo* PDT, it usually takes 1 or 2 days until sufficient Pc 4 reaches the tumour site, which then can be irradiated with 672 nm light for therapy [342]. With the NP–Pc4 conjugates, the time for the maximum drug accumulation to the target tumour has been greatly reduced to only < 2 h, compared to 2 days for the free Pc4 (**Figure 30B**).

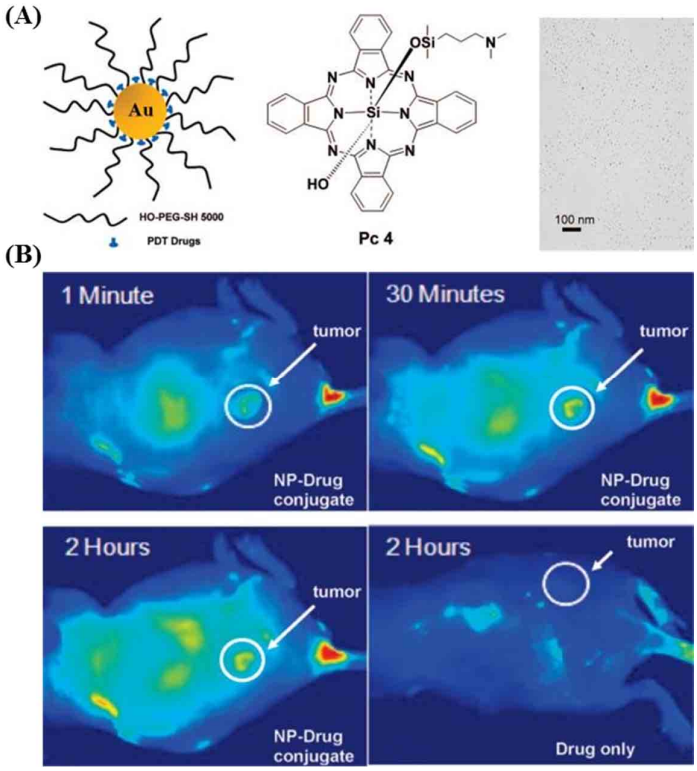

Figure 30: Conjugation (A) and in vivo tumour accumulation (B) of a PDT photosensitizer–Au nanoparticle conjugate [340]**.**

AuNPs also possess other properties that can be employed in drug delivery applications. Due to strong NIR light absorption, the majority of interest in gold nanoparticle cancer therapy is in photothermal therapy (PTT), so the amount of heat generated by NIR irradiation is critical to effective cancer treatment. AuNP size/shape can be altered, affording the ability to tune their energy absorption profiles for use in PTT of solid tumours [80,343–345]. PTT

with AuNPs is desirable for many reasons. First, with advancements in synthesis, scientists have been able to scale up preparations of AuNPs of various sizes and shapes [346,347]. Second, compared to other metals, gold is more chemically inert, potentially rendering the AuNPs core biocompatible. Studies of short-term AuNPs exposure to various cell types suggest they are noncytotoxic and nonimmunogenic at clinically relevant concentrations [348,349]. Therefore, the effect of a chosen surface ligand on cell viability and cell behavior is an important consideration before biological exposure. Third, since AuNPs are highly tunable in their size, shape, and surface chemistry it may be possible to engineer them for maximum tumour accumulation *in vivo* [350]. Nanoparticles that are 60–400 nm in diameter can extravasate in solid tumours due to the leakiness of tumour vasculature, allowing for a passive form of tumour targeting. This is known as the enhanced permeability and retention (EPR) effect [351,352]. Finally, AuNPs can be designed to more actively target tumour sites through modification of their surface chemistry. A wide array of small molecules, proteins, and peptides have been developed to bind to specific receptors on tumour cells with varying degrees of tumour accumulation [353]. Then, once AuNPs bind to or accumulate in cells/tumours, NIR irradiation can trigger photothermal heating [354]. Nanoparticle LSPR and irradiation conditions can be designed to maximize heating efficiency [355]. Because irradiation is localized at the tumour site, this may avert unwanted side effects associated with conventional cancer treatments. However, photothermal therapy may also be used in conjunction with other cancer treatments, such as chemotherapy, to enhance tumour destruction [356]. PTT typically uses laser exposure in the NIR (650-900 nm) region due to minimal absorption by tissues and physiological fluids at these wavelengths, and to induce cytotoxic damage in diseased tissues through the selective administration of heat sufficient to induce hyperthermic cellular responses [357,358]. AuNPs such as nanorods, nanoshells and nanocages, are optimal for this treatment because they have the ability to absorb NIR light and release the absorbed energy as heat at their localized accumulation site. The first example of AuNPs-mediated photothermal cancer therapy was reported in 2003 by Halas and coworkers [80]. Gold nanoshells (AuNSs) consisting of 110 nm silica cores surrounded by 10 nm gold shells were functionalized with the biocompatible polymer polyethylene glycol (PEG) which is often used to minimize nanoparticle aggregation and to increase blood circulation and half-life. These particular nanoshells had a λmax of 820 nm, but LSPRs in gold nanoshells can be tuned from 700 to 1000 nm by increasing the core-to-shell ratio [359]. SK-BR-3 cells (human breast cancer cell line) [80], PC-3 and C4-2 (human prostate cancer

cell lines) [360] were incubated with AuNSs, without any toxic effect in the absence of NIR stimulation. Once the NIR is applied, it was seen a cell death area well-demarcated with a remarkable increase of temperature. Another important study showed the passive targeting of AuNSs in tumour, by the use of NIR laser and AuNSs on subcutaneous PC-3 mouse cancer model after intravenous (i.v.) injection of AuNSs. In the treated group (AuNSs+Laser) an increased temperature of 28.9 °C was observed compared with 13.8 °C in the control group (Saline+Laser). Tumour were isolated 21 days after treatment, with a 93% of tumour necrosis [361].

Recently, researchers have demonstrated combined PTT and imaging/diagnosis *in vivo* using multifunctional nanocomposites. Jin and co-workers designed 300 nm PEG-coated gold nanoshelled perfluorooctoyl bromide nanocapsules for photothermal therapy and bimodal contrast imaging via ultrasound and X-ray computed tomography. The authors were able to enhance contrast in U87 human glioblastoma tumour-bearing nude mice, and photothermal heating (808 nm, 1.3 W/cm^2, 10 min) resulted in a 35 °C temperature increase and decreased tumour volume by 68% after 16 days [362]. Lin *et al.* combined T2 magnetic resonance imaging (MRI) and photothermal heating using 60 nm PEG-functionalized gold nanoshells containing Fe3O4/Ag cores (λmax = 800 nm). B16–F10 melanoma tumours were implanted in C57BL/6 mice and could be detected by MRI when the nanoparticles were present. PTT (808 nm, 4 W/cm^2, 30 s) resulted in complete elimination of the tumour after 13 days when the nanoshells were injected directly into the tumour. However, treatment only slowed growth when the nanoparticles were injected intravenously (**Figure 31**) [363].

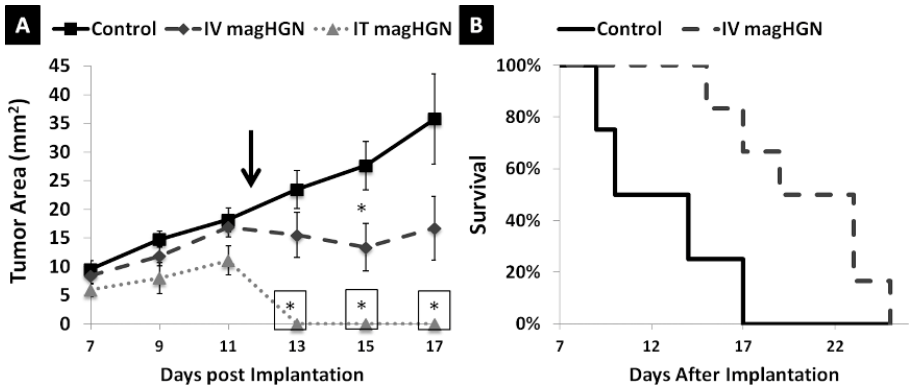

Figure 31: PTT efficacy evaluation of magnetic hollow gold nanoshell (magHGN) in a melanoma tumour murine model. A) Tumour growth measured in days post implantation. The arrow denoted the PTT treatment with intravenous or intratumour injections of magHGNs. (*p < 0.05 in comparison to the control). B) Survival percentage measured in days after PTT treatment [363]**.**

These examples demonstrate the potential versatility of multifunctional AuNPs for in vivo diagnostic imaging and PTT. Systems such as these may be beneficial for clinical application because therapy can be limited to the detected diseased area, potentially preventing side effects associated with part or whole-body treatments.

Photothermal chemotherapy of gold–drug nanoconjugates has also been employed *in vivo* to enhance tumour destruction. Nam *et al.* designed 10 nm gold nanospheres (λmax = 535–540 nm) with pH-responsive ligands covalently linked to DOX via carbodiimide coupling. In the acidic tumour environment DOX release was triggered via hydrolysis. Also, the negatively charged surfaces were converted to a mixture of negative and positive charges, reducing electrostatic repulsion, and resulted in rapid nanoparticle aggregation and a broadening/red-shift in the LSPR to 650 nm (**Figure 32**). Laser irradiation (660 nm, 0.5 W/cm^2, 5 min) in nu/nu nude mice having B16–F10 melanoma tumours demonstrated tumour temperature increases of 15 °C, and tumour growth was halted. This was more effective than DOX or nanoparticles alone, which only slowed tumour growth [364].

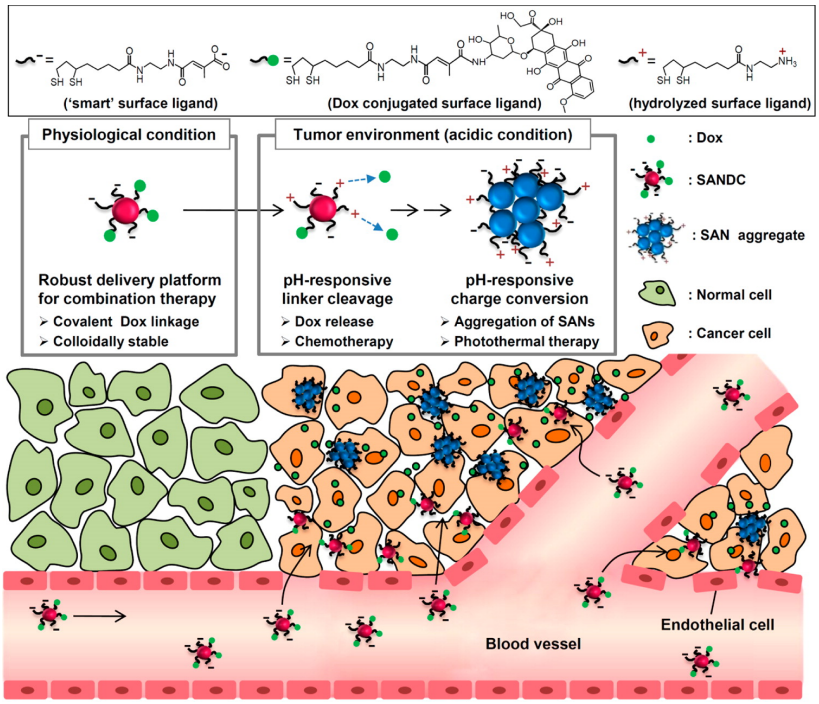

Figure 32: Schematic illustration the mechanism of "smart" AuNPs doxorubicin conjugate [364]**.**

These examples reveal that combination photothermal chemotherapy treatment can also be synergistic and effective *in vivo* for tumour destruction. Further work to maximize drug

conjugation and better control release rates *in vivo* may serve to increase their potential for clinical application.

2.7. Silver Nanoparticles

Silver nanoparticles (AgNPs) are nanoparticles of silver in the range of 1 and 100 nm in size. AgNPs have unique properties, which help in molecular diagnostics, therapies, as well as in devices that are used in several medical procedures. Metallic silver, has been widely used for thousands of years in human applications, including currency coins, jewellery, photography, surgical prosthesis, and dental alloy. Silver vessels were used in ancient times to preserve water and wine. The silver powder (e.g. silver nitrate) have beneficial healing and anti-disease properties and was employed for the treatment of ulcers in the 17th and 18th centuries [365]. In 1881, German obstetrician C.S.F. Crede introduced 1% silver nitrate as an eye solution to prevent gonococcal ophthalmia for new born babies [366]. Further, in 1967, C.L. Fox introduced a formulation containing silver, silver sulfadiazine (Flammazine®, Silvadene®) in the treatment of burn patients, and even today silver sulfadiazine cream remains the most widely used as standard antibacterial treatment for serious burn wounds [367]. However, prolonged exposure to silver or silver compounds may resulting in irreversible pigmentation of the skin or eyes, i.e. argyria or argyrosis, due to silver deposition in the body [368]. Because of this problem and with the advent of antibiotics such as penicillins and cephalosporins, silver's medicine largely faded away as an anti-infection agent. However, the advancement of modern science helped silver to revive, under the large increase in the number of multiple-resistant bacterial strains due to the abuse of antibiotics and the discovery that AgNPs showed excellent performance in antibacterial application. The AgNPs with its antimicrobial activity was regulated for wound management in the 1920s by the FDA [369]. An important aspect of the antimicrobial activity of AgNPs is the synergistic effect that occurs when these particles are combined with others natural and synthetic compounds [370,371]. Moreover, their particular structure and the different modes of establishing an interaction with bacterial surfaces may offer a unique antibacterial mechanism to exploit. It was reported that AgNPs show biocidal action by the slow release of silver ions, and by multiple mechanisms, such as inhibition of DNA replication, induction of oxidative stress, and interaction with thiol groups in proteins and enzymes, making it more difficult to produce resistant strains [372–376]. Different methods have been developed to synthesize AgNPs with various shapes and sizes, such as physical,

chemical, and biological methods. In physical approach, evaporation-condensation and laser ablation are the most important methods for the synthesis of AgNPs. Evaporation-condensation technique [377] was carried out using a tube furnace at atmospheric pressure. However, the synthesis of AgNPs using this approach has several drawbacks because the tube furnace occupies a large space and consumes a great amount of energy while raising the environmental temperature around the source material, and requires a lot of time to achieve thermal stability. A tube furnace requires power consumption and a preheating time to attain a stable operating temperature [378]. The absence of solvent contamination in the prepared film and the uniformity of NPs distribution are the advantage of this method in comparison with chemical approaches [378]. It was demonstrated that AgNPs could be synthesized via a small ceramic heater, which is used to evaporate source materials [377,379,380]. The evaporated vapor can cool at a suitably rapid rate, because the temperature gradient in the vicinity of the heater surface is very steep in comparison with that of a tube furnace. This makes possible the formation of stable small NPs in high concentration [379]. Furthermore, AgNPs have been synthesized by laser ablation of metallic bulk in solution [381–383]. The production of AgNPs by this approach depends on many parameters, such as the wavelength of the laser impinging the metallic target, the duration of the laser pulses, the ablation time duration and the effective medium, with or without the presence of surfactant [384,385]. The advantage of laser ablation compared to other methods for production of metal colloids is the absence of chemical reagents in solutions. Therefore, pure and uncontaminated metal colloids for further applications can be prepared by this method [383]. The physical methods produce large quantities of AgNPs in a single process with narrow size distribution. Recently, biosynthetic methods using naturally capping/reducing agents such as polymers [386–388], polysachharides [389,390], biological microorganism such as bacteria [391,392], fungi [393,394], algae [395], and plant extracts [396,397] have been emerged for the synthesis of AgNPs as environmentally and eco-friendly process. The synthesis of NPs using plant extracts can be advantageous over other biological processes by eliminating the elaborate process of maintaining cell cultures and can also be suitably scaled up for large-scale synthesis of NPs [398]. The most popular chemical approaches, including chemical reduction [399–402], electrochemical techniques [403,404], irradiation-assisted chemical [405,406], pyrolysis [407] and microemulsion techniques [408,409] are widely used for the synthesis of AgNPs. Besides those approaches, chemical reduction is the most common method for the synthesis of AgNPs. In general,

different reducing agents (such as sodium citrate, sodium borohydride, and ascorbate) are used for reduction of silver ions (Ag^{+}) in aqueous or non-aqueous solutions, leading to the formation of metallic silver (Ag^{0}). The formation of colloidal solutions from the reduction of silver salts involves two stages of nucleation and growth. The size and shape of AgNPs synthesized are strongly dependent on these stages. The nucleation and the growth of initial nuclei can be controlled by adjusting the reaction parameters such as temperature, pH, precursors, reduction agents (e.g. sodium borohydride, sodium citrate), and stabilizing agents. Polymeric compounds such as polyvinyl alcohol (PVA), polyvinylpyrrolidone (PVP), and sodium oleate have been reported to be effective protective agents to stabilize AgNPs [410–412]. It is important to use stabilizing agents to stabilize the dispersive NPs during the preparation of metal NPs, and protect the NPs from agglomeration [400]. The optical properties of AgNPs result from their unique interaction with light, which causes the collective coherent oscillation of their free conduction band electrons (LSPR). The width and position of the LSPR peaks depends on the size, shape and dispersion of the NPs [413], which can be used to tune the plasmon peaks of AgNPs in the range of 393-738 nm [414] and 500-1000 nm [415]. Therefore, LSPR of AgNPs showed in strong visible and NIR scattering and absorption, which enables the development of photothermal and laser therapies [416,417]. Moreover, it was revealed that AgNPs could enhance the effect of cancer cell killing in radiation treatment [418]. AgNPs are also used for Surface-enhanced Raman spectroscopy (SERS), which enhance their efficiencies and allow the identification of single molecules [419]. Apart from the antimicrobial and antifungal application of AgNPs [420,421], they also have various applications in some other fields such as photosensitizers and/or radiosensitizers [416–418,422], and anticancer therapeutic agents in leukemia [423,424], breast cancer [425,426], hepatocellular carcinoma [427,428], lung carcinoma [429], and colon carcinoma [430]. AgNPs are used as photosensitizers and/or radiosensitizers due to the LSPR of NPs, which enable the use of AgNPs in nonionizing and ionizing radiation. Wu *et al.* reported an aptamer-Ag-Au shell-core nanostructure-based NIR photothermal therapy of lung adenocarcinoma cells (A549 cells) at a very low irradiation power density (0.20 W cm^{-2}) without destroying the healthy cells and the surrounding normal tissues [416]. Moreover, Shi *et al.* reported that graphene oxide@Ag-doxorubicin-DSPE-PEG2000-NGR (GO@Ag-DOX-NGR) showed excellent chemo-photothermal therapeutic efficacy, tumour-targeting property, NIR laser-controlled drug releasing function and X-ray imaging ability, with a great potential of GO@Ag-DOX-NGR for cancer

diagnosis and therapy [417]. AgNPs have proven promising anticancer effects. Several investigators have reported that AgNPs induced a cytotoxic effect against leukemic cells. Guo *et al.* reported that PVP-coated AgNPs could effectively reduce viability of acute myeloid leukemia (AML) cells, through the generation of reactive oxygen species (ROS), release of silver ions, which led to DNA damage and apoptosis [423]. It has also been observed by Gurunathan *et al.* that AgNPs might be a potential alternative agent for human breast cancer therapy. AgNPs showed dose-dependent cytotoxicity against MDA-MB-231 cells through activation of caspase-3, ROS generation, leading to induction of apoptosis and DNA fragmentation [425,426]. Recently, Sahu *et al.* revealed a significant concentration-dependent cytotoxicity of AgNPs in human liver (HepG2) cells was observed in the concentration range of 1 to 20 µg/ml, and that a different mechanism of AgNPs-induced mitochondrial injury leads to the cytotoxicity [427]. However, Faedmaleki *et al.* showed that AgNPs had 44 times stronger inhibitory effect on the growth of cancerous cells (HepG2 cell line) compared to the normal cells (primary liver cells of mice), which might further justify AgNPs as a cytotoxic agents and a potential anticancer candidate [428]. AgNPs have also been shown to display cytotoxicity to the lung cancer cells. Foldbjerg *et al.* observed a dose-dependent reduction in mitochondrial function of human alveolar cell line A549 cells exposed to PVP-coated AgNPs (0–20 µg/ml). Furthermore, an AgNP-mediated increase in ROS was associated with DNA damage, apoptosis and necrosis [429]. Also, El-Deeb *et al.* report a simple, cost-effective and environmentally synthesis of AgNPs using honey bee for the treatment of colon carcinoma CaCo2 cells. They indicated that the AgNPs obtained could be used safely with concentrations up to 39 µg/ml with 60% inhibition on CaCo2 cell proliferation [430]. Benyettou *et al.* presents the synthesis of AgNPs based drug-delivery system that achieves the simultaneous intracellular delivery of doxorubicin (Dox) and alendronate (Ald) and improves the anticancer therapeutic indices of both drugs (**Figure 33**) [431]. AgNPs were coated with Ald molecules by chelating bisphosphonate moieties. This mode of Ald binding leaves the ammonium group of the drug free in solution. The ammonium group serves as an attachment site for either Rhodamine B (RhB), a hydrophilic, drug-like molecule, or Dox. RhB was attached by amide formation, and Dox, by imine formation. Both types of bond are pH sensitive and allow for intracellular release of RhB or Dox within the acidic microenvironment of late endosomes and lysosomes.

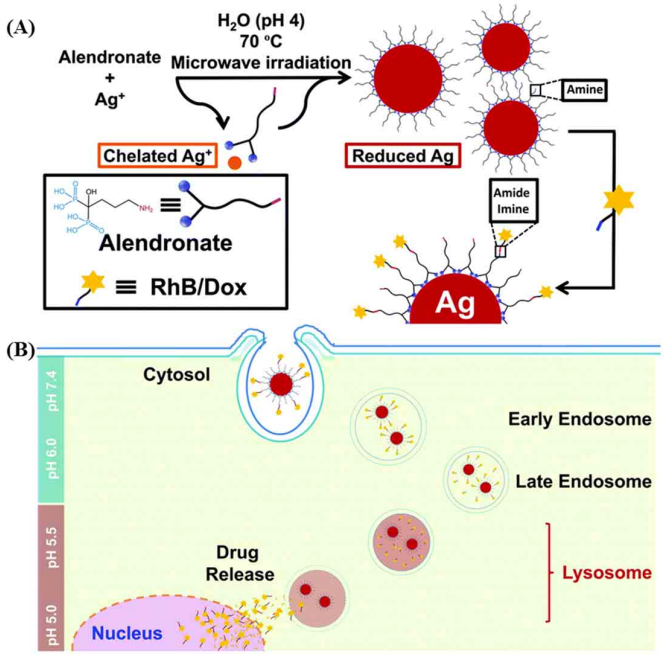

Figure 33: (A) Schematic representation of Ald@AgNP formation and dye/drug conjugation. (B) Schematic representation of the uptake of drug–Ald@AgNPs into cells and drug cargo release [431]**.**

Dox release from Dox–Ald@AgNPs was monitored over time by measuring Dox fluorescence in solution. Two aqueous samples were analyzed: one at physiological pH (7.4) and the other at a pH typically found within late endosomes and lysosomes (5.4). **Figure 34** shows the corresponding drug release profiles. A small amount (~9%) of Dox was released over seven days at pH 7.4, whereas up to 95% of the drug was released at pH 5.4 over the same period. The release of Dox from the NPs resulted from acid-promoted hydrolysis of the imine-linkage between Dox and Ald. The pH-sensitive Dox–Ald@AgNPs exhibit limited premature drug-release in the bloodstream (pH 7.4), but effectively kill cancer cells following cell internalization and Dox release within endocytic compartments at pH 6.5–4.5.

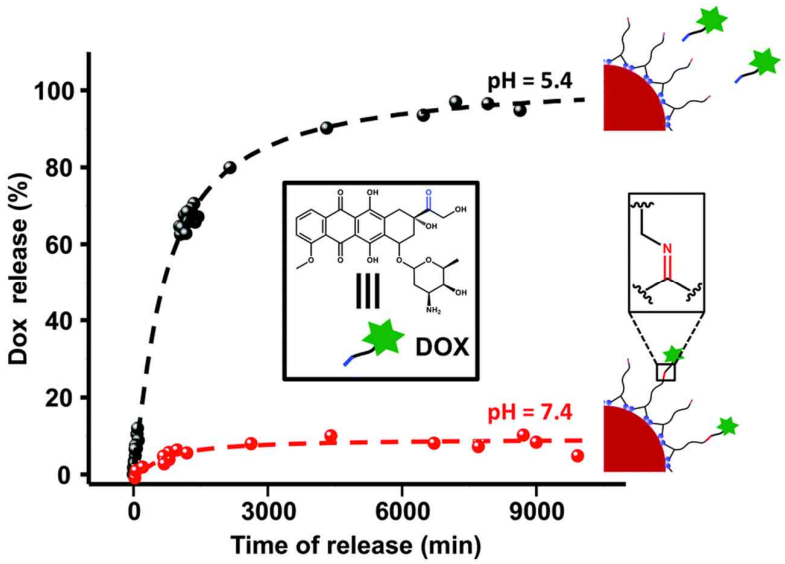

Figure 34: *In vitro* Dox release profiles for Dox–Ald@AgNPs conducted over seven days at 37 °C and either pH 7.4 or pH 5.4. Schematic representations show the imine linkage that breaks under acidic conditions to release Dox [431]**.**

The intracellular localization of Dox–Ald@AgNPs following uptake by endocytosis was determined by confocal laser scanning microscopy. HeLa cells were incubated with Dox–Ald@AgNPs for 3 h at 37 °C. After incubation, Dox was found to be distributed within the cytoplasm (**Figure 35**), which indicates that Dox is released from endolysosomal compartments after endocytosis. The facile release of Dox into the cytoplasm is highly advantageous and makes Ald@AgNPs well-suited for intracellular drug delivery.

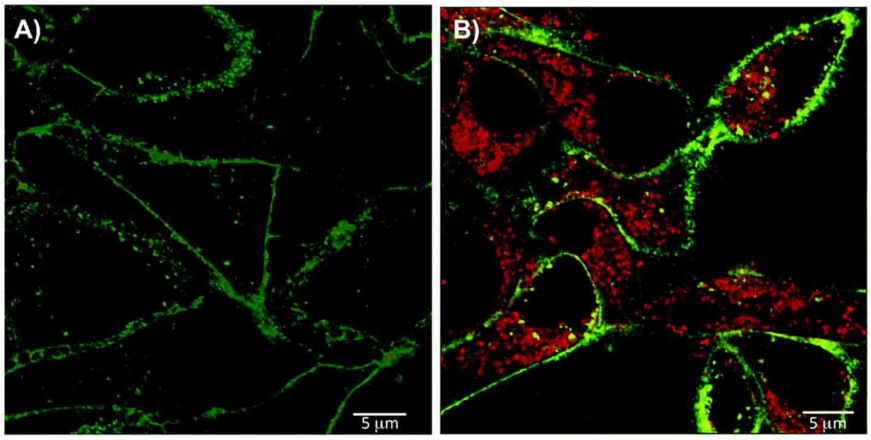

Figure 35: Confocal images of HeLa cells incubated for 3 h at 37 °C with (A) phosphate buffered saline as a control or (B) Dox–Ald@AgNPs, which are seen distributed evenly in the cytosol and appear red as a result of Dox fluorescence ([Ag] = 0.1 µM, [RhB] = 1.2 µM). Cell membranes are labeled with the green dye Alexa Fluor® 488 [431]**.**

2.8. Magnetic Iron oxide Nanoparticles

Iron oxide nanoparticles (IONPs) are one of the most investigated inorganic nanoparticles used in the development of medical and diagnostic applications such as magnetic resonance imaging (MRI) [432], cell separation [433], hyperthermia [434,435], drug delivery [436,437], biolabeling and magnetic sensors [438]. IONPs have many advantages over other nanoparticles due to the innate magnetic responsiveness, which can be controlled and facilitate particle targeting [439], imaging [440], localized heating in a magnetic field to produce hyperthermia/ablation of tissue [441,442], their biocompatibility and biodegradability [443]. IONPs have been most used as contrast agents for diagnostic imaging in combination with magnetic resonance imaging (MRI) [444]. The unique magnetic properties of IOPNs that result from their ability to enhance proton relaxation in tissues which leads to enhanced MRI images, and the ability to function at the cellular and molecular level of biological interactions making them an attractive platform as contrast agents for MRI and as carriers for drug delivery [445]. Colloidal IONPs, such as superparamagnetic iron oxides (SPIO) and ultrasmall superparamagnetic iron oxides (USPIO), are composed of a magnetic core formed from nanocrystalline magnetite (Fe_3O_4) or maghemite (γ-Fe_2O_3) and a non-magnetic coating of different surface chemistry. Hydrodynamic particles sizes range from 50-500 nm (SPIO) and less than 50 nm (USPIO), influence their magnetization, dispersibility, and stability in solution [446,447]. The sizes of 10-100 nm are optimal for *in vivo* delivery, as they escape rapid renal clearance (< 10 nm) and sequestering by the reticuloendothelial system (RES) of the spleen and liver (> 200 nm) [446]. Ligands such as targeting agents, permeation enhancers, optical dyes, and therapeutic agents can be conjugated on the surface or incorporated within these structures (**Figure 36**) [448]. Without surface coating, IONPs have hydrophobic surfaces with large surface area to volume ratios and tends to agglomerate [447].

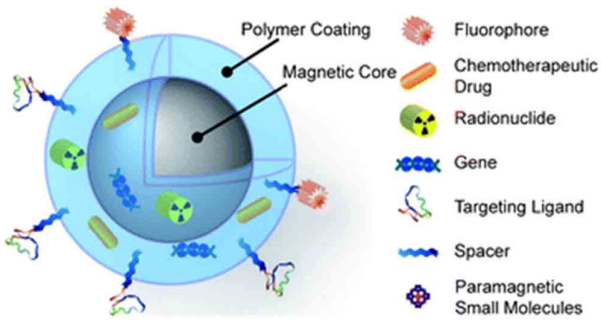

Figure 36: Magnetic NPs possessing various ligands to enable multifunctionality from a single nanoparticle platform [448]**.**

In order to increase their stability, circulation half-life and biocompatibility, IONPs are commonly coated with organic polymers (dextran, chitosan, polysorbate, PEG, polyaniline), organic surfactants (sodium oleate and dodecylamine) or other metallic materials (gold, silica or carbon), providing limited cargo space for therapeutic payloads within the protective coatings [449,450]. The modifications mitigate the fast uptake of magnetic nanoparticles by human fibroblasts, which result in the eventual cell death. The coating of dextran and proteins onto the magnetite nanoparticle surface mediates the interactions between the modified nanoparticles and cell membrane so as to retain the magnetic nanoparticles only to adhere onto the cell outside surface and thus keep the cells viable. There are a variety of methodologies used for the synthesis of IONPs, including physical or wet chemical approaches. Concerning physical methods, there are some methodologies, including gas-phase deposition and electron beam lithography [451,452]. Numerous chemical methods can be used to synthesize IONPs, including microemulsions [453], sol-gel synthesis [454], sonochemical reactions [455], hydrothermal reactions [456], flow injection synthesis [457], oxidation methods [458,459], and chemical coprecipitation [460–462].

The coprecipitation method is the simplest and most efficient chemical route to obtain a large scale of magnetic nanoparticles. Iron oxide (Fe_3O_4 or γ-Fe_2O_3) are prepared by mixing ferric and ferrous ions (Fe^{3+}/Fe^{2+}) in a 2:1 molar ratio at pH between 8 and 14, in a non-oxidizing oxygen environment [463]. However, magnetite (Fe_3O_4) is not very stable and is sensitive to oxidation, which is transformed into maghemite (γ-Fe_2O_3) in the presence of oxygen. Various electron or ion transfers depending upon the pH of the suspension are involved also in the transformation of Fe_3O_4 into γ-Fe_2O_3. Two stages are involved in the coprecipitation process: A short burst of nucleation occurs when the concentration of the species reach critical supersaturation, and then, a slow growth of the nuclei by diffusion of the solutes to the surface of the crystal [464,465]. Many factors can be adjusted in the synthesis of IONPs to control size, magnetic characteristics, or surface properties [460,466,467]. The size and shape of the nanoparticles can be controlled by adjusting pH, ionic strength, temperature, nature of salts, and the concentration ratio of Fe^{2+}/Fe^{3+}. The influence of these parameters on magnetic properties and size has been studied in a basic coprecipitation process [468]. The addition of chelating organic anions (such as citric, gluconic, or oleic acid) or polymer surface complexing agents (such as dextran, starch, or polyvinyl alcohol) during the formation of IONPs can help to control the size of

nanoparticles. Depending on the molar ratio between the organic ion and the iron salts, the chelation of the organic ions on the iron oxide surface can prevent nucleation and lead to larger particles, or inhibit the growth of the crystal nuclei, leading to small nanoparticles [469]. The first controlled preparation of IONPs (Fe_3O_4) using alkaline precipitation of $FeCl_2$ and $FeCl_3$ was developed by Massart in 1979 without molecules for stabilization [470]. The magnetite (Fe_3O_4) particles was spherical with 8 nm of diameter measured by X-ray diffraction (XRD). The parameters of this process were studied to demonstrate the influence of the base (ammonia, CH_3NH_2, and NaOH), the pH value, the cations added (NaOH, LiOH, KOH, and NH_4OH) and the Fe^{2+}/Fe^{3+} ratio on the yield of the coprecipitation reaction, the diameter and polydispersity of NPs [471]. Recently, several modified coprecipitation methods has been developed. For example, Pereira *et al.* [472] synthesize superparamagnetic Fe_3O_4 NPs with sizes of 4.9-6.3 nm by a one-step aqueous coprecipitation method based on the use of alkanolamines (e.g. isopropanolamine (MIPA) and diisopropanolamine (DIPA)) as base, leading to nanoparticles with enhanced magnetization and smaller size than those prepared with traditional bases (NaOH). Currently, many surfactants and biomolecules have been introduced directly in the coprecipitation process to resolve the problems of aggregation and biocompatibility of IONPs, which hinder their applications in biomedical fields. Salavati-Niasari *et al.* [461] have reported a facile chemical coprecipitation method for the synthesis of Fe_3O_4 NPs with a size range of 25 nm by using octanoic acid as surfactant in the reaction to improve the dispersity of nanoparticles. Recently, Suh *et al.* [462] reported an in situ synthesis of multifunctional and nonspherical magnetic IONPs with strong magnetic properties in a carboxyl functionalized polymer matrix, in which the iron ions diffused into the polymer particles, and chelate with the carboxylate groups, nucleated and finally grew to the IONPs in the polymer particles (**Figure 37**). This method can be used to add multiple functionalities, such as the addition of biomolecules after subsequent reactions.

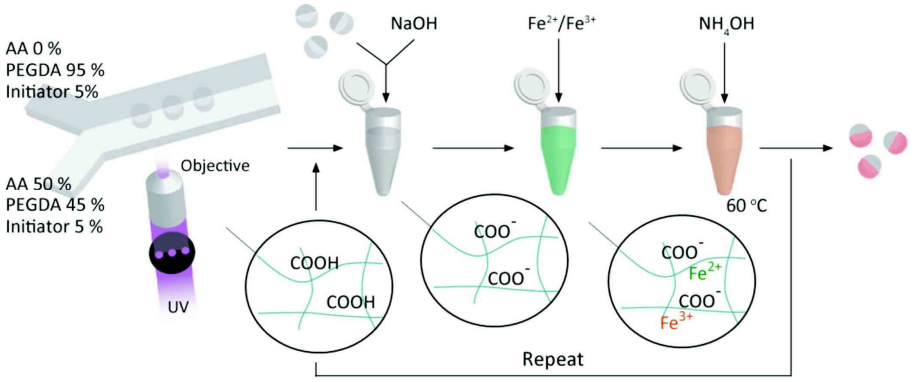

Figure 37: Schematic showing the in situ co-precipitation synthesis process of IONPs in polymer [462]**.**

The first example for the use of IONPs for cancer therapy was in 1957 [473]. Since that time, a lot of progress accompanied the synthesis and design of SPIONs. In the concept of SPIONs combined with alternating magnetic field for heat generation, a moderate hyperthermia treatment (42°C - 45°C) for a duration of 30–60 minutes showed an alteration of cellular metabolism depending of the applied thermal dose. Ablative temperatures more than 50 °C for a duration of 4 to 6 minutes cause irreversible damages in cancer cells which induce their necrosis [474,475]. In addition, the use of SPIONs as an internal heating sources destroy tumour tissues with high selectivity and low adverse effects [476]. Several studies have focused on the same concept of the SPIONs thermal ablation *in vitro* and *in vivo* for cancer therapy with highly interesting results regarding cancer cells destroying by the generation of heat spots [477,478].

By conjugating multiple components such as fluorescent molecules, tumour-targeting moieties, anticancer drugs, to the polymer-coated SPIONs, these multifunctional nanoparticles can target human cancers, and they can also be imaged inside the body by both magnetic resonance (MR) and fluorescence imaging [479]. The capability to simultaneously image and treat tumours with nanoparticles may prove advantageous over conventional chemotherapy. Drug molecules are conjugated onto the surface modified magnetic nanoparticles, and then the organic/inorganic superparamagnetic nanohybrids are concentrated at a specific target site within the body by an external, high-gradient magnetic field [480,481]. Kohler *et al.* [479] developed a methotrexate-immobilized IONPs drug carrier that may potentially be used for real-time monitoring of drug delivery through MRI. Methotrexate (MTX) was immobilized on the nanoparticle surface via a poly(ethylene glycol) self-assembled monolayer (PEG SAM) (**Figure 38**). This method of MTX

immobilization by covalent binding creates a linker between the PEG SAM and the glutamic acid residue of the MTX molecule, which is stable under intravenous conditions.

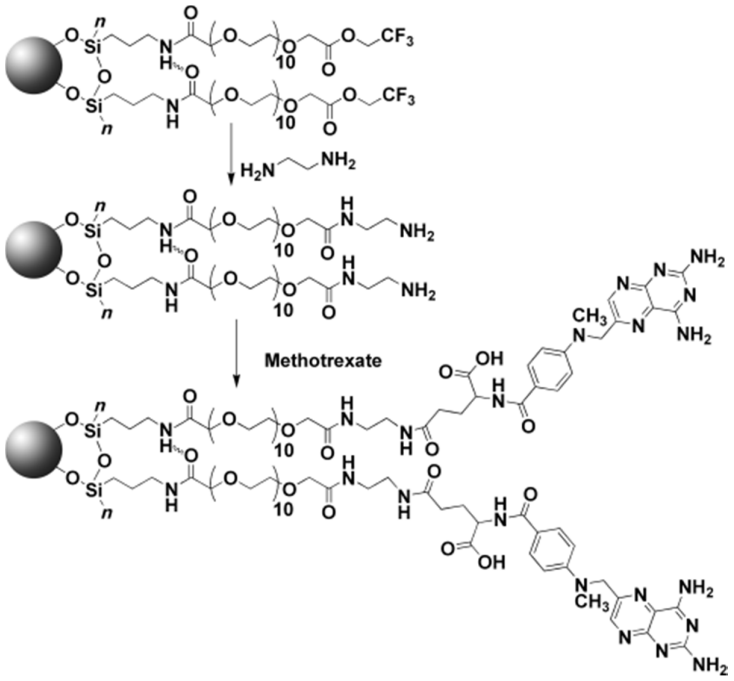

Figure 38: Immobilization of PEG-MTX on IONPs [479]**.**

The PEG coating serves as a protective biological layer to improve particle stability, preventing particle agglomeration and protein adsorption and increasing efficiency of the particle internalization by target cells [482]. Further, the presence of the amide bond between the 3-aminopropyltriethoxysilane self-assembled monolayer and the PEG linker provides monolayer stabilization through hydrogen bonding [483]. It is envisioned that the covalent modification of the nanoparticle with MTX via an amide bond will result in release of the MTX through the action of proteinase K enzyme following intracellular uptake of the conjugate into the target cells. The cytotoxicity assay, and MRI, results of the NP-PEG-MTX conjugates suggest that the nanoparticle conjugate developed by kohler *et al.* [479] may be a viable solution to chemotherapeutic drug delivery for treatment of gliomas and other cancers that highly express folate receptors. This nanoparticle conjugate demonstrated an increased MRI contrast enhancement through intracellular uptake by target cells. Leucovorin, an MTX antidote, was used to rescue the cells (9L glioma cells) that had been exposed to NP-PEG-MTX or free MTX, and the experiment verified the biocompatibility of NP-PEG-MTX conjugates and the MTX on NP-PEG-MTX conjugates to be the source of the cytotoxicity to the target cells. Kohler *et al.* demonstrated that the NP-PEG-MTX

conjugate can be specifically delivered to tumour cells, detectable by MRI, and induce cellular apoptosis, suggesting both the diagnostic and therapeutic roles of the developed nanoparticle conjugate. Chang *et al.* developed a pH-responsive drug release system based on the conjugates of PAMAM dendrimers-doxorubicin (PAMAM–DOX) and superparamagnetic iron oxide (Fe_3O_4) nanoparticles (IONPs) (**Figure 39**) [484]. The IONPs were stabilized by mPEG-G2.5 PAMAM dendrimers (PAMAM–DOX@IONPs). The anticancer drug DOX was conjugated to the dendrimer segments of amino-stabilized IONPs using hydrazine as the linker via hydrazone bonds, which is acid cleavable and can be used as an ideal pH-responsive drug release system.

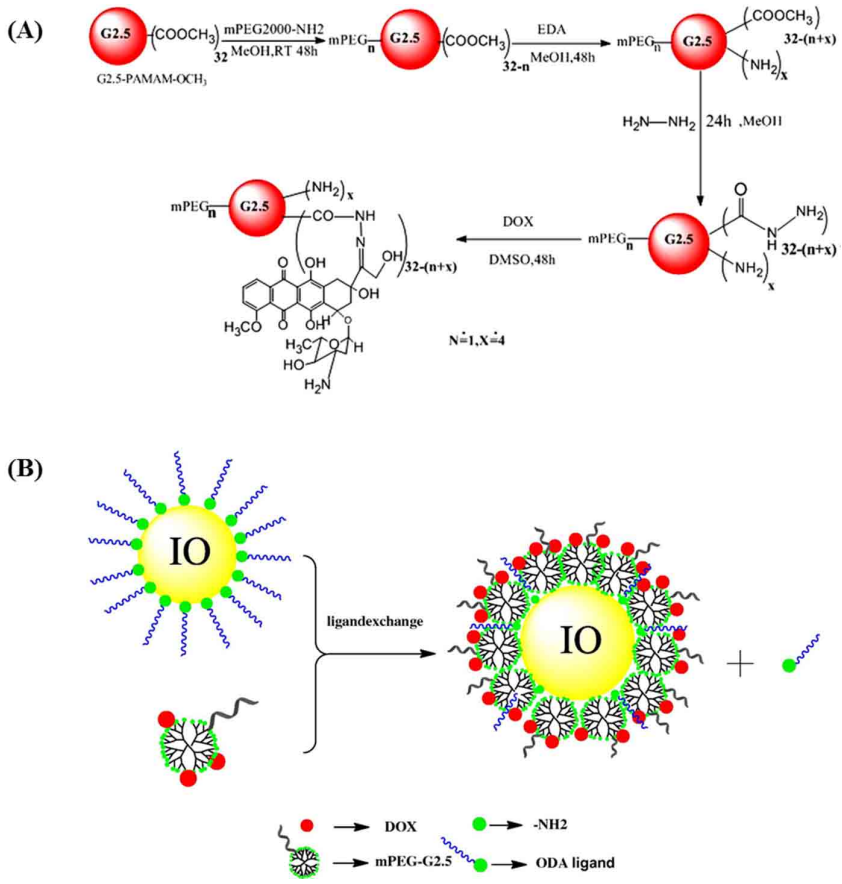

Figure 39: (A) Synthesis of mPEG-G2.5-DOX@IONPs, and (B) Direct exchange reactions between the monovalent capping ligand ODA and the mPEG-G2.5-DOX ligand [484]**.**

The drug release profiles of DOX–PAMAM dendrimer conjugates were studied at pH 5.0 and 7.4 (**Figure 40**). The results showed that the hydrolytic release profile can be obtained only at the condition of lysosomal pH (pH = 5.0), and IONPs participated in carrying DOX to the tumour by the Enhanced Permeability and Retention (EPR) effect.

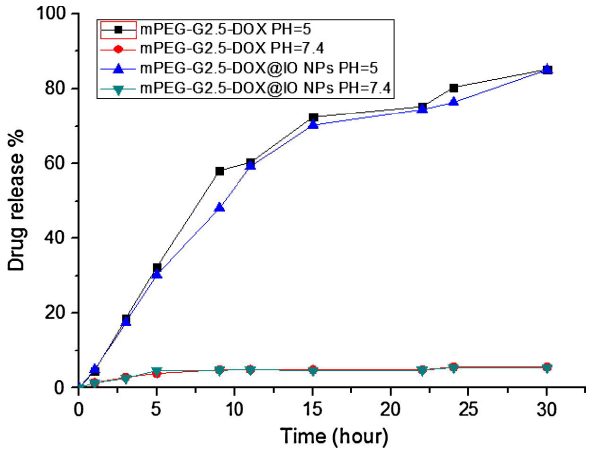

Figure 40: The DOX release profile from the DOX conjugates in a releasing environment with pH values of 5.0 and 7.4 [484]**.**

Moreover, Chang *et al.* found that DOX released from the conjugates were localized within the cells at the perinuclear regions as well as the nuclei, which can enhance the cytotoxicity of DOX and IONPs can be used as MR probe. These DOX conjugates have the potential to enhance the effect of MRI contrast and cancer therapy in the course of delivering anticancer drugs to their target sites by EPR [484].

Recently, Marcu *et al.* developed IONPs for targeted drug delivery in breast cancer. IONPs (8–10 nm) produced by laser pyrolysis, with uniform size and high magnetic properties were coated with the anthracycline antibiotic Violamycine B1 (VB1) and tested for the anti-tumour effect on MCF-7 cells. VB1 has a high binding efficiency to DNA but its clinical use is not allowed due to severe side-effects, such as cardiotoxicity. VB1 is the only anthracycline antibiotic with two amino-sugar groups which are supposed to play a role in the coating process on the nanoparticle surface. VB1 was attached to nanoparticles by electrostatic interaction between iron oxide groups on to the surface of nanoparticles and amino sugars present of VB1. The drug delivery system produced by Marcu *et al.* may provide better and more targeted drug accumulation in the tumour cells, thus lowering the therapeutic dose and consequently the side-effects of chemotherapy [485].

NanoTherm® is the first therapeutic formulation of magnetic nanoparticles approved in Europe in 2010 for the treatment of glioblastoma multiforme (brain tumour). The concept is based on the use of iron oxide core in magnetite phase (Fe_3O_4) coated with aminosilane with average size ranges from 10 to 15 nm, by intratumoural injection. An alternating magnetic field is then applied causing the rapid rotation of the nanoparticles, therefore heating the tumour with the generated friction. Depending on the duration of treatment and the increase

of temperatures within the tumour, cancer cells are irreversible damaged or sensitized for additional chemo- or radiotherapy. With this procedure, it is possible to combat the tumour from within, while sparing surrounding healthy tissue. Due to their coating, the nanoparticles remain at the treatment site, allowing repeated treatments and multimodal therapy concepts. NanoTherm® is currently under clinical development within Phase I (feasibility studies) for local ablation in prostate cancer or Phase II (efficacy studies) for pancreatic and esophageal cancers [486,487].

Chapter 3:

Carbon-Based Nanostructures

3. CARBON-BASED NANOSTRUCTURES

Among numerous types of nanomaterials developed in the past years, carbon nanomaterials have attracted particular interests in a large variety of fields including biomedicine [488–491], owing to their highly-enriched distinctive physical and chemical properties. Based on their covalent bonds linking their carbon atoms, carbon nanomaterials may be classified into sp^2- and sp^3-carbon nanomaterials (**Figure 41**). Typical sp^2-carbon nanomaterials include zero-dimensional (0D) fullerene, one-dimensional (1D) carbon nanotubes (CNTs), and two-dimensional (2D) graphene, all with well-defined structures. Carbon nanoparticles (CNPs) or carbon dots (C-dots), are nano-clusters of amorphous carbon (or composed by small crystalline structures) with sizes smaller than 10 nm, and may also be deemed as a type of 0D sp^2-carbon nanomaterials. Sp^3-carbon nanomaterials, usually are nano-diamonds (NDs) with crystal sizes in the nano-range.

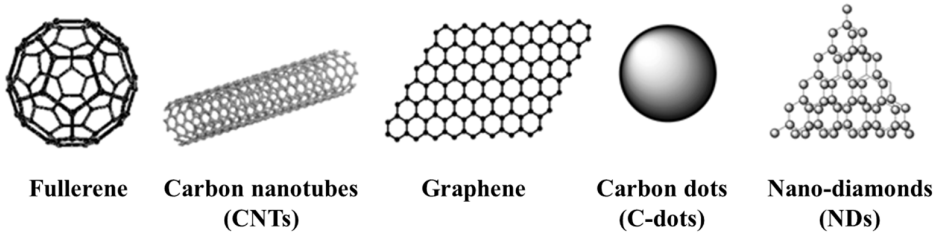

Figure 41: Different types of carbon nanomaterials explored for biomedical applications.

Many carbon nanomaterials, including CNTs, graphene derivatives, C-dots, and NDs, show interesting inherent optical properties such as fluorescence, making them useful contrast agents in optical imaging and sensing [492–495]. The excellent electrical properties of CNTs and graphene, allow them to be extensively used in a wide range of biosensing platforms [496,497]. Sp^2-carbon nanomaterials especially single-walled carbon nanotubes (SWCNTs) and graphene with all carbon atoms exposed on their surfaces, exhibit ultra-high surface area available for efficient drug loading and bioconjugation [488,498–500]. For fullerene and CNTs with hollow structures, the inside space may be utilized to load other functional species for theranostic purposes [501,502]. CNTs and graphene derivatives with strong optical absorbance in the NIR region are also useful for photothermal ablation of cancer [503–506]. Moreover, compared with many other inorganic nanomaterials such as quantum dots (QDs), which usually contain heavy metals, carbon nanomaterials composed simply by carbon are relatively safe at least in term of elementary composition.

3.1. Fullerenes

Fullerene or Buckminsterfullerene (C60) is a carbon allotrope discovered in 1985 by Kroto, Curl and Smalley [25]. Fullerene are composed entirely of carbon, in form of a hollow sphere, ellipsoid or tube. Spherical fullerenes are also referred to as buckyballs (**Figure 41**). An important property of C60 molecule is its high symmetry. There are 120 symmetrical operations, like rotation around the axis and reflection in a plane, which map the molecule onto itself. This makes C60 the most symmetrical molecule [507]. The C60 fullerene surface contains 20 hexagons and 12 pentagons. All the rings are fused; all the double bonds are conjugated. Fullerenes belong to the class of inorganic nanoparticles and show wide availability due to their small size (~ 1 nm) and biological activity. However, the difficult processability of fullerenes has presented a major problem in hectic search for medicinal applications. C60 are insoluble in aqueous media and aggregate very easily [508]. There have been several attempts to overcome the poor solubility of fullerenes. They can be entrapped in cyclodextrins [509], calixarenes [510–512], polyvinylpyrrolidone [513], micelles and liposomes [514]. In addition, the combination of fullerenes and lipid membranes has led to very interesting results. Lipid bilayers are dynamically mobile structures, partially ordered and of biopharmaceutical interest for covering biocompatible surfaces or for the controlled release of drugs [515]. Various functionalizations have been utilized to increase the hydrophilicity (e.g. with amino acid, carboxylic acid, polyhydroxyl group, amphiphilic polymers) and to prepare new compounds presenting biological and pharmacological activity. The empty interior cavity of the fullerene molecule makes it an ideal site for containment of a metal atom to form metallofullerene. This special structure of metallofullerene shows advantages compared to the metal itself or metal chelate complexes. One of their most important and novel electronic properties is the so-called intra-fullerene electron transfer from the encaged metal atom to the fullerene cage, which has been suggested to use in MRI [516]. Most likely due to its unique chemical structure, C60 possesses interesting photo-physical properties and generates reactive oxygen species (ROS) by exposure to visible light, making it a potentially strong agent for photodynamic therapy in biological systems [517]. The specific physicochemical properties of fullerenes promoted the development of tumour theranostic; consequently, functionalized fullerenes are currently under extensive investigation due to their potential application to cancer imaging such as MRI [518–521] and cancer therapy such as photodynamic therapy (PDT) [522–524], radiotherapy [525,526] and chemotherapeutics [501,527,528].

Among many imaging strategies, such as optical imaging (OI), computed tomography (CT), MRI, ultrasound (US), and radionuclide imaging with positron emission tomography (PET), MRI is a versatile, non-invasive medical diagnostic technique that can provide both physiological and anatomical information, while not requiring the use of ionizing radiation. In addition, in many applications it is often the most sensitive method available to depict soft tissues. Therefore, it has been extensively used for brain and central nervous system imaging, for assessing cardiac function and for detecting abnormal tissues such as tumours [529]. Paramagnetic metal ions, especially gadolinium (Gd^{3+}), have been proposed as MR contrast agents. Conventional T1 contrast agents have been developed in the form of more stable and less toxic metallochelates, including gadolinium(III) diethyltriaminepentaacetic acid (Gd(III)-DTPA) and gadolinium-tetraazacyclododecanetetraacetic acid (Gd(III)-DOTA), which are currently marketed as Omniscan® and ProHance®, respectively [258,530]. However, the main limitation for Gd^{3+} chelate complexes is the release of metal ions *in vivo* during metabolic processes and the subsequent toxicity. Since gadolinium-containing metallofullerenes were first used as excellent contrast agents for MRI with relatively high spatiotemporal resolution, they have attracted much attention for their potential application in clinical diagnosis. The Gd^{3+} ion encapsulated in the fullerene cage, preserves the properties of the metal ion, avoids any leakage and thus prevents its dissociation *in vivo* [530]. After specific chemical modifications, various $Gd@C_n$ (n=60, 82) derivatives have been developed and widely explored (**Figure 42**) [531,532].

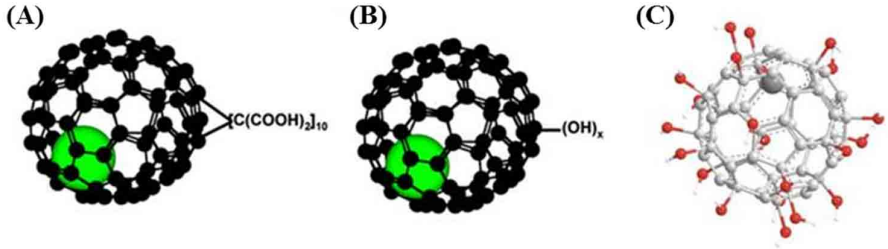

Figure 42: Schematic representation of (A) $Gd@C_{60}[C(COOH)_2]_{10}$, (B) $Gd@C_{60}(OH)_x$, (C) $Gd@C_{82}(OH)_{22}$ [531,532]**.**

$Gd@C_{82}(OH)_n$ has shown a water proton relaxivity twenty times higher than the commercial Gd-DTPA. After intravenous (i.v) administration of $Gd@C_{82}(OH)_{40}$ at a dose of 1/20 of the typical clinical dose of Gd-DTPA, a higher signal enhancement was measured *in vivo* (**Figure 43**) [518]. To achieve better bio-distribution, modification of the fullerene cages with biologically active groups has often been proposed. For example, the organic

phosphonate modified $Gd@C_{82}O_2(OH)_{16}(C(PO_3Et_2)_2)_{10}$ has exhibited high affinity to bone [533].

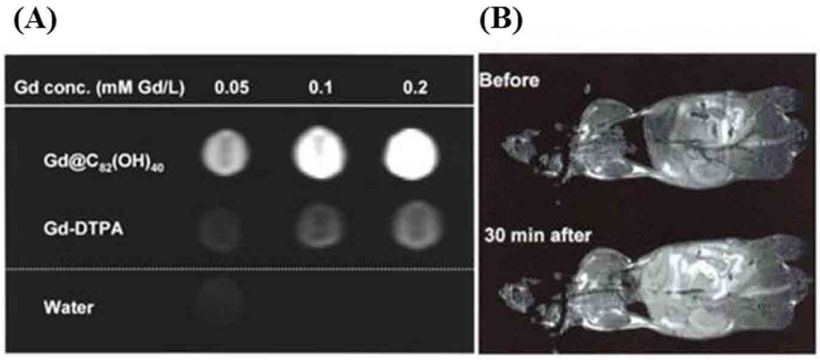

Figure 43: (A) T1-weighted MRI of $Gd@C_{82}(OH)_{40}$ and Gd-DTPA phantom at a concentration of 0.05, 0.1, and 0.2 mmol Gd/L, (B) CDF1 mice before and 30 min after i.v. administration of $Gd@C_{82}(OH)_{40}$ via tail vein as a dose of 5 µmol Gd/kg [518]**.**

However, tumour-targeting by directly administering fullerenes into tumour tissue is certainly a subsequent challenge for tumour imaging. Shu *et al.* conjugated antibodies of the green fluorescent protein (anti-GFP) to endohedral gadofulleride, $Gd@C_{82}O_6(OH)_{16}$-$(NHCH_2CH_2COOH)_8$, as a model for "tumour-targeted" imaging agents, and could be detected by using a fluorescent GFP probe. The results revealed that the antibody activity was well preserved after the conjugation, and the MRI activity was higher than that of unconjugated gadofulleride [520]. Recently, a more encouraging result was obtained. Fillmore *et al.* conjugated a carboxyl functionalized metallofullerene $Gd_3N@C_{80}(OH)_{26}(CH_2CH_2COOH)_{16}$ to an interleukin-13 (IL-13) peptide, the receptor of which was expressed on glioblastoma multiforme cells. This preliminary finding demonstrated that functionalized gadolinium metallofullerenes could serve as a platform to deliver imaging and therapeutic agents to tumour cells [521].

Photodynamic therapy (PDT) is a non-invasive treatment for various types of tumour. The combination of a photosensitizing agent and focused irradiation is used to controlled production of reactive oxygen species in a localized area, leading to cell destruction. By using highly focused light irradiation, photodynamic therapy has the potential to act specifically at the desired site of action with low levels of collateral damage to healthy cells [534]. Fullerenes can efficiently generate reactive oxygen species when exposed to visible light, which means it may be an effective cytotoxic agent.

After the ideal molecular size, water-solubility, and tumour targeting were developed through various modifications, functionalized fullerenes are now available for cancer PDT

both in tumour cells and tumour-bearing mice [535,536]. Liu *et al.* demonstrated the use of poly ethylene glycol (PEG)-conjugated fullerene containing Gd^{3+} ions for photodynamic therapy in combination with magnetic resonance imaging (MRI). The authors demonstrate through experimental data that tumour PDT effect was significantly promoted by photosensitizer tumour targetability and MRI activity. C60-PEG-Gd was injected into tumour bearing mice. The MRI activity was introduced into C60-PEG of PDT photosensitizer. The chelate incorporation of Gd^{3+} ions could convert C60-PEG derivative to a photosensitizer with both the diagnostic and therapeutic functions [537]. Ji *et al.* also studied the biodistribution and tumour uptake of $C_{60}(OH)_x$ in five kinds of tumour models by radiotracer ^{125}I-labeled $C_{60}(OH)_x$. The accumulation ratios of ^{125}I-$C_{60}(OH)_x$ in tumour compared to normal muscle tissue (T/N) and blood (T/B) at different time points revealed that $C_{60}(OH)_x$ could be accumulated in several tumours readily and persistently, especially in mouse H22 hepatocarcinoma, suggesting that it could be used as a good photosensitizer in photodynamic tumour therapy [538].

Besides surgery, chemotherapeutics is another principal method for tumour therapy. In recent years, functionalized fullerenes have been found to have some good characteristics to aid with antitumour treatments, and some of them have exhibited the potential for tumour inhibition [539]. Zhu *et al.* also tested the tumour-inhibitory effect of $C_{60}(OH)_x$ on the murine H22 hepatocarcinoma model [527]. In the $C_{60}(OH)_x$ treated group, significant tumour inhibition rates and reduced damage to liver were shown, in accordance to the histological results of inhibited tumour infiltration. Additionally, the anti-metastatic activities of fullerenol $C_{60}(OH)_{20}$ was observed in cancer metastasis models [528]. Mroz *et al.* investigated the photodynamic activity of fullerenes derivatized with hydrophilic and cationic groups against a range of mouse cancer cell lines [524]. They found that, monocationic fullerene is highly effective photosensitizer for killing cancer cells by rapid induction of apoptosis after illumination.

Moreover, some fullerenes could increase the chemo-sensitization of tumour cells to chemotherapeutic agents and result in antitumour drug-mediated cell death, especially in some drug-resistant cancer cells [501].

The direct delivery of drugs and biomolecules through cell membrane into cells has attained increasing attention and has put a main focus on the development of efficient and safe carriers to transport drugs. Transport of any compound into the nucleus of an intact cell is a major challenge, as transfer is limited by at least three membrane barriers, which are the cell

membrane, the endosomal membrane and the nuclear membrane. A fullerene-paclitaxel conjugate (**Figure 44**) has been designed by Zakharian *et al.* as a slow-release drug for aerosol liposome delivery of paclitaxel for lung cancer therapy via enzymatic hydrolysis [540].

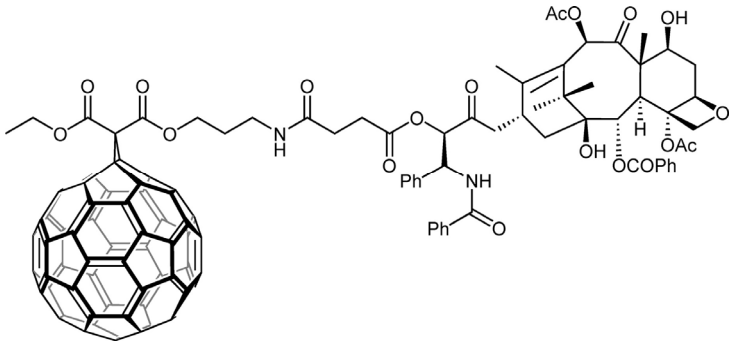

Figure 44: Fullerene-Pacliltaxel Conjugate [540]**.**

The C60-paclitaxel conjugate is stable in the solid state and in aprotic organic solvents as well as in aqueous media (10% DMSO) at physiological pH. However, incubation of C60-paclitaxel conjugate with bovine plasma at 37 °C resulted in the release of paclitaxel, with the half-life of hydrolysis around 80 min. Assuming a similar half-life for C60-paclitaxel conjugate *in vivo* and the ability of C60-paclitaxel conjugate to remain in lungs, a several-fold increase in the exposure time of cancer cells to the drug should be achieved by C60-paclitaxel conjugate since the half-life of paclitaxel itself in the lungs has been reported to be only 20 min after delivery by aerosol [541]. A liposome formulation of the C60-paclitaxel conjugate has been prepared using dilauroylphosphatidylcholine (DLPC), and showed a significant anticancer activity in human epithelial lung carcinoma A549 cells. With both clinically relevant kinetics of hydrolysis and significant cytotoxicity in tissue culture, the C60-paclitaxel conjugate holds promise for enhanced therapeutic efficacy of paclitaxel *in vivo* [540]. Furthermore the ability of fullerenes to penetrate through intact skin is widening their application in cellular drug delivery [542].

3.2. Carbon nanotubes

Carbon nanotubes (CNTs) represent one of the most studied allotropes of carbon. Since their discovery in 1991 by Sumio Iijima [26], CNTs have raised considerable attention due to their important electrical, chemical, thermal, mechanical, and structural properties which have made them an area of great research interest [543]. The large surface area, size stability on the nanoscale, ability to encapsulate therapeutic/diagnostic agent and suitability for

surface modifications made CNTs suitable for theranostic applications [544–546]. The carbon atoms in CNTs are arranged to form a cylinder of graphite layers. CNTs are classified into single-walled carbon nanotubes (SWCNTs) which are formed of one layer of graphene have diameters of around 0.4-2 nm and are several micrometers long, with an empty internal space; or multi-walled carbon nanotubes (MWCNTs) which are formed of multiple layers of graphene. CNTs are commonly synthesized by chemical vapor deposition (CVD), laser-ablation method, and arc-discharge method (**Figure 45**) [546–548].

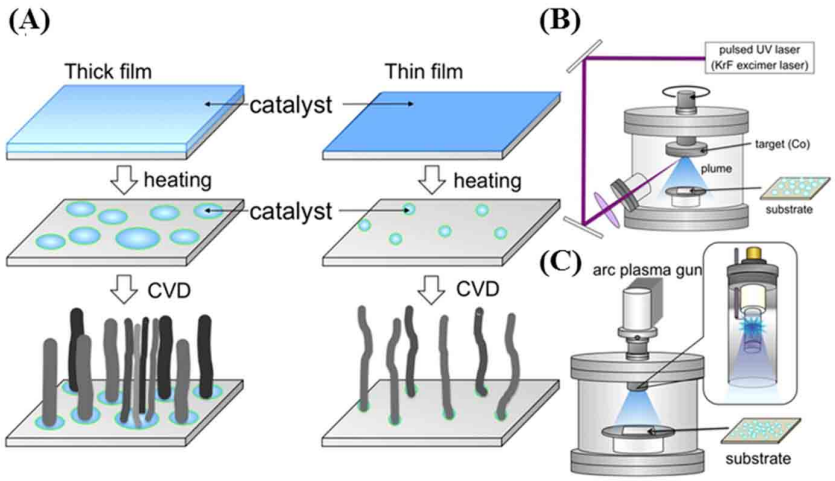

Figure 45: Schematic illustration showing different synthesis methods of carbon nanotubes. (A) Chemical vapor deposition (CVD) method used for carbon nanotubes synthesis. (B) Laser-ablation technique used in the synthesis of carbon nanotubes. (C) Carbon arc-discharge technique performed to synthesize carbon nanotubes [549]**.**

Through appropriate functionalization (**Figure 46**), CNTs have been used as nanocarriers to transport anticancer drugs, genes, and proteins for chemotherapy. They have also been used as mediators for photothermal therapy (PTT) and photodynamic therapy (PDT) to directly destroy cancer cells. Therefore, the interaction between CNTs and the biological environment is very complex and sometimes unpredictable. Researchers have found that CNTs can show different levels of toxicity depending on their synthesis, surface-to-volume ratio, shape, concentration, aspect ratio, extent of oxidation, composition, functional groups, and the applied dosage [550,551].

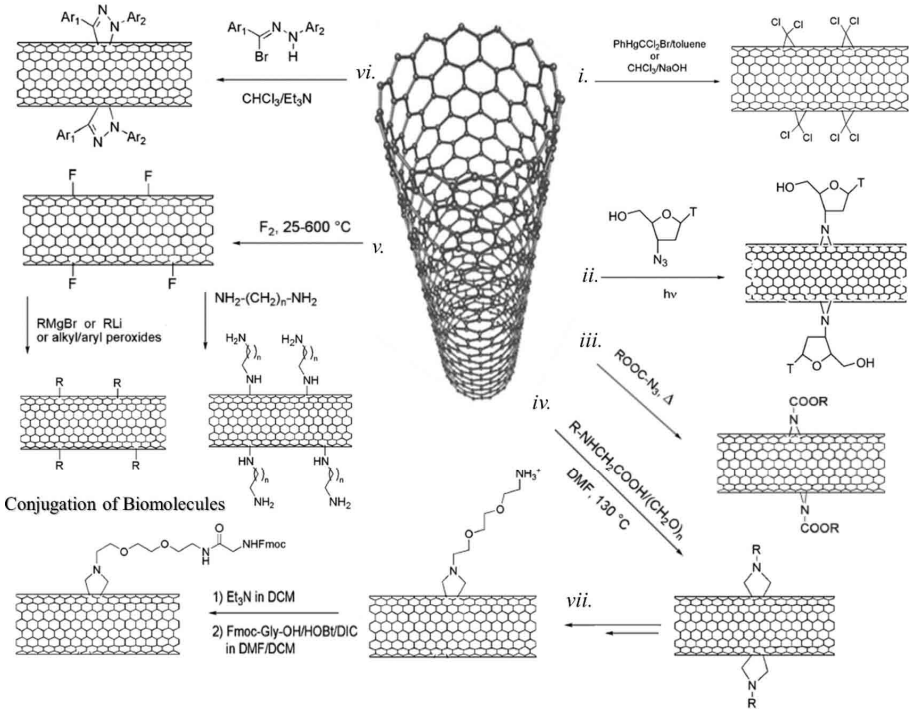

Figure 46: Different functionalization strategies of CNTs showing (i) cycloaddition with in situ generated dichlorocarbene, (ii) photoinduced generation of reactive nitrenes, (iii) functionalization by nitrenes, (iv) 1,3 dipolar cycloaddition of azomethine ylides, (v) reaction scheme for fluorination of nanotubes, defunctionalization, and further derivatization; (vi) 1,3 dipolar cycloaddition of nitrile amines; (vii) reaction pathway for obtaining water-soluble ammonium-modified nanotubes [552]**.**

In addition, CNTs are highly hydrophobic, which plays a major role in reducing their biocompatibility [553]. Therefore, it is critical to functionalize CNTs to make them more soluble and allow their integration into many organic, inorganic, and biological systems and applications [552]. CNTs have the ability to damage the DNA and the cell membrane as well. They can also cause toxicity through oxidative stress, mitochondrial activities modification, protein synthesis, and altered intracellular metabolic routes [551]. The most common CNTs mechanisms that lead to cytotoxicity also include necrosis and apoptosis [551]. There are three main approaches for CNTs modification, namely, (a) the covalent functionalization of the π-conjugated skeleton of CNTs using various chemical groups and reactions; (b) the endohedral filling of their inner empty cavity; and (c) the noncovalent adsorption of numerous functional bio/molecules (**Figure 47**) [552].

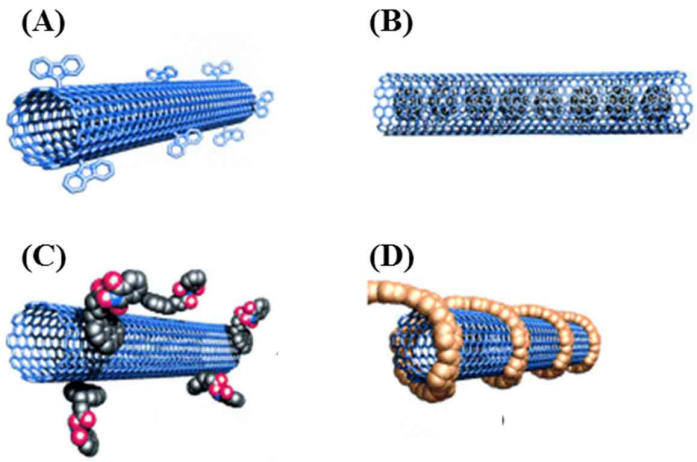

Figure 47: Modification possibilities for CNTs (A) covalent sidewall functionalization, (B) Endohedral functionalization of the inner empty cavity, (C) Non-covalent surfactant encapsulation, and (D) Non-covalent polymer wrapping [554]**.**

Covalently conjugated drug molecules are linked to the functional groups on the CNTs surface or to the polymer coating of CNTs, usually via cleavable bonds. Anti-cancer drugs were linked by 1,3-dipolar cycloaddition to functionalized CNTs via amide bonds for drug delivery [555,556].

Traditionally, chemotherapy is used to diminish cancers with other treatment techniques such as radiation and surgery. However, during treatment, undesirable toxicity narrows the therapeutic window, and the nonspecificity of drugs can increase drug resistance [557]. Therefore, new methods for delivering anticancer molecules specifically to tumours to reduce side effects and improve therapeutic efficacy are greatly needed. Many drug delivery systems have been designed using CNTs for the treatment of a variety of diseases. In fact, CNTs-based anticancer drugs have attracted much attention, and depend on two strategies: (1) selective targeting, which is accomplished through functionalization with specific tumour receptors, and (2) the controlled release of the drugs usually present in tumour environment such as lower pH [558–560]. Aromatic molecules with a flat structure can be adsorbed on the surface of CNTs via non-covalent π-π stacking. In 2007, Liu *et al.* discovered that DOX could be stacked on the surface of PEGylated SWCNTs with a remarkably high loading capacity of up to 4 grams of DOX per 1 gram of CNTs (**Figure 48A**), owing to the ultra-high surface area of SWCNTs [561]. DOX bounded onto SWCNTs was pH-dependent, decreasing from a loading factor of ~4 to ~2 and ~0.5 as pH was reduced from 9 to 7 and 5, respectively (**Figure 48B**). This trend was attributed to the increased hydrophilicity and higher solubility of DOX at lower pH caused by increased

protonation of amino groups on DOX, thereby reducing the hydrophobic interaction between DOX and SWCNTs. In term of release, DOX stacked on SWCNTs remained stably bound in physiological buffers. In an acidic solution of pH 5.5, they observed a release of DOX from SWCNTs by ~40% over 1 day, attributed to the increased hydrophilicity and solubility of DOX at this pH (**Figure 48C**) [561]. The pH-dependent drug release from SWCNTs could be exploited for drug delivery applications since the micro-environments of extracellular tissues of tumours and intracellular lysosomes and endosomes are acidic, potentially facilitating active drug release from SWCNT delivery vehicles.

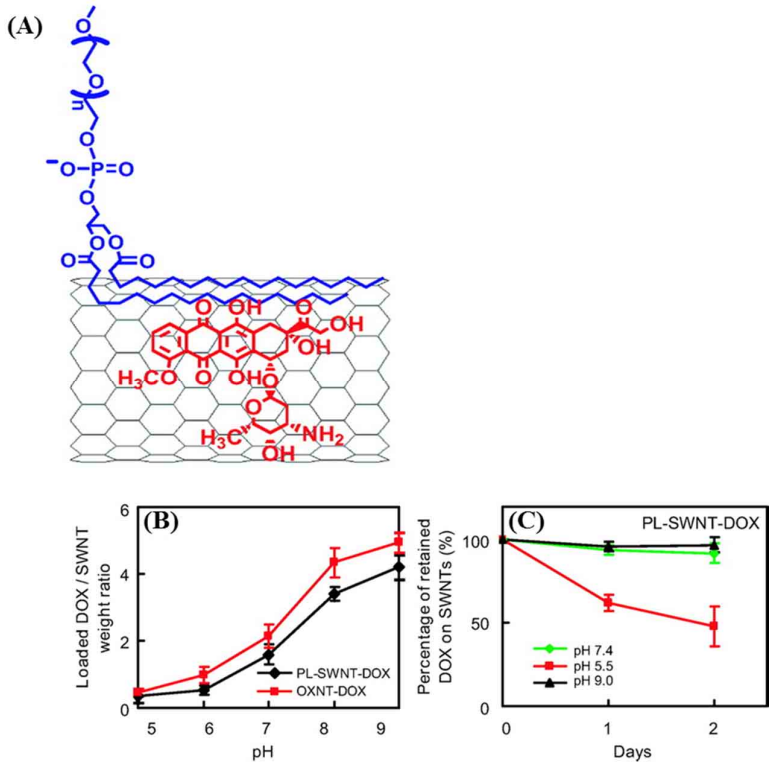

Figure 48: (A) A scheme showing supramolecular π-π stacking of DOX on PEGylated SWCNTs, (B) Doxorubicin loading efficiency at various pH values for SWCNTs, and (C) Doxorubicin retained on PL-PEG-SWCNTs over time in buffers at the three pH values indicated [561]**.**

PEGylated SWCNTs loaded with DOX by π-π stacking could also be used for *in vivo* cancer treatment in a Raji B-cell lymphoma model. The SWCNT-DOX complex, while only exhibiting marginally improved tumour growth inhibition compared with free DOX, was much less toxic to the treated mice, thus offering a remarkably improved therapeutic outcome (**Figure 49**) [562].

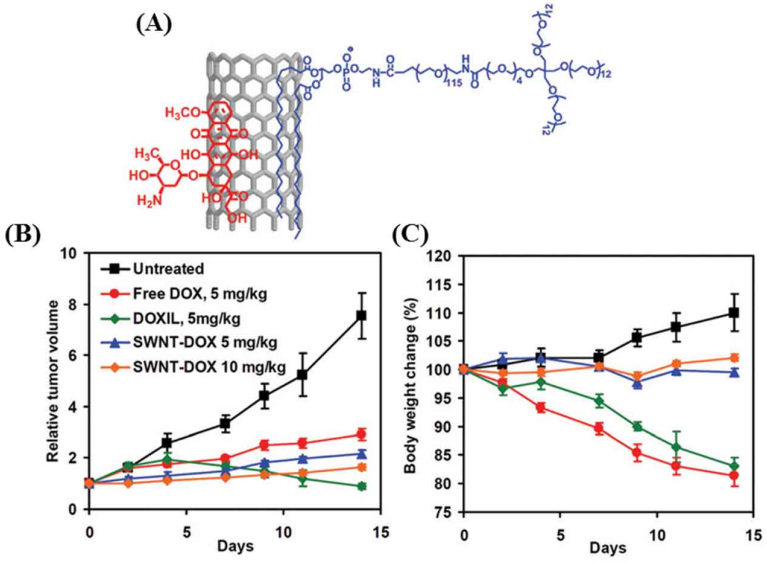

Figure 49: *In vivo* doxorubicin delivery with carbon nanotubes for cancer treatment. (A) A scheme showing supramolecular π-π stacking of DOX on PEGylated SWCNTs. (B) Tumour sizes of untreated (n = 7), 5 mg/kg free DOX treated (n = 10, 2 mice died in the second week), 5 mg/kg Doxil treated (n = 5), 5 mg/kg SWCNT-DOX treated (n = 10) and 10 mg/kg SWCNT-DOX treated (n = 10) mice were measured. (C) SWCNT-DOX resulted in far less weight loss than DOX and DOXIL. Averaged tumour volumes and body weights were normalized to day 0 [562]**.**

Using a similar strategy, Ali-Boucetta *et al.* formed MWCNTs complexes with DOX via π–π stacking interactions. Their complexes showed enhanced cytotoxicity in human breast cancer MCF-7 cells [563]. The enhanced cytotoxicity suggests that MWCNTs can mediate the delivery of doxorubicin and hence improve the cellular uptake of the drug.

In another study, Tian *et al.* prepared the poorly water-soluble anticancer Camptothecin (CPT)-loaded MWCNTs with tri-block copolymer through π–π stacking interactions to improve antitumour activity. The MWCNTs were coated with the tri-block copolymer Pluronic P123 to enhance aqueous solubility. The polymer-coated MWCNTs formed non-covalent supramolecular complexes with CPT. *In vitro* cytotoxicity studies using HeLa cells showed that these complexes had enhanced antitumour activity compared to free CPT. These results suggest that functionalized MWCNTs improve the activity of anticancer drugs [564].

Tripisciano *et al.* encapsulated irinotecan, a more water-soluble semisynthetic analog of CPT, within MWCNTs. It was observed that a larger inner diameter tube exhibited higher filling amount of irinotecan than a smaller one and a loading efficiency of 32% was achieved. Because the stability and hydrophilicity of irinotecan are increased under acidic conditions (tumour environment), rapid and complete release was observed (pH 6.0 vs 7.0) in a mild acidic environment [565].

Paclitaxel is a poorly water-soluble anticancer molecule. The commercialized paclitaxel product (Taxol) used Cremophor EL to solubilize the drug. Unfortunately, the toxicity of Cremophor EL itself makes finding a suitable alternative a high priority. Moreover, the circulation time of Taxol is very short. Coating the nanocarriers with hydrophilic polymers such as polyethylene glycol (PEG) has been established as a strategy to prolong circulation of the nanocarrier-entrapped molecules in the blood by making the carrier highly evasive to uptake by the blood macrophages [566,567]. PEGylation of paclitaxel increases the circulation time in the blood over Taxol [568]. Liu *et al.* conjugated functionalized SWCNTs with paclitaxel (PTX) through branched PEG chains via a cleavable ester bond to obtain a SWCNT-PTX conjugate highly soluble and stable in aqueous solutions (**Figure 50A**). They performed an i*n vitro* cell toxicity tests with a 4T1 murine breast cancer cell line and found that SWCNT-PTX exhibited similar toxicity as Taxol and PEGylated PTX without any loss of cancer cell destruction ability (**Figure 50B**).

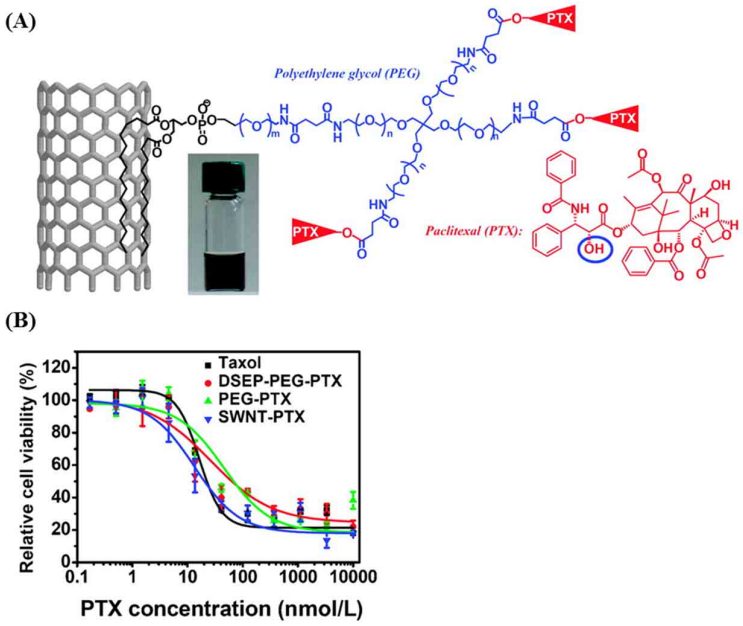

Figure 50: (A) Schematic illustration of PTX conjugation to SWCNT functionalized by phospholipids with branched PEG chains. (B) Cell survival versus concentration of PTX for 4T1 cells treated with Taxol, PEG-PTX, DSPE-PEG-PTX, or SWCNT-PTX for 3 d. The PTX concentrations to cause 50% cell viability inhibition (IC_{50} values) were determined by sigmoidal fitting to be 16.4 ± 1.7 nmol/L for Taxol, 23.5 ± 1.1 nmol/L for DSPE-PEG-PTX, 28.4 ± 3.4 nmol/L for PEG-PTX, and 13.4 ± 1.8 nmol/L for SWCNT-PTX [569]**.**

The strong therapeutic efficacy of SWCNT-PTX is shown by its ability to slow down tumour growth *in vivo* even at a low drug dose (5 mg/kg PTX). They observe higher tumour uptake of PTX and higher ratios of tumour to normal organ PTX uptake for SWCNT-PTX than

Taxol and PEG-PTX, highly desired for higher treatment efficacy and lower side effect (**Figure 51**) [569].

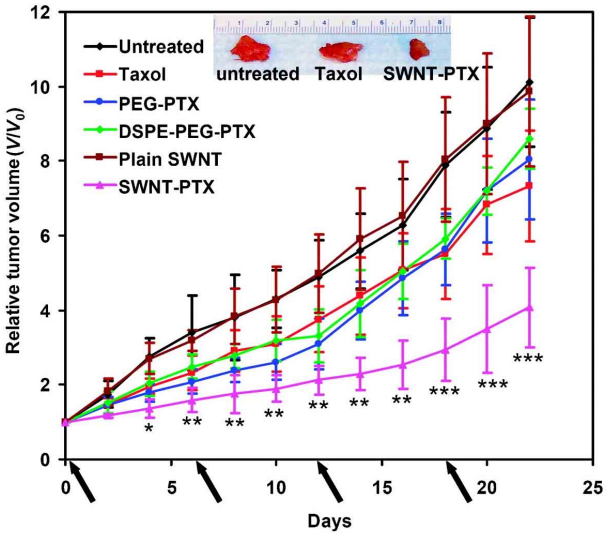

Figure 51: Tumour growth curves of 4T1 tumour-bearing mice that received different treatments indicated. The same PTX dose (5 mg/kg) was injected (on days 0, 6, 12, and 18, marked by *arrows*) for Taxol, PEG-PTX, DSPE-PEG-PTX, and SWCNT-PTX. *$P < 0.05$; **$P < 0.01$; ***$P < 0.001$, Taxol versus SWCNT-PTX. Number of mice used in experiments: 8 mice per group for untreated, 5 mice per group for SWCNT only, 9 mice per group for Taxol, 5 mice per group for PEG-PTX, 6 mice per group for DSPE-PEG-PTX, and 14 mice per group for SWCNT-PTX. Inset, a photo of representative tumours taken out of an untreated mouse (*left*), a Taxol-treated mouse (*middle*), and a SWCNT-PTX–treated mouse (*right*) after sacrificing the mice at the end of the treatments [569]**.**

As compared to DOX, PTX has much lower solubility in aqueous solution and has no extended π-structures larger than one aromatic ring. PTX cannot be loaded onto CNTs by adsorption from aqueous solution directly like DOX. Lay *et al.* developed an approach to physically load PTX onto the side walls of CNTs by immersing PEGylated SWCNTs or MWCNTs in a saturated solution of PTX in methanol. The physical loading of PTX onto the side walls of PEGylated CNTs might be attributed to a strong hydrophobic interaction among PTX and the side walls of CNTs. Due to the low solubility of PTX in aqueous solution, the release rate of free PTX is very slow. After loaded PTX onto CNTs, they can be released faster but still in a sustained profile. Both PEGylated SWCNTs and MWCNTs show low cytotoxicity in HeLa cells and MCF-7 cells, but PTX loaded PEGylated SWCNTs and MWCNTs have strong efficacy to kill cancer cells with IC_{50} lower than free PTX [570]. Platinum (Pt) based compounds have been studied as a class of effective anticancer agents [571]. They kill cancer cells by chelating DNA and forming adducts that affect key cellular processes, such as transcription and replication, and trigger apoptosis [572]. Inert Pt(IV)

prodrugs and the combination between Pt(II) drugs and drug carriers have been widely studied [573,574]. Pt(IV)-conjugated CNTs were constructed to effectively deliver cisplatin [575–579]. Therefore, targeted drug-delivery constructs are much desired. In general, a tumour-targeting drug-delivery system consists of a cell surface recognition moiety and a chemical warhead connected directly or through a suitable linker to a delivery system such as a SWCNTs (**Figure 52**). The conjugate itself should be nontoxic and the linker must be stable in blood circulation. Upon internalization into the cancer cell, the conjugate should be readily cleaved to generate the active agent.

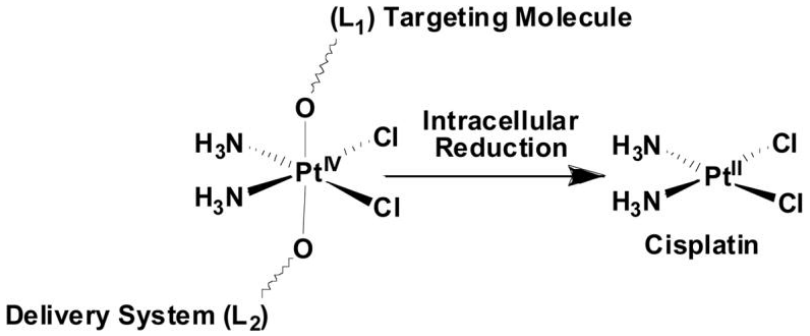

Figure 52: Targeted prodrug-delivery system [575]**.**

A variety of receptors have been identified as markers for carcinomas. Among these is the folate receptor (α-FR), and its substrate folic acid (FA) has the potential to target several types of cancer cells because of its ability to react with this high-affinity, membrane-anchored protein [580]. Expression of α-FR on tumour cell surfaces has led to the exploitation of FA as an important ligand for specific targeting by diagnostic or therapeutic cancer cell agents [581,582].

Dhar *et al.* have developed amine-functionalized SWCNTs (SWCNTs-phospholipid-PEG-NH_2) as a "longboat delivery system" for targeting delivery of cisplatin upon reduction in the cell (**Figure 53**). They designed a Pt(IV) complex having succinate as one of its axial ligands for conjugation with amine-functionalized SWNTs. The second axial ligand contains a folic acid derivative separated from the platinum center by a PEG spacer. The use of PEG makes the compound more water soluble and biocompatible. Pt(IV) complex has been reported to be taken up by cancer cells via endocytosis, followed by the release of the drug and its subsequent interaction with the nuclear DNA [575].

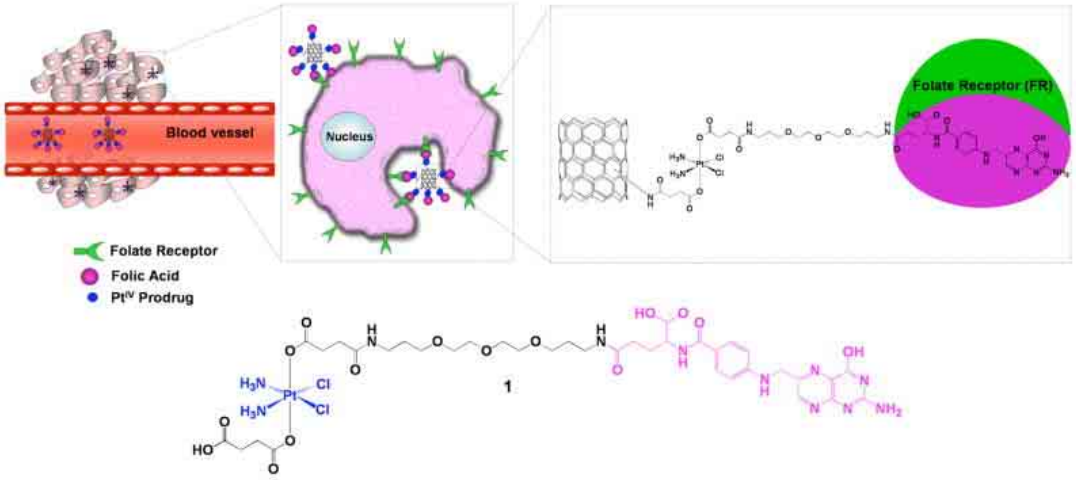

Figure 53: The "longboat" anticancer system in which the chemotherapeutic agent cisplatin is attached from one end to the FA derivative and from the opposite end to a SWCNT via an amide link [575]**.**

Magnetic functionalization of CNTs combined with Pt-based anticancer agents show potential as magnetic carriers in drug delivery. Yang *et al.* developed magnetic CNTs containing anticancer agents [576]. Magnetite (Fe_3O_4) nanoparticle layers were synthesized on the inner surface of CNTs, and chemotherapeutic agents, such as 5-fluorouracil and cisplatin, were incorporated into the pores of the CNTs. Individualized CNTs were non-covalently functionalized by phospholipids with a PEG moiety and FA terminal group to enhance drug delivery to cancer cells. Their magnetic CNTs were retained in the draining targeted lymph nodes for several days and continuously released chemotherapeutic drugs, enabling the selective killing of tumour cells. They also studied the lymphatic distribution of magnetic CNTs *in vivo* [583] . They prepared magnetic MWCNTs functionalized with poly(acrylic acid), which were subcutaneously injected into mice. The degree of black staining of lymph nodes and the concentration of magnetic CNTs were found to be dose dependent. The injection of CNTs did not show local or systemic toxicity. Their results demonstrated the potential of using magnetic CNTs for diagnosing and treating cancer.

Another platinum anticancer, namely, carboplatin, after being incorporated into CNTs has been shown to inhibit the proliferation of urinary bladder cancer cells *in vitro*. In another study, anticancer effects have been shown to be dependent on the method used to entrap the drug in the CNTs, which highlighted the possible effects of preparation conditions on the therapeutic activity of therapeutic molecules associated with CNTs [584].

Chemical functionalization of CNTs offers the advantage that the functional groups, further modified with a therapeutic, targeting or imaging molecule, are stably attached on the nanotube backbone, and therefore avoid the risk of macromolecule desorption or exchange with serum proteins and other blood components following administration. For example, Khazaei *et al.* found that covalent functionalization of SWCNT with amide and ester bonds facilitates the slow administration of drug for longer periods and improves the solubility in aqueous and organic media [585]. Recently, Das *et al.* designed a theranostic MWCNTs by including acid-oxidized MWCNTs with four varieties of functional moieties: a fluorochrome (Alexa-fluor, AF488/647), targeting agent (i.e, folic acid), radionucleide (Technitium-99m), and methotrexate (MTX). MTX was conjugated to MWCNTs via a serum-stable yet intracellularly hydrolysable ester linkage to ensure minimum drug loss in circulation. The cellular uptake studies showed the selective internalization of theranostic MWCNTs by folate receptor positive human lung (A549) and breast (MCF-7) cancer cells through folate receptor mediated endocytosis. The tumour specific accumulation of targeted theranostic MWCNTs in xenografted mice after 24 h was 19.14 and 8.62 times higher in comparison to free and non-targeted theranostic MWCNTs. This study shows the controlled delivery of MTX from theranostic MWCNTs, receptor mediated delivery, optical detectability of fluorochromes, and radio-traceability of ^{99m}Tc. MWCNTs could be a promising multimodal theranostic platform for cancer diagnosis and therapy [586].

Because of the unique properties of CNTs that can generate singlet oxygens, which are cytotoxic, through photochemistry and generate significant amounts of heat upon excitation with NIR light, CNTs have been evaluated as candidate materials in photothermal therapy (PTT) and photodynamic therapy (PDT). PTT and PDT are two methods that can be utilized for cancer treatment and show noninvasiveness and minimal side effects compared to other strategies including radiotherapy and chemotherapy (**Figure 54**) [587].

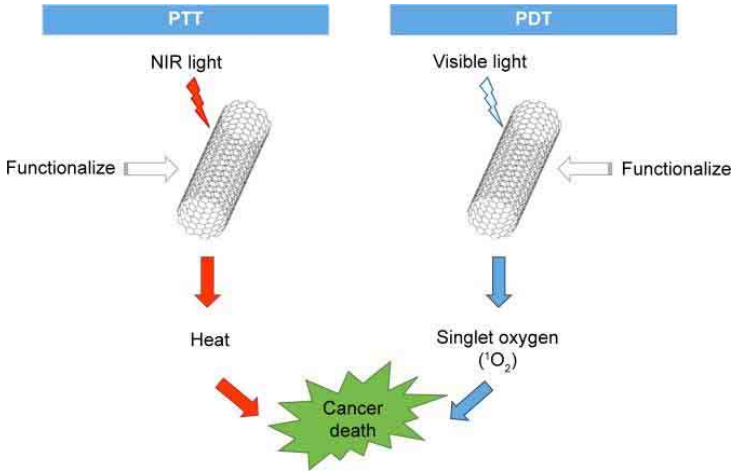

Figure 54: PTT and PDT using CNTs [587]**.**

CNTs can effectively absorb NIR light, and the absorbed NIR light transmits heat to the nanotubes. Therefore, when the optical coupling effect of light and CNTs is applied, external heat energy can be transmitted inside the body [588]. This unique property of CNTs has been exploited as a method for killing cancer cells via thermal effects [506,589–591]. The optical coupling of light with CNTs can be enhanced by the surface defects of CNTs and by creating intentional surface defects to increase nanotube heating [589]. This physicoelectronic characteristic of the engineered CNTs can be employed to thermally destruct the tumour cells by using CNTs that have good heat conducting properties.

Torti *et al.* proposed a photo-ablative model using MWCNTs and NIR light to kill kidney cancer cells. They confirmed that an effective NIR coupling effect occurs at nanotube lengths exceeding half of the wavelength of the radiating NIR, as demonstrated by the antenna theory. This radiation increased the temperature of MWCNTs through induction processes, and then the generated heat from MWCNTs was transferred to the surrounding media to continue killing cancer cells at lower radiation doses. Their work showed that nanotube lengths of 700 and 1100 nm are much more desirable in killing tumour cells compared with the length of 300 nm (**Figure 55**) [589].

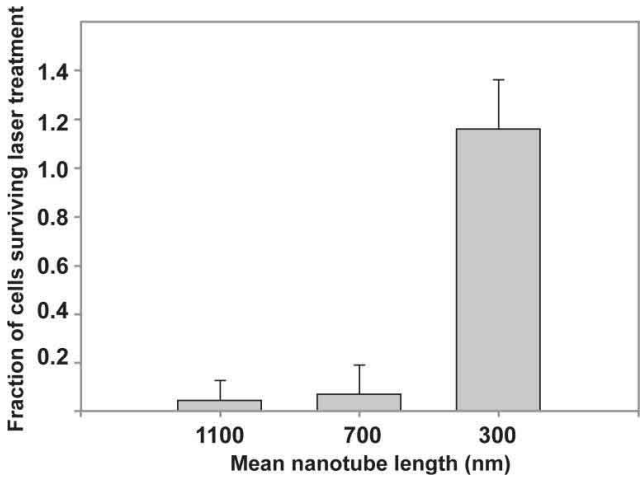

Figure 55: Comparison plot of 300, 700 and 1100 nm nanotube lengths versus cell survival [589]**.**

Zhou *et al.* utilized SWCNTs with a uniform size (~0.81 nm) and a narrow absorption peak at 980 nm for selective PTT to kill cancer cells. Their SWCNTs were conjugated to FA, which can specifically bind to the tumour surface. The FA-SWCNT-targeted tumour cells were irradiated by a 980 nm laser. According to *in vitro* and *in vivo* experiments, FA-SWCNTs effectively improved the photothermal destruction of tumour cells while noticeably minimizing the photothermal destruction of nontargeted normal cells. The combination of laser and SWCNTs showed remarkable efficacy for suppressing breast cancer growth and complete tumour regression in some cases [590]. Moon *et al.* studied the *in vivo* obliteration of solid malignant tumours by combined treatment with SWCNTs and NIR irradiation (**Figure 56**) [506]. The tumours were completely destroyed in mice in the photothermal treatment group, and harmful side effects or tumour recurrence was not observed over 6 months. However, the tumours in other control groups treated only with SWCNTs or NIR irradiation continued to grow until the mice eventually died. In addition, most injected SWCNTs were excreted from the bodies of mice within 2 months via the biliary or urinary pathways.

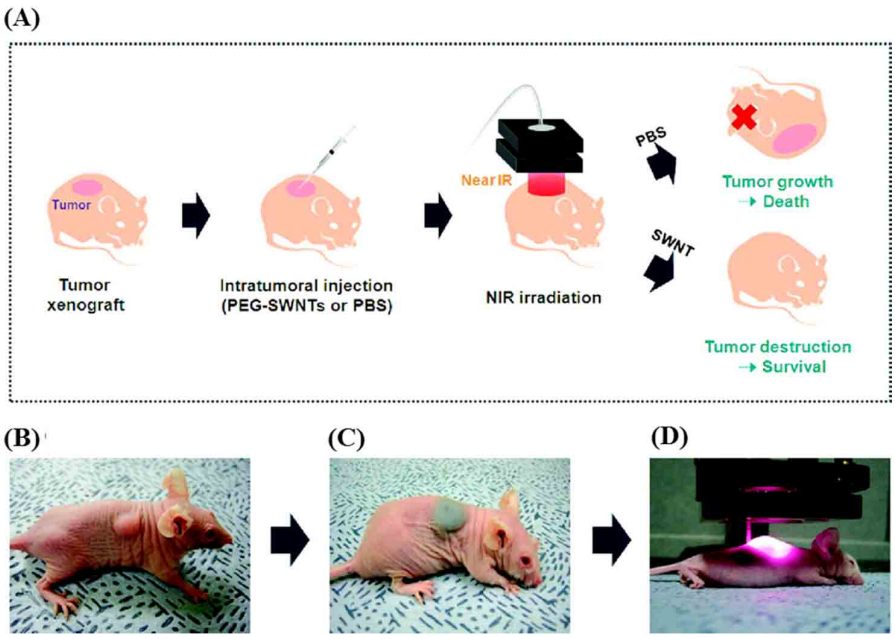

Figure 56: PTT for *in vivo* tumour ablation using PEG-SWNTs: (A) schematic view of the procedure and results of PEG-SWNTs mediated photothermal treatment of tumours in mice; (B) photograph of a mouse bearing KB tumour cells (~70 mm^3); (C) photograph of a mouse after intratumoural injection of PEG-SWNTs solution (~120 mg/L, 100 µL); (D) photograph of NIR irradiation (808 nm, 76 W/cm^3) for 3 min to tumour region [506].

PDT is a noninvasive cancer therapy with minimal side effects. To utilize PDT, a light source, photosensitizer, and molecular oxygen are required (**Figure 54**). After the uptake of a photosensitizer into cancerous cells, the photosensitizer is activated by light at a specific wavelength and the excited photosensitizer transfers energy to oxygen molecules. Energy received by oxygen in a ground state is changed to excited singlet oxygen, which is cytotoxic. This cytotoxic oxygen irreversibly damages cancerous cells [592]. Thus, CNTs show great potential as carriers of photosensitizers. Erbas *et al.* proposed a pyrenyl-functionalized distyryl-Bodipy PDT sensitizer, which is attached to SWCNTs via non-covalent π–π stacking. This sensitizer generated singlet oxygen when excited at 660 nm with a red light emitting diode array and showed slightly lower activity than the free compound. This work revealed the potential of SWCNTs as alternative carriers with a visibility of PDT sensitizers [593]. In another study, Huang *et al.* studied polyamidoamine dendrimer-modified MWCNTs as carriers of the photosensitizer 5-aminolevulinic acid (5-ALA) for tumour treatment. The incubation of human gastric cancer MGC-803 cells with the nanocomposites resulted in significant accumulation of protoporphyrin IX in the tumour cells and substantially increased their destruction after PDT treatment at 632 nm. Their

results suggested that these nanocarriers have remarkable photodynamic antitumour effects [594]. Although PDT-based cancer therapy is currently in an early stage of development, PDT has shown potential for selective and controllable treatments.

3.3. Carbon Nanoparticles or Carbon dots

Carbon nanoparticles (CNPs) or carbon dots (C-dots) are a new class of carbon nanomaterials have been acknowledged as quasispherical particles with sizes below 10 nm [27,595]. The accidental discovery of C-dots during the separation and purification of SWCNTs by Xu *et al.* in 2004 triggered subsequent studies to exploit the fluorescence properties of C-dots and create a new class of viable fluorescent nanomaterials [27]. Fluorescent CNPs received their name carbon quantum dots (CQDs), or carbon dots (C-dots), or carbon nanodots (CNDs) in 2006 from Sun *et al.* who proposed a synthetic route to produce C-dots with much enhanced fluorescence emissions via surface passivation [493]. C-dots contain amorphous to nanocrystalline cores with predominantly graphitic or turbostratic carbon (sp^2 carbon) or graphene and graphene oxide sheets fused by diamond-like sp^3 hybridized carbon insertions (**Figure 57**) [596].

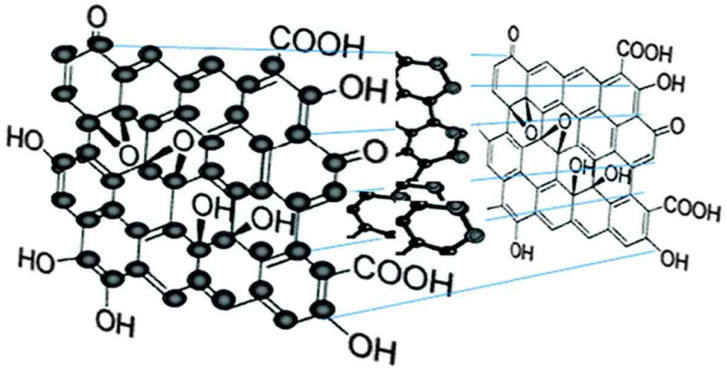

Figure 57: Chemical structure of C-dots [596]**.**

As shown in **Figure 57** there are many carboxyl moieties on the C-dots surface, which impart excellent water solubility and suitable chemically reactive groups for further functionalization and surface passivation with various organic, polymeric, inorganic or biological materials to C-dots. Upon surface passivation, the fluorescence properties of C-dots are enhanced. Surface functionalization also modifies their physical properties, like their solubility in aqueous and non-aqueous solvents [30,596]. C, O and H are the main components and elements of C-dots. Meanwhile, a number of heteroatom-doped C-dots can also be created. Resulting from their diverse composition and alterable structure,

advantageous characteristics of C-dots have been found, such as tunable fluorescence with high quantum yield, high water solubility, excellent chemical stability, non-toxicity, good biocompatibility and ease of modification. Particularly, C-dots have wide applications including bioimaging [30,597–599], drug delivery [491,600–602], photodynamic therapy [603–605], sensors [36,606–608], optoelectronics [609] and photocatalysis [610]. Moreover, researchers recently found that C-dots exhibit strong luminescence upon two-photon excitation in the near-infrared (NIR) region, which further expands their applications in bioimaging [32,611]. In fact, the colorful photoluminescence, high photostability, and low toxicity of C-dots enable them strong competitors and potential alternatives to those heavy metal-based semiconductor quantum dots (QDs) currently in use [612].

In recent years, much progress has been made in terms of the synthesis, properties and applications of C-dots [612,613]. Many methods have been proposed to prepare C-dots during the last decade, which can be roughly classified into "Top-down" and "Bottom-up" approaches, and they can be modified during preparation or post-treatment. Top-down methods consist of arc discharge [27], laser ablation [30–32,34,493,614], and electrochemical oxidation [615–618], where the C-dots are formed or "broken off" from a larger carbon structure. Bottom-up approaches consist, for example, of combustion/thermal/hydrothermal [619–624], microwave [625], or ultrasonication methods [611,626] during which the C-dots are formed from molecular precursors. Typically, their surfaces are oxidized by nitric acid (HNO_3) and further purified by using centrifugation, dialysis, electrophoresis, or another separation technique. Three problems facing C-dots preparation need to be noticed: (a) carbonaceous aggregation during carbonization, which can be avoided by using electrochemical synthesis, confined pyrolysis or solution chemistry methods, (b) size control and uniformity, which is important for uniform properties and mechanistic study, and can be optimized via post-treatment, such as gel electrophoresis, centrifugation, and dialysis and (c) surface properties that are critical for solubility and selected applications, which can be tuned during preparation or post-treatment.

3.3.1. Synthetic Methods of C-dots

3.3.1.1. Top-Down Approaches

3.3.1.1.1. Arc-Discharge Methods

In 2004, Xu *et al.* isolated an unknown fluorescent carbon nanomaterial while purifying SWCNTs derived from arc-discharge soot (**Figure 58**). To improve the

hydrophilicity of the material, they oxidized the arc soot with 3.3 M HNO_3 to introduce carboxyl functional groups, and then extracted the sediment with a NaOH solution (pH 8.4) to produce a stable black suspension. The suspension was separated by gel electrophoresis into SWCNTs, short tubular carbons, and a fast moving band of highly fluorescent material, which was composed of C-dots [27].

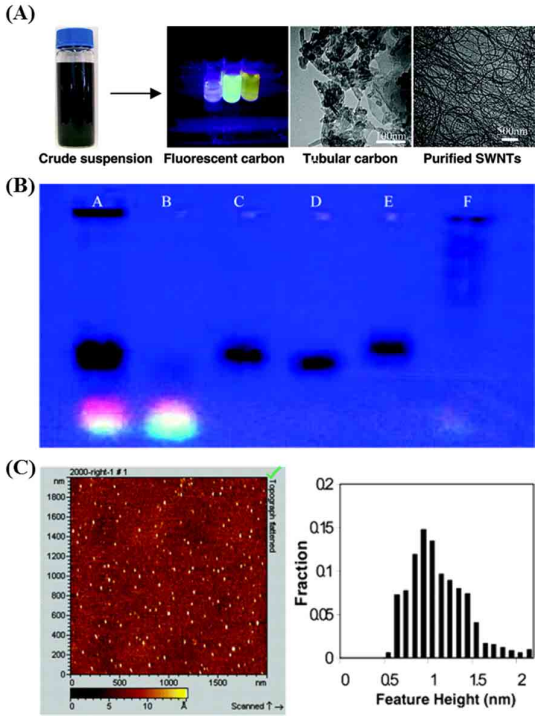

Figure 58: (A) Picture of different fractions of fluorescent carbon under 365 nm, TEM images of short tubule carbon, and purified SWNTs, (B) The PAGE results for the arc-discharge soot, (C) AFM image (left) and feature height distribution (right) of the C-dots from the arc-discharge soot [27]**.**

3.3.1.1.2. Laser-Ablation Methods

Sun *et al.* produced C-dots via laser ablation of a carbon target in the presence of water vapor with argon as a carrier gas at 900 °C and 75 kPa [493]. Upon post surface passivation of PEG_{1500N} (**Figure 59A**), the final C-dots can emit strong and tunable photoluminescence in both solution and solid states, depending on the excitation wavelength progressively changing from 400 nm to 600 nm. Hu *et al.* reported the synthesis and the passivation of fluorescent C-dots by laser irradiation of a suspension of carbon materials in organic solvent (**Figure 59B**). By selecting organic solvents, the surface states of C-dots could be modified to achieve tunable light emission. Based on control experiments, the origin of the

luminescence was attributed to the surface states related to the ligands on the surface of C-dots. In this approach, a pulsed Nd:YAG laser was used to irradiate graphite or carbon black dispersed in diamine hydrate, diethanolamine, or PEG_{200N} for 2 h while under ultrasonication to aid in particle dispersal. After laser irradiation, centrifugation was used to precipitate residual carbon powder fragments while C-dots remained suspended in the supernatant. These C-dots averaged 3 nm in size, with lattice spacings varying from 0.20-0.23 nm, similar to that of diamond [614].

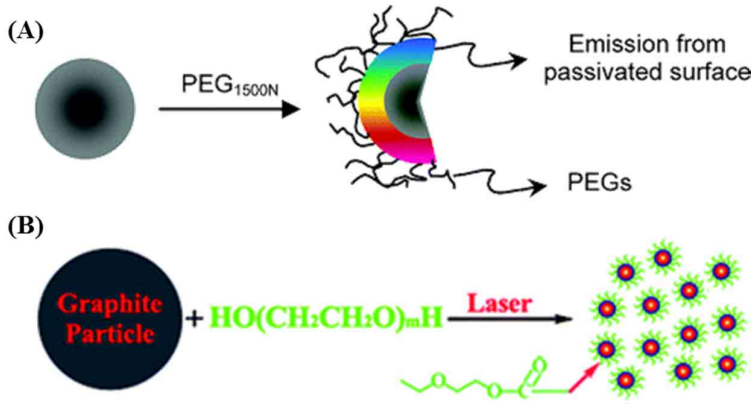

Figure 59: (A) Schematic illustration of the fluorescence change of C-dots after surface modification with PEG_{1500N} [493]**, (B) One-step synthesis of C-dots in PEG_{200N} solvent** [614]**.**

3.3.1.1.3. Electrochemical Synthesis

Electrochemical synthesis of C-dots was first demonstrated by Zhou *et al.* when they grew MWCNTs from scrolled graphene layers on carbon paper by chemical vapour deposition (CVD). These nanotubes were designed to serve as the working electrode in an electrochemical cell consisting of a platinum (Pt) wire counter electrode and a $Ag/AgClO_4$ reference electrode with degassed acetonitrile solution containing 0.1M tetrabutylammonium perchlorate ($TBA^+ClO_4^-$) as the electrolyte. Cycling the applied potential between −2.0 and +2.0 V at a scan rate of 0.5 V s^{-1} resulted in the solution changing from colorless to yellow to dark brown, which indicated the formation of C-dots with good solubility in various solvents [618].

Li *et al.* reported an alkali-assisted electrochemical method to prepare 1-4 nm C-dots with controlled sizes. It can be imagined that judicious cutting of a graphite honeycomb layer into ultrasmall particles can lead to tiny fragments of graphite, yielding C-dots, which may offer a straightforward and facile strategy to prepare high-quality C-dots. Using graphite rods as both anode and cathode, and NaOH/EtOH as electrolyte, they synthesized C-dots with a

current intensity of 10-200 mA cm^{-2}. As a reference, a series of control experiments using acids (e.g. H_2SO_4/EtOH) as electrolyte yielded no formation of C-dots. This result indicates that an alkaline environment is the key factor, and OH^- groups are essential for the formation of C-dots by this electrochemical oxidation process [627]. Another facile electrochemical approach was also reported by Ming *et al.* for the large-scale synthesis of high-quality C-dots with high purity, using only pure water as an electrolyte without any other chemical additives (**Figure 60**). The obtained C-dots feature a highly crystalline nature, excellent aqueous solubility, and remarkable down- and up-converted photoluminescence (PL) properties, and require no further purification. Moreover, they further demonstrated that the C-dots possess high photocatalytic activity under visible irradiation, and potential for high-efficiency complex catalyst design [628].

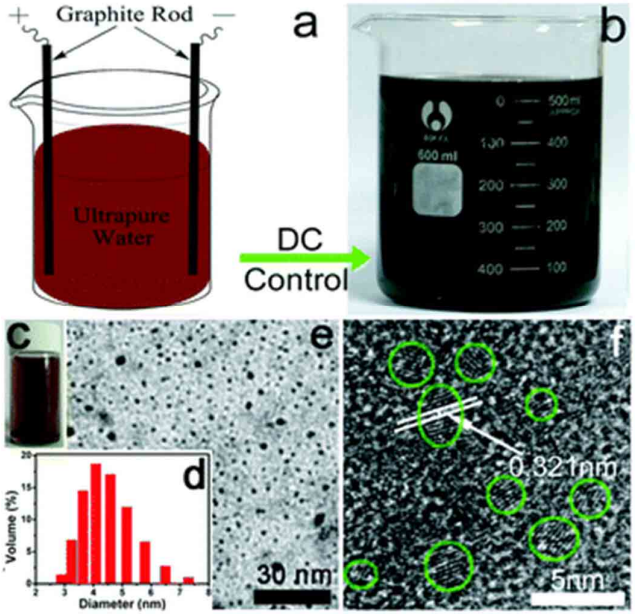

Figure 60: (A) Reaction equipment for the preparation of C-dots; digital image of C-dots solution (B) before treatment, (C) after treatment; (D) DLS histogram of C-dots; (E) TEM, (F) HRTEM image of C-dots [628]**.**

3.3.1.2. Bottom-up Approaches

3.3.1.2.1. Combustion/acidic oxidation Methods

Liu *et al.* first reported that fluorescent C-dots can be obtained from the combustion soot of candles after refluxing with oxidative acid [629]. A glass plate on the top of a burning candle was used to collect the hydrophobic soot, which could be turned hydrophilic by means of HNO_3 treatment. The suspension was allowed to perform denatured polyacrylamide gel

electrophoresis, with the aim of obtaining pure C-dots. Unexpectedly, the mixture was separated into three bands and the first one consisted of nine fast-moving fluorescent smaller bands, showing different emission spectra although they were excited at the same wavelength (**Figure 61**). This study indicated that the fluorescent emission of C-dots is size-dependent and/or charge-dependent.

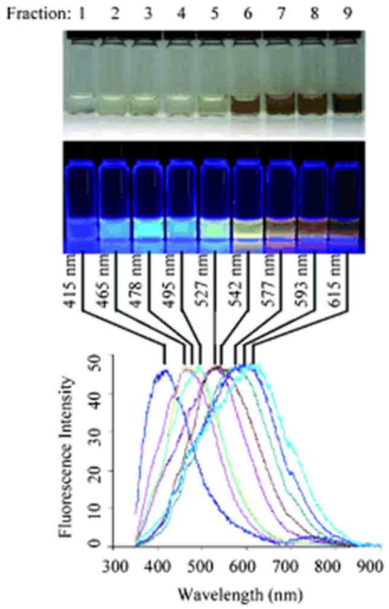

Figure 61: Optical characterization of PAGE separated C-dots produced from candle soot. Optical images illuminated under white (top) and UV light (312 nm; center). Bottom: Fluorescence emission spectra (λ_{ex} at 315 nm) of the corresponding C-dots solutions. The maximum emission wavelengths are indicated above the spectra [629]**.**

This candle-burning approach was also followed by Ray *et al.* The candle soot was similarly collected and refluxed with 5 m HNO_3 for 12 h. It was found that refluxing for under 12 h gave a lower C-dots yield, while refluxing for longer periods resulted in no appreciable gain in yield. The particles suspended in solution were then precipitated by adding acetone and centrifuging at 14 000 rpm for 10 minutes. Size separation was then performed in a solvent mixture (water/ethanol/chloroform) via high-speed centrifuge separation. Supernatant was collected at spinning speeds of 4000, 5000, 6000, and 8000-16 000 rpm, in each case starting with the supernatant collected from the previous step. The supernatant obtained with centrifugation at 8000 rpm, for which precipitate was no longer observed, contained C-dots with particle sizes in the 2-6 nm range. Precipitates at lower centrifugation speeds contained large carbon nanoparticles of 201-350 nm in size. The 2-6 nm C-dots were found to be graphitic in nature, according to lattice spacings in HRTEM images, and exhibited high PL quantum yields in comparison with the larger particles found. XPS compositional analysis,

while insensitive to hydrogen, revealed the presence of C, O, and N at 59, 37, and 4 atom %, respectively [622].

In a further study, Tian *et al.* purified C-dots from the combustion soot of natural gas. By inverting a glass beaker above the flame of a natural gas burner, they were able to collect around 100 mg of soot, which was then refluxed in 5 M HNO_3 for 12 h, followed by centrifugation and dialysis to afford purified C-dots. The as-purified C-dots exhibited PL with a λ_{ex} maximum of 310 nm and an emission wavelength (λ_{em}) maximum of 420 nm. Transmission electron microscopy (TEM) and high-resolution TEM (HRTEM) results showed that the C-dots exhibited an average diameter of (4.8 ± 0.6) nm and the crystalline lattices were consistent with graphitic carbons (**Figure 62**) [623].

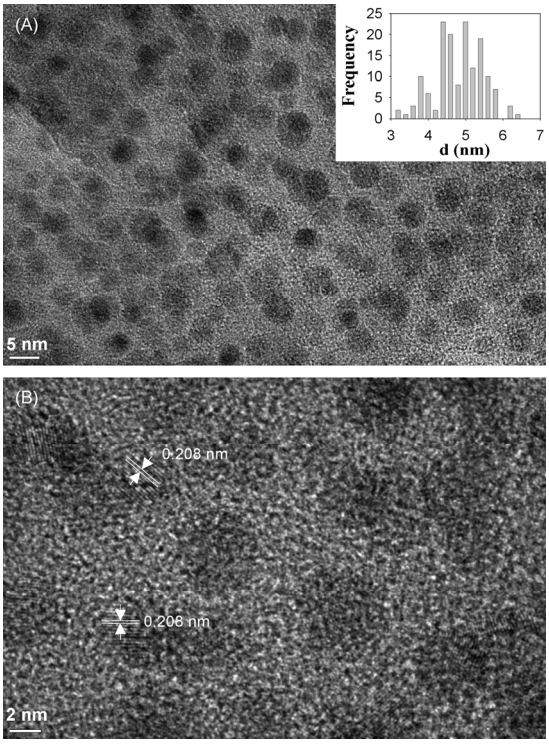

Figure 62: Representative TEM micrographs of C-dots at (A) low and (B) high resolution [623]**.**

^{13}C NMR and FTIR measurements also revealed the presence of sp^2 carbon and carboxylic/carbonyl moieties, thus leading the authors to conclude that the C-dots most likely consist of a nanocrystalline core featuring graphitic sp^2 carbon atoms and a surface functionalized with carboxylic/carbonyl moieties. Interestingly, in contrast to C-dots made from candle combustion, no N (as determined from XPS data) was found to be present in these C-dots [623].

Acidic oxidation is one of the popular methods of acquiring C-dots. Typically, in this process strong acid treatment of carbon precursors is conducted at high temperature. Leblanc's group reported an acidic oxidation route for converting carbon powder into C-dots, in which a mixture of sulfuric acid, nitric acid and carbon powder was refluxed at 110 °C for 15 h in a sand bath [630]. After a series of processes comprising cooling, crystallization, evaporation, concentration, extraction, dialysis and another concentration and evaporation, C-dots were successfully obtained as a black powder. The as-prepared C-dots were found to be able to inhibit human insulin fibrillation. Qian *et al.* reported a mild and facile synthesis of C-dots from the mixed acid treatment of activated carbon [631]. In their synthesis, a low reaction temperature of 80 °C was used and the product can be obtained just after dialysis.

3.3.1.2.2. Thermal/Hydrothermal/Solvothermal Methods

Thermal/hydrothermal carbonization is one of the most reported routes for the synthesis of C-dots, due to its low cost, easy feasibility, environmental friendliness and various carbon sources. Generally, in this process a solution of organic precursors, such as glucose [632,633], sucrose [634], polyols [635], polymers [636,637], amino acids [638,639], proteins [640,641], natural products [642–645], and some wastes [646–648] is sealed in an autoclave at high temperature. Sahu *et al.* prepared highly photoluminescent C-dots with a quantum yield (QY) of 26% in one step by hydrothermal treatment of orange juice followed by centrifugation [649]. These C-dots with sizes of 1.5-4.5 nm were applied in bioimaging due to their high photostability and low toxicity. Yang *et al.* reported a one-step synthesis of amino-functionalized fluorescent C-dots by hydrothermal carbonization of chitosan at 180 °C for 12 hours [597]. These C-dots are demonstrated as excellent probes as bioimaging agents.

Pan *et al.* reported a hydrothermal route for cutting graphene sheets into blue luminescent C-dots [650]. The obtained C-dots exhibited strong fluorescence with a quantum yield (QY) of 6.9%. Fluorescent C-dots with diameter of about 2.0 nm were also prepared directly via a simple hydrothermal method by using L-ascorbic acid as a carbon source. The solvent used in the dissolution of the acid was investigated and proved to have strong link with the PL generated by the C-dots. Among the solvents investigated, ethanol proved to be more suitable. It had not only improved on the surface states of the nanoparticles, but also provided a reaction medium for the uniform growth of the nanoparticles due to its ability to cap and inhibit the aggregation of the nanoparticles. In contrast to the previous methods, no strong

acid or further surface modification was needed for the preparation. The as-prepared C-dots with uniform shapes and sizes in the range 2.0-2.5 nm were found to be water soluble and exhibited λ_{ex} dependent emission. Experiments revealed that the emission of these C-dots exhibited good stability in reaction media of high ionic concentrations, and could as well be tuned by adjusting the pH [651]. Water-soluble and well-crystallized C-dots with a lateral size about 3.0 nm were also fabricated by a hydrothermal cutting method [652]. The atomic force microscopy (AFM) observation of the C-dots deposited on a mica substrate shows a narrow height distribution from 1.5 to 1.9 nm, suggesting that the C-dots typically consist of 2-3 graphene layers. In another study, Zhang *et al.* reported a high-yield synthesis of hydrophilic C-dots by controlled carbonization of sucrose. Green luminescent C-dots and non-luminous C-dots were effectively separated by dialysis. After surface functionalization with PEG_{2000N}, the non-luminous C-dots emitted blue fluorescence (**Figure 63**) [653].

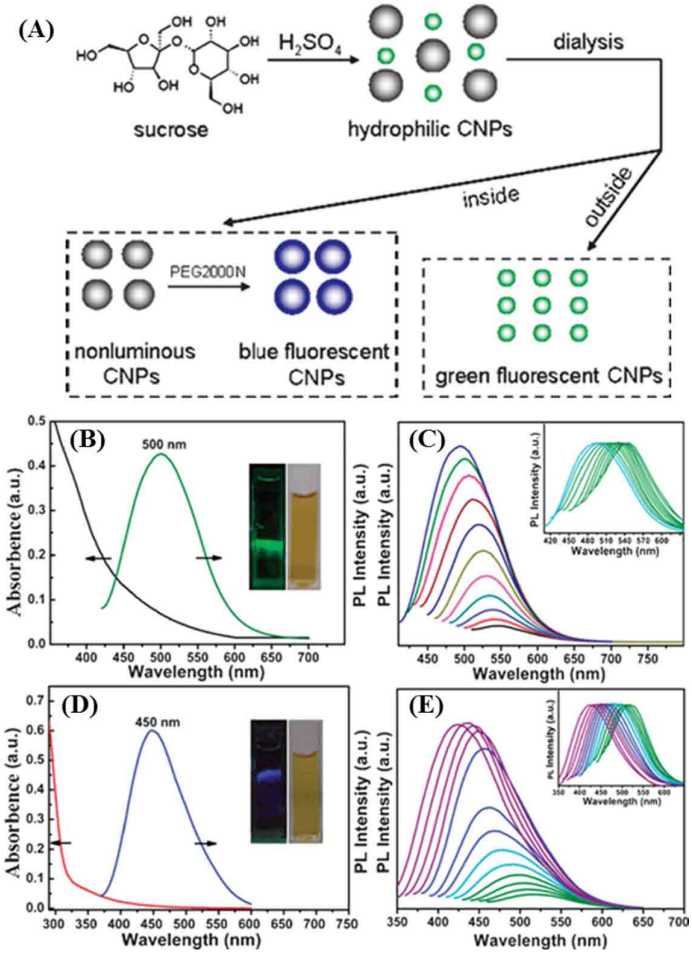

Figure 63: (A) The synthesis procedure of green and blue luminescent C-dots. Absorption and emission spectra of (B) green and (D) blue luminescent C-dots dispersed in distilled water. Inset: photographs of each kind of luminescent C-dots solution taken under a UV light in a

fluorescence spectrophotometer (left) and under visible light (right). (C) Emission spectra of green luminescent C-dots at excitation wavelengths progressively increasing from 400 nm in 10 nm increments. (E) Emission spectra of blue luminescent C-dots at excitation wavelengths progressively increasing from 330 nm in 10 nm increments. Inset: normalized emission spectra [653]**.**

Another one-step synthetic route in which the C-dots were synthesized from the hydrothermal oxidation of carbohydrates (glucose/sucrose/starch) with acid/alkali additives, was reported (**Figure 64**). The carbohydrates provided the carbon source and the acid/alkali used as additives. The HCl additive enhanced emission distribution of C-dots at longer wavelengths while the NaOH additive enhanced emission distribution of C-dots at shorter wavelengths. The authors presumed that these additives probably induce different defects on the surface of the C-dots which act as surface energy traps that result into the different PL behaviors. The as-prepared C-dots exhibited NIR emission excited by NIR excitation as well as up-conversion PL properties. The elemental analysis showed that the obtained C-dots contained predominantly elemental carbon and oxygen. It was also revealed that the functional carboxyl and hydroxyl groups on the surface of these C-dots rendered them good water dispersibility [654].

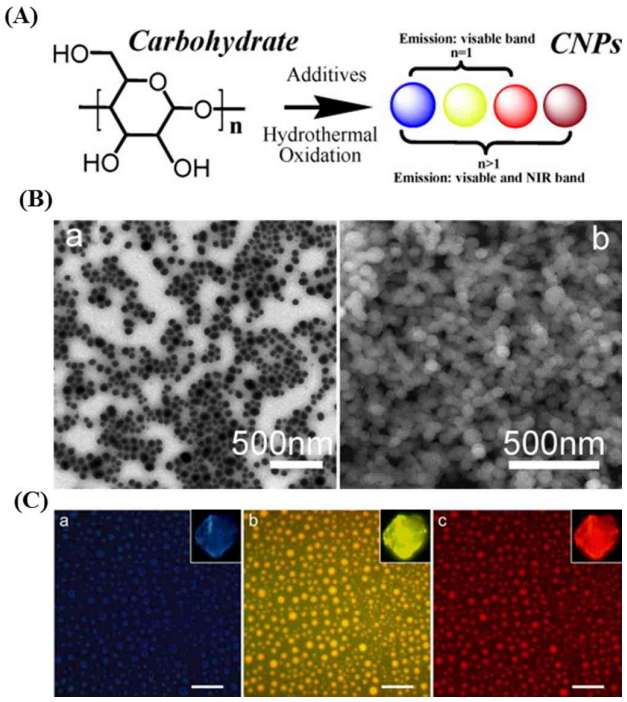

Figure 64: (A) Fabrication of C-dots capable of visible and NIR emission by acid/alkali-assisted hydrothermal oxidation, (B) Typical (a) TEM and (b) SEM images of C-dots samples prepared from carbohydrates, (C) Typical PL images (all scale bars are 20 µm) of C-dots samples prepared from starch with excitation wavelengths at (a) 365 nm, (b) 455 nm, (c) 545 nm and collection wavelengths at (a) >470 nm, (b) >515 nm, (c) 600 ± 40 nm, respectively [654]**.**

Recently, Guo *et al.* developed a simple and low-cost approach to synthesize highly fluorescent C-dots, by establishing a one-step hydrothermal treatment of sodium citrate and ammonium bicarbonate (NH_4HCO_3) in water. Experimental investigation confirmed that NH_4HCO_3 decomposed to CO_2 and NH_3 that conferred high pressure into the reaction medium, and thus facilitated the decomposition of sodium citrate into small nanoparticles that produced the C-dots. The as-prepared C-dots had an average size of about 1.59 nm, and exhibited a high PL quantum yield (68%) as well as good photostability. The XPS analysis confirmed the presence of carboxyl and hydroxyl groups on the surface of the C-dots. The obtained C-dots were found to be very stable in high concentration of ionic solution, and with good selectivity and sensitivity could be used to detect mercury ions in aqueous solution (**Figure 65**) [655].

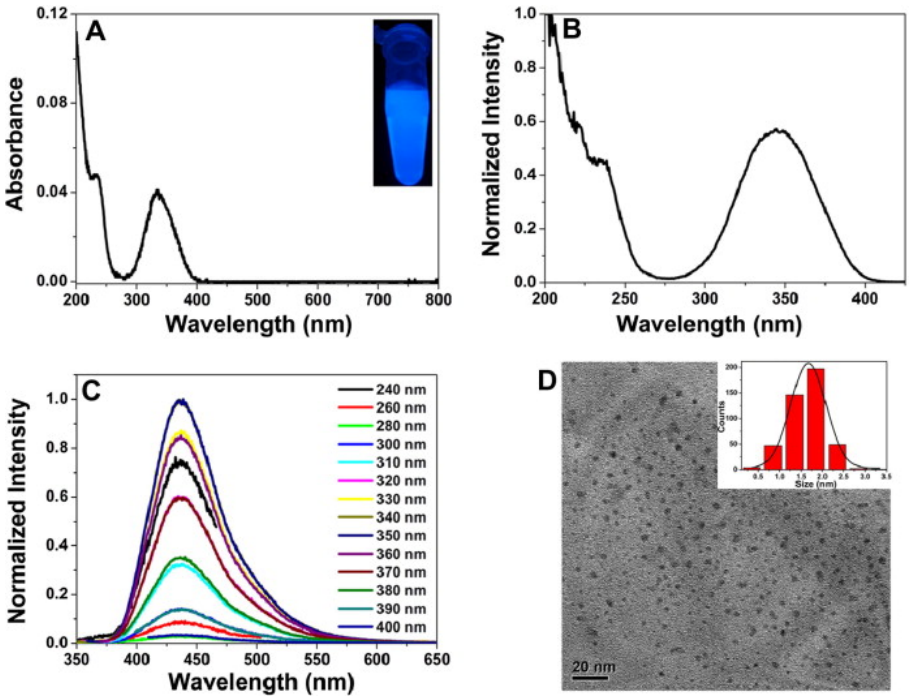

Figure 65: (A) UV–vis absorption spectrum of C-dots, the inset is the picture of C-dots illuminated by a UV lamp with 365 nm light. (B) Excitation spectrum of the C-dots. (C) Emission spectra of C-dots at different excitation wavelengths. (D) TEM image of the C-dots, the inset picture is the histogram of C-dots size distributions [655]**.**

Zhou *et al.* reported large-scale C-dots prepared by cheap and easily got watermelon peel as precursor. The fresh peel was carbonized at 220 °C for 2 h under air atmosphere, the obtained product was filtrated, centrifuged and dialyzed without any complex or post-treatment, finally, highly luminescent C-dots were obtained. The C-dots exhibited good water-

solubility, small particle size, strong blue luminescence and good stability in a wide range of pH values and at high salt concentration (**Figure 66**) [656].

Figure 66: Schematic illustration of the synthesis of water-soluble fluorescent C-dots from watermelon peel [656]**.**

In order to reinforce their PL property and broaden their application, further passivation of the C-dots with tailored organic coating materials can render C-dots brighter, better biocompatible and long-term stability. Therefore, passivation of C-dots provides an effective bridge to connect the C-dots with fascinating biological applications, such as *in vivo* bioimaging and bioprobe, and modification of C-dot has become increasingly important [657]. Apart from surface-passivation, doping with heteroatoms can significantly increase the quantum yield of C-dots. Zhu *et al.* fabricated nitrogen-doped C-dots by a hydrothermal method (**Figure 67**). Citric acid and ethylenediamine were dissolved in deionized-water, and heated at 200 °C for 5 h in a Teflon-lined autoclave. The reaction was conducted by first condensing citric acid and ethylenediamine, whereupon they formed polymer-like C-dots, which were then carbonized to form the C-dots. The quantum yield of N-doped C-dots reached up to 80.6 % at the excitation wavelength of 360 nm, nearly equal to most semiconductor QDs and fluorescent dyes [658].

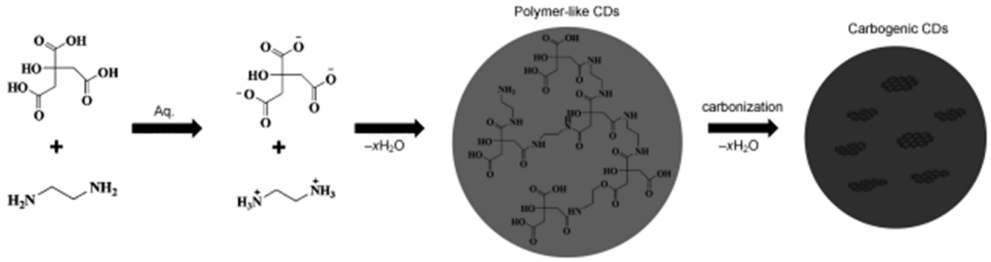

Figure 67: A synthetic route using citric acid and ethylenediamine: from ionization to condensation, polymerization, and carbonization [658]**.**

Another approach towards N-doped C-dots was recently reported by Jiang *et al.*, who synthesized color-tunable C-dots by varying the precursor materials. Instead of having two

precursor molecules, the synthesis contained only phenyldiamines, which were solvothermally heated in ethanol at 180 °C for 12 h (**Figure 68**). The variation of the functional group configuration of this precursor from ortho, to meta and para changed the emission color of the resulting C-dots from green, to blue and red [659].

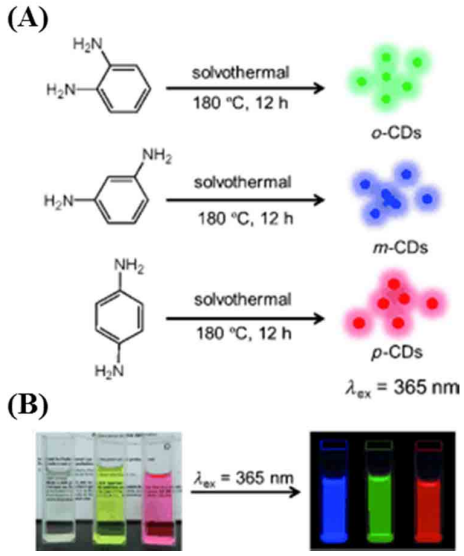

Figure 68: (A) Preparation of the red, green and blue (RGB) PL C-dots (CDs) from three different phenylenediamine isomers (i.e., oPD, mPD and pPD); (B) Photographs of m-CDs, o-CDs, and p-CDs dispersed in ethanol in daylight (left), and under λ=365 nm UV irradiation (right) [659].

More Recently, Lu *et al.* synthesized N-C-dots with an average size of 2.6 nm using a one-pot hydrothermal treatment with citric acid as carbon source in the presence of polyethylenimine (PEI) as a simultaneous nitrogen dopant and surface passivation agent. N-CDs synthesized emitted a strong blue luminescence with a QY of 51%. The N- C-dots exhibited an excellent photostability and low cytotoxicity makes the N- C-dots promising optical nanoprobes for real-time live-cell imaging. Moreover, their small size and the surface positive charge rendered by the PEI endow them with the ability to cross the BBB, making them potentially useful in traceable drug delivery in brain disorders [624].

The second prominent heteroatom, which is included into the structure of C-dots is sulfur. Aside from limited examples, where only sulfur was reported to be doped into the C-dots [660,661], most studies focus on its co-doping with nitrogen, in order to improve the optical properties of the C-dots, in particular their PL QY [662]. Dong *et al.* synthesized nitrogen-sulfur co-doped C-dots via a one-pot hydrothermal treatment of citric acid and L-cysteine at 200 °C (PL QY of 73%) [662].

Solvothermal carbonization followed by extraction with an organic solvent is a popular approach to prepare C-dots [598]. Typically, carbon-yielding compounds were subjected to heat treatment in high boiling point organic solvents, followed by extraction and concentration. Bhunia *et al.* synthesized two kinds of the C-dots, hydrophobic and hydrophilic with diameters less than 10 nm from the carbonization of carbohydrates (**Figure 69**) [598]. The hydrophobic ones were produced by mixing different amounts of carbohydrate with octadecylamine and octadecene before being heated up to 70-300 °C for 10-30 minutes. The hydrophilic ones can be synthesized by heating an aqueous solution of carbohydrate within wide pH ranges. The hydrophilic C-dots with yellow and red emissions can also be synthesized by mixing an aqueous solution of carbohydrate with concentrated phosphoric acid followed with heating at 80-90 °C for 60 min.

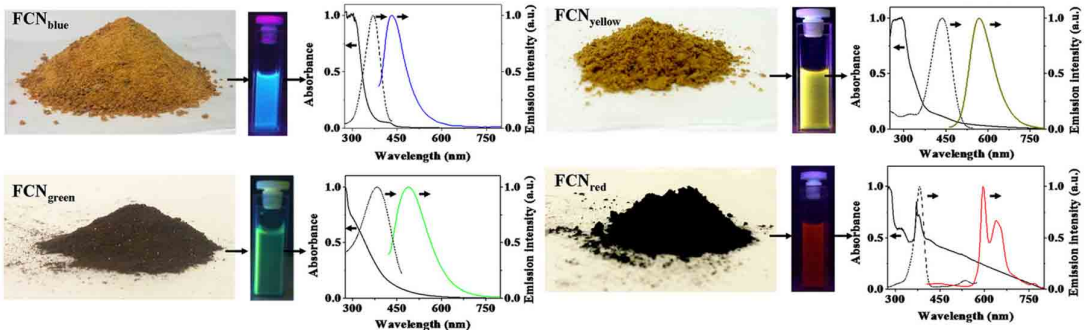

Figure 69: Digital images of C-dots solutions under appropriate excitations and their absorption (solid black lines), excitation (dashed black lines) and emission (color lines) spectra. Emission spectra were measured by excitation at 370 nm, 400 nm, 425 nm, and 385 nm for blue C-dots, green C-dots, yellow C-dots, and red C-dots, respectively. All excitation spectra were recorded in respective emission maxima [598]**.**

3.3.1.2.3. Microwave Methods

Microwave technology has become a very important process in synthetic chemistry. Compared with other approaches, it is more conveniently and rapidly to heat the carbon precursors, simplifies the synthesis process, so C-dots are readily obtained within a few minutes and with improved yield. Multicolor luminescence has been achieved by microwave synthesis of C-dots using dextrin as a starting material. A solution containing dextrin and water was prepared, to which sulfuric acid (H_2SO_4) was added while stirring vigorously. This solution was then exposed to microwaves for 2.5 min at 800 W. A light brown supernatant was obtained along with a black precipitate. The solution containing the C-dots was centrifuged to obtain a clear solution. The as-prepared C-dots were characterized using

different techniques and the luminescence spectra showed that the particles attained multicolor luminescence without any requirement for surface-passivating agents. The quantum yield was between 5 and 9 % [663]. This multicolor luminescence might be very helpful in the field of bioimaging. Wang *et al.* presented a facile one-step microwave assisted approach to prepare water-soluble phosphorus-containing with strong green fluorescence C-dots. In this synthesis process, 2 mL of 70 % phytic acid and 1 mL ethylenediamine were mixed in 25 mL ultrapure water, and then the turbid mixture was heated for about 8 min in a domestic 700 W microwave oven. After further purification of the crude product, phosphorus-containing C-dots were obtained, and phosphorus groups were covalently bonded to the graphite-like structure existed in the C-dots. Notably, the phosphorus-containing C-dots showed two-peak emissions when excited at low wavelengths, while at high excitation wavelengths (360-460 nm), the nanoparticles showed single-peak emission at 525 nm (green fluorescence). The highest quantum yield of the resulting phosphorus-containing C-dots was about 21.65 % (**Figure 70**) [664].

Figure 70: (A) Schematic diagram for synthesizing green C-dots. (B) Emission under daylight and 365 nm ultraviolet excitation [664]**.**

Qu and co-workers reported a one-step microwave heat treatment of carbohydrates to synthesize multicolored photoluminescence (PL) C-dots without any surface passivation reagents. Glycerol was mixed with phosphate solution and subjected to microwave heating for 14 min to generate the C-dots. The PL showed that the emission spectra were broad and ranged from blue to yellow depending on the excitation wavelength. The as-synthesized C-dots possessed carboxyl and hydroxyl moieties that enhanced their hydrophilicity and stability in aqueous systems, shown by their ability to maintain PL intensity even with increased in ionic strength. The obtained C-dots were biocompatible and were found to be promising in biolabelling and bioimaging. This work has also demonstrated that inorganic ions were able to effectively promote the carbonization of carbohydrates [665].

Jaiswal *et al.* developed a simple one step microwave mediated synthesis of C-dots using PEG, a biocompatible polymer, as a sole source of carbon and a passivating agent [666]. An

aqueous solution of the polymer precursor, (PEG-solution), was irradiated for 10 min to generate the amorphous C-dots with an average size estimated to be 3.6 nm or 5.4 nm. The obtained C-dots were compliant to size separation by gel electrophoresis, and possessed high photostability, which was confirmed by their ability to maintain luminescence under extended irradiation. Zhu *et al.* synthesize C-dots by combining PEG_{200} and a saccharide (for example, glucose, and fructose) in water to form a transparent solution, followed by heating in a 500 W microwave oven for 2-10 min (**Figure 71**). The solution changed from colorless, tanned to dark brown over the time course of the reaction. The recovered C-dots exhibited sizes and PL properties related to the duration of the microwave heating. Longer heating times result in the C-dots enlarging slightly and emitting at longer wavelengths. For example, the average C-dot diameters were (2.75±0.45) nm and (3.65±0.6) nm for heating times of 5 and 10 minutes, respectively. When PEG was omitted, a similar color change was observed during microwave heating, but it is noteworthy that the nonpassivated particles expressed weak and irregular PL [625].

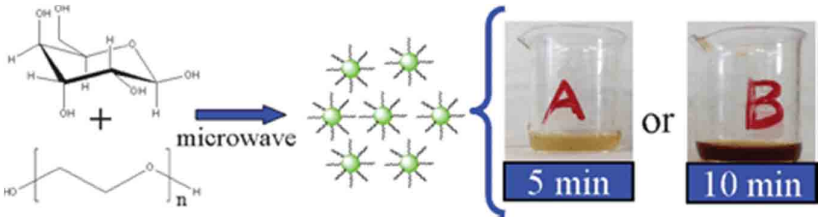

Figure 71: Microwave approach to C-dots synthesis [625]**.**

3.3.1.2.4. Ultrasonication Methods

The ultrasonication method is a process in which the ultrasonic waves produce alternating expansion and compression in a reaction solution, resulted to the growth and implosive collapse of bubbles irradiated with the waves. The mechanism causes high speed interparticle collisions, which can change the morphology, composition and reactivity of the particles. When integrated with carbonization, the energy of the ultrasonic waves generates intermediates that can be further carbonized, to generate tiny size C-dots. Li *et al.* described a simple synthesis of C-dots from glucose or active carbon by using an ultrasonic treatment method [611,626]. Such monodispersed water-soluble fluorescent C-dots could emit bright and colorful PL covering the entire visible-to-NIR spectral range (**Figure 72**). Notably, the NIR emission of C-dots could be obtained by NIR excitation. Furthermore, the C-dots had excellent up-conversion fluorescent properties [611].

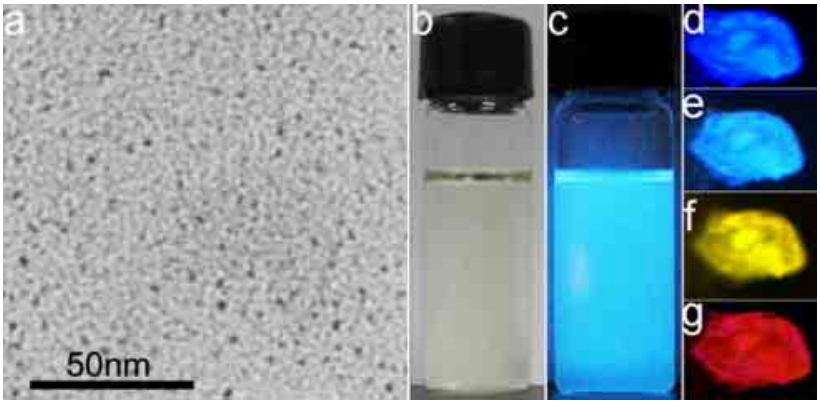

Figure 72: (a) TEM image of C-dots prepared from glucose with a diameter of less than 5 nm; (b) and (c) photographs of C-dots dispersions in water with sunlight and UV (365 nm, center) illumination, respectively; (d–g) fluorescent microscope images of C-dots under different excitation: d, e, f, and g for 360, 390, 470, and 540 nm, respectively [611]**.**

3.3.2. Chemical composition and structure of C-dots

C, H, and O are three fundamental elements of C-dots, and the ratios of the three elements are variable in different C-dots. The introduction of heteroatoms has been studied to tune the conduction/valence band position of C-dots, which confers additional functions [615,619,667]. For example, the quantum yield (QY) of C-dots could be significantly improved by incorporating the N element while C-dots with a wide band gap could be synthesized by incorporating the S element [661,662,668–670]. Furthermore, P-doped C-dots showed green fluorescence, which could be utilized as an imaging signal with low background [664,671,672]. Moreover, other heteroatoms such as Cl and B could also be doped into C-dots by changing the synthetic methods or raw materials [673,674].

Hu *et al.* reported that the selected-area electron-diffraction (SAED) experiments on C-dots with a size of about 3 nm prepared by a one-step laser ablation/passivation method revealed a ring pattern, with the ratio of the squares of the ring radius of 3:8:11:16:19. This implies a diamond-like structure, with the rings respectively corresponding to the (111), (220), (311), (400), and (331) planes of diamond [614]. This apparent structure was observed whether or not the C-dot was synthesized in PEG_{200N} as the passivating ligand or in water. The lattice spacings observed was 0.2-0.23 nm and are, in fact, quite close to the (100) facet of graphite. The lattice fringes of the diffraction planes of diamond-like and graphitic carbon lie very close to one other, thus rendering unambiguous assignment difficult without other corroborating evidence.

Additionally, Ray *et al.* found that the C-dots prepared from oxidizing candle soot had 0.208 nm lattice spacings, which suggests sp^3 diamond-like carbon or sp^2 graphitic carbon [622]. By using ^{13}C NMR studies, Tian *et al.* were able to confirm the presence of sp^2 carbon with signals in the δ=90-180 ppm range, while the absence of signals in the δ=8-80 ppm range led to the assertion of a lack of detectable sp^3 carbon. Furthermore, FTIR measurements also confirmed the presence of C=C aromatic ring stretches. Therefore, they concluded that their C-dots consisted of a nanocrystalline core of graphitic sp^2 carbon atoms functionalized with peripheral carboxylic/carbonyl moieties [623]. One-step thermal decomposition reactions of citrate salts produced C-dots with a size of 7 nm, whose XRD patterns were indicative of disordered carbon alongside the respective passivation agent [620]. The XRD pattern of C-dots made from octadecylammonium citrate shows two superimposed broad reflections: a broad one centered at 4.3 Å and a sharper peak at 4.14 Å, which are indicative of disordered carbon and densely packed alkyl groups arising from the octadecyl chains, respectively. The XRD pattern of C-dots prepared by supported method displayed a sharp, low-intensity reflection centered at d_{002} = 3.3 Å, which was very close to the graphite (002) lattice spacing [619]. However, the XRD pattern of the hydrophilic C-dots (prepared by controlled carbonization of sucrose) showed an (002) interlayer spacing of 4.2 Å, which is larger than that of bulk graphite (3.3 Å), indicating poor crystallization [653].

It can generally be concluded that the most C-dots consist of an amorphous to nanocrystalline core with predominantly sp^2 carbon, the lattice spacings of which are consistent with graphitic or turbostratic carbon. However, some C-dots showed poor crystallization (the C-dots prepared by controlled carbonization of sucrose). Unless otherwise modified, oxidized C-dots generally feature carboxylic moieties at their surface, with overall oxygen contents ranging from 5-50 weight (wt) %, depending upon the experimental conditions used [612].

3.3.3. Optical properties of C-dots

3.3.3.1. Absorbance

C-dots typically show strong optical absorption in the UV region, with a tail extending out into the visible range (**Figure 73**) [493].

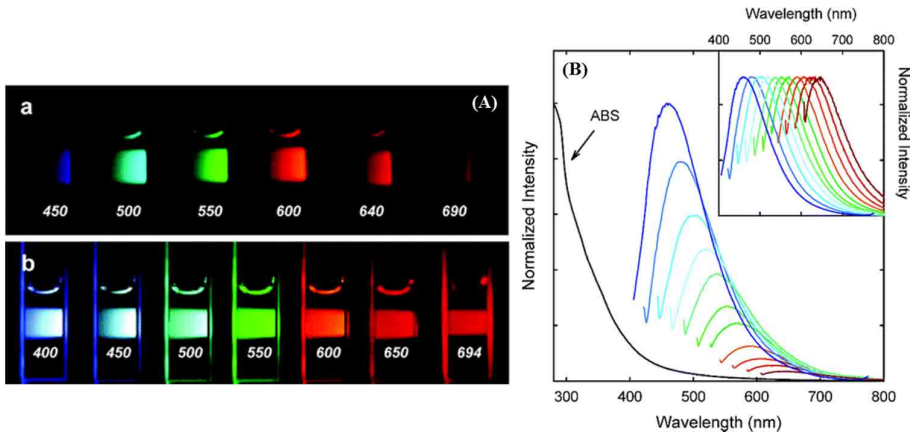

Figure 73: (A) Aqueous solutions of PEG_{1500N}-passivated C-dots (a) excited at 400 nm and (b) excited at the indicated wavelengths; (B) absorption and emission spectra of PPEI-EI passivated C-dots in water with increasing λ_{ex} from 400 nm on the left with 20 nm increments. Inset: emission intensities normalized to quantum yields [493]**.**

Most of the C-dots, such as those prepared by laser-passivation [614], electrochemical oxidation [618], or microwave/ultrasonic method [625,626], have an absorption band around 260-320 nm. The several shoulder peaks in UV absorption spectra are generally attributed to the transitions from π-π* of benzene rings and the C=C bonds or from n-π* of C=O bonds or other sub-fluorophore groups [675]. However, the absorbance of C-dots was found to increase to longer wavelength in the 350 to 550 nm range after surface passivation with 4,7,10-trioxa-1,13-tridecanediamine (TTDDA) [676].

3.3.3.2. Photoluminescence

One of the most fascinating characterizations of C-dots, from a fundamental viewpoint to application, is their photoluminescence (PL). The most prominent feature of PL from C-dots is the tunable emission wavelength and intensity, which may originate from the broad size distribution, different surface defects, different surface states or different degrees of π conjugation. Similarly, the requirement for surface passivation is little understood, but appears to be linked to the synthetic method. As reported by Sun *et al.*, emission from C-dots passivated with PEG_{1500N} covers the visible light region from purple to red and spreads to the NIR region with the excitation wavelength progressively increasing from 400 nm on the left in 20 nm increments (**Figure 73**) [493]. Upon surface passivation with organic or polymeric materials, such as poly(propionyl ethyleneimine-co-ethyleneimine) (PPEI-EI) attached to the C-dots surface, surface defects are stabilized and strong fluorescence emissions both in solution-like suspension and in solid state were detected. The emissions

of such passivated C-dots covered a broad range of the visible region and extended into the NIR region as shown in **Figure 73**. It should be noted that the surface passivation agents used were not emissive in the visible and NIR regions, thus any fluorescence emissions observed must have originated from the surface passivated C-dots. The tunable emission property of C-dots is clearly demonstrated in **Figure 73**. From the fluorescence spectra of PPEI-EI-passivated C-dots, it is evident that the emissions are broad and excitation wavelength-dependent [493,677]. The tunable emissions of the surface-passivated C-dots could be a result of varied fluorescence characteristics of particles of different sizes of the C-dots and the distribution of different emissive sites on the surface of the C-dots.

By comparing with larger carbon nanoparticles, Mohapatra *et al.* unambiguously confirmed the red shift in emission wavelength of C-dots with increasing size when both were excited at 390 nm [649]. Evidently, if the size of C-dots is changed, the nature and content of sp^2 hybridized sites and the band gap from the quantum confinement effect would vary. The authors pointed out that excitation dependent photoluminescence could be caused by surface states, excitons of carbon, emissive traps, aromatic conjugation structures and free zig-zag sites.

Li *et al.* presented definitive evidence for luminescence arising from quantum-confinement effects and size-dependent optical properties of C-dots prepared by alkali-assisted electrochemical method [627]. **Figure 74a** shows the optical images of C-dots of four typical sizes, illuminated by white and UV light. The bright blue, green, yellow, and red PL of C-dots is strong enough to be seen with the naked eye. **Figure 74b** shows the corresponding emission spectra, in which the red, black, green, and blue lines show the PL spectra for blue-, green-, yellow-, and red-emitting C-dots, respectively. The PL properties vary sensitively with C-dot size (**Figure 74c**), with small C-dots (1.2 nm, center) giving UV light emission, medium-sized C-dots (1.5-3 nm) visible light emission (400–700 nm), and large C-dots (3.8 nm, center) NIR emission. To confirm that strong emission of C-dots came from the quantum-sized fragment of graphite, the as-synthesized C-dots were treated by hydrogen plasma to remove the surface oxygen. A series of control experiments showed no obvious change in the PL spectra of C-dots before and after hydrogen plasma. To further confirm that and explain why the strong emission comes from the quantum-sized graphite fragment of C-dots, they performed theoretical calculations to investigate the relationship between luminescence and cluster size [627]. **Figure 74d** shows the dependence of HOMO–LUMO gap on the size of the graphene fragments. As the size of the fragment increases, the gap

decreases gradually, and the gap energy in the visible spectral range is obtained from graphene fragments with a diameter of 14-22 Å, which agrees well with the visible emission of C-dots with diameters of <3 nm. Thus, they deduced that the strong emission of C-dots comes from the quantum-sized graphite structure instead from the carbon–oxygen surface [627].

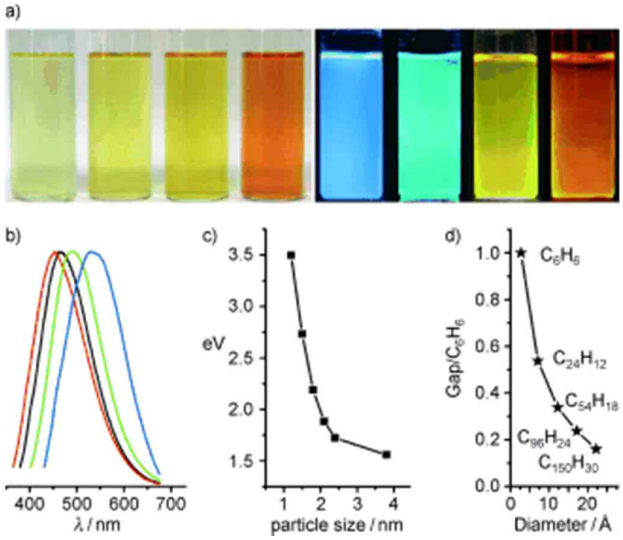

Figure 74: (a) Typical sized C-dots optical images illuminated under white (left; daylight lamp) and UV light (right; 365 nm); (b) PL spectra of typical sized C-dots: the red, black, green, and blue lines are the PL spectra for blue-, green-, yellow-, and red-emission C-dots, respectively; (c) relationship between the C-dots size and the PL properties; (d) HOMO–LUMO gap dependence on the size of the graphene fragments [627]**.**

C-dots produced from glucose using an ultrasonic treatment method reported by Li *et al.* exhibited NIR emission upon excitation by NIR light (**Figure 75**) [611]. It should be noted that such NIR PL emission excited by NIR excitation is particularly significant and useful for bioapplications because of the transparency of body tissues in the NIR "water window".

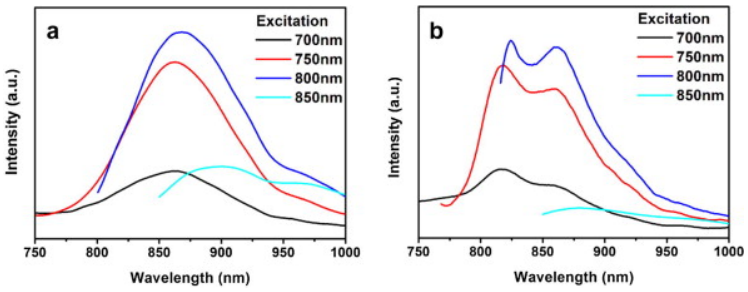

Figure 75: Photoluminescence spectra of C-dots under NIR excitation (emission in NIR range): (a) C-dots prepared from glucose/NaOH, (b) C-dots prepared from glucose/HCl [611]**.**

Moreover, pH-dependent PL emission was also reported and this phenomenon can be reasonably explained by surface states, as Qu *et al.* have discussed [678]. Functional groups

such as N–H and O–H on the surface of C-dots can form intramolecular and intermolecular hydrogen bonds, which endows the C-dots with different surface states. When pH increases or decreases, deprotonation or protonation of functional groups can lead to the variation of surface states and fluorescence. Except for excitation and pH tunable fluorescence, solvent polarity can also tune the fluorescence emission of C-dots. Jia *et al.* reported that C-dots prepared from direct heating of ascorbic acid solution show a practically linear dependence on the pH of the solution in the range of 4.0 to 8.0. The fluorescence intensity decreased by as much as 90% from pH 4.0 to 8.0. Varying the pH of the solution from 4.0 to 8.0, corresponding to the deprotonation of the carboxyl groups on the surface of the C-dots, might cause electrostatic doping/charging to the C-dots and shift the Fermi level [679]. Gao *et al.* observed the enhancement of fluorescence when the solvent changed from water to ethylene glycol. This may be due to the change of surface states and the decrease of non-irradiative transitions [635]. It is worthy of noting that some C-dots exhibit fluorescence that is independent on excitation wavelength and pH [680,681].

Although C-dots possess excellent photostability, which is a key factor for bioimaging. Photostability means the fluorescence emission intensity keeps stable during a long-time continuous excitation. Wei *et al.* synthesized a series of C-dots using glucose and the serial amino acid analogues as starting materials. Under 60 min excitation, the PL intensity of all the C-dots decreased slightly, preserving 90 % of the initial intensity. PL of the C-dots was much more stable than that of fluorescein isothiocyanate (FITC) dye, CdTe QDs and the previously reported polymer nanoparticles or dye-doped silica (**Figure 76**) [668].

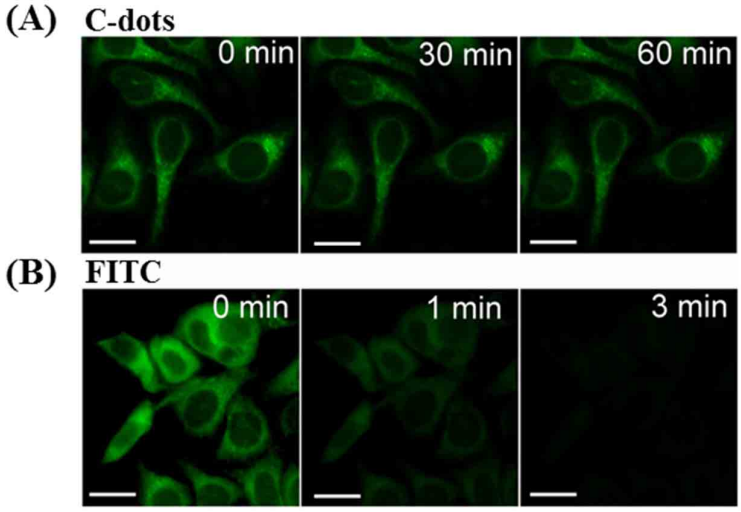

Figure 76: Stability comparison of fluorescence signals of HeLa cells labeled by C-dots (A), and FITC (B). Scale bar = 10 µm [668]**.**

Ge *et al.* prepared red-emissive C-dots using polythiophene phenylpropionic acid as precursor, and the photostability of the C-dots was investigated. Fixed-cell images of the C-dot labeled HeLa cells showed intense red fluorescence, which was clearly resolved even after laser irradiation for 120 min. By contrast, the fluorescence of FITC, a frequently used dye, quickly dropped below undetectable levels in only 10 min, indicating high photostability of the C-dots *in vitro* (**Figure 77**) [682].

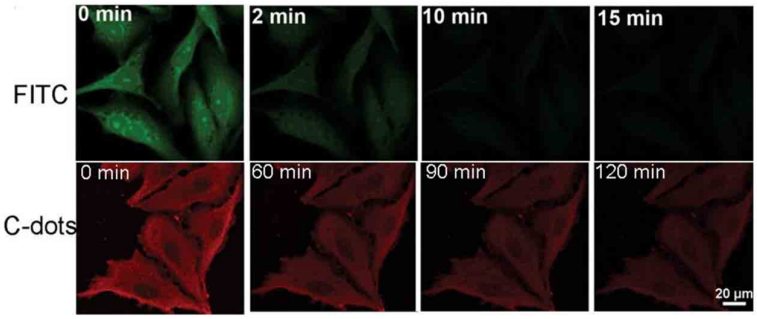

Figure 77: Fluorescent images of C-dots at different exposure time *in vitro* with FITC as a control [682]**.**

Due to unstable surface defects leading to reduced radiative recombination, raw C-dots usually have very low quantum yields (QY) [683]. Thus, the drawback limited the application of C-dots in many areas. In order to improve the luminescence of C-dots, great effort has been taken through physical and chemical methods. Wang *et al.* reported that C-dots with PL QY of 55-60 % can be acquired through column chromatography purification of C-dots mixture with 16-20 % PL QY [684]. To enhance the QY of C-dots, diverse designs have been developed including surface passivation, element doping, and inorganic salt doping. Passivation is the common way to improve the QY of C-dots due to its facile processibility and high efficiency. Passivation usually utilizes the strategy of oxidation or reduction of the C-dots surface and subsequently capping the C-dots with organic polymers or diamine compounds. Zheng *et al.* reported that original C-dots prepared with graphite oxide as precursor were reduced by $NaBH_4$, and the QY of the reduced-state C-dots enhanced greatly from 2 to 24 %, meanwhile, the maximum emission wavelength shifted from 520 to 450 nm under the excitation wavelength of 360 nm (**Figure 78**) [685].

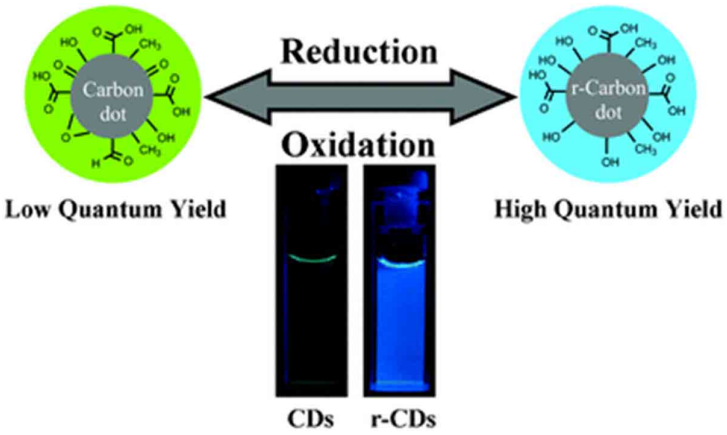

Figure 78: Graphical representation of the synthesis of reduced state C-dots (r-CDs) with blue luminescence from original C-dots. Inset: photographs of aqueous solutions of the C-dots (CDs) (left) and the r-CDs (right) obtained under UV light (360 nm) [685]**.**

To stabilize and maximize fluorescence, C-dots were usually doped with inorganic salts and other elements. One approach is to dope newly-produced C-dots with heteroatoms. Nitrogen is widely used as a doping element to synthesize N-doped C-dots with a high QY using various nitrogenous compounds [668,686,687]. Jiang *et al.* prepared C-dots with high QY (44.9 %) from amino acids as the raw materials via a microwave method [688]. Since some nitrogenous compounds can serve as both surface passivation and nitrogen source, it should be noted that the element doping and surface passivation of nitrogenous reagents are hard to discriminate. For instance, Li *et al.* prepared nitrogen and sulfur co-doped C-dots via hydrothermal method with extremely high QY (73%) [662]. In this method, L-cysteine was used as both surface passivation and element-doped source. To our knowledge, the QY of N, S- C-dots is highest (>70%) among all the luminescent C-dots by introducing both nitrogen and sulfur elements. In addition, Xu *et al.* synthesized S-doped C-dots with significant fluorescence QY (67%) via a hydrothermal method, which indicated that the sulfur doping achieved an efficient QY improvement [689]. Moreover, some other methods have been developed to improve the QY of C-dots. For example, Sun *et al.* developed C-dots doped with inorganic salt to achieve high QY. An aqueous suspension of the C-dots and $Zn(CH_3COO)_2$ was hydrolysed with NaOH, then $Zn(OH)_2$ was converted to ZnO by thermal annealing, the QY of the ZnO-doped C-dots in aqueous solution were around 45%. For the latter, the suspension of the C-dots and $Zn(CH_3COO)_2$ was precipitated with Na_2S, the QY of the ZnS-doped C-dots were consistently higher than 50%. Sun *et al.* speculated that, combined with the organic passivation agents, dopant might provide another form of surface passivation or enhance the surface passivation effect. Under the two-photo excitation

at 800 nm, these doped C-dots emitted bright luminescence in the visible region, suggesting promising potentials for imaging applications [690].

3.3.3.3. Up-conversion photoluminescence

In addition to normal fluorescence, a new and interesting phenomenon has been found in recent studies, such as up-conversion fluorescence emission. Up-conversion fluorescence is anti-Stokes behavior, in that a longer excitation wavelength produces a shorter emission wavelength. As shown by Sun *et al.*, C-dots were strongly emissive in the visible region under irradiation by an argon-ion laser (458 nm) or a femtosecond pulsed laser for two-photon excitation in the NIR range (800 nm) [32]. **Figure 79** shows that the one- and two-photon luminescence images for the same scanning area of C-dots are well matched. The representative two-photon luminescence spectrum shows that such C-dots have UCPL properties. Results from further bioimaging experiments *in vitro* also showed the UCPL property of C-dots.

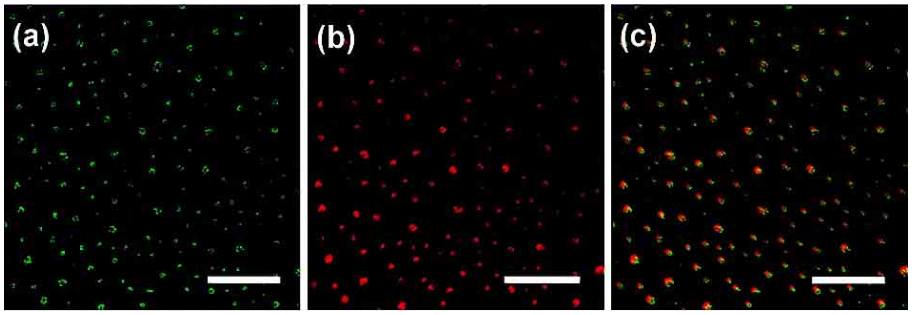

Figure 79: Luminescence images (all scale bars 20 µm) of the C-dots with (a) argon ion laser excitation at 458 nm and (b) femtosecond pulsed laser excitation at 800 nm; (c) is an overlay of (a) and (b) [32]**.**

Recently, Jiang *et al.* reported that C-dots emitted strong up-conversion photoluminescence (UCPL) under excitation with a femtosecond pulsed laser (λ = 800 nm) and this has been demonstrated to be a two-photon excitation process [659].

Stan *et al.* studied the up-conversion fluorescence of N-doped C-dots in the wavelength range of 750-960 nm [691]. Interestingly, distinct from the down-conversion case, up-conversion fluorescence showed excitation wavelength independent and solvent polarity dependent emission. Moreover, such up-conversion fluorescence can be easily observed by the naked eye. Shen *et al.* fabricated C-dots surface-passivated with PEG by a one-pot hydrothermal reaction. The PL quantum yield of the C-dots at the excitation wavelength of 360 nm was about 28.0 %. The C-dots possessed the up-conversion PL properties, emitted blue PL in the fluorescent microscopy images both under the ultraviolet and 808 nm laser

[692]. As shown in **Figure 80a**, when the excitation wavelength changed from 700 to 980 nm, the up-converted emission peaks shifted from 431 to 544 nm, respectively. The shifting between the energy of up-converted emission light (E_m) and excitation light (E_x) was almost unchanged, about 1.1 eV. **Figure 80b** shows the linear relationship between E_m and E_x, and the function of the fit line is $E_m = 1.00E_x + \delta E$ ($R^2 = 0.9747$) with $\delta E = 1.1$ eV. The authors speculate on the UCPL due to the anti-Stokes PL, where the δE between the π and σ orbitals is near 1.1 eV [677].

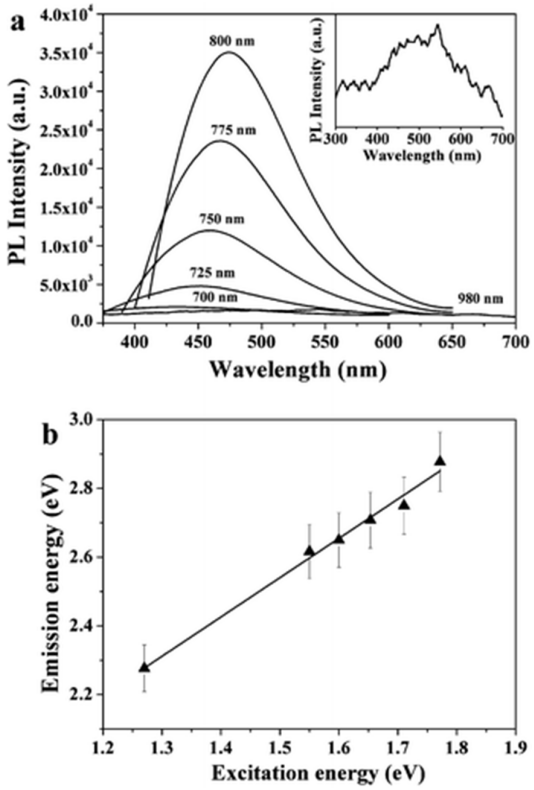

Figure 80: (a) Upconverted PL properties of the C-dots-PEG, inset is the enlarged image of the PL spectrum excited at a 980 nm laser. (b) The energy of the excitation light as a function of the emission [677]**.**

To further confirm that and explain how UCPL comes from the C-dots, an energy level structural model was established, in which the UCPL spectrum could be regarded as an anti-Stokes transition (**Figure 81**). The energy levels of π and σ orbitals were provided by the carbene ground-state multiplicity, which is related to the energy difference (δE) between the π and σ orbitals. The energy between the excitation light and the emission light in the up-conversion process was close to 1.1 eV (Hoffmann determined δE should be below 1.5 eV). When a bunch of low-energy photons excite the electrons in the π orbital, the π electrons would transition to a high-energy state such as the LUMO, and then fall back to a low-energy

state. Thus, an UCPL is emitted if the electrons transition back to the σ orbital. The electrons in the σ orbital can also be excited, they only can emit normal PL (**Figure 81a and b**). This explains why the difference between up-conversion excitation and emission light is a constant energy related to the energy difference of the π and σ orbitals [677].

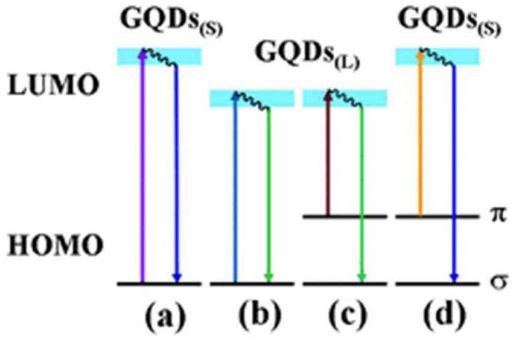

Figure 81: A schematic illustration of various typical electronic transitions processes of C-dots. Normal PL mechanisms in C-dots for small size (a) and large size (b); UCPL mechanisms in C-dots for large size (c) and small size (d) [677]**.**

The UCPL of C-dots opens up new opportunities for cell imaging with two-photon luminescence microscopy, as well as highly efficient catalyst design, for applications in bioscience and energy technology.

3.3.3.4. Chemiluminescence

Chemiluminescence (CL) refers to a phenomenon whereby during a chemical reaction, a substance can absorb chemical energy to turn into an excited state and then go back to the ground state by light irradiation. CL properties of C-dots were firstly discovered when the C-dots coexisted with some oxidants, such as potassium permanganate ($KMnO_4$) and cerium(IV) [693]. During this process, the C-dots with surface energy traps serve as electron acceptors for the electron donator $O_2^{\cdot -}$ and strong CL emitter. The electron paramagnetic resonance (EPR) reveals that oxidants, such as $KMnO_4$ and cerium(IV), can inject holes into the C-dots. This process increases the population of the holes in the C-dots and accelerates the electron-hole annihilation, resulting in energy release in the form of CL emission. This is the first CL route accounting for the CL (CL1). The other important route (CL2) is the Mn(II)* excited state, which returns to the ground state with CL emission at 650 nm (**Figure 82**). Moreover, the CL intensity was dependent on the concentration of the C-dots in a certain range. It was also found that increasing the temperature had a positive effect on the CL due to the thermal equilibrium of electron distribution in the C-dots (**Figure 82**). It is interesting

for this system that the CL properties can be designed by changing their surface groups [694].

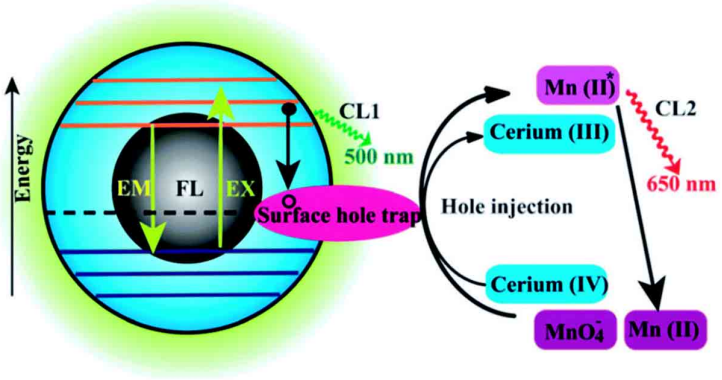

Figure 82: Schematic illustration of the FL and CL mechanisms in the C-dots-$KMnO_4$ and C-dots–cerium(IV) systems. CL1 and CL2 represent two CL routes in the system [693].

A novel CL phenomenon was also observed for the as-prepared C-dots in a strong alkaline solution (NaOH or KOH). The C-dots exhibited excellent electron donor ability towards dissolved oxygen to form the superoxide anion radical ($O_2^{\cdot -}$) in a solution of NaOH. These results directly provided evidence for the excellent electron-donating ability of C-dots [695]. Radiative recombination of the injected electrons by "chemical reduction" of the C-dots and thermally excited generated holes was suggested to account for the CL behavior in strong alkaline solutions [695]. The dual role of C-dots as an electron donor and acceptor offers great potential in optronics and catalysis.

3.3.3.5. Electrochemiluminescence

Different from the fluorescence and CL, electrochemiluminescence (ECL) happens when the substances produced in an electrochemical reaction transition to an excited state via electron injection and then emit light to return back to ground state. The ECL emission of C-dots (2.0 nm) produced by Zheng *et al.* from the electrochemical oxidation of graphite was observed as the potential was cycled between +1.8 and −1.5 V (**Figure 83A**) [617]. The suggested ECL mechanism involves the formation of excited-state C-dots (R^*) by electron-transfer annihilation of negatively charged ($R^{\cdot -}$) and positively charged ($R^{\cdot +}$) species (ET1 route in **Figure 83B**). $R^{\cdot +}$ is the more stable of the two species, as indicated by the greater intensity of the cathodic ECL (**Figure 83A**). Interestingly, when produced by microwave synthesis, 3 nm PEG_{200}-functionalized C-dots also exhibited ECL behavior, but the $R^{\cdot -}$ species was found to be more stable in this case [696]. The presence of peroxydisulfate ($S_2O_8^{2-}$) enhanced the ECL (ET2 route in **Figure 83B**) in the cathodic potential range and

produced a stable and sensitive (as no other co-reactants tested elicited an ECL enhancement) ECL response, thus suggesting the application of C-dots for ECL sensing [617].

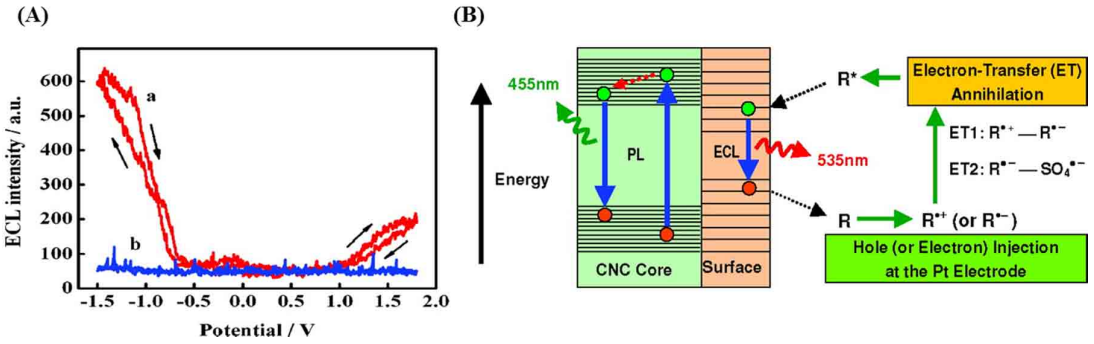

Figure 83: (A) ECL responses a) with and b) without C-dots at a Pt electrode in 0.1 M phosphate buffer solution (pH 7.0) with a scan rate of 0.1 V s^{-1}; (B) The ECL and PL mechanisms in C-dots [617].

3.3.4. Biological properties of C-dots

The biocompatibility and low toxicity are two prerequisite properties that facilitate the bioapplications of nanomaterials. Although the biocompatibility of C-dots *in vitro* has been demonstrated by many groups [697,698], the evaluation of the biocompatibility of C-dots *in vivo* is still encouraged for the further application of C-dots [31,699–701]. Systematic cytotoxicity evaluations were carried out on both raw C-dots and passivated C-dots in the past few years [700,702]. Sun's group utilized two kinds of raw C-dots for cytotoxicity assay: one was commercially supplied carbon nanopowder; another was produced by the arc-discharge of graphite rods and then refluxed in HNO_3 for 12 h. The bare C-dots were apparently nontoxic to cells up to a relatively high concentration of 0.4 mg mL^{-1}. Luminescent C-dots synthesized by the electrochemical treatment of graphite were also evaluated in terms of cytotoxicity assay using a human kidney cell line, in which the cell viability was not affected by the dots [703]. Furthermore, Ray *et al.* improved a soot-based approach for C-dots synthesis with diameters of 26 nm [622]. The experimental results of cell viability also confirmed that the C-dots showed negligible cytotoxicity at concentrations required for fluorescence bioimaging.

The cytotoxicity of the C-dots passivated with functional groups, such as PEG [30], PPEI-EI [32], PEI [700], BPEI (branched poly(ethylenimine)) [704], and PAA (poly(acrylic acid)) [705], were also evaluated in cytotoxicity assays. The PEGylated C-dots in all available

configurations were non-cytotoxic up to concentrations much higher than that is necessary for cell imaging and related applications [31,706]. In addition, C-dots functionalized with PEG_{1500N} were injected into mice for toxicity evaluation up to 28 days, and the results suggested no significant toxic effects *in vivo* [31]. Moreover, experimental results indicated that the PPEI-EI-passivated C-dots were mostly nontoxic to the cells below a relatively high threshold of carbon core-equivalent PPEI-EI concentration [32]. According to the MTT assay, a PEI free sample was apparently nontoxic to HT-29 cells even at relatively high concentrations. However, the PEI-functionalized C-dots were more cytotoxic than PPEI-EI-functionalized C-dots. The more ethylenimine (EI) units within the PEI may be associated with the lower concentration thresholds for the C-dots to become cytotoxic, as PEI is the homopolymer corresponding to PPEI-EI with an extreme EI fraction of 100%. Free PAA in a nonaqueous solution was found to be harmful to cells even at relatively low concentrations (50 μg mL^{-1}). The PAA-functionalized C-dots were generally comparable to free PAA at the same C-dots core-equivalent concentrations, both were toxic to the cells with an exposure time of 24 h, but less so when the exposure time was shortened to 4 h. Overall, molecules with low cytotoxicity even at high concentrations such as PEG and PPEI-EI are suitable for C-dots functionalization for *in vivo* imaging and biosensing. Molecules with higher cytotoxicity including BPEI and PAA, can still be used to functionalize C-dots used *in vivo* if their concentrations are maintained low enough and the incubation time short as well [700].

Huang *et al.* explored the effect of injection routes on the distribution, clearance, and tumour uptake of C-dots. They used the PEG-functionalized NIR dye ZW800-conjugated C-dots to investigate the effect of the three different injection routes: intravenous (iv), subcutaneous (sc), and intramuscular (im). Firstly, they studied the biodistribution of C-dots by different injection routes. The results showed that, after injections via all the three routes, the majority of the C-dots were accumulated in kidneys at 1 h. Meanwhile, the signal of the C-dots was quantified and ranked based on the injection routes as im > sc > iv. After 24 h, no available signal was detected in any organ, which indicated that the C-dots were swept out of the body irrespective of the injection routes. Then, a urine clearance analysis of C-dots was performed. The results showed that the C-dots were efficiently and rapidly discharged from the body after the three injection routes. The clearance rate of C-dots was ranked as iv > im > sc. Finally, they investigated the tumour uptake of C-dots by three injection routes, and they found that the different injection routes resulted in different tumour uptake efficiencies,

ranked as sc > iv > im [699]. Their results clearly showed that injection routes affected the distribution, clearance, and tumour uptake of C-dots evidently.

3.3.5. Applications of C-dots

The novel properties of C-dots make them applicable in a wide range of areas. As C-dots are a very new area of research, not many applications have yet been commercialized by making use of these nanoparticles. Indeed a lot of research has been done on the applicability of these particles to different areas.

3.3.5.1. Photocatalysis

Advanced materials for electrocatalytic and photoelectrochemical (PEC) hydrogen evolution reaction (HER) are central to the area of renewable energy. C-dots modified P25 TiO_2 composites (C-dots/P25) were prepared via a facile, one-step hydrothermal reaction [707]. C-dots/P25 exhibited improved photocatalytic H_2 evolution under irradiation with UV-Vis and visible light ($\lambda > 450$ nm) because of the C-dots acting as an electron reservoir to improve the efficient separation of the photoinduced electron–hole pairs of P25 and a photosensitizer to sensitize P25 into a visible light response structure for H_2 evolution. It is expected to utilize the NIR region of sunlight for its large share of sun's energy. C-dots with the UCPL properties can improve the PEC properties of C-dots/CdSe/TiO_2 NR photoanodes at the NIR region (over 750 nm) (**Figure 84**) [708]. The one-dimensional ordered TiO_2/CdSe core/shell heterostructural network (**Figure 84A**) not only provides a large surface area for efficient loading of up-conversion C-dots, but also allows an excellent interfacial chemical reaction between the CdSe and electrolyte. Subsequently, C-dots were electrodeposited on the surface of the TiO_2/CdSe core/shell nanorods (NRs) to construct a C-dots/CdSe/TiO_2 composite photoanode. **Figure 84B** is the schematic diagram illustrating the whole PEC process under NIR illumination. The C-dots can absorb NIR photons and emit visible photons through the up-conversion effect to excite CdSe. Subsequently, the excited electrons in the conduction band of CdSe would rapidly inject into the conduction band of TiO_2, and then transfer along the axial direction of the TiO_2 NRs to the FTO substrate. The electrons would finally be transferred to the Pt counter electrode under the assistance of a little external bias voltage, and then drive the hydrogen evolution reaction. The holes remaining in the valence band of CdSe would be consumed by the sacrificial agent**.**

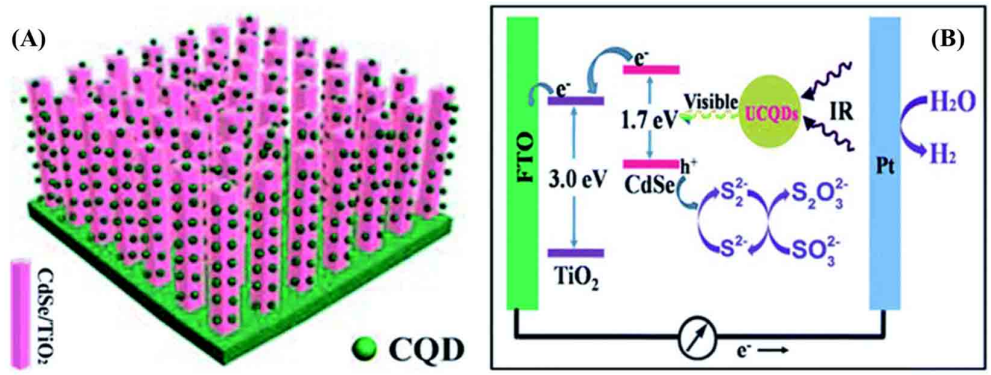

Figure 84: (A) A schematic diagram showing the C-dots (CQD)/CdSe/TiO_2 NR photoanode, (B) A schematic diagram to illustrate how up-conversion of the C-dots (UCQDs) served as spectral converters for the CdSe/TiO_2 NR photoanode [708]**.**

Dey *et al.* showed the fabrication of C-dots from a bio-precursor and used them for the reduction of $PdCl_4^{2-}$ salts leading to the formation of Pd@C-dots core–shell nanostructures. Although bare C-dots were not capable of preventing the agglomeration of the Pd nanoparticles during the Suzuki and Heck reactions, addition of a co-stabilizer in the form of poly-(N-vinyl-2-pyrrolidone) (PVP) led to an efficient composite that showed high catalytic activity towards the formation of C–C bonds. The Pd@C-dots-PVP catalysts were reused in subsequent reactions and the results showed efficient catalytic activity after the third cycle even with obvious structural changes [709].

3.3.5.2. Optoelectronics

3.3.5.2.1. Light-emitting diodes

As new kinds of luminescent materials, C-dots are expected to replace phosphors in white light emitting diodes (LEDs) with rear earth metals and toxic elements such as cadmium and lead because of their low cost, high quantum yield (QY), high stability and eco-friendliness. Consequently, some efforts have been paid to fulfill the applications of C-dots in LEDs. They can work both as phosphors in white LEDs or active layers in electroluminescent devices. Large-scale (20 × 20 cm) free-standing luminescent films of the C-dots embedded PMMA matrix were fabricated. The polymer matrix provides mechanical support and disperse the C-dots to prevent solid-state quenching. The obtained films are cost-effective, fully flexible, easily scalable, thermally stable, eco-friendly, and mechanically robust, and they show great potential in large-scale flexible solid-state lighting systems. White LEDs consist of the obtained films as the color-converting phosphors and InGaN blue LEDs as the illuminators were also demonstrated. C-dots-based LEDs with a driving current controlled

color change have been reported [710]. These devices consist of a C-dots emissive layer sandwiched between an organic hole transport layer and an organic or inorganic electron transport layer (**Figure 85A**) fabricated by a solution-based process. By tuning the device structure and the injecting current density (by changing the applied voltage), it is possible to obtain multicolor emission of blue, cyan, magenta, and white from the same C-dots (**Figure 85B**). It is the first observation of switchable EL behavior with white emission in single emitting layer structured nanomaterial LEDs. This interesting current density-dependent emission was useful for the development of colorful LEDs. The pure blue and white emissions were obtained by tuning the electron transport layer materials and the thickness of the electrode.

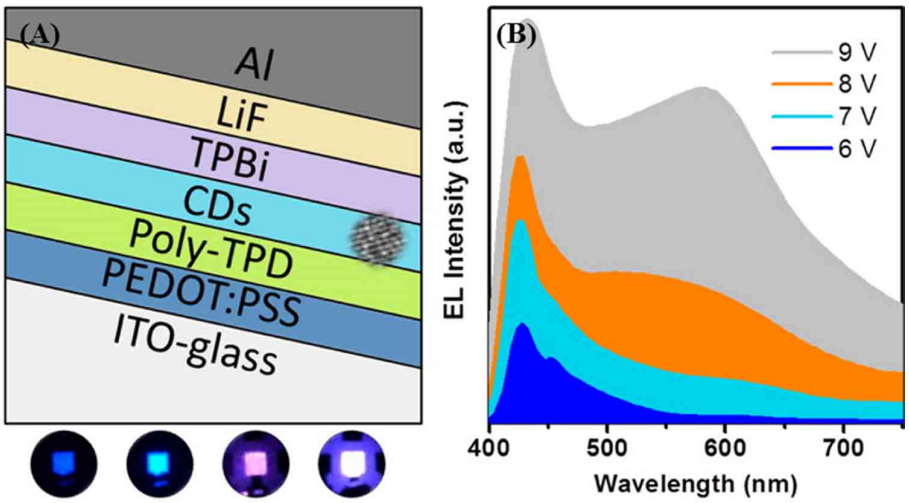

Figure 85: (A) Sandwiched structure of LEDs using C-dots as a single emitting layer. (B) Electroluminescence (EL) spectra and true color photographs of the blue, cyan, magenta, and white emissions [710]**.**

Chen *et al.* prepared C-dots with broad yellow fluorescence by a one-step pyrolysis from *N*-acetylcysteine (**Figure 86A**) [711]. The as-prepared C-dots are well-dispersed in various hydrophilic and hydrophobic solvents and possess high QY of 13 % without further surface treatment. The emission spectra of the white LED consists of two emission bands, blue emission centering at 460 nm from the LED chip and broad yellow emission from C-dots (**Figure 86B**). These two emission bands are combined to give a spectrum that produces white light. As seen in **Figure 86C**, the device provided a bright white illumination. The as-prepared white LEDs exhibit white light with the Commission Internationale d'Eclairage (CIE) chromaticity coordinates of (0.34, 0.35) (**Figure 86D**), which is very close to the

balanced white light emission (0.33, 0.33), and hence it exhibits warm white light approximating natural sunlight.

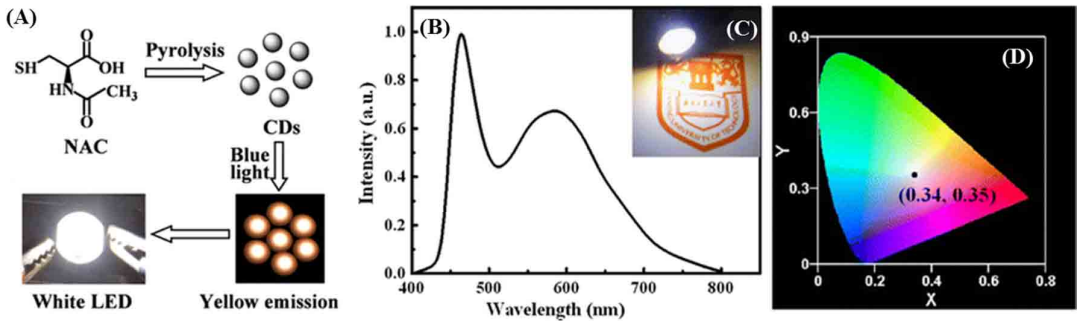

Figure 86: (A) Schematic of the formation of C-dots (CDs) from *N*-acetylcysteine and application in white LEDs, (B) Emission spectrum of a prototype white LED, (C) The photograph of a prototype white LED operated at 3.0 V, (D) Placement of the LED emission spectrum on the CIE 1931 chromaticity chart [711]**.**

3.3.5.2.2. Photovoltaics

C-dots have recently emerged as viable alternatives to traditional semiconductor quantum dots (QDs) because of their facile and low cost synthesis, long term colloidal stability, and low environmental and biological toxicity. The compatible surface chemistry, good solubility in polar solvents and extensive optical absorption throughout the visible and NIR wavelength regions render C-dots as potentially useful for photovoltaic applications [712]. Many kinds of solar cells have been reported, such as organic solar cells (OSCs) [713,714], and dye-sensitized solar cells (DSSCs) [715,716]. The C-dots can play different roles of photo absorption agents, sensitizers and transporting layers and the efficiency varied from 0.1 to 9%.

Organic and dye sensitized solar cells have attracted much attention because of their low cost, large area, random substrate and facile and scalable engineering such as spin-coating, inject printing and roll-to-roll methods. These devices can also benefit from the broad absorption, special band structure and electron transportation ability of C-dots. Li *et al.* fabricated a bulk heterojunction (BHJ) OSC based on an composite layer of poly(3-hexylthiophene) (P3HT) and C-dots (**Figure 87A**) [35]. The LUMO energy level of C-dots is in the range of 4.2-4.4 eV, which is just between the LUMO of P3HT and the work function of Al (**Figure 87B**), forming an electron transport cascade. This band structure will facilitate the dissociation of excitons and good crystallinity of C-dots will improve the charge transport through the active layer. Thus, a photo conversion efficiency of 1.28% was

obtained and such structure without C60 was accepted by other groups to fabricate OSCs [717,718]. Though the efficiency of these devices is still low compared to conventional organic solar cells, it is expected that C-dots can be promising alternatives to the expensive C60 as electron acceptors.

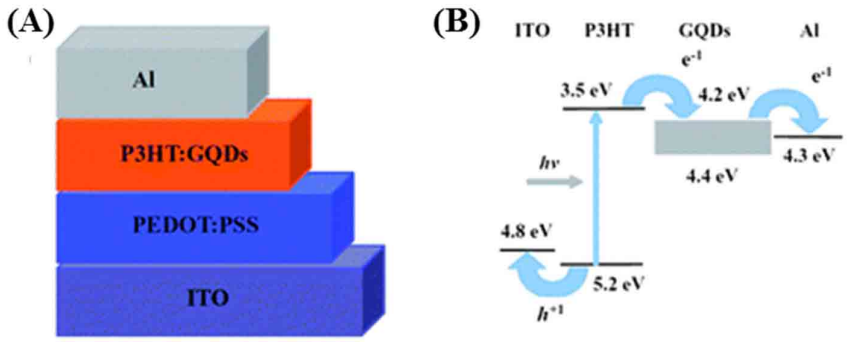

Figure 87: (A) Schematic and (B) energy band diagram of the C-dots (GQDs) based organic solar cell [35]**.**

Organic/inorganic hybrid solar cells combined with metal oxides and organic semiconductors have also achieved researchers' attention while it remains challenges to match the energy levels of the donor-acceptor system. Qin *et al.* demonstrated the insertion of C-dots in organic/inorganic layers or combination with organic semiconductors, which led to an enhancement of the power conversion efficiency [719]. As shown in **Figure 88A**, a cascaded alignment of energy levels similar to that of above discussed devices is obtained, facilitating the separation of photogenerated carriers. On the other hand, most of the applied oxides and organics can only absorb the solar energy partially and the insertion of C-dots with broad absorption spectra enhances the harvest of incident light. All of these factors contribute to the performance of solar cells (**Figure 88B**).

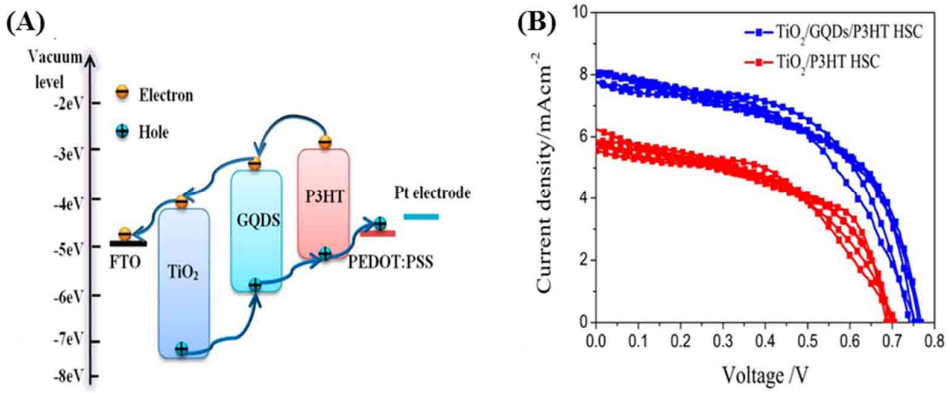

Figure 88: (A) Energy band diagram of organic/inorganic hybrid solar cell. (B) Current-Voltage curves with and without C-dots [719]**.**

Dye-sensitized solar cells (DSSCs) is another kind of photovoltaic device that utilizes dyes to absorb sun light. DSSCs have aroused intense attention due to their diversity, low cost and easy processing. Though DSSCs benefit from the diversity of organic dyes and get respectable efficiency, the photobleaching of organic dyes or the high cost and toxicity of ruthenium containing dyes, even the volatile electrolyte may hamper its widely application. C-dots with stable light absorption made from broad and cheap sources show its potential in DSSCs. After the first attempt by Mirtchev *et al.*, who introduced C-dots as a sensitizer to capture sunlight in DSSCs [716], much research work has been performed to use this emergent nanolight to improve the performance of DSSCs. As the charge recombination of photogenerated electrons in the porous electrode with either the oxidized dye or the electrolyte will reduce the efficiency of DSSCs. Inspired by natural photosystems, Ma *et al.* developed a C-dots-bridged dye/semiconductor complex system for the fabrication of highly efficient photoelectric conversion systems. C-dots not only enhanced the UV-vis absorbance of rhodamine B (RhB) solutions due to the synergistic hyperchromic effect between RhB and C-dots (**Figure 89**), but also effectively suppressed the recombination of photogenerated electrons, thereby leading to a significantly enhanced photoelectric conversion efficiency [720]. Doping of C-dots into the dye/semiconductor complex significantly improved the photoelectric conversion efficiency of the complex by 7 times.

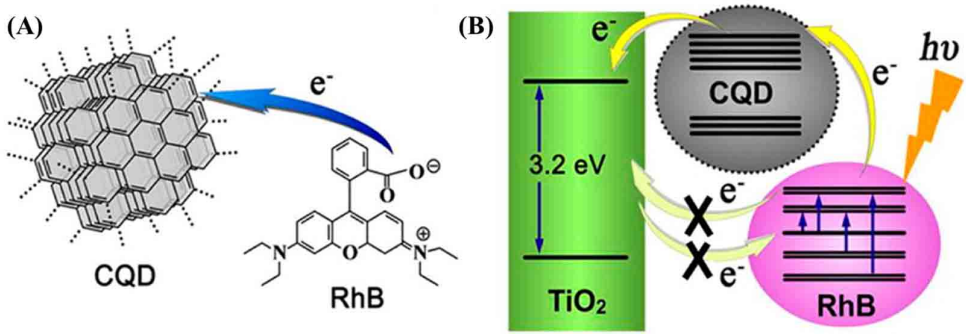

Figure 89: (A) Scheme of electron transfer from RhB to C-dots (CQDs). (B) C-dots serve as an electron transfer intermediary for bridging the photogenerated electrons and suppressing their recombination [720]**.**

3.3.5.3. Bioimaging

Bioimaging is an essential tool in the field of biology. It is basically necessary for targeted drug delivery and discovering a defective site in a body. The field of nanotechnology is rapidly advancing for its application in biology. Fluorescent nanomaterials are of basic

interest for the purpose of bioimaging. C-dots have multiple advantages over semiconductor quantum dots (QDs), including comparable optical properties and good chemical and photochemical stability. Most importantly, carbon is largely non-toxic and environmentally friendly. An important parameter for bioimaging is photoluminescence (PL). This important property is exhibited by C-dots that are synthesized from various materials. C-dots are known for their tunable PL and also multicolor PL properties. These properties make C-dots very desirable as alternatives to semiconductor QDs for application in bioimaging both *in vitro* and *in vivo* [721].

The possibility of using C-dots as fluorescent labels for cellular imaging was first demonstrated by Cao *et al.* who used PPEI-EI passivated C-dots for two-photon luminescence microscopy using human breast cancer MCF-7 cells [32]. After incubation of the cells with C-dots for 2 h at 37 °C followed by washing to remove any extracellular C-dots, they exhibited bright luminescence in both the cell membrane and cytoplasm regions when imaged using a fluorescence microscope with excitation by 800 nm laser pulses (**Figure 90**). The ability of the cells to uptake C-dots was found to be temperature-dependent, with no C-dots internalized at 4 °C.

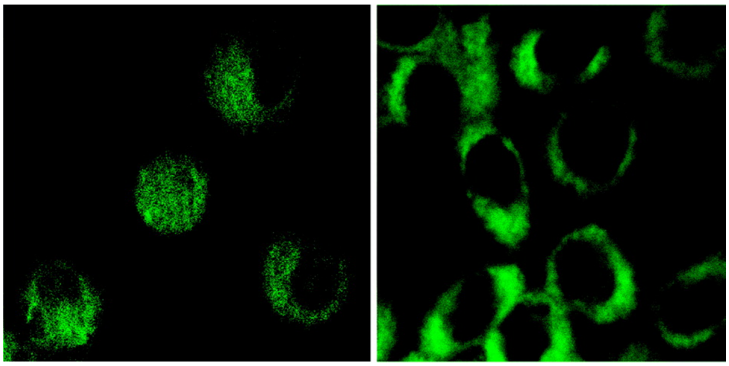

Figure 90: Two-photon luminescence image of human breast cancer MCF-7 cells with internalized C-dots passivated with PPEI-EI [32]**.**

In another study, fluorescent C-dots were synthesized from several carbohydrates such as glucose, glucosamine, sucrose, dextrans of different molecular weights, cellulose and ascorbic acid. The obtained nanoparticles were then incubated with HeLa cells for 3–6 hours and imaged using fluorescence microscopy. The C-dots exhibited very low binding to the cells due to their small size and low surface charge. As seen in **Figure 91**, the particles fluoresced different colors based on their size [598]. All these findings suggest that few C-dots are capable of penetrating into the cell membrane and a few just help in staining the cells and cell nuclei. Hence, the size and surface functionalization of C-dots play a major

role for applications in bioimaging. Also, the results mentioned above suggest that C-dots are nontoxic and biocompatible in nature.

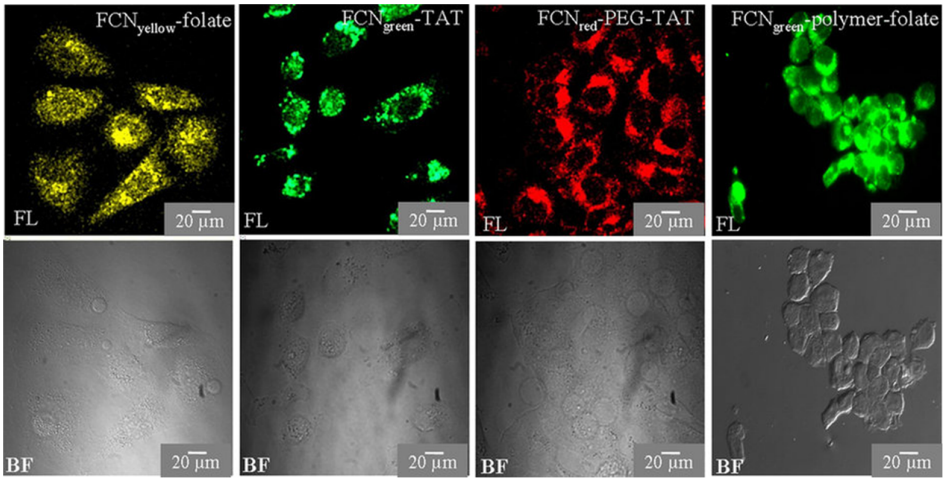

Figure 91: C-dots are incubated with HeLa cells for 3–6 hours and labeled cells are imaged under fluorescence microscope. Cells are imaged under bright field (BF) and fluorescence (FL) mode [598]**.**

C-dots are able to exhibit multicolor emissions, which is a huge advantage that sets them apart from the majority of labelling agents. This allows researchers to control and choose the excitation and emission wavelengths [722,723].

Zhai *et al.* synthesized photoluminescent C-dots with a QY of 30.2% to label L929 cells [723]. The C-dots incubated cells emitted blue, green, and red fluorescence upon excitation at 405, 488, and 543 nm, respectively (**Figure 92**). Those areas from which the fluorescence was emitted reflected the presence of C-dots, which were distinctly located in the cell membrane and cytoplasm, around the cell nucleus. Until now, nearly all C-dots without specific modifications basically label the cell membrane and cytoplasm areas without reaching the nuclei mainly through passive endocytosis [602].

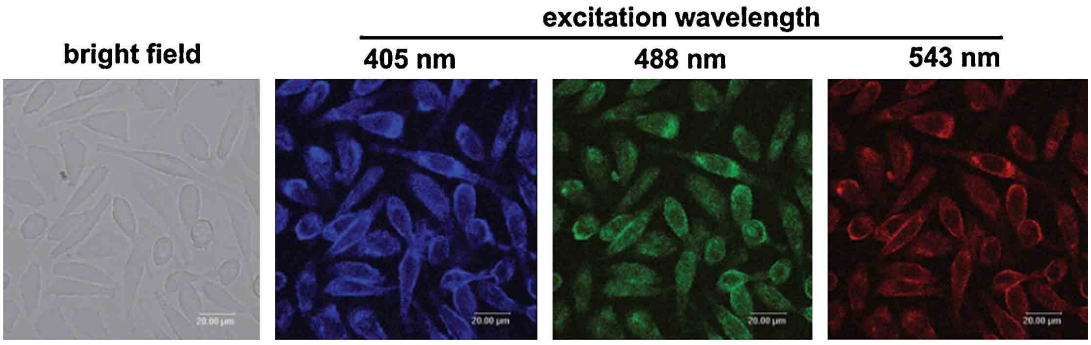

Figure 92: Laser scanning confocal microscopy images of ethylenediamine (EDA)-C-dots labeled L929 cells [723]**.**

If the excitation wavelength is red-shifted enough, C-dots could emit in the NIR region. Although the emission in the NIR region is relatively weak, C-dots have great potential for *in vivo* fluorescence tracking studies because the animal body is practically transparent in the NIR region [722].

Yang *et al.* was the first to explore the viability of C-dots as contrast agents in live mice. They obtained C-dots and ZnS-doped C-dots from chemical processing of raw nanomaterial by laser ablation. After PEG_{1500N} modifications, they were used for *in vivo* optical imaging of mice. C-dots or ZnS-doped C-dots solutions were injected in the mice body with various injection methods and high fluorescence was observed in the parts where the C-dots were injected but fluorescence faded away after 24 h [30].

As seen in **Figure 93**, C-dots were intravenously injected into the bladder of mice. The images also show fluorescence imaging of the dissected kidneys and liver. It was also observed that the injected C-dots were removed from the body via the urine excretion pathway.

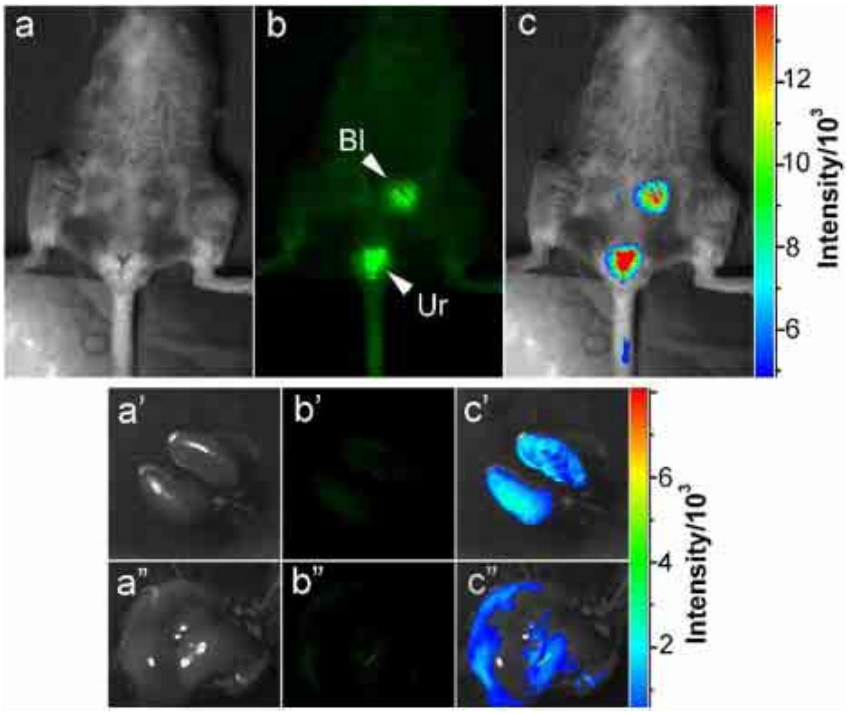

Figure 93: Intravenous injection: (a) bright field, (b) as-detected fluorescence (Bl: bladder and Ur: urine), and (c) color-coded images. The same order for the images of the dissected kidneys (a'–c') and liver (a"–c") [30]**.**

3.3.5.4. Biosensing

In addition to their superior biocompatibility, C-dots possess the ability to serve as either excellent electron donors or electron acceptor. Therefore, C-dots can be used for intracellular detection of ions, biological pH value, protein, enzymes, vitamins, and nucleic acid. By monitoring the changes in their fluorescence intensity under external physical or chemical stimuli, C-dots were used to detect substances such as DNA [724], PO_4^{3-} [725], thrombin [726], nitrite [727], glucose [728], biothiol [36], Cr^{3+} [37], Fe^{3+} [678,729], pH [730], Ag^{+} [731], Hg^{2+} [36,732,733], Cu^{2+} [607,644], and Cd^{2+} [729]. The surface functional groups on C-dots indicate distinctive affinities to different target ions, which results in the quench of PL intensity through an electron or energy transfer process and high selectivity to other ions. The detection of heavy metals is of importance because of their hazardous effect on the environment and human health. One of the first attempts of utilizing C-dots in sensing is the selective detection of Hg^{2+} in aqueous solutions [655,734] and live cells [735].

Based on the quenching effect of Hg^{2+} on the fluorescence of C-dots, Yan *et al.* adopted the Hg^{2+}–C-dots system for selective detection of Hg^{2+} in aqueous solution as well as in live cells [735]. The authors reported the synthesis of two types of C-dots using citric acid with 1,2-ethyldiamine (C-dots-1) and N-(b-aminoethyl)-g-aminopropyl (C-dots-2) that possess high QY of 65.5 and 55.4%, respectively. They studied the effective and selective quenching of fluorescence emissions of C-dots-1 and C-dots-2 by Hg^{2+}. Both C-dots acted as selective and sensitive fluorescent probes for the detection of traces of Hg^{2+} in both aqueous solutions and live cells. Upon the addition of 20 mM of Hg^{2+}, the fluorescence intensity of C-dots-1 was rapidly quenched by 80%, while that of C-dots-2 was quenched by 55%, and both remained stable after 1 h of observation (**Figure 94**). This substantiates the viability of using C-dots-1 and C-dots-2 as chemical sensing probes for Hg^{2+}. The selectivity of C-dots-1 and C-dots-2 toward Hg^{2+} was then assessed by comparing the extent of fluorescence quenching of C-dots-1 and C-dots-2 by the addition of 20 mM of different metal ions. As shown in **Figure 94**, among all metal ions tested, Hg^{2+} quenched both the fluorescence of C-dots-1 and C-dots-2 to the largest extent. Such quenched fluorescence was reversible and could be recovered by adding a strong chelating agent such as ethylene diamine tetraacetic acid (EDTA), making these C-dots reversible fluorescent probes. Furthermore, successful attempts were made in detecting Hg^{2+} in cultured cells [735].

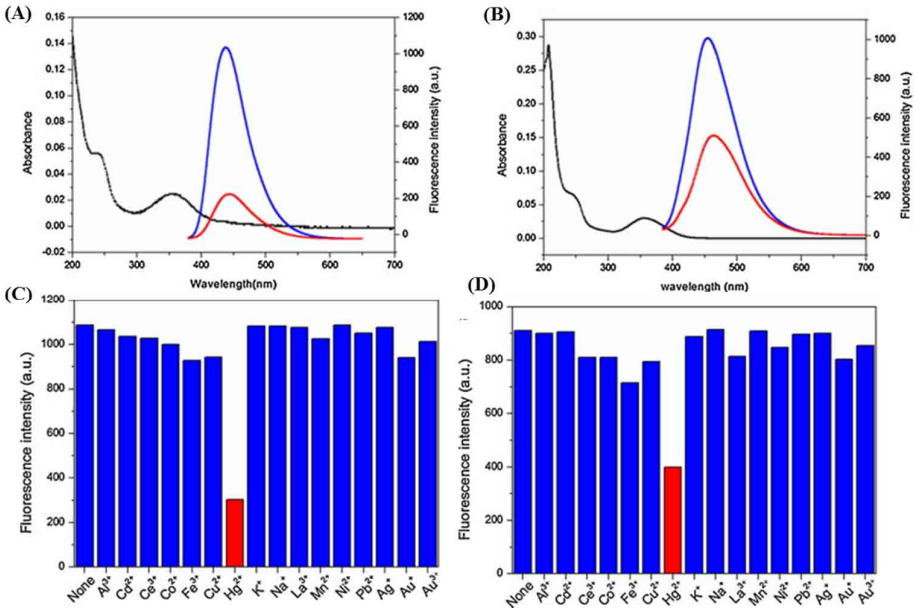

Figure 94: UV-vis (black lines) and fluorescence spectra of (A) C-dots-1 and (B) C-dots-2 aqueous solutions in the absence (blue lines) and presence (red lines) of Hg^{2+}; fluorescence responses of (C) C-dots-1 and (D) C-dots-2 aqueous solutions in the presence of 20 mM of different metal ions. (λ_{ex} = 360 nm) [735]**.**

Qu *et al.* reported a preparative route toward distinctive fluorescent C-dots from dopamine (DA). Such C-dots exhibit excellent PL properties, and they can be used for multicolor bioimaging. More importantly, these C-dots were used as a new type of sensor for label-free detection of Fe^{3+} and dopamine (DA) with high sensitivity and selectivity [736]. The method relies on the fact that Fe^{3+} can oxidize the hydroquinone groups on the surfaces of C-dots to the quinone species, which can quench the fluorescence of the C-dots and DA can effectively shelter the fluorescence quenching due to their competition with C-dots to react with Fe^{3+} (**Figure 95**). It offers a convenient "mix-and-detect" protocol for rapid detection of Fe^{3+} and DA and can be easily accomplished with a rapid one-step (within 10 min) operation. Moreover, this sensing platform exhibits high sensitivity and selectivity toward Fe^{3+} and DA *versus* other metal ions and the other DA analogues. Furthermore, no further chemical modification of the C-dots was required, which offers the advantages of simplicity, cost efficiency and environmentally friendliness.

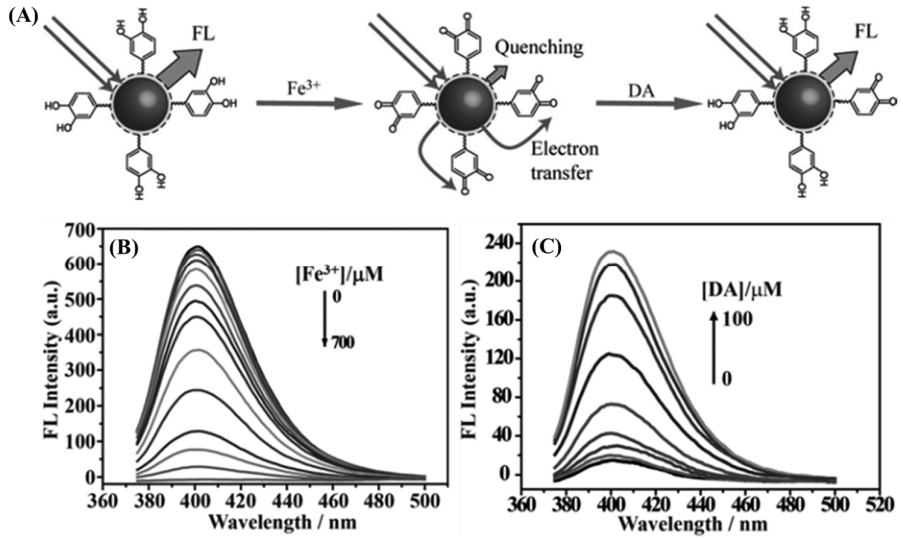

Figure 95: (A) Schematic representation of fluorescent C-dots for the detection of Fe^{3+} ions and dopamine (DA). (B) Representative fluorescence emission spectra of C-dots in the presence of increasing Fe^{3+} concentration (0–700 µM) in a HEPES buffer (10 mM) at pH 7.0. (C) Fluorescence emission spectra of C-dots containing Fe^{3+} (600 µM) with increase in DA concentration (0–100 µM) [736]**.**

Dong *et al.* designed branched poly(ethylenimine)-functionalized C-dots (BPEI-C-dots) as a fluorescence sensor for copper ion (Cu^{2+}) detection (**Figure 96**). On account of the inner filter effect, in that the excitation and emission wavelengths of the C-dots were absorbed by the cupric amine complex formed on the surface, a quenching phenomenon would happen. Under the optimum experimental conditions, the C-dots show a good sensitivity and selectivity towards Cu^{2+} and the limit of detection and linear response range were determined to be 6 nM and 10-1100 nM, respectively [704].

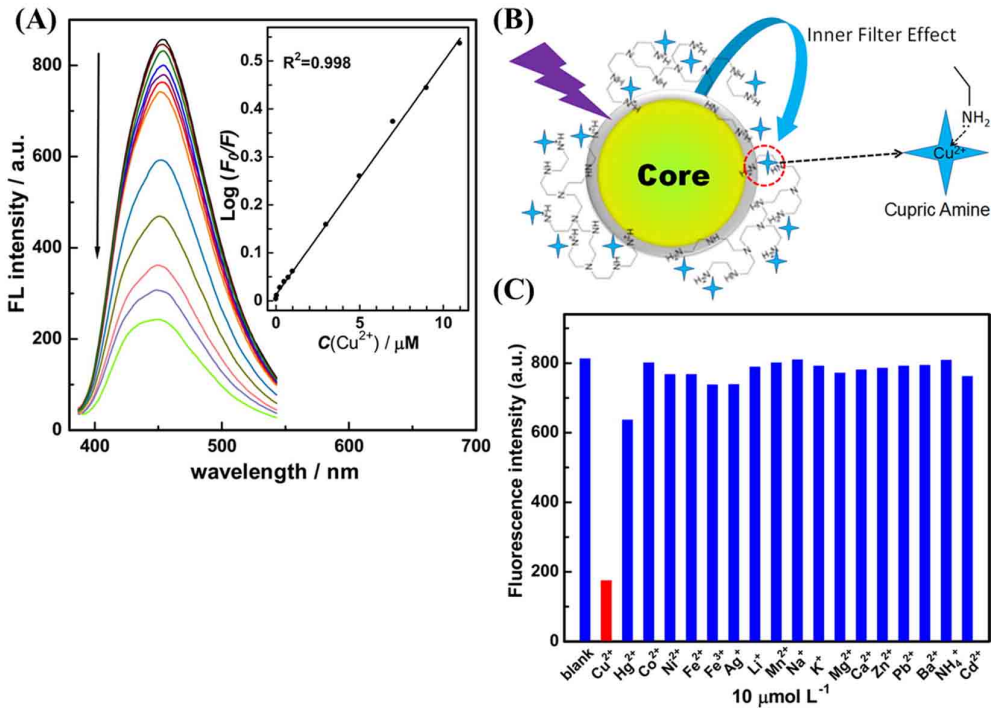

Figure 96: (A) Fluorescence response of BPEI–C-dots upon the addition of various concentrations of Cu^{2+} in a pH 4 PBS solution. Inset: Semilogarithmic plot of F_0/F of BPEI–C-dots vs. the concentration of Cu^{2+}. (B) Schematic illustration of the fluorescence of the BPEI–C-dots quenched by Cu^{2+}. (C) Selectivity of the BPEI–C-dots sensor for Cu^{2+} over other ions in a pH 4 PBS solution. The concentrations of C-dots and metal ions are 16.8 μg ml^{-1} and 10 μM, respectively [704].

More interestingly, a tunable ratiometric pH sensor was developed for the quantitative measurement of the intracellular pH of cells based on C-dots [737]. The amino-coated C-dots were functionalized with pH-sensitive fluorescein isothiocyanate (FITC) and pH-insensitive rhodamine B isothiocyanate (RBITC), resulting in the dual-emission probe upon a single excitation. The pH sensor exhibited low cytotoxicity, good cell-permeability, and an excellent reversibility between pH 5-9. Thus, real-time quantitative determination of intracellular pH of intact HeLa cells and the pH fluctuations associated with oxidative stress were successfully performed [737]. Zhu *et al.* developed a dual-emission nanohybrid system consisting of C-dots and CdSe/ZnS QDs for intracellular sensing and imaging of Cu^{2+} ions [738]. As shown in **Figure 97A**, prior to the addition of Cu^{2+}, the emission at 485 nm due to the presence of C-dots is more intense than that at 644 nm due to the presence of QDs, and thus a blue fluorescence is observed from the solution under excitation. After the addition of Cu^{2+}, the molecular receptors on the C-dots surface bind with Cu^{2+} ions specifically to quench the fluorescence of C-dots. Since the emission at 644 nm remained

constant, the decrease of the blue fluorescence results in an observable fluorescent color change to pink. Even though there is little change in the detection performance spectroscopically, the involvement of the second signal as reference does improve the sensing sensitivity visually (**Figure 97B**). As an extension of the fluorescent sensing platform, the same group immobilized the molecular receptor-functionalized C-dots on the electrode, developing a highly selective electrochemical strategy for the determination of Cu^{2+} ion in complex brain system with a detection limit of 100 nM [739].

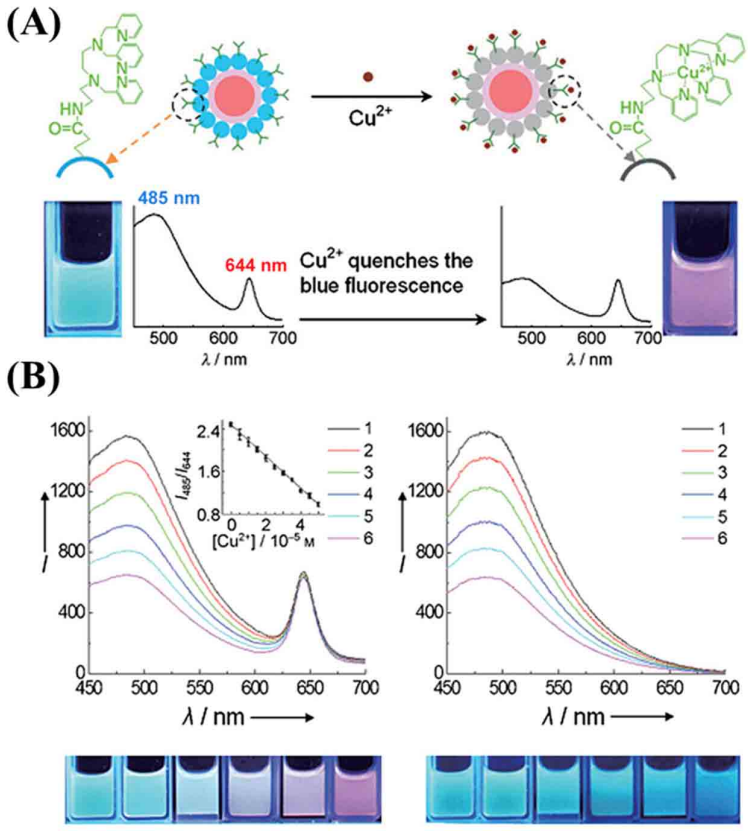

Figure 97: (A) Diagram for the dual-emission fluorescent sensing of Cu^{2+} ion based on a CdSe/ZnS-C-dots nanohybrid. (B) Comparison between fluorescent spectra and fluorescent colors of the nanohybrid probe and C-dots probe after exposure to $CuCl_2$. The concentrations of $CuCl_2$ from 1 to 6 for the spectra and from left to right for the colored solutions both correspond to 0, 10, 20, 30, 40, and 50 µM, respectively [738].

The π–π stacking interactions between C-dots and DNA (**Figure 98**) can also be used as binding strategy for detection of DNA [724]. The fluorescence from dye-labeled single-stranded DNA probe is quenched after adsorption onto the C-dots surface via π–π interaction. When the target DNA matches the dye-labeled DNA to form double-stranded DNA, the fluorescence is recovered. This strategy is also employed for determination of

metal ions such as Hg^{2+} and Ag^{+} through T-Hg^{2+}-T and C-Ag^{+}-C base pairs, respectively [731,732].

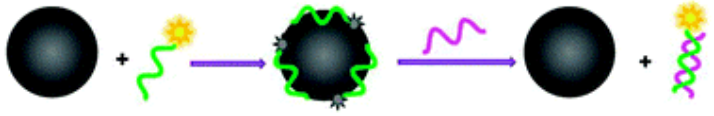

Figure 98: π–π stacking interaction between dye-labeled ss-DNA probe and the surface of the C-dots [724]**.**

Apart from utilizing the fluorescence of C-dots as an analytical signal, recent studies have revealed that C-dots exhibit good chemiluminescence (CL) [740] and electrochemiluminescence (ECL) [741]. For example, Wang *et al.* developed a paper-based DNA biosensor by using C-dots as CL signals and nanoporous gold (NPG) as a signal amplification agent. First, they constructed microfluidic paper-based analytical devices (μPADs) that were modified with *N,N′*-disuccinimidyl carbonate (DSC). Then, the capture DNA (S1) with thiol groups on its terminal was immobilized onto the μPADs. Furthermore, in the presence of target DNA (S2), the signal DNA (S3) could fix on the surface of μPADs through hybridization with S2. Finally, by injecting $KMnO_4$, the CL reaction was triggered and the concentration of target DNA S2 could be easily measured in the luminescence analyzer (**Figure 99**). The detection limit of the sensor was estimated to be 8.56×10^{-19} M with a linear range of 10^{-18}–10^{-14} M [740].

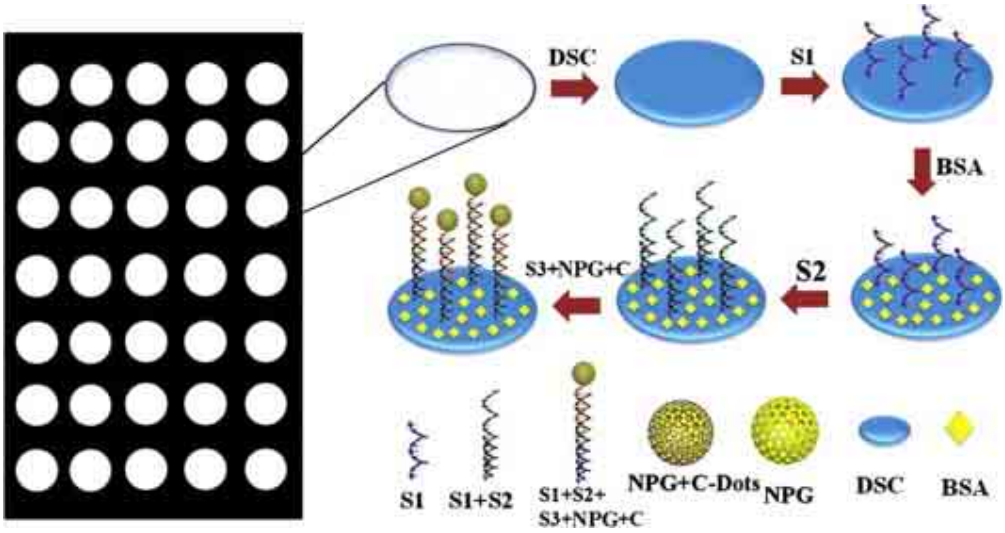

Figure 99: The C-dots-based CL sensor for the detection of DNA [740]**.**

Wu *et al.* constructed an assay for cancer cell detection by using modified C-dots as ECL sensors and graphene as signal amplification agents (**Figure 100**) [741]. The sensors was

developed as following: first, the electrode was modified with amino-functionalized graphene that had been covalently grafting poly(allyl amine hydrochloride) (PAH) on it. Then the C-dots@Ag composite was introduced onto the surface of the electrode. After linking cysteine, folic acid was further conjugated with cysteine to modify the electrode. Each modifying process played a unique and important role in the sensitivity/selectivity of the sensor: (1) The graphene conjugation could facilitate electron transfer due to its good conductivity and large surface area. (2) Folic acid could specifically target folate receptors with high affinity, which enabled them to act as a bridge between the electrode and cancer cells. (3) The metal shell on C-dots accelerated the electron transfer between C-dots@Ag and graphene. Due to the specificity and affinity of folic acid, the fabricated electrode could selectively recognize the surface of human cervical cancer cells (HeLa) and human breast cancer cells (MCF-7) by targeting folate receptor (FR). The presence of cancer cells caused remarkable decrease in the ECL signal which originated from blocking of the C-dots@Ag nanocomposite surface and preventing them from coming into contact with the ECL coreactant $N_2S_2O_8$. The detection limit was calculated to be 10 cells per mL at 3σ.

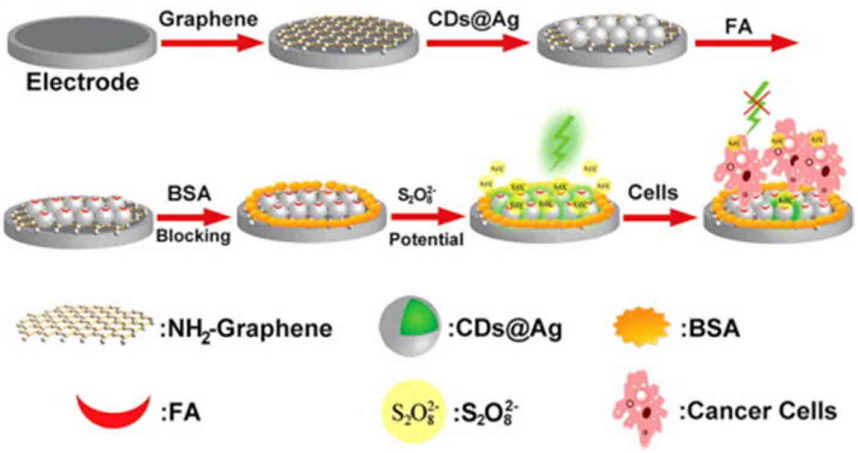

Figure 100: The C-dots-based ECL platform for detection of cancer cells [741]**.**

3.3.5.5. Drug delivery and Therapy

Drug delivery systems (DDSs) based on nanotechnology are increasingly developed in recent years. The most widely investigated DDSs are based on AuNPs, but the issue of toxicity limits their applications in clinical therapy [349]. AuNPs also require thiol groups for drug loading through Au-thiol interaction, which imposes a further limitation of drug choice [742]. In addition, AuNPs are difficult to track in *in vivo* systems because they cause

the quenching of fluorophores [743]. Therefore, C-dots serve as good alternatives to AuNPs since different functionalization could result in many possibilities for conjugation with drug molecules in combination with targeting agents, expanding the drug choices for delivery [742]. Tang *et al.* reported a Förster resonance energy transfer (FRET)-based C-dots drug delivery system that could perform real-time monitoring of drug release (**Figure 101**) [744]. They used the fluorescent drug molecule doxorubicin (DOX) as model to illustrate the system. The DOX adsorbed onto the surface of C-dots via π–π stacking. Then the FRET occurred between the C-dots and DOX, which resulted in a decrease of the FL of C-dots and increase of the FL of DOX. With the release of DOX from the surface of C-dots, the FRET between C-dots and DOX was weakened while the FL of C-dots increased, which could be used to monitor the release of DOX [744].

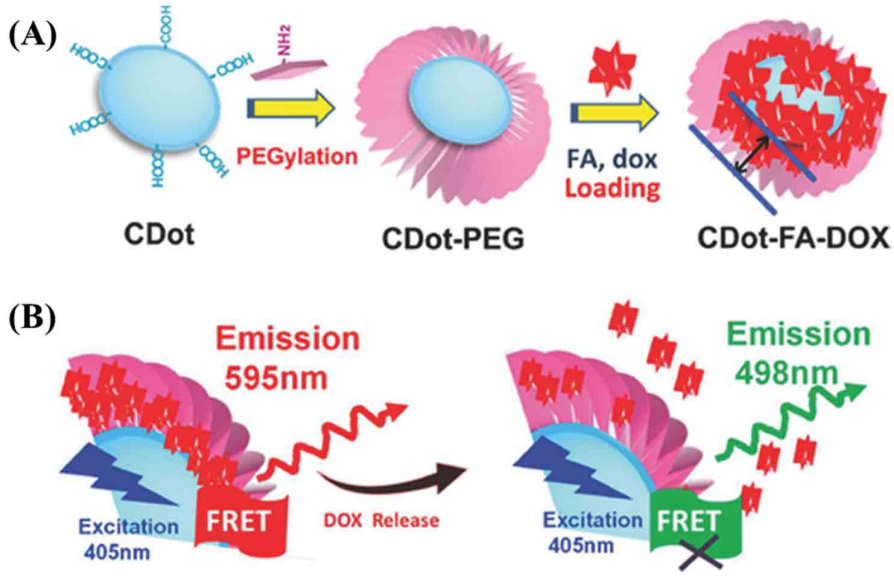

Figure 101: (a) The drug delivery system that could perform real-time monitoring of drug release based on PEG-functionalized C-dots. Doxorubicin (DOX) was used as a drug molecule, which was adsorbed onto the surface of C-dots through π–π stacking. (b) Proposed mechanism of real-time monitoring of DOX release based on the FRET process between DOX and C-dots [744]**.**

The obtained system showed excellent targeted delivery and drug release efficiency towards cancer cells at acidic pH environments. At pH 7.4, the fluorescence barely increases over the course of the 72 h, exhibiting a very low value of total release (<10% fluorescence intensity of the original C-dots-FA-DOX conjugates); this indicates a negligible DOX release at the neutral condition (**Figure 102**). A substantial increase of drug release rate is observed for acidic solutions, in which the release rate in pH 5.0 solution is higher than that

in pH 6.0 solution. In addition, compared with those of free DOX molecules, which complete release within ≈10 h, the release accumulation profiles for both pH 5.0 and 6.0 solutions show sustained release over a long period (>72 h). The percentages of accumulated release in the pH 5.0 solution are 55%, 72%, and 78% after 24, 48, and 72 h, respectively [744].

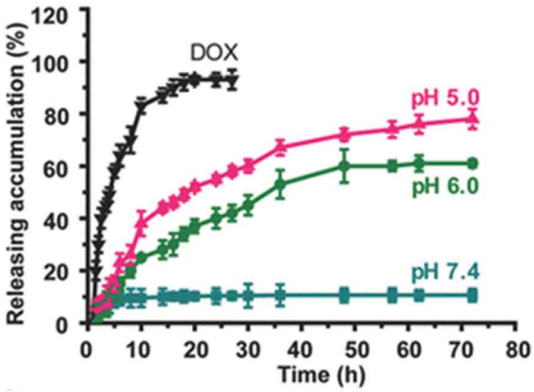

Figure 102: Time-dependent release profiles of DOX from C-dots-FA-DOX at different pH values: 7.4, 6.0, and 5.0. The release profile of free DOX molecules at a pH of 7.4 is also displayed for comparison [744]**.**

This enhanced drug release rate at low pHs is particularly advantageous for cancer treatment. The slow DOX release at neutral environments can minimize the extracellular loss of drug molecules before reaching the tumour targets, as well as potential damage to normal cells. However, most of the DOX can persistently be released when the drug delivery capsules are internalized by tumour cells at low pHs (4.5-6.0), leading to enhanced cancer therapy.

Recently, Zeng *et al.* developed a green-emitting C-dots with a carboxyl-rich surface which can be utilized as a trackable drug delivery agent for localized cancer treatment in a mouse model. The C-dots are conjugated with DOX, via non-covalent bonding, utilizing the native carboxyl groups on C-dots and the amine moiety on DOX molecules. The pH difference between cancer and normal cells was exploited as the triggering mechanism for DOX release. An *in vivo* study demonstrated that the fluorescent C-dots can serve as a targeted drug delivery system for localized therapy, and the stimuli-responsive non-covalent bonding between the C-dots and DOX molecule is sufficiently stable in complex biological systems (**Figure 103**) [491].

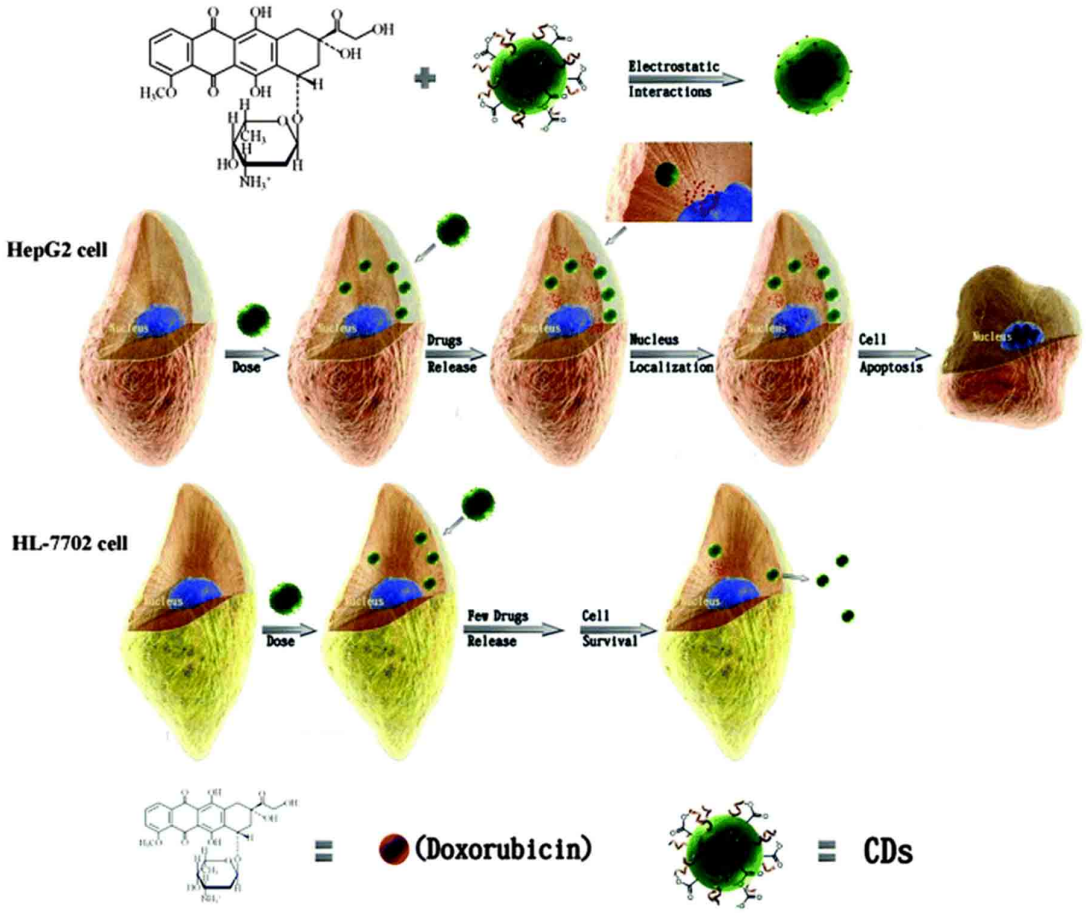

Figure 103: Schematic illustration of the design overview. (a) The amines (–NH_2) on DOX bind with the carboxylic acid (–COOH) on C-dots (CDs) via electrostatic interactions or hydrogen bonding. (b) Delivery of CD–DOX conjugates to HepG2 cancer cells and HL-7702 normal cells with strong green signal imaging tracking. The CD–DOX conjugates are expected to release DOX in HepG2 cancer cells, but not HL-7702 normal liver cells, due to low pH in cancer cells [491]**.**

Similarly, a theranostic nanomedicine (C-dots-Oxa) was synthesized by condensation reaction between the amino groups on the surface of fluorescent C-dots and the carboxyl group of the oxaliplatin derivative Oxa(IV)-COOH. The C-dots-Oxa were taken up by cancer cells through endocytosis and the drug was released upon the reduction of Oxa(IV)–COOH to oxaliplatin(II) because of the highly reducing environment in cancer cells. It was also demonstrated that the distribution of the C-dots-Oxa can be closely tracked by monitoring the fluorescence signal of the C-dots, thereby offering great help in the customization of the injection time and dosage of the medicine (**Figure 104**) [745].

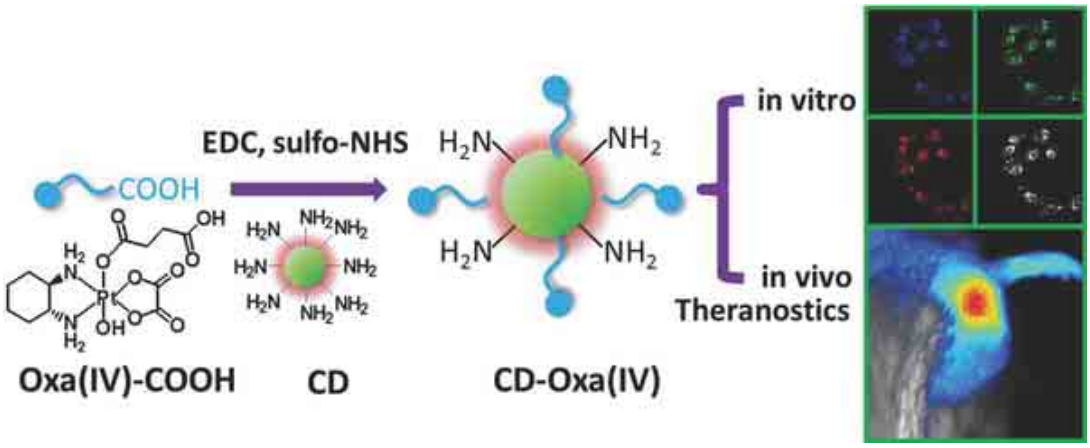

Figure 104: Synthetic scheme for C-dots-Oxa (CD-Oxa) and its applications in bioimaging and theranostics [745]**.**

In an attempt to enhance the loading capacity of C-dots, Mewada *et al.* tested the drug carrying and folic acid-mediated delivering capacities of highly fluorescent swarming C-dots. Folic acid on the C-dots surface was used as a navigational molecule thanks to its widespread association with most types of cancer cells. The drug loading capacity for an anti-cancer drug DOX was estimated to be 86% and the release of DOX from the DOX-loaded C-dots followed first order release kinetics at physiological pH – an ideal drug release profile. More interestingly, due to the better targeting ability of the folic acid molecule, the DOX-loaded C-dots showed a higher killing rate of cancer cells than free DOX and were less toxic to normal cells [746].

Based on the ability of C-dots to absorb NIR light, Wu *et al.* first conducted photoacoustic (PA) imaging of sentinel lymph nodes (SLN) *in vivo* by using C-dots passivated by macromolecules. Observable signal enhancement of the SLN was exceptionally rapid within 2 min after injection of the agent. This nanoprobe exhibited strong optical absorption in the NIR region, small size, and rapid lymphatic transport, offering valuable potential for faster resection of SLN and may lower complications caused by using dyes or low-resolution imaging techniques [747].

The C-dots can be used for photodynamic therapy (PDT). PDT is an approved therapeutic treatment for a number of cancers. In the presence of oxygen and light, photosensitizer (PS) can transfer the absorbed photon energy to surrounding oxygen molecules to form reactive oxygen species (ROS) such as singlet oxygen ($^1O_2$) and free radicals, resulting in cell death and tissue destruction. Huang *et al.* designed a PS-conjugated Cdots system featured by FRET for both enhanced fluorescence imaging and PDT therapy. Chlorin e6 (Ce6) was

selected as the PS, which emitted bright red fluorescence at 668 nm upon excitation at 430 nm due to the efficient FRET process with carbon dots. The feasibility of the system for fluorescence imaging-guided PDT was investigated in nude mice. After intravenous injection, the fluorescence from Ce6 became visible in tumour sites at 2-4 h post-injection and reached a plateau at 4-8 h post-injection, and thus the suitable time point to implement PDT was selected at 8 h (**Figure 105**) [748].

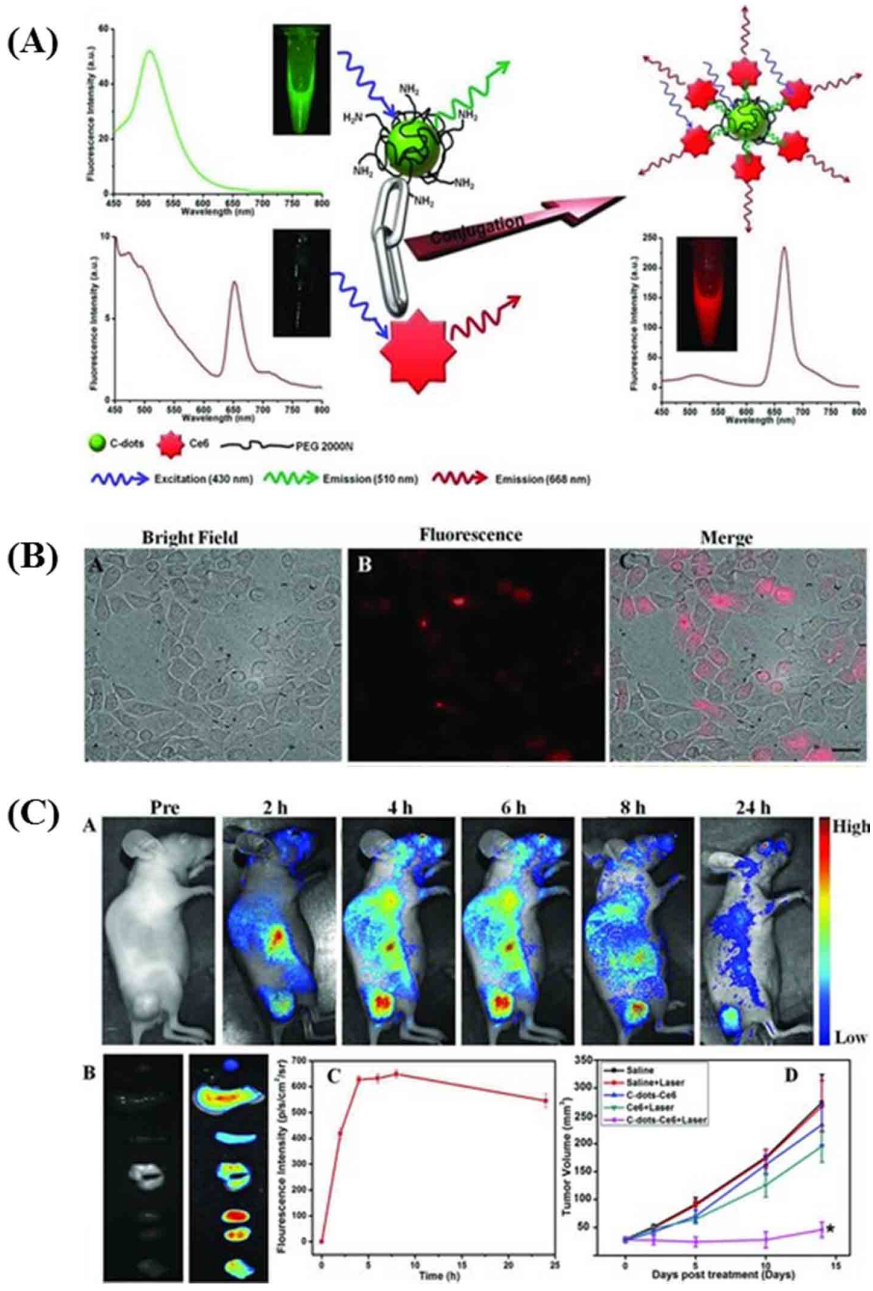

Figure 105: (A) Förster (fluorescence) resonance energy transfer (FRET) process between C-dots and Ce6. (B) (A-C) Subcellular localization of C-dots-Ce6, monitored by fluorescence

imaging. MGC803 cells were incubated with C-dots-Ce6 at a concentration of 10 μM for 2 h at 37 °C (scale bar is 25 μm). (C) A: Real-time *in vivo* NIR fluorescence images after intravenous injection of C-dots-Ce6 in nude mice at different time points; B: *ex vivo* images of mice tissues (from top to bottom: heart, liver, spleen, lung, kidneys, tumour); C: the average fluorescence intensities from the tumour area at 24 h post-injection (n = 5); D: MGC803 tumour growth curves after various treatments (n = 5). (*, P < 0.05 for other groups versus C-dots-Ce6 + laser group) [748]**.**

In addition to phototherapy, C-dots can be used for radiotherapy. Kleinauskas *et al.* developed a PEG-C-dots coated with a silver shell (C-Ag-PEG C-dots) which could be used as radiosensitizers in Du145 cells. When irradiated with low energy X-rays, electrons were ejected from the C-Ag-PEG C-dots, which in turn generates free radicals and damages the cancer cells surrounding the C-dots, reducing the damage of normal cells and increasing therapeutic selectivity [749].

Chapter 4:

Experimental Section

OBJECTIVES OF THE THESIS

The Aims of the thesis is to create a novel drug delivery system based on CNPs to ameliorate the antitumour effect of doxorubicin (doxo).

In the first part of the work, the attention has been focused on a simple and economic synthesis of CNPs from a green source, "black tea" by nitric acid (HNO_3) oxidation; and on the characterizations of the synthesized CNPs. The CNPs has been characterized by TEM to identify their sizes and morphology, by zeta potential to measure the charge, by FT-IR and XRD to determine the functional groups and the phase of CNPs, by XPS to identify the elemental composition of CNPs.

The optical properties were studied by UV-Vis absorption and fluorescence. As we have discussed and shown in the **chapter 3**, fluorescent CNPs were used for drug delivery and for the imaging of cells. Due to the increasing number of papers focused on exosome biology and the possibility of utilizing exosomes in liquid biopsies, the CNPs were tested for use as potential fluorescent probes. Exosomes are extracellular vesicles with a diameter range of 30-200 nm and diagnostic and therapeutic potential. Exosomes were incubated with CNPs, collected and verified by NTA analysis.

The second part of the thesis was to study *in vitro* the toxicity of the CNPs synthesized on HeLa, MDA-MB-231, LoVo and DLD-1 cancer cell lines. After that, CNPs were loaded with doxorubicin (doxo) and study the kinetics of drug release under neutral and acidic pH to demonstrate the ability of creation of a drug delivery system, which exhibit controlled release under acidic conditions, as in the tumour microenvironment. In this part, the cytotoxicity of CNPs on MDA-MB-231, LoVo and DLD-1 cancer cell lines treated with Cdoxo were also tested.

The third part of the thesis was to study *in vivo* the toxicity on a mouse model of breast cancer and study the biodistribution and the pharmacokinetics of Cdoxo.

4. EXPERIMENTAL SECTION

4.1. Materials and Instrumentations

4.1.1. Reagents

Commercially available Brooke Bond Taaza tea was utilized. HNO_3 (70%) and sodium hydroxide (NaOH) were purchased from Sigma Aldrich (St. Louis, Missouri, US), doxorubicin (doxo) was obtained from Accord Healthcare Ltd. (Durham, NC, US) and daunorubicin was purchased from Teva Pharmaceutical Industries Ltd. (Petah Tikva, Israel).

All reagents were used as received without further purification. Minisart® syringe filters with a pore size of 0.2 μm were from Sartorius Stedim Biotech (Concord, CA, US), and a dialysis membrane (MWCO 0.5-1 kDa) was purchased from Spectrum Laboratories (Rancho Dominguez, CA, US) for CNP purification. LysoTracker® deep red probe was purchased from Life Technologies (Carlsbad, CA, US). Exosomes were prepared from exosome-depleted medium conditioned for 48 hours and purified with an AB cell culture-nanovesicle solution according to the instructions (AB ANALITICA, Padova, Italy).

DLD-1 and LoVo (colon) and MDA-MB-231 (breast) and HeLa (cervical) cancer cells were grown as indicated by the supplier (ATCC, Manassas, VA, US). Nude and FVB mice were purchased from Harlan Laboratories (Udine, Italy); the procedures were approved by the Italian Ministry of Health n°788/2015-PR and performed in accordance with the institutional guidelines. Data are reported as the mean and standard error.

4.1.2. Equipments

Water was obtained from a Milli-Q water purification system (18.2 Ω; EMD Millipore, Billerica, MA, US). UV-Vis absorption spectra were collected using a NanoDrop 2000c (Thermo Fischer Scientific, Waltham, MA, US). Fluorescence spectra were collected on an Infinite M1000 PRO and cell viability analyzed using an Infinite 200 PRO (Tecan, Männedorf, Switzerland). X-ray diffraction (XRD) data were collected on a Philips X'Pert vertical goniometer with Bragg-Brentano geometry. Transmission electron microscopy (TEM) was carried out using a Philips EM 208 microscope (Philips, Amsterdam, Netherlands). Fourier transform infrared (FT-IR) spectra were obtained on a NEXUS FT-IR spectrometer implementing a Nicolet Avatar diffuse reflectance accessory. X-ray photoelectron spectroscopy (XPS) was performed on a PHI Quantera SXM spectrometer using monochromatic Al-Kα X-ray sources at 1486.6 eV and 24.8 W with a beam diameter of 100.0 μm, a 1.2 V and 20.0 μA neutralizer, and FAT analyzer mode. Zeta potential (ζ) measurements were collected on a Zetasizer ZS90 (Malvern Instruments, Malvern, UK) using a 632 nm He-Ne laser as the light source. Fluorescence microscopy was carried out using a Nikon microscope at 20x and 40x magnification (Nikon, Chiyoda, Tokyo, Japan). The PK and biodistribution were evaluated by liquid chromatography-tandem mass spectrometry (LC-MS/MS) on a 4000 QTRAP MS/MS system equipped with a Turbo ESI source (AB Sciex, MA, USA). The exosome particle size was determined with an L10 NanoSight instrument (Malvern Instruments Ltd, UK).

4.2. Synthesis of CNPs

CNPs were synthesized from tea in the following steps: (1) carbonization of commercial tea followed by (2) oxidation with HNO_3. The carbonized carbon was prepared by heating the commercial black tea at 200 °C for approximately 3 hours, followed by evaporation of water and heating again at 200 °C for approximately 5 hours. The so-formed carbonized tea powder was cooled to room temperature, dried on rotary evaporator and stored in a glass bottle. Then, 500 mg of the carbonized carbon was dispersed in HNO_3 (0.065 mol, 5 M, 13 ml) and refluxed at 80 °C for 20 hours under vigorous stirring. Then, the orange solution was cooled to room temperature and centrifuged (4300g, 25 min, room temperature) to separate out any unreacted carbon. The orange supernatant was collected, neutralized by 5 M NaOH and filtered through a 0.2 μm Minisart® syringe. To remove salts and impurities, the raw solution was dialyzed against Milli-Q water using a dialysis membrane (MWCO 0.5-1 kDa) for at least 2 days. Finally, the obtained golden-yellow solution was dried on a rotary evaporator and used for further characterization (yield: 26%).

4.3. Fluorescence imaging

A droplet of an aqueous CNPs dispersion (25 mg/ml) was imaged on a Nikon fluorescence microscope under different filter sets (nm), Ex 350/Em 460 (blue), Ex 490/Em 520 (green), Ex 550/Em 570 (red) and Ex 630/Em 670 (violet), at 20x magnification.

4.4. CNPs cellular localization

The CNPs cellular internalization was evaluated by plating HeLa cells at a density of 7.5 x 10^4 cells/slide. The next day, the cells were marked with 50 nM LysoTracker® deep red probe (Thermo Fisher, MA, US) for 2 h at 37 ºC. After incubation, the cells were washed twice with 1X PBS and incubated for 24 h with 2 mg/ml CNPs. After incubation, the cells were washed twice with 1X PBS and fixed with 4% PFA for 10 min, and the slides were mounted with Alexa FluorSave solution (Thermo Fisher Scientific, Waltham MA, US). The images were obtained on a Nikon fluorescence microscope at 40x magnification using Ex 630/Em 670 nm filters for the lysosomes and Ex 350/Em 460 nm filters for the CNPs.

4.5. Imaging of CNPs-loaded exosomes

To load exosomes with CNPs, HeLa cells were grown until 70% confluence, treated with 2 mg/mL CNPs for 2 h, washed and then incubated in exosome-free medium for 24 h. The

medium was collected, and the exosomes were extracted using an AB cell culture-nanovesicle solution. The next day, the medium was centrifuged at 103,000g and 4 °C for 80 min, and the pellet was resuspended in 1X PBS. The exosomes were characterized by NTA analysis (nanoparticle tracking analysis, Malvern, UK). For imaging, the exosomes loaded with CNPs were spotted on a slide and analyzed with a Nikon fluorescence microscope at 40x magnification under different filter sets (nm): Ex 350/Em 460 (blue), Ex 490/Em 520 (green), Ex 550/Em 570 (red) and Ex 630/Em 670 (violet).

4.6. Doxorubicin loading efficiency and release

CNPs (0.5 mg/ml) were incubated with doxo (0.25 mg/mL) in 1X PBS for 2 h at room temperature. The unbound doxo was eliminated by centrifugation at 13000g for 10 min and washed twice with 1X PBS. The drug loading capacity for doxo was calculated as follows: (weight of loaded doxo)/(weight of CNPs). The weight of free doxo was measured on a UV-Vis spectrophotometer from the absorbance at 450 nm based on a doxo standard curve, and the weight of CNPs was measured from the absorbance at 289 nm based on a CNPs standard curve. The release of doxo and Cdoxo (50 μg/500 μL) was evaluated using a dialysis membrane (15,000 MWCO) dipped into 1 L of 1X PBS at pH 7.4 or pH 5.5.

4.7. Toxicity, cytotoxicity and apoptosis tests

The toxicity of the CNPs was tested in HeLa, MDA-MB-231, LoVo and DLD-1 cancer cell lines. The cytotoxicity of the free doxo, CNPs and Cdoxo was tested in MDA-MB-231, LoVo and DLD-1 cancer cell lines. Toxicity and cytotoxicity were evaluated by the CellTiter-Glo® luminescence assay (Promega, Madison, Wisconsin, US) using an Infinite 200 PRO instrument (Tecan, Switzerland). Cells were seeded in 96-well plates (Falcon BD, San Jose, CA, US) at a density of 10^3 cells/well and incubated for 24 h to allow for cell attachment. The cells were incubated with doxo, CNPs, and Cdoxo at the same drug concentrations for 96 h. The experiments were performed in triplicate. Apoptosis was evaluated after 24 hours by fluorescence-activated cell sorting (FACS; BD Biosciences, San Jose, CA, US) utilizing the PE Annexin V Apoptosis Detection Kit I (BD Biosciences, San Jose, CA, US).

4.8. *In vivo* CNPs toxicity and efficacy

This experiment was carried out using 8 weeks old female nude mice, which were administered by i.v. (intravenous) injection of 4 concentrations of CNPs diluted in PBS 1X

(5, 10, 20 and 40 mg/kg). The body weights of the mice were monitored for more than 45 days.

To evaluate the anti-tumour efficacy of Cdoxo compared to doxo, 3 x 10^6 MDA-MB-231 cells diluted in DMEM w/o phenol red/30% matrigel HC (Corning, New York, US) were inoculated in the mammary fat pad of nude mice.

Histopathology: The organs of the mice were collected and fixed in 10% formalin buffered with PBS, embedded in paraffin, sectioned at a thickness of 3 µm and stained with hematoxylin and eosin (H&E). The tissues were analyzed with light microscopy using different magnifications.

4.9. Pharmacokinetics (PK) and biodistribution

The PK experiments were performed in 8 weeks old FVB mice treated with 3 mg/kg (i.v.) of the drug diluted in PBS 1X, and approximately 100 µl of blood was collected after 0.5, 1, 3, 6, 24, 48, 96 and 192 hours. Blood was collected from each mouse twice: from the mandibular vein (live mouse) and the right ventricle of the heart (sacrificed mouse). A total of 12 mice were utilized. Serum samples were stored at -80 °C. For analysis of the drug tissue distribution, the mice were sacrificed at 3 and 24 hours, and their organs were washed with 10 ml of cold PBS/heparin before collection. The organs were diluted in 500 µl of 4% PBS/BSA and homogenized with a Qiagen TissueRuptor for 20 sec at power 4 in ice (Qiagen, Hilden, Germany).

The doxo concentrations in serum and tissues were measured by LC-MS/MS. The proteins were precipitated with 2 volumes of cold acetonitrile containing 20 ng/ml daunorubicin as an internal standard. After vortexing and spinning at 13000 rpm for 15 min at 4 °C, the cleared supernatant was diluted with 2 volumes of 0.2% formic acid, and 10 µl of the dilution were injected into the LC-MS/MS system. Chromatographic separation was performed on an Accucore 150-C18 column (2.6 µm, 30x2.1 mm; Thermo Scientific, Waltham, MA USA) equilibrated with 0.2% formic acid/acetonitrile (95:5) at 0.7 ml/min and maintained at 50 °C. An elution gradient B from 5% to 80% acetonitrile was applied over 5 min. A 4000 QTRAP MS/MS system equipped with a Turbo ESI source (AB Sciex, Framingham, MA, USA) was equilibrated for 3 min in positive-ion mode. The transitions of doxo and daunorubicin were monitored in multiple reaction monitoring mode at m/z 544.1→397.2 and 528.2→321.1, respectively. The spray voltage was set at 5000 V, with a source

temperature of 400 °C. The curtain gas, nebulizer gas (gas1) and auxiliary gas (gas 2) were set at 20, 50 and 50 arbitrary units, respectively. The declustering potential and collision energy voltages were set at 45 V and 16 V, respectively, for both doxo and daunorubicin.

Chapter 5:

Results and Discussions

5. RESULTS AND DISCUSSIONS

5.1. Characterization of CNPs prepared from black tea

The CNPs were prepared from tea by HNO_3 oxidation and characterized by UV-Vis absorption spectroscopy, fluorescence spectroscopy, powder XRD, FT-IR spectroscopy and TEM. The zeta potential of the CNPs was also measured at -16.6 mV, indicating a negative charge on the CNP surface due to the presence of carboxylic groups.

Figure 106 shows the UV-Vis absorption and fluorescence spectra of CNPs excited at 360 nm. The UV-Vis absorption spectrum contained two distinct peaks: one at 300 nm that could be assigned to the n-π* transition of the C=O groups on the surface of the CNPs and one at 242 nm that could be assigned to π-π* transitions of the polycyclic aromatic systems (C=C) contained in the polyphenols of the tea [750]. The CNP solution produced a maximum emission peak centered at 470 nm when excited at 360 nm (**Figure 106A**). To investigate the optical properties of the CNPs, emission spectra were recorded at various excitation wavelengths from 300 to 570 nm; the emission peaks were red-shifted from 390 to 570 nm while the intensities decreased (**Figure 106B and C**). These optical properties mainly result from the different sizes and different distributions of emissive sites, which is generally a characteristic of fluorescent carbon nanomaterials [493]. The fluorescence properties of CNPs are always dependent on the size and the presence of organic functional groups in the carbon source [751].

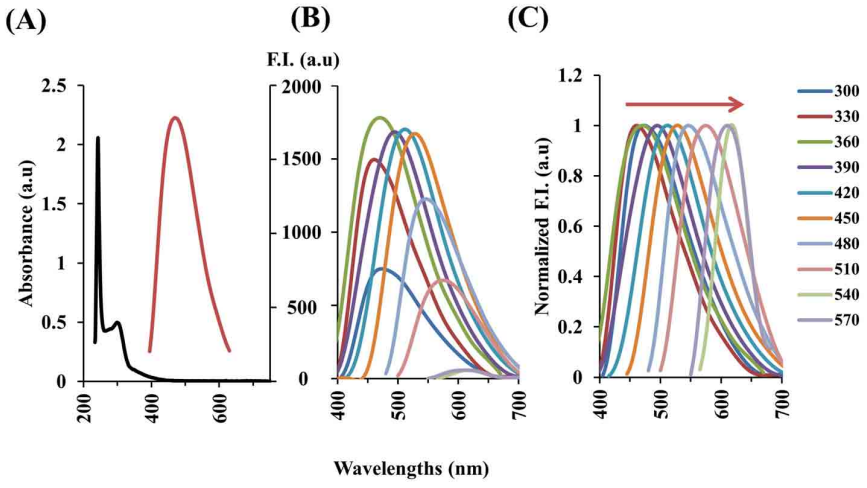

Figure 106: (A) UV-VIS absorption spectrum (Black line) and fluorescence spectrum of CNPs excited at 360 nm (Red line). (B) Fluorescence emission spectra and (C) normalized spectra of CNPs obtained at different excitation wavelengths progressively increasing from 300 nm to 570 nm with 30 nm increments. F.I. fluorescence Intensity; a.u Arbitrary Units.

We applied XRD and FT-IR analyses to identify the functional groups and the phase of the CNPs. The powder XRD spectrum (**Figure 107**) contained a broader peak at 2θ = 24.8°, revealing an amorphous carbon phase in the CNPs.

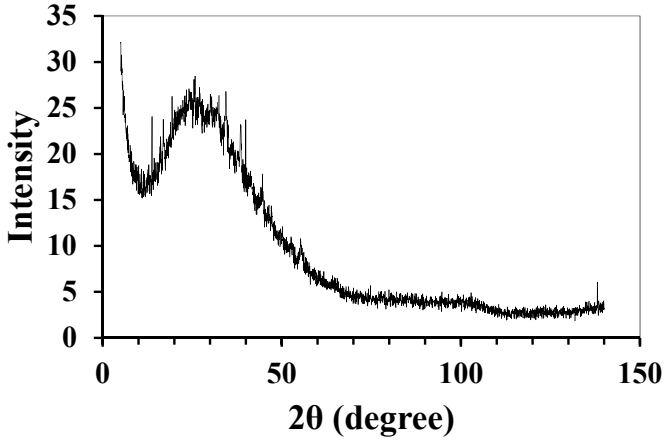

Figure 107: Powder XRD of CNPs (X axis = 2 theta (2θ) Bragg angle (°); Y axis = Intensity (arbitrary units)).

The FT-IR spectrum (**Figure 108**) indicated that the CNPs have many oxygen- and nitrogen-containing functional groups on their surface. The broad peak centered at 3294 cm^{-1} revealed O-H/N-H bonding, and the absorptions at 2937 and 2866 cm^{-1} could be attributed to C-H stretching vibrations. Moreover, the absorption peaks at 1652 and 1752 cm^{-1} are indicative of C=O bonds. The absorptions at 1110 and 1195 cm^{-1} could be attributed to C-O-C bonds, and the absorptions at 1318 and 1337 cm^{-1} confirm the presence of C-O bonds. Furthermore, the absorption peaks at 1594 cm^{-1} could be attributed to the C=N and C=C groups of aromatic hydrocarbons, indicating the presence of sp^2 hybridization, whereas the absorption peaks at 1406 and 1431 cm^{-1} could be related to C-N bonds. These data suggest that the CNPs were functionalized with hydroxyl, alkyl, carbonyl, carboxylic, and amine groups derived from the organic molecules in the black tea and the use of HNO_3.

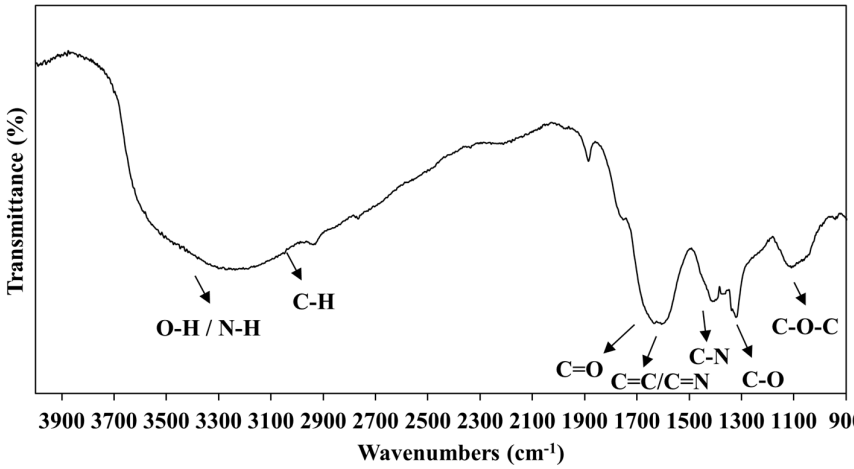

Figure 108: FT-IR spectrum of CNPs.

XPS analysis was used to confirm the functional groups on the CNPs surface. From the XPS spectrum (**Figure 109**), C, N and O were detected from the peaks at 285 eV (C1s), 400.2 eV (N1s), and 532 eV (O1s), respectively, with 62.56% carbon, 31.43% oxygen, and 6.01% nitrogen. The C1s peaks at 283.5, 284, 285.3, and 287.2 eV could be assigned to carbon in the form of C-H, sp^2 (C=C), C-O/C-N and C=O/C=N, respectively [752–754]. The N1s peaks consisted of three Gaussian peaks centered at 399, 408.8 and 405 eV, corresponding to C=N-C, C-NH-C, and oxidized N-species such as N-O/N=O, respectively [753,754]. The O1s peaks could be deconvoluted into three Gaussian peaks centered at 530.4, 532.2 and 534.7 eV, corresponding to C-O/N-O, C=O/N=O, and COO^-, respectively [754]. The surface components of the CNPs are in agreement with the FTIR results. It is well known that HNO_3 oxidation produces hydroxyl and carboxylic groups on CNP surfaces, which makes the particles water soluble and negatively charged. In addition, this oxidation can also induce nitration [755].

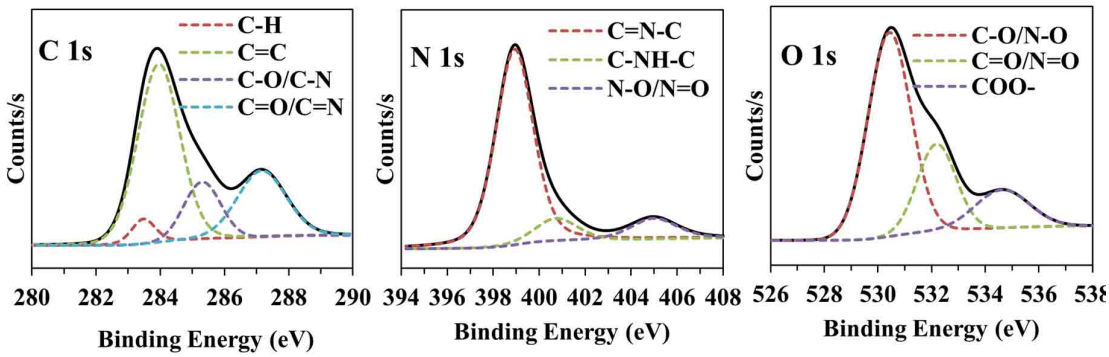

Figure 109: C1s, N1s, and O1s XPS spectra of CNPs.

Our experimental data suggest that refluxing the carbonized carbon derived from tea with HNO_3 induces partial oxidation of the carbons; introduces functional groups, such as OH, COOH, and NO_2; and causes nitrogen doping into the CNPs. The introduction of functional groups imparts water solubility and a surface charge to the CNPs. This oxidation step could also be considered a chemical route to incorporating nitrogen into the CNPs, as observed from the chemical composition analysis.

The morphology and size of the CNPs were investigated by TEM. As shown in **Figure 110**, the CNPs had a narrow size distribution and were spherical with an average diameter of 17 nm.

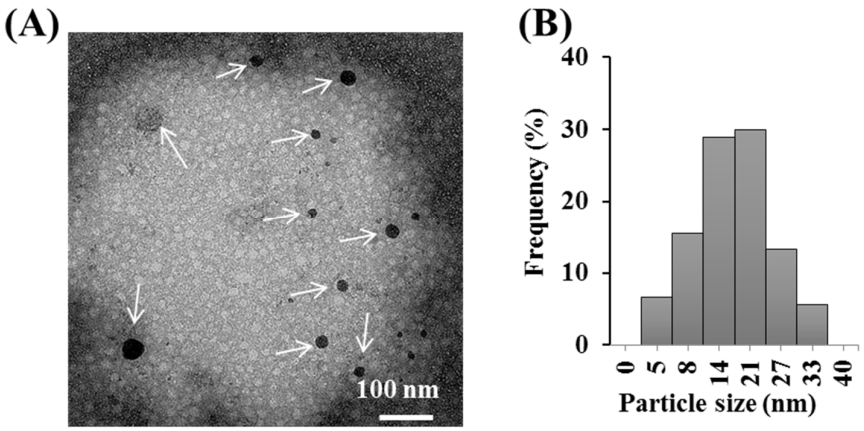

Figure 110: (A) TEM image and (B) particle size distribution histogram of CNPs (17.3 ± 7.6 nm). Arrows indicate CNPs.

5.2. CNPs were biocompatible and suitable for bioimaging of cellular and subcellular (exosomes) compartments

The CNPs were reported to be not toxic in different experimental set-ups [31,616]. *In vitro* experiments showed that CNPs do not alter cell viability at concentrations up to 200 μg/ml [682]. A toxicity test was performed with HeLa, MDA-MB-231, LoVo and DLD-1 cells. Our CNPs were not toxic at up to 1 mg/ml, illustrating very high biocompatibility (**Figure 111**), and sustained further testing in *in vivo* experiments.

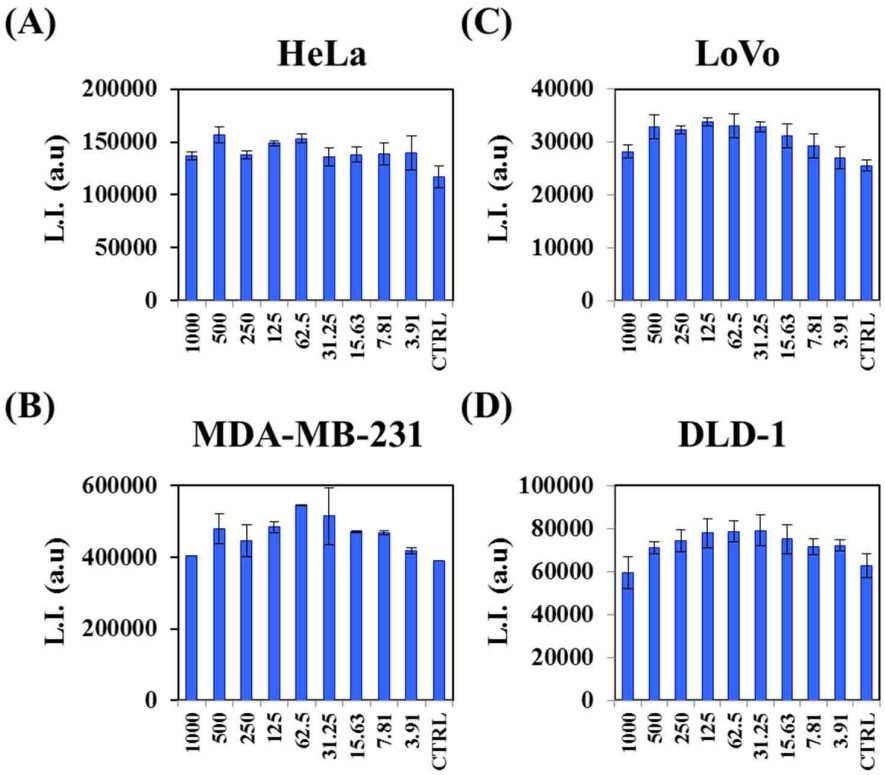

Figure 111: Toxicity of CNPs on (A) HeLa, (B) MDA-MB-231, (C) LoVo and (D) DLD1 cell lines. Cells were treated with increasing the concentration of CNPs as indicated on the X axis (µg/ml). L.I.: luminescence intensity. a.u.: Arbitrary Units.

To strengthen these results, an apoptosis test was performed and the results are presented in **Figure 112**. Cells were treated with 1 mg/ml CNPs, and the expression of Annexin V on the surface of the cells was measured by FACS after 24 hours. No change in the percentage of apoptotic cells was observed in the CNPs-treated cells over the control.

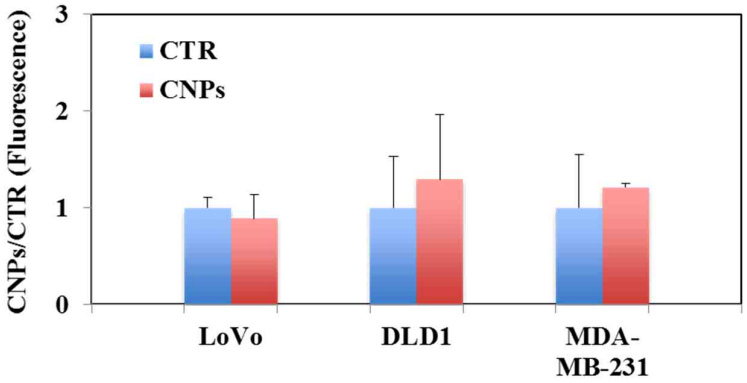

Figure 112: Annexin V assay. Cells were treated with 1 mg/ml of CNPs and marked with annexin V antibody.

Although the CNPs were designed and synthetized for drug delivery applications. A droplet of CNPs (25 mg/ml) was deposited on a cover slip under a fluorescent microscope and imaged under different excitation wavelengths commonly utilized for biological experiments. Fluorescence of the CNPs was detected in all the ranges utilized (**Figure 113**). For biological applications, a wavelength range over 600 nm is more suitable (**Figure 113D**) and does not overlap with the fluorescence of doxo, which has a maximal excitation/emission of approximately 490/590 nm.

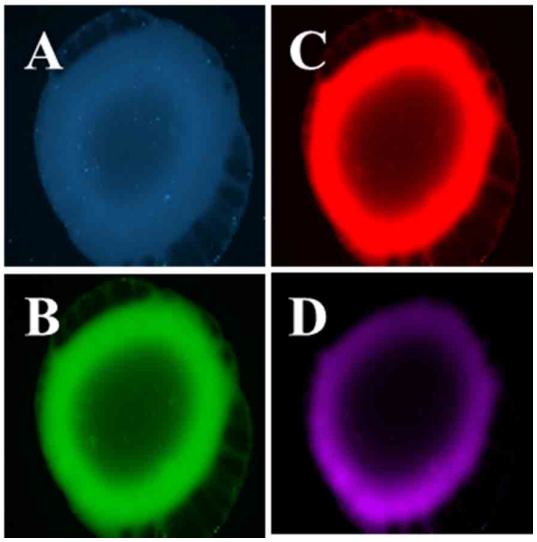

Figure 113: (A-D) Fluorescence microscopy photographs of an aqueous solution of CNPs under different excitation filter sets: (A) 350 nm, (B) 490 nm, (C) 550 nm and (D) 630 nm.

Due to the increasing number of papers focused on exosome biology and the possibility of utilizing exosomes in liquid biopsies, the CNPs were tested for use as potential fluorescent probes. Exosomes are extracellular vesicles with nanometric dimensions (30-200 nm) and diagnostic [756] and therapeutic potential [757]. Exosomes incubated with CNPs were collected after 24 hours and verified by NTA analysis (**Figure 114**).

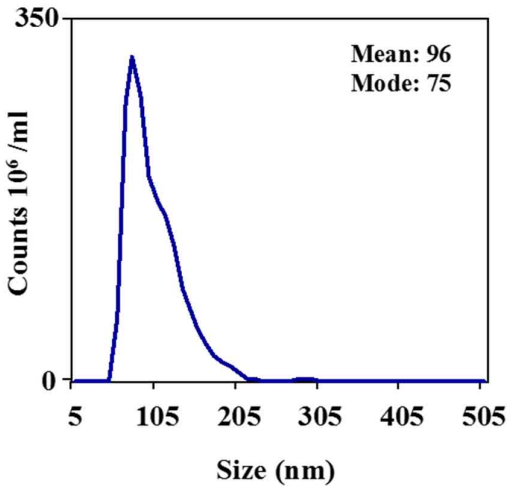

Figure 114: NTA of exosomes extracted from MDA-MB-231 cell culture medium.

Equal quantities of exosomes were evaluated under fluorescence microscopy from CNPs-treated and untreated cells. A clearly noticeable dotted appearance of CNPs-loaded exosomes can be observed in **Figure 115**, suggesting that these CNPs can be utilized to probe exosomes for biological applications.

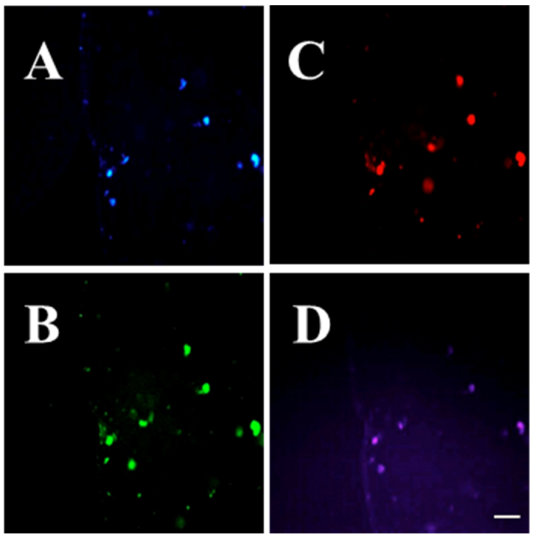

Figure 115: Exosomes isolated from the cell culture medium of MDA-MB-231 cells treated with CNPs (2 mg/ml) for 2 h and collected after 48 h. Images were acquired with different excitation filter sets: (A) 350 nm, (B) 490 nm, (C) 550 nm and (D) 630 nm. Scale bar: 20 µm.

5.3. CNPs avoided lysosomal entrapment and delivered doxo efficiently in *in vitro* experiments

Lysosomal degradation is a natural process by which cells eliminate unnecessary endogenous and exogenous materials [758]. The failure of many nanomaterials is due to their accumulation inside lysosomes [759]. Escaping lysosomal degradation is a desirable functional property for drug delivery applications. Under this scope, HeLa cells were probed with LysoTracker for 2 hours and incubated with 2 mg/ml CNPs for 24 hours. Under fluorescence microscopy, the CNPs (green) had a clearly uniform distribution in the cytoplasm and nucleus, and the typically punctuated appearance of lysosomal accumulation (red) was not apparently observed (**Figure 116**).

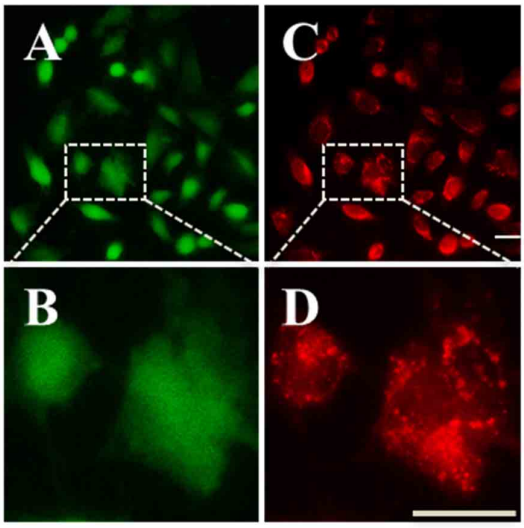

Figure 116: HeLa cells (A) treated with 2 mg/ml CNPs after 24 h and marked with (C) LysoTracker. (B) and (D) Zoom-in of (A) and (C). Scale bar: 20 µm.

A desirable property of nanomaterials is an intrinsic ability for loading therapeutic drugs and a controlled release over time under physiological conditions [760,761]. To demonstrate this concept, the CNPs were loaded with doxo, and the kinetics of drug release was calculated from a dialysis experiment in PBS at 37 °C at different pH values. For drug loading, the CNPs were mixed with doxo at room temperature, and the drug loading was calculated to be approximately 60% (**Figure 117**).

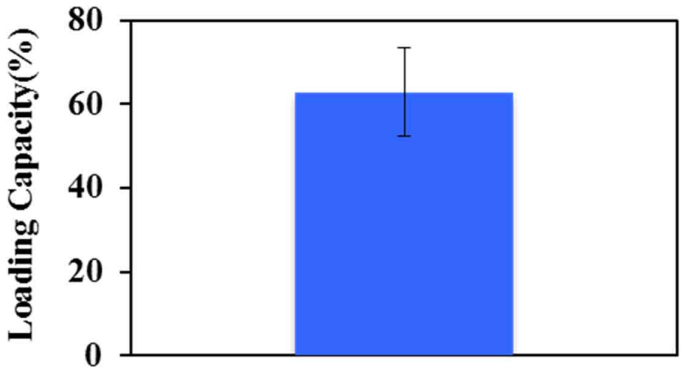

Figure 117: Loading capacity of Cdoxo. The graph displays the percentage of doxo loading (y-axis).

Doxo is a weak amphipathic base with pKa= 8.3. At physiological pH (7.4), the protonated fraction of doxo is still 10-fold that of the free base, while the carboxylic acid moieties on the CNPs surface are nearly completely dissociated to their negative carboxylate form (pKa range: 3-5) [762,763]. Thus, the doxo molecules retain their electrostatic interactions with the CNPs at physiological pH. At pH 4, the carboxylic acid groups on the CNPs are partially dissociated, decreasing the negative charge on the CNPs and reducing the electrostatic interactions of the drug carrier with protonated doxo. To support our conclusion, CNPs were loaded with doxo at different pH levels: 4, 5.5 and 7.4 (**Figure 118**). The percentage of loading positively correlated with the pH.

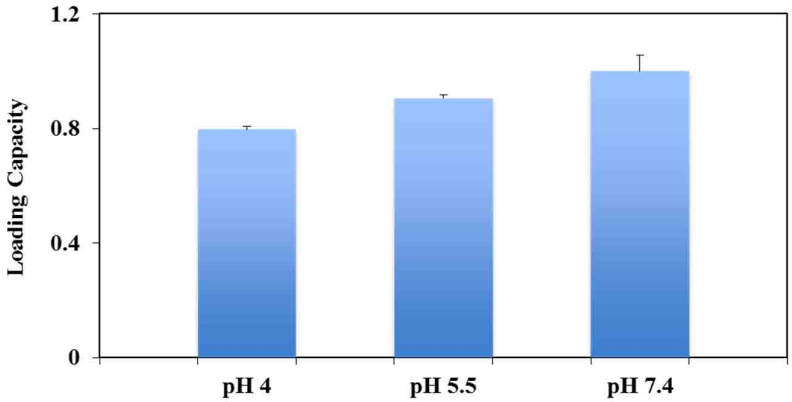

Figure 118: Loading capacity of CNPs at different pH (4, 5.5 and 7.4).

The extracellular pH (pHe) of tumour tissues is acidified by the metabolism of tumour cells [764]. Cell survival is conditioned by maintenance of a favorable acid-base balance (pH). Because of cellular metabolism, which produces CO_2 and lactic acid, cancer cells are continuously exposed to large acid-base fluxes, which would disturb the pH. In contrast to

normal cells, most tumour cells preferentially convert glucose and other substrates to lactic acid, even under aerobic conditions. This phenomenon, termed “the Warburg effect”, was reported by Warburg and co-workers in the 1920s [765–767]. Due to increased glucose metabolism, tumours possess a greater capacity to pump lactic acid and protons out to the extracellular spaces to maintain an appropriate neutral-alkaline intracellular pH (pHi), which is essential for cell vitality. The inefficient removal of protons and lactic acid from extracellular spaces creates a reversed gradient characterized by an acidic pHe and alkaline pHi [768–770]. *In vitro* and *in vivo* studies revealed that tumour cells have a pHi ranging from 7.1 to 7.6 (pHi of normal cells: 7.0 to 7.2) and a pHe of 6.2-6.9 (pHe of normal extracellular space: 7.3-7.4) [771]. The intravesicular pH along the endocytic pathway ranges from pH 6.0–6.5 in early endosomes to pH 4.5–5.5 in late endosomes and lysosomes [772].

A drug delivery system that is able to release its cargo more efficiently around the tumour site at low pH (approximately pH 6) represents an intelligent system to specifically target tumour cells [773]. To study the capacity and release of Cdoxo over different pH gradients, we carried out a release experiment at pH 5.5 and 7.4 to mimic the bloodstream, tumour microenvironments and intracellular endosome/lysosome pathway (**Figure 119**) [499,774]. The release of doxo was derived from a log-log plot of the cumulative release versus time. Noticeably, the CNPs maintained a stable interaction with doxo at alkaline pH (pH of the bloodstream) with a slow release profile (approximately 15 hours), compared to a fast release profile (approximately 1 hour) when the medium was acidified to levels of the extracellular space of the tumour and in subcellular compartments. This pH gradient increases the ratio of the tumoural/non-tumoural drug concentration, thereby elevating the therapeutic index of doxo.

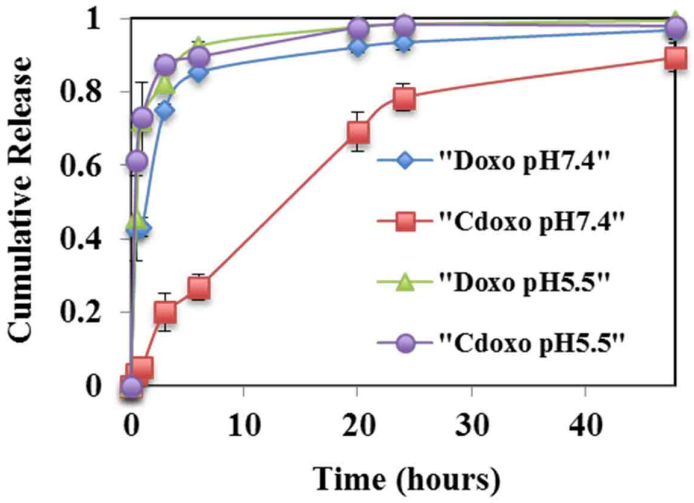

Figure 119: Release of doxo from CNPs. The cumulative release of doxo was evaluated by measuring the fluorescence of doxo, which resides inside the dialysis membrane at each time point at pH 5.5 and 7.4.

Subsequently, the cell viability of MDA-MB-231, LoVo and DLD-1 cells treated with Cdoxo was tested. Cells were treated with 3 different concentrations of free doxo or Cdoxo, and the cell viability was assessed after 96 hours (**Figure 120**). Cdoxo exhibited better cytotoxicity than free doxo in MDA-MB-231 and DLD-1 cells (p value < 0.05). Based on these results, we further evaluated the CNPs as a drug delivery system in a mouse model of breast cancer.

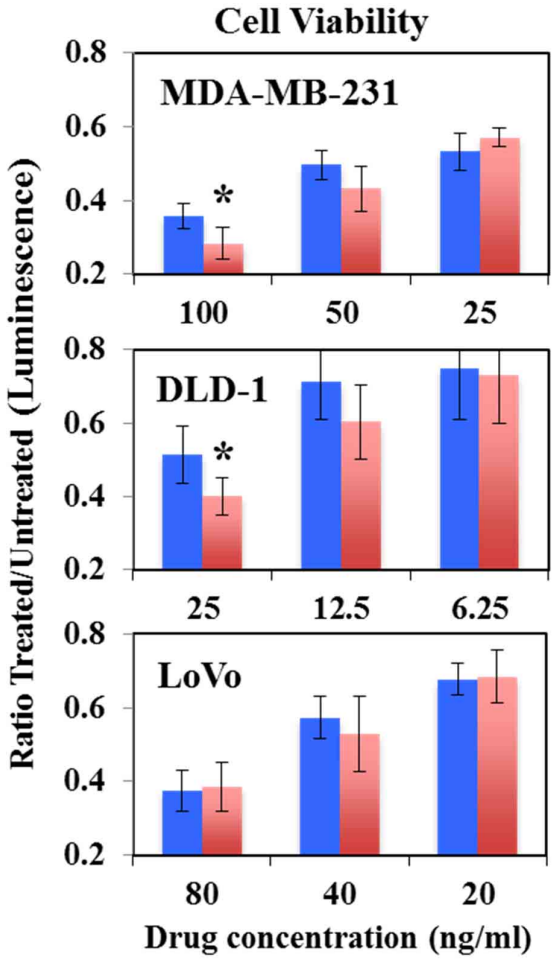

Figure 120: Cytotoxic effects of Cdoxo on MDA-MB-231, DLD-1 and LoVo cell lines treated with increasing concentrations of doxo (blue) or Cdoxo (red), as indicated on the x-axis (ng/ml). *p value <0.05 (y-axis).

5.4. CNPs were not toxic in mice and increased the efficacy of doxo

In vitro experiments demonstrated that our CNPs were not toxic at concentrations above the necessary dosage for drug delivery applications. To better predict toxicity in humans, nude mice were treated with a single i.v. injection of 5, 10, 20 and 40 mg/kg CNPs. Their body weight was monitored as an objective parameter of mice wellness. The mice were followed over a period of approximately 2 months. We did not observe any symptoms of stress or clinical illness. The body weight of the mice increased during the observational period (**Figure 121**).

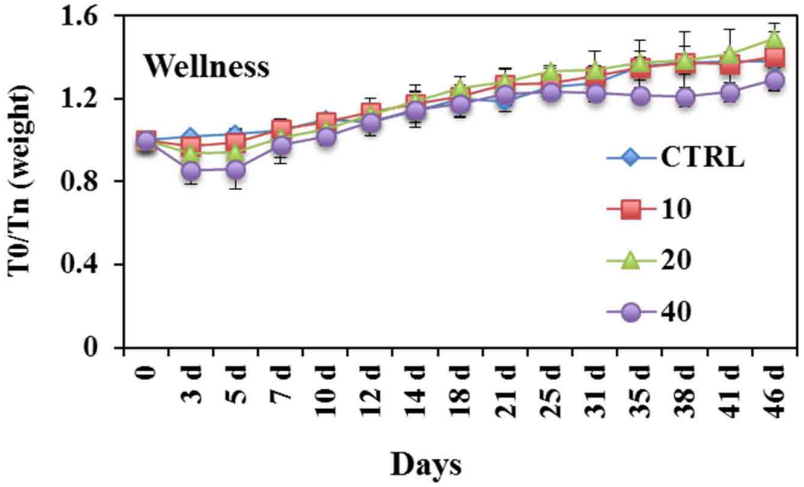

Figure 121: Weight of mice treated with different concentrations (mg/kg) of CNPs as indicated.

After more than 6 months, the mice were sacrificed, and their tissues were histopathologically analyzed. No obvious signs of toxicity were observed (**Figure 122**).

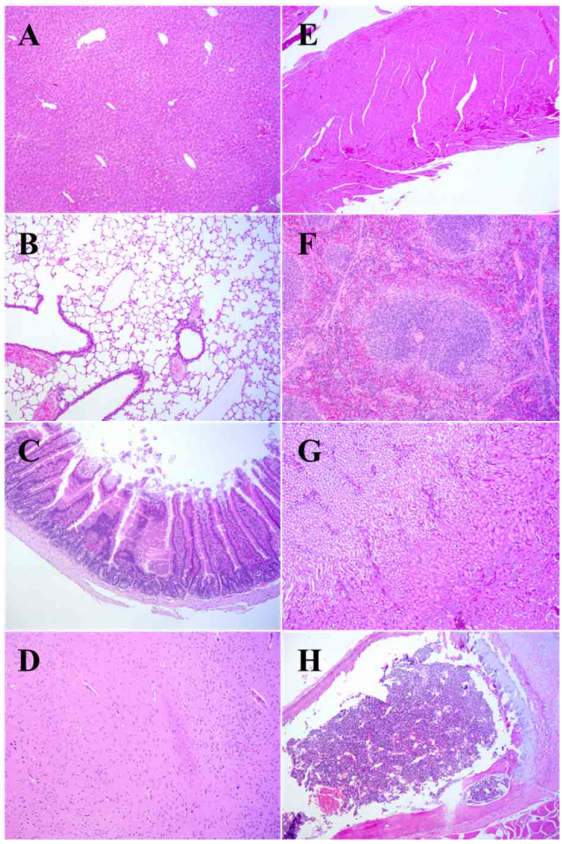

Figure 122: Histopathology analysis of different tissues of mice treated with 40mg/kg of CNPs. (A) Liver, (B) lung, (C) intestine, (D) brain, (E) heart, (F) spleen (G) kidney and (H) bone marrow.

Supported by this encouraging data, MDA-MB-231 cells were orthotopically inoculated in the mammary fat pad of nude mice. After the tumours had reached an average volume of 57 ± 8 mm^3, the mice were treated 3 times on a weekly base with 3 mg/kg Cdoxo or free doxo. **Figure 123A** demonstrates that the tumour volume of the Cdoxo-treated mice was reduced compared to the tumours of mice treated with free doxo (p value < 0.05). The body weight of the mice was similar among the groups of mice tested during the experiment (**Figure 123B**).

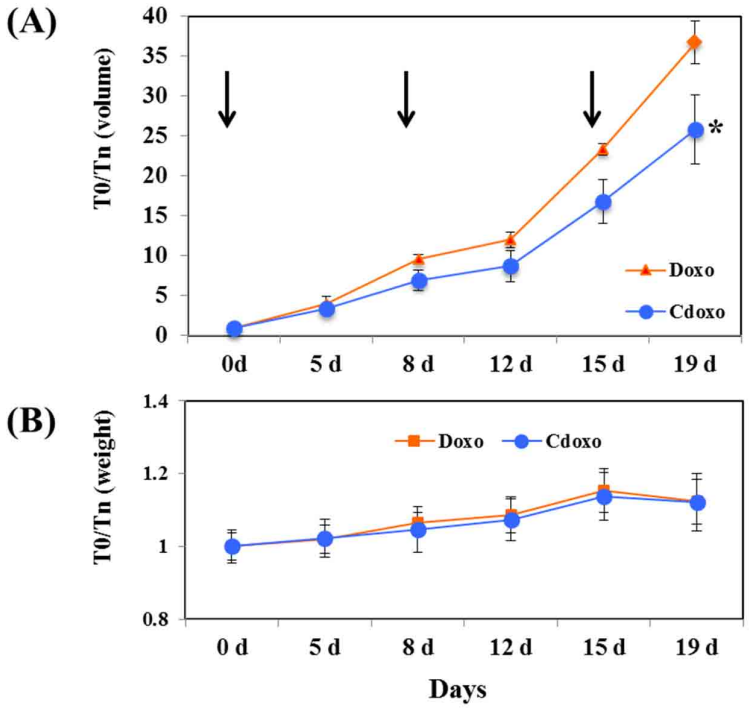

Figure 123: (A) Mice were treated 3 times (arrows) at 3 mg/kg Cdoxo or free doxo, and the tumour volume was measured (y-axis). *p value <0.05 (B) Weight of mice treated as in (B). T0: time at the beginning of the experiment; Tn: time on day n as indicated. Eight tumours were analyzed per data point.

5.5. CNPs altered the biodistribution and prolonged the circulation time of doxo

Data obtained from well-known and successful liposomal formulations revealed that drug efficacy can be increased by a longer circulation time, avoiding rapid clearance [775]. To investigate the potential changes in the PK profile, we administered 3 mg/kg doxo (i.v.) and Cdoxo to FVB/N mice. The PK profile of doxo in blood and tissues was qualitatively similar when administered as the free drug or Cdoxo. Both PK profiles were characterized by fast

first-phase elimination. However, in the late phase of elimination, up to 4 days, the concentration of doxo in blood remained higher when administered as Cdoxo (**Figure 124**) compared to free doxo. This result is consistent with the increase in the mean residence time from 14.1 ± 2 to 20.1 ± 0.5 hours (p value < 0.01) and the apparent constant elimination from 0.07 ± 0.01 $hour^{-1}$ to 0.050 ± 0.01 $hour^{-1}$ (p value < 0.05) for free doxo and Cdoxo, respectively.

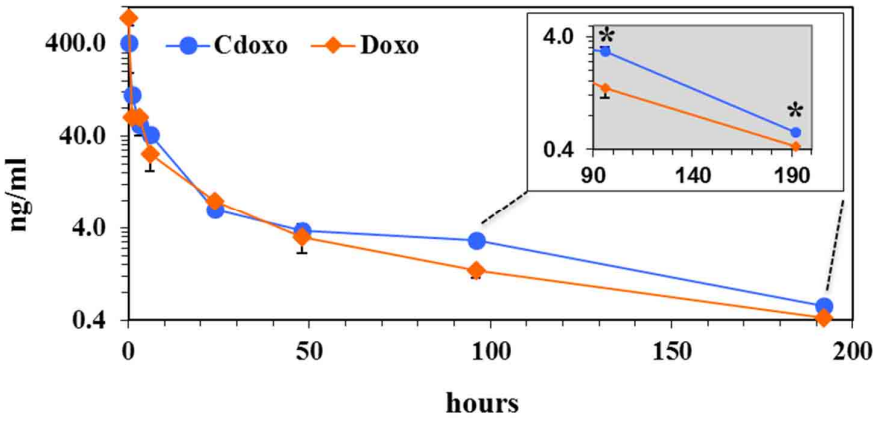

Figure 124: PK profile of free doxo and Cdoxo at 0.5, 1, 3, 6, 24, 48, 96 and 192 hours. In the insert, the time points 96 and 192 hours were zoomed in. *p value <0.05.

The tissue distribution of the drug 3 hours post-injection demonstrated a similar profile between Cdoxo and free doxo, except in the skin (**Figure 125A**). After 24 hours, the distribution of Cdoxo changed, with an accumulation in the liver and intestine and a reduction in the skin (p value < 0.05; **Figure 125B**). These data suggest that Cdoxo could reduce the skin toxicity associated with liposomal formulations of doxo and be utilized to treat gastro-intestinal cancers.

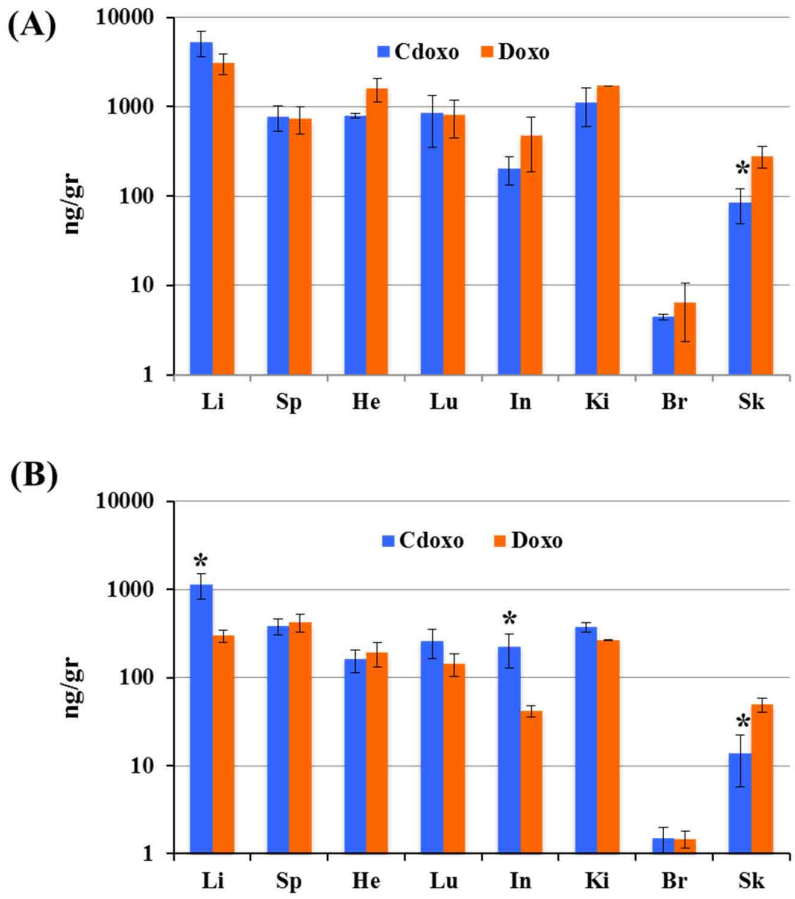

Figure 125: (A) and (B) Biodistribution of free doxo and Cdoxo at 3 (A) and 24 (B) hours. At 3 hours, less Cdoxo was present in the skin. At 24 hours, increased accumulation of Cdoxo in the liver and intestine was observed. The y-axis is in logarithmic scale (ng/gr of drug/tissue). Li: liver, Sp: spleen, He: heart, Lu: lung, In: intestine, Ki: kidney, Br: brain, Sk: skin. Three mice were utilized for each data point.

Chapter 6:

Conclusions

6. CONCLUSIONS

CNPs have been widely used in nanomedicine due to their biocompatibility and low toxicity. Different synthetic methods, starting materials, and surface modification processes can generate a wide variety of CNPs, which have shown immense potential to play a big role in nanotechnology for the development of assays, sensors, bioimaging agents both *in vitro* and *in vivo*, smart drug delivery vehicles, phototherapy, photocatalysis and electrocatalysis.

Nonetheless, some problems still exist that impede the further bioapplications of CNPs: (1) the difficulty to synthesize CNPs with uniform size. Proverbially, the uniformity has a great influence on the properties of CNPs, which further disturb their bioapplications. Consequently, almost all of the synthesized CNPs need further separation and purification. (2) CNPs obtained from different batches often show different properties, such as size, QY, and fluorescence. This problem limits the commercialization of CNPs, which needs to be settled urgently. (3) Some CNPs obtained at the very start are not fluorescent, which need further passivation.

Despite the fact that many optical and electronic properties of CNPs are not well understood yet, there is no doubt that CNPs will play a huge role in bioimaging and biomedical research in the near future upon further development. The fact that the advantages of CNPs are being recognized by researchers with interest in areas as diverse as materials science, synthetic chemistry, drug delivery, nanomedicine and clean energy suggests that research on CNPs will continue to grow in synergistic relationship with intellectually adjacent fields. It seems clear that the future of CNPs remains promising.

In this study, we prepared a new nanovector that can be used to image subcellular compartments such as exosomes with excellent properties for drug delivery. These CNPs can be efficiently loaded with doxo, a widely used chemotherapeutic drug, and exhibit controlled release under acidic conditions, as in the tumour microenvironment. Cdoxo was more effective *in vivo* than free doxo due to a different PK profile. Hence, a simple and green synthesis starting from tea could produce a tunable and safe drug delivery nanocarrier with excellent biocompatible properties.

REFERENCES

[1] Mansoori, G.; Fauzi Soelaiman, T. Nanotechnology — An Introduction for the Standards Community. *J. ASTM Int.*, **2005,** *2*(6), 1–22.

[2] Gnach, A.; Lipinski, T.; Bednarkiewicz, A.; Rybka, J.; Capobianco, J.A. Upconverting nanoparticles: assessing the toxicity. *Chem. Soc. Rev.*, **2015,** *44*(6), 1561–1584.

[3] National Nanotechnology Initiative (NNI). www.nano.gov (Accessed Oct 3, **2016**).

[4] Allhoff, F. On the Autonomy and Justification of Nanoethics. *Nanoethics*, **2007,** *1*(3), 185–210.

[5] Feynman, R.P. There's plenty of room at the bottom. *Eng. Sci.*, **1960,** *23*(5), 22–36.

[6] Taniguchi, N. On the Basic Concept of 'Nano-Technology. In *Proc. Intl. Conf. Prod. Eng. Tokyo, Part II, Japan Society of Precision Engineering.*; **1974**, ; pages 18–23.

[7] Drexler, E.K. *Engines of Creation: The Coming Era of Nanotechnology.*; Anchor Press, Garden city: New York, **1986**, .

[8] Drexler, E.K.; Peterson, C.; Pergamit, G. *Unbounding the Future: the Nanotechnology Revolution.*; New York: William Morrow, **1991**, .

[9] The British Museum. www.britishmuseum.org/research/collection_online/collection_object_details.aspx?objobjec=61219&partId=1 (Accessed Oct 12, **2016**).

[10] Barber, D.J.; Freestone, I.C. An investigation of the origin of the colour of the Lycurgus Cup by analytical transmission electron microscopy. *Archaeometry*, **1990,** *32*(1), 33–45.

[11] Freestone, I.; Meeks, N.; Sax, M.; Higgitt, C. The Lycurgus Cup — A Roman nanotechnology. *Gold Bull.*, **2007,** *40*(4), 270–277.

[12] Wagner, F.E.; Haslbeck, S.; Stievano, L.; Calogero, S.; Pankhurst, Q.A.; Martinek, K.-P. Before striking gold in gold-ruby glass. *Nature*, **2000,** *407*(6805), 691–692.

[13] The New York Times. www.nytimes.com/imagepages/2005/02/21/science/20050222_NANO1_GRAPHIC.html (Accessed Oct 12, **2016**).

[14] Pradell, T.; Climent-Font, A.; Molera, J.; Zucchiatti, A.; Ynsa, M.D.; Roura, P.; Crespo, D. Metallic and nonmetallic shine in luster: An elastic ion backscattering study. *J. Appl. Phys.*, **2007,** *101*(10), 103518.

[15] Poole, C.P.; Owens, F.J. *Introduction to Nanotechnology.*; John Wiley & Sons, Ltd, **2003**, .

[16] Reibold, M.; Paufler, P.; Levin, A.A.; Kochmann, W.; Pätzke, N.; Meyer, D.C. Materials: Carbon nanotubes in an ancient Damascus sabre. *Nature*, **2006,** *444*(7117), 286–286.

[17] Faraday, M. The Bakerian Lecture: Experimental Relations of Gold (and Other Metals) to Light. *Philos. Trans. R. Soc. London*, **1857,** *147*, 145–181.

[18] Binnig, G. Tunneling through a controllable vacuum gap. *Appl. Phys. Lett.*, **1982,** *40*(2), 178.

[19] Binnig, G.; Rohrer, H.; Gerber, C.; Weibel, E. Surface Studies by Scanning Tunneling Microscopy. *Phys. Rev. Lett.*, **1982,** *49*(1), 57–61.

[20] Binnig, G.; Rohrer, H.; Gerber, C.; Weibel, E. 7 × 7 Reconstruction on Si(111) Resolved in Real Space. *Phys. Rev. Lett.*, **1983,** *50*(2), 120–123.

[21] Institute of physics Polish Academy of Sciences. http://info.ifpan.edu.pl/~wawro/subframes/Surfaces.htm (Accessed Oct 18, **2016**).

[22] Eigler, D.M.; Schweizer, E.K. Positioning single atoms with a scanning tunnelling microscope. *Nature*, **1990,** *344*(6266), 524–526.

[23] Binnig, G.; Quate, C.F.; Gerber, C. Atomic Force Microscope. *Phys. Rev. Lett.*, **1986,** *56*(9), 930–933.

[24] Binnig, G. Atomic force microscope and method for imaging surfaces with atomic resolution.; *US4724318 A*, **1988**.

[25] Kroto, H.W.; Heath, J.R.; O'Brien, S.C.; Curl, R.F.; Smalley, R.E. C60: Buckminsterfullerene. *Nature*, **1985,** *318*(6042), 162–163.

[26] Iijima, S. Helical microtubules of graphitic carbon. *Nature*, **1991,** *354*(6348), 56–58.

[27] Xu, X.; Ray, R.; Gu, Y.; Ploehn, H.J.; Gearheart, L.; Raker, K.; Scrivens, W.A. Electrophoretic Analysis and Purification of Fluorescent Single-Walled Carbon Nanotube Fragments. *J. Am. Chem. Soc.*, **2004,** *126*(40), 12736–12737.

[28] Baker, S.N.; Baker, G. a Luminescent carbon nanodots: emergent nanolights. *Angew. Chem. Int. Ed. Engl.*, **2010,** *49*(38), 6726–6744.

[29] Esteves da Silva, J.C.G.; Gonçalves, H.M.R. Analytical and bioanalytical applications of carbon dots. *TrAC Trends Anal. Chem.*, **2011,** *30*(8), 1327–1336.

[30] Yang, S.-T.; Cao, L.; Luo, P.G.; Lu, F.; Wang, X.; Wang, H.; Meziani, M.J.; Liu, Y.; Qi, G.; Sun, Y.-P. Carbon Dots for Optical Imaging in Vivo. *J. Am. Chem. Soc.*, **2009,** *131*(32), 11308–11309.

[31] Yang, S.-T.; Wang, X.; Wang, H.; Lu, F.; Luo, P.G.; Cao, L.; Meziani, M.J.; Liu, J.-H.; Liu, Y.; Chen, M.; Huang, Y.; Sun, Y.-P. Carbon Dots as Nontoxic and High-Performance Fluorescence Imaging Agents. *J. Phys. Chem. C. Nanomater. Interfaces*, **2009,** *113*(42), 18110–18114.

[32] Cao, L.; Wang, X.; Meziani, M.J.; Lu, F.; Wang, H.; Luo, P.G.; Lin, Y.; Harruff, B.A.; Veca, L.M.; Murray, D.; Xie, S.-Y.; Sun, Y.-P. Carbon Dots for Multiphoton Bioimaging. *J. Am. Chem. Soc.*, **2007,** *129*(37), 11318–11319.

[33] Li, Q.; Ohulchanskyy, T.Y.; Liu, R.; Koynov, K.; Wu, D.; Best, A.; Kumar, R.; Bonoiu, A.; Prasad, P.N. Photoluminescent Carbon Dots as Biocompatible Nanoprobes for Targeting Cancer Cells in Vitro. *J. Phys. Chem. C*, **2010,** *114*(28), 12062–12068.

[34] Wang, X.; Cao, L.; Lu, F.; Meziani, M.J.; Li, H.; Qi, G.; Zhou, B.; Harruff, B.A.; Kermarrec, F.; Sun, Y.-P. Photoinduced electron transfers with carbon dots. *Chem. Commun.*, **2009,** (25), 3774.

[35] Li, Y.; Hu, Y.; Zhao, Y.; Shi, G.; Deng, L.; Hou, Y.; Qu, L. An Electrochemical Avenue to Green-Luminescent Graphene Quantum Dots as Potential Electron-Acceptors for Photovoltaics. *Adv. Mater.*, **2011,** *23*(6), 776–780.

[36] Zhou, L.; Lin, Y.; Huang, Z.; Ren, J.; Qu, X. Carbon nanodots as fluorescence probes for rapid, sensitive, and label-free detection of Hg 2+ and biothiols in complex matrices. *Chem. Commun.*, **2012,** *48*(8), 1147–1149.

[37] Liu, L.; Li, Y.; Zhan, L.; Liu, Y.; Huang, C. One-step synthesis of fluorescent hydroxyls-coated carbon dots with hydrothermal reaction and its application to optical sensing of metal ions. *Sci. China Chem.*, **2011,** *54*(8), 1342–1347.

[38] Rothemund, P.W.K. Folding DNA to create nanoscale shapes and patterns. *Nature*, **2006,** *440*(7082), 297–302.

[39] Seeman, N.C. Nucleic acid junctions and lattices. *J. Theor. Biol.*, **1982,** *99*(2), 237–247.

[40] Sciau, P. Nanoparticles in Ancient Materials: The Metallic Lustre Decorations of Medieval Ceramics. In *The Delivery of Nanoparticles*; InTech, **2012**, .

[41] Mie, G. Beiträge zur Optik trüber Medien, speziell kolloidaler Metallösungen. *Ann. Phys.*, **1908,** *330*(3), 377–445.

[42] Synge, E.H. XXXVIII. A suggested method for extending microscopic resolution into the ultra-microscopic region. *London, Edinburgh, Dublin Philos. Mag. J. Sci.*, **1928,** *6*(35), 356–362.

[43] Knoll, M.; Ruska, E. Beitrag zur geometrischen Elektronenoptik. II. *Ann. Phys.*, **1932,** *404*(6), 641–661.

[44] Knoll, M.; Ruska, E. Beitrag zur geometrischen Elektronenoptik. I. *Ann. Phys.*, **1932,** *404*(5), 607–640.

[45] Müller, E.W. Experimente zur Theorie der Elektronenemission unter dem Einfluß starker Felder. *Phys. Z.*, **1936,** *37*, 838–841.

[46] Shockley, W. Circuit element utilizing semiconductive material.; *US2569347 A*, **1951**.

[47] Müller, E.W. Das Feldionenmikroskop. *Zeitschrift fuer Phys.*, **1951,** *131*(1), 136–142.

[48] Müller, E.W.; Bahadur, K. Field Ionization of Gases at a Metal Surface and the Resolution of the Field Ion Microscope. *Phys. Rev.*, **1956,** *102*(3), 624–631.

[49] Watson, J.D.; Crick, F.H.C. Molecular Structure of Nucleic Acids: A Structure for Deoxyribose Nucleic Acid. *Nature*, **1953,** *171*(4356), 737–738.

[50] Von Hippel, A. Molecular Engineering. *Science*, **1956,** *123*(3191), 315–316.

[51] Esaki, L. New Phenomenon in Narrow Germanium p-n Junctions. *Phys. Rev.*, **1958,** *109*(2), 603–604.

[52] Plank, C.J.; Rosinski, E.J. Catalytic cracking of hydrocarbons with a crystalline zeolite catalyst composite.; *US3140249 A*, **1964**.

[53] Papell, S.S. Low viscosity magnetic fluid obtained by the colloidal suspension of magnetic particles.; *US3215572 A*, **1965**.

[54] Moore, G.E. Cramming more components onto integrated circuits. *Electronics*, **1965,** *38*(8), 114–117.

[55] Osawa, E. Superaromaticity. *Kagaku. Kyoto.*, **1970,** *25*, 854–863.

[56] Aviram, A.; Ratner, M.A. Molecular rectifiers. *Chem. Phys. Lett.*, **1974,** *29*(2), 277–283.

[57] Jeanmaire, D.L.; Van Duyne, R.P. Surface raman spectroelectrochemistry. *J. Electroanal. Chem. Interfacial Electrochem.*, **1977,** *84*(1), 1–20.

[58] Sagiv, J. Organized monolayers by adsorption. 1. Formation and structure of oleophobic mixed monolayers on solid surfaces. *J. Am. Chem. Soc.*, **1980,** *102*(1), 92–98.

[59] Binnig, G.; Rohrer, H. Scanning tunneling microscope .; *US4343993 A*, **1982**.

[60] Ekimov, A.; Onushchenko, A. Quantum size effect in the optical-spectra of semiconductor micro-crystals. *Sov. Phys. Semicond.*, **1982,** *16*(7), 775–778.

[61] Drexler, E.K. Molecular engineering: An approach to the development of general capabilities for molecular manipulation. *Proc. Natl. Acad. Sci. U. S. A.*, **1981,** *78*(9), 5275–5278.

[62] Pinheiro, A. V.; Han, D.; Shih, W.M.; Yan, H. Challenges and opportunities for structural DNA nanotechnology. *Nat. Nanotechnol.*, **2011,** *6*(12), 763–772.

[63] Rossetti, R.; Nakahara, S.; Brus, L.E. Quantum size effects in the redox potentials, resonance Raman spectra, and electronic spectra of CdS crystallites in aqueous solution. *J. Chem. Phys.*, **1983,** *79*(2), 1086.

[64] Steigerwald, M.L.; Alivisatos, A.P.; Gibson, J.M.; Harris, T.D.; Kortan, R.; Muller, A.J.; Thayer, A.M.; Duncan, T.M.; Douglass, D.C.; Brus, L.E. Surface derivatization and isolation of semiconductor cluster molecules. *J. Am. Chem. Soc.*, **1988,** *110*(10), 3046–3050.

[65] Averin, D. V.; Likharev, K.K. Coulomb blockade of single-electron tunneling, and coherent oscillations in small tunnel junctions. *J. Low Temp. Phys.*, **1986,** *62*(3–4), 345–373.

[66] Kresge, C.T.; Leonowicz, M.E.; Roth, W.J.; Vartuli, J.C.; Beck, J.S. Ordered mesoporous molecular sieves synthesized by a liquid-crystal template mechanism. *Nature*, **1992,** *359*(6397), 710–712.

[67] Beck, J.S.; Vartuli, J.C.; Roth, W.J.; Leonowicz, M.E.; Kresge, C.T.; Schmitt, K.D.; Chu, C.T.W.; Olson, D.H.; Sheppard, E.W.; McCullen, S.B.; Higgins, J.B.; Schlenker, J.L. A new family of mesoporous molecular sieves prepared with liquid crystal templates. *J. Am. Chem. Soc.*, **1992,** *114*(27), 10834–10843.

[68] Iijima, S.; Ichihashi, T. Single-shell carbon nanotubes of 1-nm diameter. *Nature*, **1993,** *363*(6430), 603–605.

[69] Bethune, D.S.; Klang, C.H.; de Vries, M.S.; Gorman, G.; Savoy, R.; Vazquez, J.; Beyers, R. Cobalt-catalysed growth of carbon nanotubes with single-atomic-layer walls. *Nature*, **1993,** *363*(6430), 605–607.

[70] Mirkin, C.A.; Letsinger, R.L.; Mucic, R.C.; Storhoff, J.J. A DNA-based method for

rationally assembling nanoparticles into macroscopic materials. *Nature*, **1996,** *382*(6592), 607–609.

[71] Zyvex Technologies. www.zyvex.com (Accessed Oct 18, **2016**).

[72] Tans, S.J.; Verschueren, A.R.M.; Dekker, C. Room-temperature transistor based on a single carbon nanotube. *Nature*, **1998,** *393*(6680), 49–52.

[73] Piner, R.D. "Dip-Pen" Nanolithography. *Science*, **1999,** *283*(5402), 661–663.

[74] Hersam, M.C.; Guisinger, N.P.; Lyding, J.W. Isolating, imaging, and electrically characterizing individual organic molecules on the Si(100) surface with the scanning tunneling microscope. *J. Vac. Sci. Technol. A Vacuum, Surfaces, Film.*, **2000,** *18*(4), 1349.

[75] Lok, C. Nanotechnology: Small wonders. *Nature*, **2010,** *467*(7311), 18–21.

[76] Montemagno, C.D. Nanomachines: A Roadmap for Realizing the Vision. *J. Nanoparticle Res.*, **2001,** *3*(1), 1–3.

[77] Williams, K.A.; Veenhuizen, P.T.M.; de la Torre, B.G.; Eritja, R.; Dekker, C. Nanotechnology: Carbon nanotubes with DNA recognition. *Nature*, **2002,** *420*(6917), 761–761.

[78] 21st Century Nanotechnology Research and Development Act. www.congress.gov/bill/108th-congress/senate-bill/189 (Accessed Oct 18, **2016**).

[79] Loo, C.; Lin, A.; Hirsch, L.; Lee, M.-H.; Barton, J.; Halas, N.; West, J.; Drezek, R. Nanoshell-Enabled Photonics-Based Imaging and Therapy of Cancer. *Technol. Cancer Res. Treat.*, **2004,** *3*(1), 33–40.

[80] Hirsch, L.R.; Stafford, R.J.; Bankson, J.A.; Sershen, S.R.; Rivera, B.; Price, R.E.; Hazle, J.D.; Halas, N.J.; West, J.L. Nanoshell-mediated near-infrared thermal therapy of tumors under magnetic resonance guidance. *Proc. Natl. Acad. Sci.*, **2003,** *100*(23), 13549–13554.

[81] Novoselov, K.S. Electric Field Effect in Atomically Thin Carbon Films. *Science*, **2004,** *306*(5696), 666–669.

[82] Shirai, Y.; Osgood, A.J.; Zhao, Y.; Kelly, K.F.; Tour, J.M. Directional Control in Thermally Driven Single-Molecule Nanocars. *Nano Lett.*, **2005,** *5*(11), 2330–2334.

[83] Morin, J.-F.; Shirai, Y.; Tour, J.M. En Route to a Motorized Nanocar. *Org. Lett.*, **2006,** *8*(8), 1713–1716.

[84] Knoll, A.W.; Pires, D.; Coulembier, O.; Dubois, P.; Hedrick, J.L.; Frommer, J.; Duerig, U. Probe-Based 3-D Nanolithography Using Self-Amplified Depolymerization Polymers. *Adv. Mater.*, **2010,** *22*(31), 3361–3365.

[85] GLOBOCAN 2012: estimated cancer incidence, mortality and prevalence worldwide in 2012, World Health Organization. globocan.iarc.fr/Pages/fact_sheets_cancer.aspx (Accessed Mar 23, **2016**).

[86] European Science Foundation's Forward look Nanomedicine: An EMRC Consensus Opinion. www.esf.org (Accessed Oct 31, **2016**).

[87] Peer, D.; Karp, J.M.; Hong, S.; Farokhzad, O.C.; Margalit, R.; Langer, R. Nanocarriers as an emerging platform for cancer therapy. *Nat. Nanotechnol.*, **2007,** *2*(12), 751–760.

[88] Picard, F.J.; Bergeron, M.G. Rapid molecular theranostics in infectious diseases. *Drug Discov. Today*, **2002,** *7*(21), 1092–1101.

[89] Aaronson, N.K.; Ahmedzai, S.; Bergman, B.; Bullinger, M.; Cull, A.; Duez, N.J.; Filiberti, A.; Flechtner, H.; Fleishman, S.B.; Haes, J.C.J.M. d.; Kaasa, S.; Klee, M.; Osoba, D.; Razavi, D.; Rofe, P.B.; Schraub, S.; Sneeuw, K.; Sullivan, M.; Takeda, F. The European Organization for Research and Treatment of Cancer QLQ-C30: A Quality-of-Life Instrument for Use in International Clinical Trials in Oncology. *JNCI J. Natl. Cancer Inst.*, **1993,** *85*(5), 365–376.

[90] Granchi, C.; Rizzolio, F.; Bordoni, V.; Caligiuri, I.; Manera, C.; Macchia, M.; Minutolo, F.; Martinelli, A.; Giordano, A.; Tuccinardi, T. 4-Aryliden-2-methyloxazol-5(4H)-one as a new scaffold for selective reversible MAGL inhibitors. *J. Enzyme Inhib. Med. Chem.*, **2016,** *31*(1), 137–146.

[91] Tuccinardi, T.; Granchi, C.; Rizzolio, F.; Caligiuri, I.; Battistello, V.; Toffoli, G.; Minutolo, F.; Macchia, M.; Martinelli, A. Identification and characterization of a new reversible MAGL inhibitor. *Bioorg. Med. Chem.*, **2014,** *22*(13), 3285–3291.

[92] Poli, G.; Tuccinardi, T.; Rizzolio, F.; Caligiuri, I.; Botta, L.; Granchi, C.; Ortore, G.; Minutolo, F.; Schenone, S.; Martinelli, A. Identification of New Fyn Kinase Inhibitors Using a FLAP-Based Approach. *J. Chem. Inf. Model.*, **2013,** *53*(10), 2538–2547.

[93] Manera, C.; Saccomanni, G.; Malfitano, A.M.; Bertini, S.; Castelli, F.; Laezza, C.; Ligresti, A.; Lucchesi, V.; Tuccinardi, T.; Rizzolio, F.; Bifulco, M.; Di Marzo, V.; Giordano, A.; Macchia, M.; Martinelli, A. Rational design, synthesis and anti-proliferative properties of new CB2 selective cannabinoid receptor ligands: an investigation of the 1,8-naphthyridin-2(1H)-one scaffold. *Eur. J. Med. Chem.*, **2012,** *52*, 284–294.

[94] Cooper, E.L. From Darwin and Metchnikoff to Burnet and Beyond. In *Trends in Innate Immunity*; KARGER: Basel, **2008**, pages 1–11.

[95] Ehrlich, P. Address in Pathology, ON CHEMIOTHERAPY: Delivered before the Seventeenth International Congress of Medicine. *Br. Med. J.*, **1913,** *2*(2746), 353–359.

[96] Bangham, A.D. Lipid Bilayers and Biomembranes. *Annu. Rev. Biochem.*, **1972,** *41*(1), 753–776.

[97] Gregoriadis, G.; Leathwood, P.D.; Ryman, B.E. Enzyme entrapment in liposomes. *FEBS Lett.*, **1971,** *14*(2), 95–99.

[98] Papahadjopoulos, D.; Mayhew, E.; Poste, G.; Smith, S.; Vail, W.J. Incorporation of lipid vesicles by mammalian cells provides a potential method for modifying cell behaviour. *Nature*, **1974,** *252*(5479), 163–6.

[99] Cornu, G.; Michaux, J.-L.; Sokal, G.; Trouet, A. Daunorubicin-DNA: Further clinical trials in acute non-lymphoblastic leukemia. *Eur. J. Cancer*, **1974,** *10*(11), 695–700.

[100] Ringsdorf, H. Structure and properties of pharmacologically active polymers. *J. Polym. Sci. Polym. Symp.*, **2007,** *51*(1), 135–153.

[101] Duncan, R.; Kopeček, J. Soluble synthetic polymers as potential drug carriers. In *Advances in Polymer Science*; Springer Berlin Heidelberg, **1984**, pages 51–101.

[102] Duncan, R.; Spreafico, F. Polymer Conjugates. *Clin. Pharmacokinet.*, **1994,** *27*(4), 290–306.

[103] Hurwitz, E.; Levy, R.; Maron, R.; Wilchek, M.; Arnon, R.; Sela, M. The covalent binding of daunomycin and adriamycin to antibodies, with retention of both drug and antibody activities. *Cancer Res.*, **1975,** *35*(5), 1175–1181.

[104] Speiser, P.P. Non-liposomal nanocapsules, methodology and application. *Front. Biol.*, **1979,** *48*, 653–668.

[105] Kreuter, J.; Speiser, P.P. In Vitro Studies of Poly(methyl Methacrylate) Adjuvants. *J. Pharm. Sci.*, **1976,** *65*(11), 1624–1627.

[106] Couvreur, P.; Tulkenst, P.; Roland, M.; Trouet, A.; Speiser, P. Nanocapsules: A new type of lysosomotropic carrier. *FEBS Lett.*, **1977,** *84*(2), 323–326.

[107] Davis, F.F. The origin of pegnology. *Adv. Drug Deliv. Rev.*, **2002,** *54*(4), 457–458.

[108] Trouet, A.; Masquelier, M.; Baurain, R.; Deprez-De Campeneere, D. A covalent linkage between daunorubicin and proteins that is stable in serum and reversible by lysosomal hydrolases, as required for a lysosomotropic drug-carrier conjugate: in vitro and in vivo studies. *Proc. Natl. Acad. Sci. U. S. A.*, **1982,** *79*(2), 626–629.

[109] Gros, L.; Ringsdorf, H.; Schupp, H. Polymeric Antitumor Agents on a Molecular and on a Cellular Level? *Angew. Chemie Int. Ed. English*, **1981,** *20*(4), 305–325.

[110] Yokoyama, M.; Miyauchi, M.; Yamada, N.; Okano, T.; Sakurai, Y.; Kataoka, K.; Inoue, S. Characterization and anticancer activity of the micelle-forming polymeric anticancer drug adriamycin-conjugated poly(ethylene glycol)-poly(aspartic acid) block copolymer. *Cancer Res.*, **1990,** *50*(6), 1693–1700.

[111] Slepnev, V.I.; Kuznetsova, L.E.; Gubin, A.N.; Batrakova, E. V; Alakhov VYu; Kabanov, A. V Micelles of poly(oxyethylene)-poly(oxypropylene) block copolymer (pluronic) as a tool for low-molecular compound delivery into a cell: phosphorylation of intracellular proteins with micelle incorporated [gamma-32P]ATP. *Biochem. Int.*, **1992,** *26*(4), 587–595.

[112] Van Cutsem, E.; Cervantes, A.; Adam, R.; Sobrero, A.; Van Krieken, J.H.; Aderka, D.; Aranda Aguilar, E.; Bardelli, A.; Benson, A.; Bodoky, G.; Ciardiello, F.; D'Hoore, A.; Diaz-Rubio, E.; Douillard, J.-Y.; Ducreux, M.; Falcone, A.; Grothey, A.; Gruenberger, T.; Haustermans, K.; Heinemann, V.; Hoff, P.; Köhne, C.-H.; Labianca, R.; Laurent-Puig, P.; Ma, B.; Maughan, T.; Muro, K.; Normanno, N.; Österlund, P.; Oyen, W.J.G.; Papamichael, D.; Pentheroudakis, G.; Pfeiffer, P.; Price, T.J.; Punt, C.; Ricke, J.; Roth, A.; Salazar, R.; Scheithauer, W.; Schmoll, H.J.; Tabernero, J.; Taïeb, J.; Tejpar, S.; Wasan, H.; Yoshino, T.; Zaanan, A.; Arnold, D. ESMO consensus guidelines for the management of patients with metastatic colorectal cancer. *Ann. Oncol.*, **2016,** *27*, 1386–1422.

[113] Rizzolio, F.; Esposito, L.; Muresu, D.; Fratamico, R.; Jaraha, R.; Caprioli, G.V.; Giordano, A. RB gene family: genome-wide ChIP approaches could open undiscovered roads. *J. Cell. Biochem.*, **2010,** *109*(5), 839–843.

[114] Svenson, S. Clinical translation of nanomedicines. *Curr. Opin. Solid State Mater. Sci.*, **2012,** *16*(6), 287–294.

[115] Dianzani, C.; Zara, G.P.; Maina, G.; Pettazzoni, P.; Pizzimenti, S.; Rossi, F.; Gigliotti, C.L.; Ciamporcero, E.S.; Daga, M.; Barrera, G. Drug Delivery Nanoparticles in Skin Cancers. *Biomed Res. Int.*, **2014,** *2014*, 1–13.

[116] Chou, L.Y.T.; Ming, K.; Chan, W.C.W. Strategies for the intracellular delivery of nanoparticles. *Chem. Soc. Rev.*, **2011,** *40*(1), 233–245.

[117] Li, Y.; Stroberg, W.; Lee, T.-R.; Kim, H.S.; Man, H.; Ho, D.; Decuzzi, P.; Liu, W.K. Multiscale modeling and uncertainty quantification in nanoparticle-mediated drug/gene delivery. *Comput. Mech.*, **2014,** *53*(3), 511–537.

[118] Li, Y.; Lian, Y.; Zhang, L.T.; Aldousari, S.M.; Hedia, H.S.; Asiri, S.A.; Liu, W.K. Cell and nanoparticle transport in tumour microvasculature: the role of size, shape and surface functionality of nanoparticles. *Interface Focus*, **2016,** *6*(1), 20150086.

[119] Albanese, A.; Tang, P.S.; Chan, W.C.W. The Effect of Nanoparticle Size, Shape, and Surface Chemistry on Biological Systems. *Annu. Rev. Biomed. Eng.*, **2012,** *14*(1), 1–16.

[120] Immordino, M.L.; Dosio, F.; Cattel, L. Stealth liposomes: review of the basic science, rationale, and clinical applications, existing and potential. *Int. J. Nanomedicine*, **2006,** *1*(3), 297–315.

[121] Molineux, G. Pegylation: engineering improved pharmaceuticals for enhanced therapy. *Cancer Treat. Rev.*, **2002,** *28*, 13–16.

[122] Walkey, C.D.; Olsen, J.B.; Guo, H.; Emili, A.; Chan, W.C.W. Nanoparticle Size and Surface Chemistry Determine Serum Protein Adsorption and Macrophage Uptake. *J. Am. Chem. Soc.*, **2012,** *134*(4), 2139–2147.

[123] Pelaz, B.; del Pino, P.; Maffre, P.; Hartmann, R.; Gallego, M.; Rivera-Fernández, S.; de la Fuente, J.M.; Nienhaus, G.U.; Parak, W.J. Surface Functionalization of Nanoparticles with Polyethylene Glycol: Effects on Protein Adsorption and Cellular Uptake. *ACS Nano*, **2015,** *9*(7), 6996–7008.

[124] Perrault, S.D.; Walkey, C.; Jennings, T.; Fischer, H.C.; Chan, W.C.W. Mediating Tumor Targeting Efficiency of Nanoparticles Through Design. *Nano Lett.*, **2009,** *9*(5), 1909–1915.

[125] Otsuka, H.; Nagasaki, Y.; Kataoka, K. PEGylated nanoparticles for biological and pharmaceutical applications. *Adv. Drug Deliv. Rev.*, **2003,** *55*(3), 403–419.

[126] Lipka, J.; Semmler-Behnke, M.; Sperling, R.A.; Wenk, A.; Takenaka, S.; Schleh, C.; Kissel, T.; Parak, W.J.; Kreyling, W.G. Biodistribution of PEG-modified gold nanoparticles following intratracheal instillation and intravenous injection. *Biomaterials*, **2010,** *31*(25), 6574–6581.

[127] Godin, B.; Serda, R.E.; Sakamoto, J.; Decuzzi, P.; Ferrari, M. Nanoparticles for Cancer Detection and Therapy. In *Nanotechnology*; Wiley-VCH Verlag GmbH & Co. KGaA: Weinheim, Germany, **2010**, .

[128] Godin, B.; Tasciotti, E.; Liu, X.; Serda, R.E.; Ferrari, M. Multistage Nanovectors: From

Concept to Novel Imaging Contrast Agents and Therapeutics. *Acc. Chem. Res.*, **2011,** *44*(10), 979–989.

[129] Weissig, V.; Whiteman, K.R.; Torchilin, V.P. Accumulation of Protein-Loaded Long-Circulating Micelles and Liposomes in Subcutaneous Lewis Lung Carcinoma in Mice. *Pharm. Res.*, **1998,** *15*(10), 1552–1556.

[130] Savic, R. Micellar Nanocontainers Distribute to Defined Cytoplasmic Organelles. *Science*, **2003,** *300*(5619), 615–618.

[131] Kumar, R.; Korideck, H.; Ngwa, W.; Berbeco, R.I.; Makrigiorgos, G.M.; Sridhar, S. Third generation gold nanoplatform optimized for radiation therapy. *Transl. Cancer Res.*, **2013,** *2*(4).

[132] Lim, E.-K.; Jang, E.; Lee, K.; Haam, S.; Huh, Y.-M. Delivery of cancer therapeutics using nanotechnology. *Pharmaceutics*, **2013,** *5*(2), 294–317.

[133] Ochekpe, N.; Olorunfemi, P.; Ngwuluka, N. Nanotechnology and Drug Delivery Part 2: Nanostructures for Drug Delivery. *Trop. J. Pharm. Res.*, **2009,** *8*(3), 275–287.

[134] Zamboni, W.C. Liposomal, nanoparticle, and conjugated formulations of anticancer agents. *Clin. Cancer Res.*, **2005,** *11*(23), 8230–8234.

[135] Bangham, A.D.; Horne, R.W. Negative staining of phospholipids and their structural modification by surface-active agents as observed in the electron microscope. *J. Mol. Biol.*, **1964,** *8*(5), 660–668.

[136] Barenholz, Y. Liposome application: problems and prospects. *Curr. Opin. Colloid Interface Sci.*, **2001,** *6*(1), 66–77.

[137] Torchilin, V.P. Recent advances with liposomes as pharmaceutical carriers. *Nat. Rev. Drug Discov.*, **2005,** *4*(2), 145–160.

[138] Huang, L.; Liu, Y. In vivo delivery of RNAi with lipid-based nanoparticles. *Annu. Rev. Biomed. Eng.*, **2011,** *13*, 507–530.

[139] Mishra, G.P.; Bagui, M.; Tamboli, V.; Mitra, A.K. Recent Applications of Liposomes in Ophthalmic Drug Delivery. *J. Drug Deliv.*, **2011,** *2011*, 1–14.

[140] Jesorka, A.; Orwar, O. Liposomes: Technologies and Analytical Applications. *Annu. Rev. Anal. Chem.*, **2008,** *1*(1), 801–832.

[141] Irache, J.M.; Esparza, I.; Gamazo, C.; Agüeros, M.; Espuelas, S. Nanomedicine: novel approaches in human and veterinary therapeutics. *Vet. Parasitol.*, **2011,** *180*(1–2), 47–71.

[142] Bangham, A.D.; Standish, M.M.; Watkins, J.C. Diffusion of univalent ions across the lamellae of swollen phospholipids. *J. Mol. Biol.*, **1965,** *13*(1), 238–252.

[143] Gregoriadis, G.; Ryman, B.E. Liposomes as carriers of enzymes or drugs: a new approach to the treatment of storage diseases. *Biochem. J.*, **1971,** *124*(5), 58P.

[144] Gregoriadis, G. The Carrier Potential of Liposomes in Biology and Medicine. *N. Engl. J. Med.*, **1976,** *295*(13), 704–710.

[145] Gregoriadis, G. The Carrier Potential of Liposomes in Biology and Medicine. *N. Engl.*

J. Med., **1976,** *295*(14), 765–770.

[146] Allen, T.M.; Cullis, P.R. Liposomal drug delivery systems: from concept to clinical applications. *Adv. Drug Deliv. Rev.*, **2013,** *65*(1), 36–48.

[147] Allen, T.; K. Cheng, W.; Hare, J.; Laginha, K. Pharmacokinetics and Pharmacodynamics of Lipidic Nano-Particles in Cancer. *Anticancer. Agents Med. Chem.*, **2006,** *6*(6), 513–523.

[148] Barenholz, Y. Doxil?? - The first FDA-approved nano-drug: Lessons learned. *J. Control. Release*, **2012,** *160*(2), 117–134.

[149] Kumar, V.; Palazzolo, S.; Bayda, S.; Corona, G.; Toffoli, G.; Rizzolio, F. DNA Nanotechnology for Cancer Therapy. *Theranostics*, **2016,** *6*(5), 710–725.

[150] Kumar, V.; Bayda, S.; Hadla, M.; Caligiuri, I.; Russo Spena, C.; Palazzolo, S.; Kempter, S.; Corona, G.; Toffoli, G.; Rizzolio, F. Enhanced Chemotherapeutic Behavior of Open-Caged DNA@Doxorubicin Nanostructures for Cancer Cells. *J. Cell. Physiol.*, **2016,** *231*(1), 106–110.

[151] Min, Y.; Caster, J.M.; Eblan, M.J.; Wang, A.Z. Clinical Translation of Nanomedicine. *Chem. Rev.*, **2015,** *115*(19), 11147–11190.

[152] Chatterjee, K.; Zhang, J.; Honbo, N.; Karliner, J.S. Doxorubicin Cardiomyopathy. *Cardiology*, **2010,** *115*(2), 155–162.

[153] Gabizon, A.; Catane, R.; Uziely, B.; Kaufman, B.; Safra, T.; Cohen, R.; Martin, F.; Huang, A.; Barenholz, Y. Prolonged circulation time and enhanced accumulation in malignant exudates of doxorubicin encapsulated in polyethylene-glycol coated liposomes. *Cancer Res.*, **1994,** *54*(4), 987–992.

[154] Wang, S.; Fan, W.; Kim, G.; Hah, H.J.; Lee, Y.-E.K.; Kopelman, R.; Ethirajan, M.; Gupta, A.; Goswami, L.N.; Pera, P.; Morgan, J.; Pandey, R.K. Novel methods to incorporate photosensitizers into nanocarriers for cancer treatment by photodynamic therapy. *Lasers Surg. Med.*, **2011,** *43*(7), 686–695.

[155] Elzoghby, A.O.; Samy, W.M.; Elgindy, N.A. Albumin-based nanoparticles as potential controlled release drug delivery systems. *J. Control. Release*, **2012,** *157*(2), 168–182.

[156] Choi, K.Y.; Chung, H.; Min, K.H.; Yoon, H.Y.; Kim, K.; Park, J.H.; Kwon, I.C.; Jeong, S.Y. Self-assembled hyaluronic acid nanoparticles for active tumor targeting. *Biomaterials*, **2010,** *31*(1), 106–114.

[157] Mocanu, G.; Nichifor, M.; Sacarescu, L. Dextran based polymeric micelles as carriers for delivery of hydrophobic drugs. *Curr. Drug Deliv.*, **2016,** *13*, 1–10.

[158] Agnihotri, S.A.; Mallikarjuna, N.N.; Aminabhavi, T.M. Recent advances on chitosan-based micro- and nanoparticles in drug delivery. *J. Control. Release*, **2004,** *100*(1), 5–28.

[159] Panyam, J.; Labhasetwar, V. Biodegradable nanoparticles for drug and gene delivery to cells and tissue. *Adv. Drug Deliv. Rev.*, **2003,** *55*(3), 329–347.

[160] Vauthier, C.; Bouchemal, K. Methods for the Preparation and Manufacture of Polymeric Nanoparticles. *Pharm. Res.*, **2009,** *26*(5), 1025–1058.

[161] Jain, R.A. The manufacturing techniques of various drug loaded biodegradable poly(lactide-co-glycolide) (PLGA) devices. *Biomaterials*, **2000,** *21*(23), 2475–2490.

[162] Kumari, A.; Yadav, S.K.; Yadav, S.C. Biodegradable polymeric nanoparticles based drug delivery systems. *Colloids Surfaces B Biointerfaces*, **2010,** *75*(1), 1–18.

[163] Allémann, E.; Leroux, J.C.; Gurny, R.; Doelker, E. In vitro extended-release properties of drug-loaded poly(DL-lactic acid) nanoparticles produced by a salting-out procedure. *Pharm. Res.*, **1993,** *10*(12), 1732–1737.

[164] Nair, L.S.; Laurencin, C.T. Biodegradable polymers as biomaterials. *Prog. Polym. Sci.*, **2007,** *32*(8–9), 762–798.

[165] Fasano, M.; Curry, S.; Terreno, E.; Galliano, M.; Fanali, G.; Narciso, P.; Notari, S.; Ascenzi, P. The extraordinary ligand binding properties of human serum albumin. *IUBMB Life (International Union Biochem. Mol. Biol. Life)*, **2005,** *57*(12), 787–796.

[166] Gong, J.; Huo, M.; Zhou, J.; Zhang, Y.; Peng, X.; Yu, D.; Zhang, H.; Li, J. Synthesis, characterization, drug-loading capacity and safety of novel octyl modified serum albumin micelles. *Int. J. Pharm.*, **2009,** *376*(1–2), 161–168.

[167] Kamaly, N.; Xiao, Z.; Valencia, P.M.; Radovic-Moreno, A.F.; Farokhzad, O.C. Targeted polymeric therapeutic nanoparticles: design, development and clinical translation. *Chem. Soc. Rev.*, **2012,** *41*(7), 2971–3010.

[168] Li, J.; Stayshich, R.M.; Meyer, T.Y. Exploiting Sequence To Control the Hydrolysis Behavior of Biodegradable PLGA Copolymers. *J. Am. Chem. Soc.*, **2011,** *133*(18), 6910–6913.

[169] Bertin, A. Emergence of Polymer Stereocomplexes for Biomedical Applications. *Macromol. Chem. Phys.*, **2012,** *213*(22), 2329–2352.

[170] Rancan, F.; Papakostas, D.; Hadam, S.; Hackbarth, S.; Delair, T.; Primard, C.; Verrier, B.; Sterry, W.; Blume-Peytavi, U.; Vogt, A. Investigation of Polylactic Acid (PLA) Nanoparticles as Drug Delivery Systems for Local Dermatotherapy. *Pharm. Res.*, **2009,** *26*(8), 2027–2036.

[171] Bikiaris, D.; Karavelidis; Karavas; Giliopoulos; Papadimitriou Evaluating the effects of crystallinity in new biocompatible polyester nanocarriers on drug release behavior. *Int. J. Nanomedicine*, **2011,** *6*, 3021.

[172] Danhier, F.; Ansorena, E.; Silva, J.M.; Coco, R.; Le Breton, A.; Préat, V. PLGA-based nanoparticles: An overview of biomedical applications. *J. Control. Release*, **2012,** *161*(2), 505–522.

[173] Makadia, H.K.; Siegel, S.J. Poly Lactic-co-Glycolic Acid (PLGA) as Biodegradable Controlled Drug Delivery Carrier. *Polymers (Basel).*, **2011,** *3*(4), 1377–1397.

[174] Amann, L.C.; Gandal, M.J.; Lin, R.; Liang, Y.; Siegel, S.J. In Vitro–In Vivo Correlations of Scalable PLGA-Risperidone Implants for the Treatment of Schizophrenia. *Pharm. Res.*, **2010,** *27*(8), 1730–1737.

[175] Faisant, N.; Siepmann, J.; Benoit, J.P. PLGA-based microparticles: elucidation of mechanisms and a new, simple mathematical model quantifying drug release. *Eur. J. Pharm. Sci.*, **2002,** *15*(4), 355–366.

[176] Ramchandani, M.; Robinson, D. In vitro and in vivo release of ciprofloxacin from PLGA 50:50 implants. *J. Control. Release*, **1998,** *54*(2), 167–175.

[177] Becker, R.; Dembek, C.; White, L.A.; Garrison, L.P. The cost offsets and cost–effectiveness associated with pegylated drugs: a review of the literature. *Expert Rev. Pharmacoecon. Outcomes Res.*, **2012,** *12*(6), 775–793.

[178] Kommareddy, S.; Tiwari, S.B.; Amiji, M.M. Long-Circulating Polymeric Nanovectors for Tumor-Selective Gene Delivery. *Technol. Cancer Res. Treat.*, **2005,** *4*(6), 615–625.

[179] Esmaeili, F.; Ghahremani, M.H.; Esmaeili, B.; Khoshayand, M.R.; Atyabi, F.; Dinarvand, R. PLGA nanoparticles of different surface properties: Preparation and evaluation of their body distribution. *Int. J. Pharm.*, **2008,** *349*(1–2), 249–255.

[180] Wani, M.C.; Taylor, H.L.; Wall, M.E.; Coggon, P.; McPhail, A.T. Plant antitumor agents. VI. Isolation and structure of taxol, a novel antileukemic and antitumor agent from Taxus brevifolia. *J. Am. Chem. Soc.*, **1971,** *93*(9), 2325–2327.

[181] Wood, A.J.J.; Rowinsky, E.K.; Donehower, R.C. Paclitaxel (Taxol). *N. Engl. J. Med.*, **1995,** *332*(15), 1004–1014.

[182] Gelderblom, H.; Verweij, J.; Nooter, K.; Sparreboom, A. Cremophor EL. *Eur. J. Cancer*, **2001,** *37*(13), 1590–1598.

[183] Paál, K.; Müller, J.; Hegedûs, L. High affinity binding of paclitaxel to human serum albumin. *Eur. J. Biochem.*, **2001,** *268*(7), 2187–2191.

[184] Hawkins, M.J.; Soon-Shiong, P.; Desai, N. Protein nanoparticles as drug carriers in clinical medicine. *Adv. Drug Deliv. Rev.*, **2008,** *60*(8), 876–885.

[185] Purcell, M.; Neault, J.F.; Tajmir-Riahi, H.A. Interaction of taxol with human serum albumin. *Biochim. Biophys. Acta - Protein Struct. Mol. Enzymol.*, **2000,** *1478*(1), 61–68.

[186] John, T.A.; Vogel, S.M.; Tiruppathi, C.; Malik, A.B.; Minshall, R.D. Quantitative analysis of albumin uptake and transport in the rat microvessel endothelial monolayer. *Am. J. Physiol. - Lung Cell. Mol. Physiol.*, **2003,** *284*(1), L187–L196.

[187] Desai, N. Increased Antitumor Activity, Intratumor Paclitaxel Concentrations, and Endothelial Cell Transport of Cremophor-Free, Albumin-Bound Paclitaxel, ABI-007, Compared with Cremophor-Based Paclitaxel. *Clin. Cancer Res.*, **2006,** *12*(4), 1317–1324.

[188] Arleth, L.; Ashok, B.; Onyuksel, H.; Thiyagarajan, P.; Jacob, J.; Hjelm, R.P. Detailed Structure of Hairy Mixed Micelles Formed by Phosphatidylcholine and PEGylated Phospholipids in Aqueous Media. *Langmuir*, **2005,** *21*(8), 3279–3290.

[189] Holmberg, K.; Jönsson, B.; Kronberg, B.; Lindman, B. *Surfactants and polymers in aqueous solution.*; Second Edi.; John Wiley & Sons, Ltd, **2002**, .

[190] Won, Y.-Y.; Brannan, A.K.; Davis, H.T.; Bates, F.S. Cryogenic Transmission Electron Microscopy (Cryo-TEM) of Micelles and Vesicles Formed in Water by Poly(ethylene oxide)-Based Block Copolymers. *J. Phys. Chem. B*, **2002,** *106*(13), 3354–3364.

[191] Meng, F.; Zhong, Z.; Feijen, J. Stimuli-Responsive Polymersomes for Programmed

Drug Delivery. *Biomacromolecules*, **2009,** *10*(2), 197–209.

[192] Battaglia, G.; Ryan, A.J. Bilayers and Interdigitation in Block Copolymer Vesicles. *J. Am. Chem. Soc.*, **2005,** *127*(24), 8757–8764.

[193] Li, Y.; Gao, G.H.; Lee, D.S. Stimulus-Sensitive Polymeric Nanoparticles and Their Applications as Drug and Gene Carriers. *Adv. Healthc. Mater.*, **2013,** *2*(3), 388–417.

[194] Feng, L.; Mumper, R.J. A critical review of lipid-based nanoparticles for taxane delivery. *Cancer Lett.*, **2013,** *334*(2), 157–175.

[195] Adams, M.L.; Lavasanifar, A.; Kwon, G.S. Amphiphilic block copolymers for drug delivery. *J. Pharm. Sci.*, **2003,** *92*(7), 1343–1355.

[196] Rösler, A.; Vandermeulen, G.W.; Klok, H.-A. Advanced drug delivery devices via self-assembly of amphiphilic block copolymers. *Adv. Drug Deliv. Rev.*, **2001,** *53*(1), 95–108.

[197] Lavasanifar, A.; Samuel, J.; Kwon, G.S. Poly(ethylene oxide)-block-poly(l-amino acid) micelles for drug delivery. *Adv. Drug Deliv. Rev.*, **2002,** *54*(2), 169–190.

[198] Torchilin, V.P. Structure and design of polymeric surfactant-based drug delivery systems. *J. Control. Release*, **2001,** *73*(2–3), 137–172.

[199] Torchilin, V.P. PEG-based micelles as carriers of contrast agents for different imaging modalities. *Adv. Drug Deliv. Rev.*, **2002,** *54*(2), 235–252.

[200] Acharya, S.; Sahoo, S.K. PLGA nanoparticles containing various anticancer agents and tumour delivery by EPR effect. *Adv. Drug Deliv. Rev.*, **2011,** *63*(3), 170–183.

[201] Jeong, B.; Kibbey, M.R.; Birnbaum, J.C.; Won, Y.-Y.; Gutowska, A. Thermogelling Biodegradable Polymers with Hydrophilic Backbones: PEG- g -PLGA. *Macromolecules*, **2000,** *33*(22), 8317–8322.

[202] Park, Y.J.; Lee, J.Y.; Chang, Y.S.; Jeong, J.M.; Chung, J.K.; Lee, M.C.; Park, K.B.; Lee, S.J. Radioisotope carrying polyethylene oxide–polycaprolactone copolymer micelles for targetable bone imaging. *Biomaterials*, **2002,** *23*(3), 873–879.

[203] Yokoyama, M. Characterization of physical entrapment and chemical conjugation of adriamycin in polymeric micelles and their design for in vivo delivery to a solid tumor. *J. Control. Release*, **1998,** *50*(1–3), 79–92.

[204] Nishiyama, N.; Okazaki, S.; Cabral, H.; Miyamoto, M.; Kato, Y.; Sugiyama, Y.; Nishio, K.; Matsumura, Y.; Kataoka, K. Novel cisplatin-incorporated polymeric micelles can eradicate solid tumors in mice. *Cancer Res.*, **2003,** *63*(24), 8977–8983.

[205] Chan, J.M.; Zhang, L.; Yuet, K.P.; Liao, G.; Rhee, J.-W.; Langer, R.; Farokhzad, O.C. PLGA–lecithin–PEG core–shell nanoparticles for controlled drug delivery. *Biomaterials*, **2009,** *30*(8), 1627–1634.

[206] Veronese, F.M.; Schiavon, O.; Pasut, G.; Mendichi, R.; Andersson, L.; Tsirk, A.; Ford, J.; Wu, G.; Kneller, S.; Davies, J.; Duncan, R. PEG−Doxorubicin Conjugates: Influence of Polymer Structure on Drug Release, in Vitro Cytotoxicity, Biodistribution, and Antitumor Activity. *Bioconjug. Chem.*, **2005,** *16*(4), 775–784.

[207] Lalatsa, A.; Schätzlein, A.G.; Mazza, M.; Le, T.B.H.; Uchegbu, I.F. Amphiphilic

poly(l-amino acids) — New materials for drug delivery. *J. Control. Release*, **2012,** *161*(2), 523–536.

[208] Zhang, C.Y.; Wu, W.S.; Yao, N.; Zhao, B.; Zhang, L.J. pH-sensitive amphiphilic copolymer brush Chol-g-P(HEMA-co-DEAEMA)-b-PPEGMA: synthesis and self-assembled micelles for controlled anti-cancer drug release. *RSC Adv.*, **2014,** *4*(76), 40232.

[209] Kim, S.C.; Kim, D.W.; Shim, Y.H.; Bang, J.S.; Oh, H.S.; Kim, S.W.; Seo, M.H. In vivo evaluation of polymeric micellar paclitaxel formulation: toxicity and efficacy. *J. Control. Release*, **2001,** *72*(1–3), 191–202.

[210] Tomalia, D.A.; Naylor, A.M.; Goddard, W.A. Starburst Dendrimers: Molecular-Level Control of Size, Shape, Surface Chemistry, Topology, and Flexibility from Atoms to Macroscopic Matter. *Angew. Chemie Int. Ed. English*, **1990,** *29*(2), 138–175.

[211] Bronstein, L.M.; Shifrina, Z.B. Dendrimers as Encapsulating, Stabilizing, or Directing Agents for Inorganic Nanoparticles. *Chem. Rev.*, **2011,** *111*(9), 5301–5344.

[212] Ihre, H.; Hult, A.; Fréchet, J.M.J.; Gitsov, I. Double-Stage Convergent Approach for the Synthesis of Functionalized Dendritic Aliphatic Polyesters Based on 2,2-Bis(hydroxymethyl)propionic Acid. *Macromolecules*, **1998,** *31*(13), 4061–4068.

[213] L'Abbé, G.; Forier, B.; Dehaen, W. A fast double-stage convergent synthesis of dendritc polyethers. *Chem. Commun.*, **1996,** (18), 2143–2144.

[214] Kawaguchi, T.; Walker, K.L.; Wilkins, C.L.; Moore, J.S. Double Exponential Dendrimer Growth. *J. Am. Chem. Soc.*, **1995,** *117*(8), 2159–2165.

[215] Kesharwani, P.; Jain, K.; Jain, N.K. Dendrimer as nanocarrier for drug delivery. *Prog. Polym. Sci.*, **2014,** *39*(2), 268–307.

[216] Bhadra, D.; Yadav, A.K.; Bhadra, S.; Jain, N.K. Glycodendrimeric nanoparticulate carriers of primaquine phosphate for liver targeting. *Int. J. Pharm.*, **2005,** *295*(1–2), 221–233.

[217] Kono, K.; Liu, M.; Fréchet, J.M.J. Design of Dendritic Macromolecules Containing Folate or Methotrexate Residues. *Bioconjug. Chem.*, **1999,** *10*(6), 1115–1121.

[218] Dutta, T.; Aghase, H.B.; Vijayarajkumar, P.; Joshi, M.; Jain, N.K. Dendrosome-based gene delivery. *J. Exp. Nanosci.*, **2006,** *1*(2), 235–248.

[219] Khopade, A.J.; Caruso, F.; Tripathi, P.; Nagaich, S.; Jain, N.K. Effect of dendrimer on entrapment and release of bioactive from liposomes. *Int. J. Pharm.*, **2002,** *232*(1–2), 157–162.

[220] Chaplot, S.P.; Rupenthal, I.D. Dendrimers for gene delivery - a potential approach for ocular therapy? *J. Pharm. Pharmacol.*, **2014,** *66*(4), 542–556.

[221] Ciolkowski, M.; Pałecz, B.; Appelhans, D.; Voit, B.; Klajnert, B.; Bryszewska, M. The influence of maltose modified poly(propylene imine) dendrimers on hen egg white lysozyme structure and thermal stability. *Colloids Surfaces B Biointerfaces*, **2012,** *95*, 103–108.

[222] Gurdag, S.; Khandare, J.; Stapels, S.; Matherly, L.H.; Kannan, R.M. Activity of

Dendrimer−Methotrexate Conjugates on Methotrexate-Sensitive and -Resistant Cell Lines. *Bioconjug. Chem.*, **2006,** *17*(2), 275–283.

[223] Grassi, M.; Bonora, G.M.; Drioli, S.; Cateni, F.; Zacchigna, M. Pharmacokinetic analysis of multi PEG–theophylline conjugates. *Comput. Biol. Chem.*, **2012,** *40*, 7–14.

[224] Siewiera, K.; Labieniec-Watala, M. Ambiguous effect of dendrimer PAMAM G3 on rat heart respiration in a model of an experimental diabetes – Objective causes of laboratory misfortune or unpredictable G3 activity? *Int. J. Pharm.*, **2012,** *430*(1–2), 258–265.

[225] Yang, W.; Cheng, Y.; Xu, T.; Wang, X.; Wen, L. Targeting cancer cells with biotin–dendrimer conjugates. *Eur. J. Med. Chem.*, **2009,** *44*(2), 862–868.

[226] Imae, T.; Hamaguchi, S. Network of sodium hyaluronate with nano-knots junction of poly(amido amine) dendrimer. *Carbohydr. Polym.*, **2012,** *88*(1), 352–360.

[227] Konda, S.D.; Wang, S.; Brechbiel, M.; Wiener, E.C. Biodistribution of a 153 Gd-folate dendrimer, generation = 4, in mice with folate-receptor positive and negative ovarian tumor xenografts. *Invest. Radiol.*, **2002,** *37*(4), 199–204.

[228] Kojima, C.; Kono, K.; Maruyama, K.; Takagishi, T. Synthesis of Polyamidoamine Dendrimers Having Poly(ethylene glycol) Grafts and Their Ability To Encapsulate Anticancer Drugs. *Bioconjug. Chem.*, **2000,** *11*(6), 910–917.

[229] Gajbhiye, V.; Vijayaraj Kumar, P.; Tekade, R.K.; Jain, N.K. PEGylated PPI dendritic architectures for sustained delivery of H2 receptor antagonist. *Eur. J. Med. Chem.*, **2009,** *44*(3), 1155–1166.

[230] Pan, S.; Wang, C.; Zeng, X.; Wen, Y.; Wu, H.; Feng, M. Short multi-armed polylysine-graft-polyamidoamine copolymer as efficient gene vectors. *Int. J. Pharm.*, **2011,** *420*(2), 206–215.

[231] J. Jansen, B.A.; van der Zwan, J.; Reedijk, J.; den Dulk, H.; Brouwer, J. A Tetranuclear Platinum Compound Designed to Overcome Cisplatin Resistance. *Eur. J. Inorg. Chem.*, **1999,** *1999*(9), 1429–1433.

[232] Thomas, T.P.; Huang, B.; Choi, S.K.; Silpe, J.E.; Kotlyar, A.; Desai, A.M.; Zong, H.; Gam, J.; Joice, M.; Baker, J.R. Polyvalent Dendrimer-Methotrexate as a Folate Receptor-Targeted Cancer Therapeutic. *Mol. Pharm.*, **2012,** *9*(9), 2669–2676.

[233] Zhu, S.; Hong, M.; Zhang, L.; Tang, G.; Jiang, Y.; Pei, Y. PEGylated PAMAM Dendrimer-Doxorubicin Conjugates: In Vitro Evaluation and In Vivo Tumor Accumulation. *Pharm. Res.*, **2010,** *27*(1), 161–174.

[234] Khandare, J.J.; Jayant, S.; Singh, A.; Chandna, P.; Wang, Y.; Vorsa, N.; Minko, T. Dendrimer Versus Linear Conjugate: Influence of Polymeric Architecture on the Delivery and Anticancer Effect of Paclitaxel. *Bioconjug. Chem.*, **2006,** *17*(6), 1464–1472.

[235] Svenson, S.; Chauhan, A.S. Dendrimers for enhanced drug solubilization. *Nanomedicine*, **2008,** *3*(5), 679–702.

[236] Morgan, M.T.; Carnahan, M.A.; Immoos, C.E.; Ribeiro, A.A.; Finkelstein, S.; Lee, S.J.; Grinstaff, M.W. Dendritic Molecular Capsules for Hydrophobic Compounds. *J. Am.*

Chem. Soc., **2003,** *125*(50), 15485–15489.

[237] Morgan, M.T.; Carnahan, M.A.; Finkelstein, S.; Prata, C.A.H.; Degoricija, L.; Lee, S.J.; Grinstaff, M.W. Dendritic supramolecular assemblies for drug delivery. *Chem. Commun.*, **2005,** (34), 4309.

[238] Morgan, M.T.; Nakanishi, Y.; Kroll, D.J.; Griset, A.P.; Carnahan, M.A.; Wathier, M.; Oberlies, N.H.; Manikumar, G.; Wani, M.C.; Grinstaff, M.W. Dendrimer-Encapsulated Camptothecins: Increased Solubility, Cellular Uptake, and Cellular Retention Affords Enhanced Anticancer Activity In vitro. *Cancer Res.*, **2006,** *66*(24), 11913–11921.

[239] Neerman, M.F.; Chen, H.-T.; Parrish, A.R.; Simanek, E.E. Reduction of Drug Toxicity Using Dendrimers Based on Melamine. *Mol. Pharm.*, **2004,** *1*(5), 390–393.

[240] Papagiannaros, A.; Dimas, K.; Papaioannou, G.T.; Demetzos, C. Doxorubicin–PAMAM dendrimer complex attached to liposomes: Cytotoxic studies against human cancer cell lines. *Int. J. Pharm.*, **2005,** *302*(1–2), 29–38.

[241] Cheng, Y.; Wang, J.; Rao, T.; He, X.; Xu, T. Pharmaceutical applications of dendrimers: promising nanocarriers for drug delivery. *Front. Biosci.*, **2008,** *13*, 1447–1471.

[242] Li, M.-H.; Choi, S.K.; Thomas, T.P.; Desai, A.; Lee, K.-H.; Kotlyar, A.; Banaszak Holl, M.M.; Baker, J.R. Dendrimer-based multivalent methotrexates as dual acting nanoconjugates for cancer cell targeting. *Eur. J. Med. Chem.*, **2012,** *47*(1), 560–72.

[243] Slowing, I.I.; Vivero-Escoto, J.L.; Trewyn, B.G.; Lin, V.S.-Y. Mesoporous silica nanoparticles: structural design and applications. *J. Mater. Chem.*, **2010,** *20*(37), 7924.

[244] Lu, J.; Choi, E.; Tamanoi, F.; Zink, J.I. Light-Activated Nanoimpeller-Controlled Drug Release in Cancer Cells. *Small*, **2008,** *4*(4), 421–426.

[245] Yang, P.; Gai, S.; Lin, J. Functionalized mesoporous silica materials for controlled drug delivery. *Chem. Soc. Rev.*, **2012,** *41*(9), 3679–3698.

[246] Stöber, W.; Fink, A.; Bohn, E. Controlled growth of monodisperse silica spheres in the micron size range. *J. Colloid Interface Sci.*, **1968,** *26*(1), 62–69.

[247] Liu, J.; Qiao, S.Z.; Liu, H.; Chen, J.; Orpe, A.; Zhao, D.; Lu, G.Q.M. Extension of The Stöber Method to the Preparation of Monodisperse Resorcinol-Formaldehyde Resin Polymer and Carbon Spheres. *Angew. Chemie Int. Ed.*, **2011,** *50*(26), 5947–5951.

[248] Choma, J.; Jamioła, D.; Augustynek, K.; Marszewski, M.; Gao, M.; Jaroniec, M. New opportunities in Stöber synthesis: preparation of microporous and mesoporous carbon spheres. *J. Mater. Chem.*, **2012,** *22*(25), 12636.

[249] Grün, M.; Lauer, I.; Unger, K.K. The synthesis of micrometer- and submicrometer-size spheres of ordered mesoporous oxide MCM-41. *Adv. Mater.*, **1997,** *9*(3), 254–257.

[250] Nooney, R.I.; Thirunavukkarasu, D.; Chen, Y.; Josephs, R.; Ostafin, A.E. Synthesis of Nanoscale Mesoporous Silica Spheres with Controlled Particle Size. *Chem. Mater.*, **2002,** *14*(11), 4721–4728.

[251] Lin, Y.-S.; Tsai, C.-P.; Huang, H.-Y.; Kuo, C.-T.; Hung, Y.; Huang, D.-M.; Chen, Y.-C.; Mou, C.-Y. Well-Ordered Mesoporous Silica Nanoparticles as Cell Markers. *Chem.*

Mater., **2005,** *17*(18), 4570–4573.

[252] Lu, F.; Wu, S.-H.; Hung, Y.; Mou, C.-Y. Size Effect on Cell Uptake in Well-Suspended, Uniform Mesoporous Silica Nanoparticles. *Small*, **2009,** *5*(12), 1408–1413.

[253] Qiao, Z.-A.; Zhang, L.; Guo, M.; Liu, Y.; Huo, Q. Synthesis of Mesoporous Silica Nanoparticles via Controlled Hydrolysis and Condensation of Silicon Alkoxide. *Chem. Mater.*, **2009,** *21*(16), 3823–3829.

[254] Chiang, Y.-D.; Lian, H.-Y.; Leo, S.-Y.; Wang, S.-G.; Yamauchi, Y.; Wu, K.C.-W. Controlling Particle Size and Structural Properties of Mesoporous Silica Nanoparticles Using the Taguchi Method. *J. Phys. Chem. C*, **2011,** *115*(27), 13158–13165.

[255] Zeng, W.; Qian, X.-F.; Zhang, Y.-B.; Yin, J.; Zhu, Z.-K. Organic modified mesoporous MCM-41 through solvothermal process as drug delivery system. *Mater. Res. Bull.*, **2005,** *40*(5), 766–772.

[256] Lee, C.-H.; Cheng, S.-H.; Wang, Y.-J.; Chen, Y.-C.; Chen, N.-T.; Souris, J.; Chen, C.-T.; Mou, C.-Y.; Yang, C.-S.; Lo, L.-W. Near-Infrared Mesoporous Silica Nanoparticles for Optical Imaging: Characterization and In Vivo Biodistribution. *Adv. Funct. Mater.*, **2009,** *19*(2), 215–222.

[257] Hsiao, J.-K.; Tsai, C.-P.; Chung, T.-H.; Hung, Y.; Yao, M.; Liu, H.-M.; Mou, C.-Y.; Yang, C.-S.; Chen, Y.-C.; Huang, D.-M. Mesoporous Silica Nanoparticles as a Delivery System of Gadolinium for Effective Human Stem Cell Tracking. *Small*, **2008,** *4*(9), 1445–1452.

[258] Na, H. Bin; Hyeon, T. Nanostructured T1 MRI contrast agents. *J. Mater. Chem.*, **2009,** *19*(35), 6267.

[259] Taylor, K.M.L.; Kim, J.S.; Rieter, W.J.; An, H.; Lin, W.; Lin, W. Mesoporous Silica Nanospheres as Highly Efficient MRI Contrast Agents. *J. Am. Chem. Soc.*, **2008,** *130*(7), 2154–2155.

[260] Cotí, K.K.; Belowich, M.E.; Liong, M.; Ambrogio, M.W.; Lau, Y.A.; Khatib, H.A.; Zink, J.I.; Khashab, N.M.; Stoddart, J.F. Mechanised nanoparticles for drug delivery. *Nanoscale*, **2009,** *1*(1), 16.

[261] Vivero-Escoto, J.L.; Slowing, I.I.; Trewyn, B.G.; Lin, V.S.-Y. Mesoporous Silica Nanoparticles for Intracellular Controlled Drug Delivery. *Small*, **2010,** *6*(18), 1952–1967.

[262] Cheng, S.-H.; Lee, C.-H.; Yang, C.-S.; Tseng, F.-G.; Mou, C.-Y.; Lo, L.-W. Mesoporous silica nanoparticles functionalized with an oxygen-sensing probe for cell photodynamic therapy: potential cancer theranostics. *J. Mater. Chem.*, **2009,** *19*(9), 1252.

[263] Cheng, S.-H.; Lee, C.-H.; Chen, M.-C.; Souris, J.S.; Tseng, F.-G.; Yang, C.-S.; Mou, C.-Y.; Chen, C.-T.; Lo, L.-W. Tri-functionalization of mesoporous silica nanoparticles for comprehensive cancer theranostics—the trio of imaging, targeting and therapy. *J. Mater. Chem.*, **2010,** *20*(29), 6149.

[264] Couleaud, P.; Morosini, V.; Frochot, C.; Richeter, S.; Raehm, L.; Durand, J.-O. Silica-based nanoparticles for photodynamic therapy applications. *Nanoscale*, **2010,** *2*(7), 1083.

[265] Guo, H.; Qian, H.; Idris, N.M.; Zhang, Y. Singlet oxygen-induced apoptosis of cancer cells using upconversion fluorescent nanoparticles as a carrier of photosensitizer. *Nanomedicine Nanotechnology, Biol. Med.*, **2010,** *6*(3), 486–495.

[266] Kim, H.-J.; Shin, K.-J.; Han, M.K.; An, K.; Lee, J.-K.; Honma, I.; Kim, H. One-pot synthesis of multifunctional mesoporous silica nanoparticle incorporated with zinc(II) phthalocyanine and iron oxide. *Scr. Mater.*, **2009,** *61*(12), 1137–1140.

[267] Tu, H.-L.; Lin, Y.-S.; Lin, H.-Y.; Hung, Y.; Lo, L.-W.; Chen, Y.-F.; Mou, C.-Y. In vitro Studies of Functionalized Mesoporous Silica Nanoparticles for Photodynamic Therapy. *Adv. Mater.*, **2009,** *21*(2), 172–177.

[268] Yang, Y.; Song, W.; Wang, A.; Zhu, P.; Fei, J.; Li, J. Lipid coated mesoporous silica nanoparticles as photosensitive drug carriers. *Phys. Chem. Chem. Phys.*, **2010,** *12*(17), 4418.

[269] Vivero-Escoto, J.L.; Slowing, I.I.; Wu, C.-W.; Lin, V.S.-Y. Photoinduced Intracellular Controlled Release Drug Delivery in Human Cells by Gold-Capped Mesoporous Silica Nanosphere. *J. Am. Chem. Soc.*, **2009,** *131*(10), 3462–3463.

[270] Lu, J.; Liong, M.; Sherman, S.; Xia, T.; Kovochich, M.; Nel, A.E.; Zink, J.I.; Tamanoi, F. Mesoporous Silica Nanoparticles for Cancer Therapy: Energy-Dependent Cellular Uptake and Delivery of Paclitaxel to Cancer Cells. *NanoBiotechnology*, **2007,** *3*(2), 89–95.

[271] Lee, J.E.; Lee, N.; Kim, H.; Kim, J.; Choi, S.H.; Kim, J.H.; Kim, T.; Song, I.C.; Park, S.P.; Moon, W.K.; Hyeon, T. Uniform Mesoporous Dye-Doped Silica Nanoparticles Decorated with Multiple Magnetite Nanocrystals for Simultaneous Enhanced Magnetic Resonance Imaging, Fluorescence Imaging, and Drug Delivery. *J. Am. Chem. Soc.*, **2010,** *132*(2), 552–557.

[272] Lebold, T.; Jung, C.; Michaelis, J.; Bräuchle, C. Nanostructured Silica Materials As Drug-Delivery Systems for Doxorubicin: Single Molecule and Cellular Studies. *Nano Lett.*, **2009,** *9*(8), 2877–2883.

[273] Rosenholm, J.M.; Peuhu, E.; Bate-Eya, L.T.; Eriksson, J.E.; Sahlgren, C.; Lindén, M. Cancer-Cell-Specific Induction of Apoptosis Using Mesoporous Silica Nanoparticles as Drug-Delivery Vectors. *Small*, **2010,** *6*(11), 1234–1241.

[274] Mortera, R.; Vivero-Escoto, J.; Slowing, I.I.; Garrone, E.; Onida, B.; Lin, V.S.-Y. Cell-induced intracellular controlled release of membrane impermeable cysteine from a mesoporous silica nanoparticle-based drug delivery system. *Chem. Commun.*, **2009,** (22), 3219.

[275] Zhang, Y.; Zhi, Z.; Jiang, T.; Zhang, J.; Wang, Z.; Wang, S. Spherical mesoporous silica nanoparticles for loading and release of the poorly water-soluble drug telmisartan. *J. Control. Release*, **2010,** *145*(3), 257–263.

[276] Lin, Q.; Huang, Q.; Li, C.; Bao, C.; Liu, Z.; Li, F.; Zhu, L. Anticancer Drug Release from a Mesoporous Silica Based Nanophotocage Regulated by Either a One- or Two-Photon Process. *J. Am. Chem. Soc.*, **2010,** *132*(31), 10645–10647.

[277] Slowing, I.I.; Vivero-Escoto, J.L.; Wu, C.-W.; Lin, V.S.-Y. Mesoporous silica nanoparticles as controlled release drug delivery and gene transfection carriers. *Adv.*

Drug Deliv. Rev., **2008,** *60*(11), 1278–1288.

[278] Brevet, D.; Gary-Bobo, M.; Raehm, L.; Richeter, S.; Hocine, O.; Amro, K.; Loock, B.; Couleaud, P.; Frochot, C.; Morère, A.; Maillard, P.; Garcia, M.; Durand, J.-O. Mannose-targeted mesoporous silica nanoparticles for photodynamic therapy. *Chem. Commun.*, **2009,** (12), 1475.

[279] Gary-Bobo, M.; Hocine, O.; Brevet, D.; Maynadier, M.; Raehm, L.; Richeter, S.; Charasson, V.; Loock, B.; Morère, A.; Maillard, P.; Garcia, M.; Durand, J.-O. Cancer therapy improvement with mesoporous silica nanoparticles combining targeting, drug delivery and PDT. *Int. J. Pharm.*, **2012,** *423*(2), 509–515.

[280] Lebret, V.; Raehm, L.; Durand, J.-O.; Smaïhi, M.; Werts, M.H. V.; Blanchard-Desce, M.; Méthy-Gonnod, D.; Dubernet, C. Folic Acid-Targeted Mesoporous Silica Nanoparticles for Two-Photon Fluorescence. *J. Biomed. Nanotechnol.*, **2010,** *6*(2), 176–180.

[281] Rosenholm, J.M.; Meinander, A.; Peuhu, E.; Niemi, R.; Eriksson, J.E.; Sahlgren, C.; Lindén, M. Targeting of Porous Hybrid Silica Nanoparticles to Cancer Cells. *ACS Nano*, **2009,** *3*(1), 197–206.

[282] Tsai, C.-P.; Chen, C.-Y.; Hung, Y.; Chang, F.-H.; Mou, C.-Y. Monoclonal antibody-functionalized mesoporous silica nanoparticles (MSN) for selective targeting breast cancer cells. *J. Mater. Chem.*, **2009,** *19*(32), 5737.

[283] de Oliveira, L.F.; Bouchmella, K.; Gonçalves, K. de A.; Bettini, J.; Kobarg, J.; Cardoso, M.B. Functionalized Silica Nanoparticles As an Alternative Platform for Targeted Drug-Delivery of Water Insoluble Drugs. *Langmuir*, **2016,** *32*(13), 3217–3225.

[284] Li, H.; Zhang, J.Z.; Tang, Q.; Du, M.; Hu, J.; Yang, D. Reduction-responsive drug delivery based on mesoporous silica nanoparticle core with crosslinked poly(acrylic acid) shell. *Mater. Sci. Eng. C*, **2013,** *33*(6), 3426–3431.

[285] Giljohann, D.A.; Seferos, D.S.; Daniel, W.L.; Massich, M.D.; Patel, P.C.; Mirkin, C.A. Gold nanoparticles for biology and medicine. *Angew. Chem. Int. Ed. Engl.*, **2010,** *49*(19), 3280–3294.

[286] Edwards, P.P.; Thomas, J.M. Gold in a metallic divided state--from Faraday to present-day nanoscience. *Angew. Chem. Int. Ed. Engl.*, **2007,** *46*(29), 5480–5486.

[287] Jain, P.K.; Huang, X.; El-Sayed, I.H.; El-Sayed, M.A. Noble metals on the nanoscale: optical and photothermal properties and some applications in imaging, sensing, biology, and medicine. *Acc. Chem. Res.*, **2008,** *41*(12), 1578–1586.

[288] Jain, P.K.; Lee, K.S.; El-Sayed, I.H.; El-Sayed, M.A. Calculated absorption and scattering properties of gold nanoparticles of different size, shape, and composition: applications in biological imaging and biomedicine. *J. Phys. Chem. B*, **2006,** *110*(14), 7238–7248.

[289] Huang, X.; El-Sayed, M.A. Gold nanoparticles: Optical properties and implementations in cancer diagnosis and photothermal therapy. *J. Adv. Res.*, **2010,** *1*(1), 13–28.

[290] Abadeer, N.S.; Murphy, C.J. Recent Progress in Cancer Thermal Therapy Using Gold Nanoparticles. *J. Phys. Chem. C*, **2016,** *120*(9), 4691–4716.

[291] Turkevich, J.; Stevenson, P.C.; Hillier, J. A study of the nucleation and growth processes in the synthesis of colloidal gold. *Discuss. Faraday Soc.*, **1951,** *11*, 55.

[292] Kimling, J.; Maier, M.; Okenve, B.; Kotaidis, V.; Ballot, H.; Plech, A. Turkevich method for gold nanoparticle synthesis revisited. *J. Phys. Chem. B*, **2006,** *110*(32), 15700–15707.

[293] Brust, M.; Walker, M.; Bethell, D.; Schiffrin, D.J.; Whyman, R. Synthesis of thiol-derivatised gold nanoparticles in a two-phase Liquid–Liquid system. *J. Chem. Soc., Chem. Commun.*, **1994,** , 801–802.

[294] Waters, C.A.; Mills, A.J.; Johnson, K.A.; Schiffrin, D.J. Purification of dodecanethiol derivatised gold nanoparticles. *Chem. Commun. (Camb).*, **2003,** , 540–541.

[295] Yonezawa, T.; Kunitake, T. Practical preparation of anionic mercapto ligand-stabilized gold nanoparticles and their immobilization. *Colloids Surf. A. Physicochem. Eng. Asp.*, **1999,** *149*(1–3), 193–199.

[296] Jin, Y.; Wang, P.; Yin, D.; Liu, J.; Qin, L.; Yu, N.; Xie, G.; Li, B. Gold nanoparticles prepared by sonochemical method in thiol-functionalized ionic liquid. *Colloids Surf. A. Physicochem. Eng. Asp.*, **2007,** *302*(1–3), 366–370.

[297] Abyaneh, M.K.; Paramanik, D.; Varma, S.; Gosavi, S.W.; Kulkarni, S.K. Formation of gold nanoparticles in polymethylmethacrylate by UV irradiation. *J. Phys. D. Appl. Phys.*, **2007,** *40*(12), 3771–3779.

[298] Warren, S.C.; Jackson, A.C.; Cater-Cyker, Z.D.; DiSalvo, F.J.; Wiesner, U. Nanoparticle synthesis via the photochemical polythiol process. *J. Am. Chem. Soc.*, **2007,** *129*(33), 10072–10073.

[299] Mukherjee, P.; Ahmad, A.; Mandal, D.; Senapati, S.; Sainkar, S.R.; Khan, M.I.; Ramani, R.; Parischa, R.; Ajayakumar, P. V.; Alam, M.; Sastry, M.; Kumar, R. Bioreduction of AuCl4- Ions by the Fungus, Verticillium sp. and Surface Trapping of the Gold Nanoparticles Formed. *Angew. Chem. Int. Ed. Engl.*, **2001,** *40*(19), 3585–3588.

[300] Islam, N.U.; Jalil, K.; Shahid, M.; Rauf, A.; Muhammad, N.; Khan, A.; Shah, M.R.; Khan, M.A. Green synthesis and biological activities of gold nanoparticles functionalized with Salix alba. *Arab. J. Chem.*, **2015,** , In Press.

[301] Frens, G. Particle size and sol stability in metal colloids. *Kolloid-Z. u. Z. Polym.*, **1972,** *250*(7), 736–741.

[302] Frens, G. Controlled Nucleation for the Regulation of the Particle Size in Monodisperse Gold Suspensions. *Nat. Phys. Sci.*, **1973,** *241*(105), 20–22.

[303] Brust, M.; Fink, J.; Bethell, D.; Schiffrin, D.J.; Kiely, C. Synthesis and reactions of functionalised gold nanoparticles. *J. Chem. Soc. Chem. Commun.*, **1995,** , 1655–1656.

[304] Primo, A.; Corma, A.; García, H. Titania supported gold nanoparticles as photocatalyst. *Phys. Chem. Chem. Phys.*, **2011,** *13*(3), 886–910.

[305] Jana, N.R.; Gearheart, L.; Murphy, C.J. Seed-Mediated Growth Approach for Shape-Controlled Synthesis of Spheroidal and Rod-like Gold Nanoparticles Using a Surfactant Template. *Adv. Mater.*, **2001,** *13*(18), 1389–1393.

[306] Murphy, C.J.; Thompson, L.B.; Chernak, D.J.; Yang, J.A.; Sivapalan, S.T.; Boulos, S.P.; Huang, J.; Alkilany, A.M.; Sisco, P.N. Gold nanorod crystal growth: From seed-mediated synthesis to nanoscale sculpting. *Curr. Opin. Colloid Interface Sci.*, **2011,** *16*(2), 128–134.

[307] Xia, Y.; Li, W.; Cobley, C.M.; Chen, J.; Xia, X.; Zhang, Q.; Yang, M.; Cho, E.C.; Brown, P.K. Gold nanocages: from synthesis to theranostic applications. *Acc. Chem. Res.*, **2011,** *44*(10), 914–924.

[308] Chen, J.; Saeki, F.; Wiley, B.J.; Cang, H.; Cobb, M.J.; Li, Z.-Y.; Au, L.; Zhang, H.; Kimmey, M.B.; Li, X.; Xia, Y. Gold nanocages: bioconjugation and their potential use as optical imaging contrast agents. *Nano Lett.*, **2005,** *5*(3), 473–7.

[309] Skrabalak, S.E.; Chen, J.; Sun, Y.; Lu, X.; Au, L.; Cobley, C.M.; Xia, Y. Gold nanocages: synthesis, properties, and applications. *Acc. Chem. Res.*, **2008,** *41*(12), 1587–1595.

[310] Bridges, C.R.; DiCarmine, P.M.; Fokina, A.; Huesmann, D.; Seferos, D.S. Synthesis of gold nanotubes with variable wall thicknesses. *J. Mater. Chem. A*, **2013,** *1*(4), 1127–1133.

[311] Brown, K.R.; Natan, M.J. Hydroxylamine Seeding of Colloidal Au Nanoparticles in Solution and on Surfaces. *Langmuir*, **1998,** *14*(4), 726–728.

[312] Jana, N.R.; Gearheart, L.; Murphy, C.J. Seeding Growth for Size Control of 5−40 nm Diameter Gold Nanoparticles. *Langmuir*, **2001,** *17*(22), 6782–6786.

[313] Xu, Z.-C.; Shen, C.-M.; Xiao, C.-W.; Yang, T.-Z.; Zhang, H.-R.; Li, J.-Q.; Li, H.-L.; Gao, H.-J. Wet chemical synthesis of gold nanoparticles using silver seeds: a shape control from nanorods to hollow spherical nanoparticles. *Nanotechnology*, **2007,** *18*(11), 115608.

[314] Jana, N.R.; Gearheart, L.; Murphy, C.J. Wet Chemical Synthesis of High Aspect Ratio Cylindrical Gold Nanorods. *J. Phys. Chem. B*, **2001,** *105*(19), 4065–4067.

[315] Busbee, B.D.; Obare, S.O.; Murphy, C.J. An Improved Synthesis of High-Aspect-Ratio Gold Nanorods. *Adv. Mater.*, **2003,** *15*(5), 414–416.

[316] Duong, V.T.; Thuong, T.T.; Lien, N.T.H.; Hoa, D.Q.; Nhung, T.H. The Light-to-heat Conversion of Gold Nanoshells and Nanorods in Tissues. *Commun. Phys.*, **2014,** *24*(3S2), 83–88.

[317] Oldenburg, S.J.; Averitt, R.D.; Westcott, S.L.; Halas, N.J. Nanoengineering of optical resonances. *Chem. Phys. Lett.*, **1998,** *288*(2–4), 243–247.

[318] Prodan, E. A Hybridization Model for the Plasmon Response of Complex Nanostructures. *Science*, **2003,** *302*(5644), 419–422.

[319] Mayle, K.M.; Dern, K.R.; Wong, V.K.; Sung, S.; Ding, K.; Rodriguez, A.R.; Taylor, Z.; Zhou, Z.H.; Grundfest, W.S.; Deming, T.J.; Kamei, D.T. Polypeptide-Based Gold Nanoshells for Photothermal Therapy. *J. Lab. Autom.*, **2016,** [Epub ahead of print].

[320] Gao, Y.; Li, Y.; Wang, Y.; Chen, Y.; Gu, J.; Zhao, W.; Ding, J.; Shi, J. Controlled synthesis of multilayered gold nanoshells for enhanced photothermal therapy and SERS detection. *Small*, **2015,** *11*(1), 77–83.

[321] Zhou, C.; Tsai, T.-H.; Adler, D.C.; Lee, H.-C.; Cohen, D.W.; Mondelblatt, A.; Wang, Y.; Connolly, J.L.; Fujimoto, J.G. Photothermal optical coherence tomography in ex vivo human breast tissues using gold nanoshells. *Opt. Lett.*, **2010,** *35*(5), 700–702.

[322] Kah, J.C.Y.; Olivo, M.; Chow, T.H.; Song, K.S.; Koh, K.Z.Y.; Mhaisalkar, S.; Sheppard, C.J.R. Control of optical contrast using gold nanoshells for optical coherence tomography imaging of mouse xenograft tumor model in vivo. *J. Biomed. Opt.*, **2009,** *14*(5), 54015.

[323] Wang, Y.; Xie, X.; Wang, X.; Ku, G.; Gill, K.L.; O'Neal, D.P.; Stoica, G.; Wang, L. V. Photoacoustic Tomography of a Nanoshell Contrast Agent in the in Vivo Rat Brain. *Nano Lett.*, **2004,** *4*(9), 1689–1692.

[324] Weber, V.; Feis, A.; Gellini, C.; Pilot, R.; Salvi, P.R.; Signorini, R. Far- and near-field properties of gold nanoshells studied by photoacoustic and surface-enhanced Raman spectroscopies. *Phys. Chem. Chem. Phys.*, **2015,** *17*(33), 21190–21197.

[325] Sun, Y.; Mayers, B.T.; Xia, Y. Template-Engaged Replacement Reaction: A One-Step Approach to the Large-Scale Synthesis of Metal Nanostructures with Hollow Interiors. *Nano Lett.*, **2002,** *2*(5), 481–485.

[326] Chen, J.; Glaus, C.; Laforest, R.; Zhang, Q.; Yang, M.; Gidding, M.; Welch, M.J.; Xia, Y. Gold nanocages as photothermal transducers for cancer treatment. *Small*, **2010,** *6*(7), 811–817.

[327] Hu, M.; Novo, C.; Funston, A.; Wang, H.; Staleva, H.; Zou, S.; Mulvaney, P.; Xia, Y.; Hartland, G. V Dark-field microscopy studies of single metal nanoparticles: understanding the factors that influence the linewidth of the localized surface plasmon resonance. *J. Mater. Chem.*, **2008,** *18*(17), 1949–1960.

[328] Kim, C.; Cho, E.C.; Chen, J.; Song, K.H.; Au, L.; Favazza, C.; Zhang, Q.; Cobley, C.M.; Gao, F.; Xia, Y.; Wang, L. V In vivo molecular photoacoustic tomography of melanomas targeted by bioconjugated gold nanocages. *ACS Nano*, **2010,** *4*(8), 4559–4564.

[329] Au, L.; Zhang, Q.; Cobley, C.M.; Gidding, M.; Schwartz, A.G.; Chen, J.; Xia, Y. Quantifying the cellular uptake of antibody-conjugated Au nanocages by two-photon microscopy and inductively coupled plasma mass spectrometry. *ACS Nano*, **2010,** *4*(1), 35–42.

[330] Tong, L.; Cobley, C.M.; Chen, J.; Xia, Y.; Cheng, J.-X. Bright three-photon luminescence from gold/silver alloyed nanostructures for bioimaging with negligible photothermal toxicity. *Angew. Chem. Int. Ed. Engl.*, **2010,** *49*(20), 3485–3488.

[331] Chen, J.; Yang, M.; Zhang, Q.; Cho, E.C.; Cobley, C.M.; Kim, C.; Glaus, C.; Wang, L. V.; Welch, M.J.; Xia, Y. Gold Nanocages: A Novel Class of Multifunctional Nanomaterials for Theranostic Applications. *Adv. Funct. Mater.*, **2010,** *20*(21), 3684–3694.

[332] Li, W.; Cai, X.; Kim, C.; Sun, G.; Zhang, Y.; Deng, R.; Yang, M.; Chen, J.; Achilefu, S.; Wang, L. V; Xia, Y. Gold nanocages covered with thermally-responsive polymers for controlled release by high-intensity focused ultrasound. *Nanoscale*, **2011,** *3*(4), 1724–1730.

[333] Yavuz, M.S.; Cheng, Y.; Chen, J.; Cobley, C.M.; Zhang, Q.; Rycenga, M.; Xie, J.; Kim, C.; Song, K.H.; Schwartz, A.G.; Wang, L. V; Xia, Y. Gold nanocages covered by smart polymers for controlled release with near-infrared light. *Nat. Mater.*, **2009,** *8*(12), 935–939.

[334] Daniel, M.-C.; Astruc, D. Gold nanoparticles: assembly, supramolecular chemistry, quantum-size-related properties, and applications toward biology, catalysis, and nanotechnology. *Chem. Rev.*, **2004,** *104*(1), 293–346.

[335] Gibson, J.D.; Khanal, B.P.; Zubarev, E.R. Paclitaxel-functionalized gold nanoparticles. *J. Am. Chem. Soc.*, **2007,** *129*(37), 11653–11661.

[336] Hwu, J.R.; Lin, Y.S.; Josephrajan, T.; Hsu, M.-H.; Cheng, F.-Y.; Yeh, C.-S.; Su, W.-C.; Shieh, D.-B. Targeted Paclitaxel by conjugation to iron oxide and gold nanoparticles. *J. Am. Chem. Soc.*, **2009,** *131*(1), 66–68.

[337] Brown, S.D.; Nativo, P.; Smith, J.-A.; Stirling, D.; Edwards, P.R.; Venugopal, B.; Flint, D.J.; Plumb, J.A.; Graham, D.; Wheate, N.J. Gold Nanoparticles for the Improved Anticancer Drug Delivery of the Active Component of Oxaliplatin. *J. Am. Chem. Soc.*, **2010,** *132*(13), 4678–4684.

[338] Dreaden, E.C.; Mwakwari, S.C.; Sodji, Q.H.; Oyelere, A.K.; El-Sayed, M.A. Tamoxifen−Poly(ethylene glycol)−Thiol Gold Nanoparticle Conjugates: Enhanced Potency and Selective Delivery for Breast Cancer Treatment. *Bioconjug. Chem.*, **2009,** *20*(12), 2247–2253.

[339] Dolmans, D.E.J.G.J.; Fukumura, D.; Jain, R.K. Photodynamic therapy for cancer. *Nat. Rev. Cancer*, **2003,** *3*(5), 380–387.

[340] Cheng, Y.; C. Samia, A.; Meyers, J.D.; Panagopoulos, I.; Fei, B.; Burda, C. Highly Efficient Drug Delivery with Gold Nanoparticle Vectors for in Vivo Photodynamic Therapy of Cancer. *J. Am. Chem. Soc.*, **2008,** *130*(32), 10643–10647.

[341] Detty, M.R.; Gibson, S.L.; Wagner, S.J. Current Clinical and Preclinical Photosensitizers for Use in Photodynamic Therapy. *J. Med. Chem.*, **2004,** *47*(16), 3897–3915.

[342] Fei, B.; Wang, H.; Meyers, J.D.; Feyes, D.K.; Oleinick, N.L.; Duerk, J.L. High-field magnetic resonance imaging of the response of human prostate cancer to Pc 4-based photodynamic therapy in an animal model. *Lasers Surg. Med.*, **2007,** *39*(9), 723–730.

[343] Dreaden, E.C.; Mackey, M.A.; Huang, X.; Kang, B.; El-Sayed, M.A. Beating cancer in multiple ways using nanogold. *Chem. Soc. Rev.*, **2011,** *40*(7), 3391.

[344] Dreaden, E.C.; Alkilany, A.M.; Huang, X.; Murphy, C.J.; El-Sayed, M.A. The golden age: gold nanoparticles for biomedicine. *Chem. Soc. Rev.*, **2012,** *41*(7), 2740–2779.

[345] von Maltzahn, G.; Park, J.-H.; Agrawal, A.; Bandaru, N.K.; Das, S.K.; Sailor, M.J.; Bhatia, S.N. Computationally Guided Photothermal Tumor Therapy Using Long-Circulating Gold Nanorod Antennas. *Cancer Res.*, **2009,** *69*(9), 3892–3900.

[346] Lohse, S.E.; Eller, J.R.; Sivapalan, S.T.; Plews, M.R.; Murphy, C.J. A Simple Millifluidic Benchtop Reactor System for the High-Throughput Synthesis and Functionalization of Gold Nanoparticles with Different Sizes and Shapes. *ACS Nano*, **2013,** *7*(5), 4135–4150.

[347] Sebastian Cabeza, V.; Kuhn, S.; Kulkarni, A.A.; Jensen, K.F. Size-Controlled Flow Synthesis of Gold Nanoparticles Using a Segmented Flow Microfluidic Platform. *Langmuir*, **2012,** *28*(17), 7007–7013.

[348] Shukla, R. Biocompatibility of gold nanoparticles and their endocytotic fate inside the cellular compartment: a microscopic overview. *Langmuir*, **2005,** *21*, 10644–10654.

[349] Alkilany, A.M.; Murphy, C.J. Toxicity and cellular uptake of gold nanoparticles: what we have learned so far? *J. Nanoparticle Res.*, **2010,** *12*(7), 2313–2333.

[350] Akiyama, Y.; Mori, T.; Katayama, Y.; Niidome, T. The effects of PEG grafting level and injection dose on gold nanorod biodistribution in the tumor-bearing mice. *J. Control. Release*, **2009,** *139*(1), 81–84.

[351] Jain, R.K.; Stylianopoulos, T. Delivering nanomedicine to solid tumors. *Nat. Rev. Clin. Oncol.*, **2010,** *7*(11), 653–664.

[352] Decuzzi, P.; Godin, B.; Tanaka, T.; Lee, S.-Y.; Chiappini, C.; Liu, X.; Ferrari, M. Size and shape effects in the biodistribution of intravascularly injected particles. *J. Control. Release*, **2010,** *141*(3), 320–327.

[353] Khlebtsov, N.; Dykman, L. Biodistribution and toxicity of engineered gold nanoparticles: a review of in vitro and in vivo studies. *Chem. Soc. Rev.*, **2011,** *40*(3), 1647–1671.

[354] El-Sayed, I.; Huang, X.; El-Sayed, M. Selective laser photo-thermal therapy of epithelial carcinoma using anti-EGFR antibody conjugated gold nanoparticles. *Cancer Lett.*, **2006,** *239*(1), 129–135.

[355] Link, S.; Burda, C.; Mohamed, M.B.; Nikoobakht, B.; El-Sayed, M.A. Laser Photothermal Melting and Fragmentation of Gold Nanorods: Energy and Laser Pulse-Width Dependence. *J. Phys. Chem. A*, **1999,** *103*(9), 1165–1170.

[356] Wust, P.; Hildebrandt, B.; Sreenivasa, G.; Rau, B.; Gellermann, J.; Riess, H.; Felix, R.; Schlag, P. Hyperthermia in combined treatment of cancer. *Lancet Oncol.*, **2002,** *3*(8), 487–497.

[357] Huff, T.B.; Tong, L.; Zhao, Y.; Hansen, M.N.; Cheng, J.-X.; Wei, A. Hyperthermic effects of gold nanorods on tumor cells. *Nanomedicine*, **2007,** *2*(1), 125–132.

[358] Kampinga, H.H. Cell biological effects of hyperthermia alone or combined with radiation or drugs: A short introduction to newcomers in the field. *Int. J. Hyperth.*, **2006,** *22*(3), 191–196.

[359] Hirsch, L.R.; Gobin, A.M.; Lowery, A.R.; Tam, F.; Drezek, R.A.; Halas, N.J.; West, J.L. Metal Nanoshells. *Ann. Biomed. Eng.*, **2006,** *34*(1), 15–22.

[360] Stern, J.M.; Stanfield, J.; Lotan, Y.; Park, S.; Hsieh, J.-T.; Cadeddu, J.A. Efficacy of laser-activated gold nanoshells in ablating prostate cancer cells in vitro. *J. Endourol.*, **2007,** *21*(8), 939–943.

[361] Stern, J.M.; Stanfield, J.; Kabbani, W.; Hsieh, J.-T.; Cadeddu, J.A. Selective prostate cancer thermal ablation with laser activated gold nanoshells. *J. Urol.*, **2008,** *179*(2), 748–753.

[362] Ke, H.; Yue, X.; Wang, J.; Xing, S.; Zhang, Q.; Dai, Z.; Tian, J.; Wang, S.; Jin, Y. Gold Nanoshelled Liquid Perfluorocarbon Nanocapsules for Combined Dual Modal Ultrasound/CT Imaging and Photothermal Therapy of Cancer. *Small*, **2014,** *10*(6), 1220–1227.

[363] Lin, A.Y.; Young, J.K.; Nixon, A. V.; Drezek, R.A. Encapsulated Fe 3 O 4 /Ag Complexed Cores in Hollow Gold Nanoshells for Enhanced Theranostic Magnetic Resonance Imaging and Photothermal Therapy. *Small*, **2014,** *10*(16), 3246–3251.

[364] Nam, J.; La, W.-G.; Hwang, S.; Ha, Y.S.; Park, N.; Won, N.; Jung, S.; Bhang, S.H.; Ma, Y.-J.; Cho, Y.-M.; Jin, M.; Han, J.; Shin, J.-Y.; Wang, E.K.; Kim, S.G.; Cho, S.-H.; Yoo, J.; Kim, B.-S.; Kim, S. pH-Responsive Assembly of Gold Nanoparticles and "Spatiotemporally Concerted" Drug Release for Synergistic Cancer Therapy. *ACS Nano*, **2013,** *7*(4), 3388–3402.

[365] Klasen, H.J. Historical review of the use of silver in the treatment of burns. I. Early uses. *Burns*, **2000,** *26*(2), 117–130.

[366] Matejcek, A.; Goldman, R.D. Treatment and prevention of ophthalmia neonatorum. *Can. Fam. physician Médecin Fam. Can.*, **2013,** *59*(11), 1187–1190.

[367] Heyneman, A.; Hoeksema, H.; Vandekerckhove, D.; Pirayesh, A.; Monstrey, S. The role of silver sulphadiazine in the conservative treatment of partial thickness burn wounds: A systematic review. *Burns*, **2016,** *42*(7), 1377–1386.

[368] Drake, P.L.; Hazelwood, K.J. Exposure-related health effects of silver and silver compounds: a review. *Ann. Occup. Hyg.*, **2005,** *49*(7), 575–585.

[369] Chopra, I. The increasing use of silver-based products as antimicrobial agents: a useful development or a cause for concern? *J. Antimicrob. Chemother.*, **2007,** *59*(4), 587–590.

[370] Cardozo, V.F.; Oliveira, A.G.; Nishio, E.K.; Perugini, M.R.E.; Andrade, C.G.T.J.; Silveira, W.D.; Durán, N.; Andrade, G.; Kobayashi, R.K.T.; Nakazato, G. Antibacterial activity of extracellular compounds produced by a Pseudomonas strain against methicillin-resistant Staphylococcus aureus (MRSA) strains. *Ann. Clin. Microbiol. Antimicrob.*, **2013,** *12,* 12.

[371] Durán, N.; Marcato, P.D.; Conti, R.D.; Alves, O.L.; Costa, F.T.M.; Brocchi, M. Potential use of silver nanoparticles on pathogenic bacteria, their toxicity and possible mechanisms of action. *J. Braz. Chem. Soc.*, **2010,** *21*(6), 949–959.

[372] Franci, G.; Falanga, A.; Galdiero, S.; Palomba, L.; Rai, M.; Morelli, G.; Galdiero, M. Silver nanoparticles as potential antibacterial agents. *Molecules*, **2015,** *20*(5), 8856–8874.

[373] Marambio-Jones, C.; Hoek, E.M. V. A review of the antibacterial effects of silver nanomaterials and potential implications for human health and the environment. *J. Nanoparticle Res.*, **2010,** *12*(5), 1531–1551.

[374] Prabhu, S.; Poulose, E.K. Silver nanoparticles: mechanism of antimicrobial action, synthesis, medical applications, and toxicity effects. *Int. Nano Lett.*, **2012,** *2*(1), 32.

[375] Reidy, B.; Haase, A.; Luch, A.; Dawson, K.; Lynch, I. Mechanisms of Silver Nanoparticle Release, Transformation and Toxicity: A Critical Review of Current Knowledge and Recommendations for Future Studies and Applications. *Materials*

(Basel)., **2013,** *6*(6), 2295–2350.

[376] Manke, A.; Wang, L.; Rojanasakul, Y. Mechanisms of nanoparticle-induced oxidative stress and toxicity. *Biomed Res. Int.*, **2013,** *2013*, 942916.

[377] Harra, J.; Mäkitalo, J.; Siikanen, R.; Virkki, M.; Genty, G.; Kobayashi, T.; Kauranen, M.; Mäkelä, J.M. Size-controlled aerosol synthesis of silver nanoparticles for plasmonic materials. *J. Nanopart. Res.*, **2012,** *14*(6), 870.

[378] Kruis, F.E.; Fissan, H.; Rellinghaus, B. Sintering and evaporation characteristics of gas-phase synthesis of size-selected PbS nanoparticles. *Mater. Sci. Eng. B*, **2000,** *69–70*, 329–334.

[379] Jung, J.H.; Cheol Oh, H.; Soo Noh, H.; Ji, J.H.; Soo Kim, S. Metal nanoparticle generation using a small ceramic heater with a local heating area. *J. Aerosol Sci.*, **2006,** *37*(12), 1662–1670.

[380] Ji, J.H.; Jung, J.H.; Yu, I.J.; Kim, S.S. Long-term stability characteristics of metal nanoparticle generator using small ceramic heater for inhalation toxicity studies. *Inhal. Toxicol.*, **2007,** *19*(9), 745–751.

[381] Tajdidzadeh, M.; Azmi, B.Z.; Yunus, W.M.M.; Talib, Z.A.; Sadrolhosseini, A.R.; Karimzadeh, K.; Gene, S.A.; Dorraj, M. Synthesis of silver nanoparticles dispersed in various aqueous media using laser ablation. *ScientificWorldJournal.*, **2014,** *2014*, 324921.

[382] Valverde-Alva, M.A.; García-Fernández, T.; Villagrán-Muniz, M.; Sánchez-Aké, C.; Castañeda-Guzmán, R.; Esparza-Alegría, E.; Sánchez-Valdés, C.F.; Llamazares, J.L.S.; Herrera, C.E.M. Synthesis of silver nanoparticles by laser ablation in ethanol: A pulsed photoacoustic study. *Appl. Surf. Sci.*, **2015,** *355*, 341–349.

[383] Tsuji, T.; Thang, D.-H.; Okazaki, Y.; Nakanishi, M.; Tsuboi, Y.; Tsuji, M. Preparation of silver nanoparticles by laser ablation in polyvinylpyrrolidone solutions. *Appl. Surf. Sci.*, **2008,** *254*(16), 5224–5230.

[384] Tarasenko, N.V.; Butsen, A.V.; Nevar, E.A.; Savastenko, N.A. Synthesis of nanosized particles during laser ablation of gold in water. *Appl. Surf. Sci.*, **2006,** *252*(13), 4439–4444.

[385] Kawasaki, M.; Nishimura, N. 1064-nm laser fragmentation of thin Au and Ag flakes in acetone for highly productive pathway to stable metal nanoparticles. *Appl. Surf. Sci.*, **2006,** *253*(4), 2208–2216.

[386] Bo, L.; Yang, W.; Chen, M.; Gao, J.; Xue, Q. A simple and "green" synthesis of polymer-based silver colloids and their antibacterial properties. *Chem. Biodivers.*, **2009,** *6*(1), 111–116.

[387] Hebeish, A.; El-Shafei, A.; Sharaf, S.; Zaghloul, S. Novel precursors for green synthesis and application of silver nanoparticles in the realm of cotton finishing. *Carbohydr. Polym.*, **2011,** *84*(1), 605–613.

[388] Maity, D.; Kanti Bain, M.; Bhowmick, B.; Sarkar, J.; Saha, S.; Acharya, K.; Chakraborty, M.; Chattopadhyay, D. In situ synthesis, characterization, and antimicrobial activity of silver nanoparticles using water soluble polymer. *J. Appl. Polym. Sci.*, **2011,** *122*(4), 2189–2196.

[389] Tai, C.Y.; Wang, Y.-H.; Liu, H.-S. A green process for preparing silver nanoparticles using spinning disk reactor. *AIChE J.*, **2008,** *54*(2), 445–452.

[390] Venkatpurwar, V.; Pokharkar, V. Green synthesis of silver nanoparticles using marine polysaccharide: Study of in-vitro antibacterial activity. *Mater. Lett.*, **2011,** *65*(6), 999–1002.

[391] Korbekandi, H.; Iravani, S.; Abbasi, S. Optimization of biological synthesis of silver nanoparticles using Lactobacillus casei subsp. casei. *J. Chem. Technol. Biotechnol.*, **2012,** *87*(7), 932–937.

[392] Kalishwaralal, K.; Deepak, V.; Ramkumarpandian, S.; Nellaiah, H.; Sangiliyandi, G. Extracellular biosynthesis of silver nanoparticles by the culture supernatant of Bacillus licheniformis. *Mater. Lett.*, **2008,** *62*(29), 4411–4413.

[393] Naqvi, S.Z.H.; Kiran, U.; Ali, M.I.; Jamal, A.; Hameed, A.; Ahmed, S.; Ali, N. Combined efficacy of biologically synthesized silver nanoparticles and different antibiotics against multidrug-resistant bacteria. *Int. J. Nanomedicine*, **2013,** *8*, 3187–3195.

[394] Kathiresan, K.; Manivannan, S.; Nabeel, M.A.; Dhivya, B. Studies on silver nanoparticles synthesized by a marine fungus, Penicillium fellutanum isolated from coastal mangrove sediment. *Colloids Surf B Biointerfaces.*, **2009,** *71*(1), 133–137.

[395] Govindaraju, K.; Basha, S.K.; Kumar, V.G.; Singaravelu, G. Silver, gold and bimetallic nanoparticles production using single-cell protein (Spirulina platensis) Geitler. *J. Mater. Sci.*, **2008,** *43*(15), 5115–5122.

[396] Arokiyaraj, S.; Arasu, M.V.; Vincent, S.; Prakash, N.U.; Choi, S.H.; Oh, Y.-K.; Choi, K.C.; Kim, K.H. Rapid green synthesis of silver nanoparticles from Chrysanthemum indicum L and its antibacterial and cytotoxic effects: an in vitro study. *Int. J. Nanomedicine*, **2014,** *9*, 379–388.

[397] Kumara Swamy, M.; Sudipta, K.M.; Jayanta, K.; Balasubramanya, S. The green synthesis, characterization, and evaluation of the biological activities of silver nanoparticles synthesized from Leptadenia reticulata leaf extract. *Appl. Nanosci.*, **2015,** *5*(1), 73–81.

[398] Shankar, S.S.; Rai, A.; Ahmad, A.; Sastry, M. Rapid synthesis of Au, Ag, and bimetallic Au core-Ag shell nanoparticles using Neem (Azadirachta indica) leaf broth. *J. Colloid Interface Sci.*, **2004,** *275*(2), 496–502.

[399] Wiley, B.; Sun, Y.; Mayers, B.; Xia, Y. Shape-controlled synthesis of metal nanostructures: the case of silver. *Chemistry*, **2005,** *11*(2), 454–463.

[400] Oliveira, M.M.; Ugarte, D.; Zanchet, D.; Zarbin, A.J.G. Influence of synthetic parameters on the size, structure, and stability of dodecanethiol-stabilized silver nanoparticles. *J. Colloid Interface Sci.*, **2005,** *292*(2), 429–35.

[401] Zhang, Y.; Peng, H.; Huang, W.; Zhou, Y.; Yan, D. Facile preparation and characterization of highly antimicrobial colloid Ag or Au nanoparticles. *J. Colloid Interface Sci.*, **2008,** *325*(2), 371–6.

[402] Chen, M.; Feng, Y.-G.; Wang, X.; Li, T.-C.; Zhang, J.-Y.; Qian, D.-J. Silver nanoparticles capped by oleylamine: formation, growth, and self-organization.

Langmuir, **2007,** *23*(10), 5296–5304.

[403] Roldán, M.V.; Pellegri, N.; de Sanctis, O. Electrochemical Method for Ag-PEG Nanoparticles Synthesis. *J. Nanoparticles*, **2013,** *2013*, 1–7.

[404] Tseng, K.-H.; Chen, Y.-C.; Shyue, J.-J. Continuous synthesis of colloidal silver nanoparticles by electrochemical discharge in aqueous solutions. *J. Nanoparticle Res.*, **2011,** *13*(5), 1865–1872.

[405] Lei, Y.; Gao, G.; Liu, W.; Liu, T.; Yin, Y. Synthesis of silver nanoparticles on surface-functionalized multi-walled carbon nanotubes by ultraviolet initiated photo-reduction method. *Appl. Surf. Sci.*, **2014,** *317*, 49–55.

[406] Huang, H.; Yang, Y. Preparation of silver nanoparticles in inorganic clay suspensions. *Compos. Sci. Technol.*, **2008,** *68*(14), 2948–2953.

[407] Sotiriou, G.A.; Teleki, A.; Camenzind, A.; Krumeich, F.; Meyer, A.; Panke, S.; Pratsinis, S.E. Nanosilver on nanostructured silica: Antibacterial activity and Ag surface area. *Chem. Eng. J.*, **2011,** *170*(2–3), 547–554.

[408] Zhang, W.; Qiao, X.; Chen, J. Synthesis of nanosilver colloidal particles in water/oil microemulsion. *Colloids Surf. A. Physicochem. Eng. Asp.*, **2007,** *299*(1–3), 22–28.

[409] Solanki, J.N.; Murthy, Z.V.P. Controlled Size Silver Nanoparticles Synthesis with Water-in-Oil Microemulsion Method: A Topical Review. *Ind. Eng. Chem. Res.*, **2011,** *50*(22), 12311–12323.

[410] Chen, S.-F.; Zhang, H. Aggregation kinetics of nanosilver in different water conditions. *Adv. Nat. Sci. Nanosci. Nanotechnol.*, **2012,** *3*(3), 35006.

[411] Dung Dang, T.M.; Tuyet Le, T.T.; Fribourg-Blanc, E.; Dang, M.C. Influence of surfactant on the preparation of silver nanoparticles by polyol method. *Adv. Nat. Sci. Nanosci. Nanotechnol.*, **2012,** *3*(3), 35004.

[412] Patil, R.S.; Kokate, M.R.; Jambhale, C.L.; Pawar, S.M.; Han, S.H.; Kolekar, S.S. One-pot synthesis of PVA-capped silver nanoparticles their characterization and biomedical application. *Adv. Nat. Sci. Nanosci. Nanotechnol.*, **2012,** *3*(1), 15013.

[413] Tolaymat, T.M.; El Badawy, A.M.; Genaidy, A.; Scheckel, K.G.; Luxton, T.P.; Suidan, M. An evidence-based environmental perspective of manufactured silver nanoparticle in syntheses and applications: a systematic review and critical appraisal of peer-reviewed scientific papers. *Sci. Total Environ.*, **2010,** *408*(5), 999–1006.

[414] Huang, T.; Nancy Xu, X.-H. Synthesis and Characterization of Tunable Rainbow Colored Colloidal Silver Nanoparticles Using Single-Nanoparticle Plasmonic Microscopy and Spectroscopy. *J. Mater. Chem.*, **2010,** *20*(44), 9867–9876.

[415] Mahmoud, M.A.; El-Sayed, M.A. Different Plasmon Sensing Behavior of Silver and Gold Nanorods. *J. Phys. Chem. Lett.*, **2013,** *4*(9), 1541–1545.

[416] Wu, P.; Gao, Y.; Lu, Y.; Zhang, H.; Cai, C. High specific detection and near-infrared photothermal therapy of lung cancer cells with high SERS active aptamer-silver-gold shell-core nanostructures. *Analyst*, **2013,** *138*(21), 6501–6510.

[417] Shi, J.; Wang, L.; Zhang, J.; Ma, R.; Gao, J.; Liu, Y.; Zhang, C.; Zhang, Z. A tumor-

targeting near-infrared laser-triggered drug delivery system based on GO@Ag nanoparticles for chemo-photothermal therapy and X-ray imaging. *Biomaterials*, **2014,** *35*(22), 5847–5861.

[418] Zhao, D.; Sun, X.; Tong, J.; Ma, J.; Bu, X.; Xu, R.; Fan, R. A novel multifunctional nanocomposite C225-conjugated Fe3O4/Ag enhances the sensitivity of nasopharyngeal carcinoma cells to radiotherapy. *Acta Biochim. Biophys. Sin. (Shanghai).*, **2012,** *44*(8), 678–684.

[419] Qian, X.-M.; Nie, S.M. Single-molecule and single-nanoparticle SERS: from fundamental mechanisms to biomedical applications. *Chem. Soc. Rev.*, **2008,** *37*(5), 912–920.

[420] Tran, Q.H.; Nguyen, V.Q.; Le, A.-T. Silver nanoparticles: synthesis, properties, toxicology, applications and perspectives. *Adv. Nat. Sci. Nanosci. Nanotechnol.*, **2013,** *4*(3), 33001.

[421] Dos Santos, C.A.; Seckler, M.M.; Ingle, A.P.; Gupta, I.; Galdiero, S.; Galdiero, M.; Gade, A.; Rai, M. Silver nanoparticles: therapeutical uses, toxicity, and safety issues. *J. Pharm. Sci.*, **2014,** *103*(7), 1931–1944.

[422] Braun, G.B.; Friman, T.; Pang, H.-B.; Pallaoro, A.; Hurtado de Mendoza, T.; Willmore, A.-M.A.; Kotamraju, V.R.; Mann, A.P.; She, Z.-G.; Sugahara, K.N.; Reich, N.O.; Teesalu, T.; Ruoslahti, E. Etchable plasmonic nanoparticle probes to image and quantify cellular internalization. *Nat. Mater.*, **2014,** *13*(9), 904–911.

[423] Guo, D.; Zhu, L.; Huang, Z.; Zhou, H.; Ge, Y.; Ma, W.; Wu, J.; Zhang, X.; Zhou, X.; Zhang, Y.; Zhao, Y.; Gu, N. Anti-leukemia activity of PVP-coated silver nanoparticles via generation of reactive oxygen species and release of silver ions. *Biomaterials*, **2013,** *34*(32), 7884–7894.

[424] Guo, D.; Zhao, Y.; Zhang, Y.; Wang, Q.; Huang, Z.; Ding, Q.; Guo, Z.; Zhou, X.; Zhu, L.; Gu, N. The cellular uptake and cytotoxic effect of silver nanoparticles on chronic myeloid leukemia cells. *J. Biomed. Nanotechnol.*, **2014,** *10*(4), 669–678.

[425] Gurunathan, S.; Han, J.W.; Eppakayala, V.; Jeyaraj, M.; Kim, J.-H. Cytotoxicity of biologically synthesized silver nanoparticles in MDA-MB-231 human breast cancer cells. *Biomed Res. Int.*, **2013,** *2013*, 535796.

[426] Gurunathan, S.; Raman, J.; Abd Malek, S.N.; John, P.A.; Vikineswary, S. Green synthesis of silver nanoparticles using Ganoderma neo-japonicum Imazeki: a potential cytotoxic agent against breast cancer cells. *Int. J. Nanomedicine*, **2013,** *8*, 4399–4413.

[427] Sahu, S.C.; Zheng, J.; Graham, L.; Chen, L.; Ihrie, J.; Yourick, J.J.; Sprando, R.L. Comparative cytotoxicity of nanosilver in human liver HepG2 and colon Caco2 cells in culture. *J. Appl. Toxicol.*, **2014,** *34*(11), 1155–1166.

[428] Faedmaleki, F.; H Shirazi, F.; Salarian, A.-A.; Ahmadi Ashtiani, H.; Rastegar, H. Toxicity Effect of Silver Nanoparticles on Mice Liver Primary Cell Culture and HepG2 Cell Line. *Iran. J. Pharm. Res.*, **2014,** *13*(1), 235–242.

[429] Foldbjerg, R.; Dang, D.A.; Autrup, H. Cytotoxicity and genotoxicity of silver nanoparticles in the human lung cancer cell line, A549. *Arch. Toxicol.*, **2011,** *85*(7), 743–750.

[430] El-Deeb, N.M.; El-Sherbiny, I.M.; El-Aassara, M.R.; Hafez, E.E. Novel Trend in Colon Cancer Therapy Using Silver Nanoparticles Synthesized by Honey Bee. *J. Nanomed. Nanotechnol.*, **2015,** *6*, 265.

[431] Benyettou, F.; Rezgui, R.; Ravaux, F.; Jaber, T.; Blumer, K.; Jouiad, M.; Motte, L.; Olsen, J.-C.; Platas-Iglesias, C.; Magzoub, M.; Trabolsi, A. Synthesis of silver nanoparticles for the dual delivery of doxorubicin and alendronate to cancer cells. *J. Mater. Chem. B*, **2015,** *3*(36), 7237–7245.

[432] Fattahi, H.; Laurent, S.; Liu, F.; Arsalani, N.; Vander Elst, L.; Muller, R.N. Magnetoliposomes as multimodal contrast agents for molecular imaging and cancer nanotheragnostics. *Nanomedicine (Lond).*, **2011,** *6*(3), 529–544.

[433] Kuhara, M.; Takeyama, H.; Tanaka, T.; Matsunaga, T. Magnetic cell separation using antibody binding with protein a expressed on bacterial magnetic particles. *Anal. Chem.*, **2004,** *76*(21), 6207–6213.

[434] Quinto, C.A.; Mohindra, P.; Tong, S.; Bao, G. Multifunctional superparamagnetic iron oxide nanoparticles for combined chemotherapy and hyperthermia cancer treatment. *Nanoscale*, **2015,** *7*(29), 12728–12736.

[435] Bañobre-López, M.; Teijeiro, A.; Rivas, J. Magnetic nanoparticle-based hyperthermia for cancer treatment. *Reports Pract. Oncol. Radiother.*, **2013,** *18*(6), 397–400.

[436] Zhou, L.; He, B.; Zhang, F. Facile One-Pot Synthesis of Iron Oxide Nanoparticles Cross-linked Magnetic Poly(vinyl alcohol) Gel Beads for Drug Delivery. *ACS Appl. Mater. Interfaces*, **2012,** *4*(1), 192–199.

[437] Dilnawaz, F.; Singh, A.; Mohanty, C.; Sahoo, S.K. Dual drug loaded superparamagnetic iron oxide nanoparticles for targeted cancer therapy. *Biomaterials*, **2010,** *31*(13), 3694–3706.

[438] Haun, J.B.; Yoon, T.-J.; Lee, H.; Weissleder, R. Magnetic nanoparticle biosensors. *Wiley Interdiscip. Rev. Nanomedicine Nanobiotechnology*, **2010,** *2*(3), 291–304.

[439] Chertok, B.; Moffat, B.A.; David, A.E.; Yu, F.; Bergemann, C.; Ross, B.D.; Yang, V.C. Iron oxide nanoparticles as a drug delivery vehicle for MRI monitored magnetic targeting of brain tumors. *Biomaterials*, **2008,** *29*(4), 487–496.

[440] Kooi, M.E.; Cappendijk, V.C.; Cleutjens, K.B.J.M.; Kessels, A.G.H.; Kitslaar, P.J.E.H.M.; Borgers, M.; Frederik, P.M.; Daemen, M.J.A.P.; van Engelshoven, J.M.A. Accumulation of ultrasmall superparamagnetic particles of iron oxide in human atherosclerotic plaques can be detected by in vivo magnetic resonance imaging. *Circulation*, **2003,** *107*(19), 2453–2458.

[441] Reddy, L.H.; Arias, J.L.; Nicolas, J.; Couvreur, P. Magnetic nanoparticles: design and characterization, toxicity and biocompatibility, pharmaceutical and biomedical applications. *Chem. Rev.*, **2012,** *112*(11), 5818–5878.

[442] Arruebo, M.; Fernández-Pacheco, R.; Ibarra, M.R.; Santamaría, J. Magnetic nanoparticles for drug delivery. *Nano Today*, **2007,** *2*(3), 22–32.

[443] Arbab, A.S.; Bashaw, L.A.; Miller, B.R.; Jordan, E.K.; Lewis, B.K.; Kalish, H.; Frank, J.A. Characterization of biophysical and metabolic properties of cells labeled with superparamagnetic iron oxide nanoparticles and transfection agent for cellular MR

imaging. *Radiology*, **2003,** *229*(3), 838–846.

[444] Laurent, S.; Forge, D.; Port, M.; Roch, A.; Robic, C.; Vander Elst, L.; Muller, R.N. Magnetic iron oxide nanoparticles: synthesis, stabilization, vectorization, physicochemical characterizations, and biological applications. *Chem. Rev.*, **2008,** *108*(6), 2064–2110.

[445] Sun, C.; Lee, J.S.H.; Zhang, M. Magnetic nanoparticles in MR imaging and drug delivery. *Adv. Drug Deliv. Rev.*, **2008,** *60*(11), 1252–1265.

[446] Gupta, A.K.; Gupta, M. Synthesis and surface engineering of iron oxide nanoparticles for biomedical applications. *Biomaterials*, **2005,** *26*(18), 3995–4021.

[447] Lu, A.-H.; Salabas, E.L.; Schüth, F. Magnetic nanoparticles: synthesis, protection, functionalization, and application. *Angew. Chem. Int. Ed. Engl.*, **2007,** *46*(8), 1222–1244.

[448] Fang, C.; Zhang, M. Multifunctional Magnetic Nanoparticles for Medical Imaging Applications. *J. Mater. Chem.*, **2009,** *19*, 6258–6266.

[449] Singh, A.; Sahoo, S.K. Magnetic nanoparticles: a novel platform for cancer theranostics. *Drug Discov. Today*, **2014,** *19*(4), 474–481.

[450] Luk, B.T.; Zhang, L. Current advances in polymer-based nanotheranostics for cancer treatment and diagnosis. *ACS Appl. Mater. Interfaces*, **2014,** *6*(24), 21859–21873.

[451] Mathur, S.; Barth, S.; Werner, U.; Hernandez-Ramirez, F.; Romano-Rodriguez, A. Chemical Vapor Growth of One-dimensional Magnetite Nanostructures. *Adv. Mater.*, **2008,** *20*(8), 1550–1554.

[452] King, J.G.; Williams, W.; Wilkinson, C.D.W.; McVitie, S.; Chapman, J.N. Magnetic properties of magnetite arrays produced by the method of electron beam lithography. *Geophys. Res. Lett.*, **1996,** *23*(20), 2847–2850.

[453] Chin, A.B.; Yaacob, I.I. Synthesis and characterization of magnetic iron oxide nanoparticles via w/o microemulsion and Massart's procedure. *J. Mater. Process. Technol.*, **2007,** *191*(1–3), 235–237.

[454] Albornoz, C.; Jacobo, S.E. Preparation of a biocompatible magnetic film from an aqueous ferrofluid. *J. Magn. Magn. Mater.*, **2006,** *305*(1), 12–15.

[455] Hee Kim, E.; Sook Lee, H.; Kook Kwak, B.; Kim, B.-K. Synthesis of ferrofluid with magnetic nanoparticles by sonochemical method for MRI contrast agent. *J. Magn. Magn. Mater.*, **2005,** *289*, 328–330.

[456] Wan, J.; Chen, X.; Wang, Z.; Yang, X.; Qian, Y. A soft-template-assisted hydrothermal approach to single-crystal Fe3O4 nanorods. *J. Cryst. Growth*, **2005,** *276*(3–4), 571–576.

[457] Salazar-Alvarez, G.; Muhammed, M.; Zagorodni, A.A. Novel flow injection synthesis of iron oxide nanoparticles with narrow size distribution. *Chem. Eng. Sci.*, **2006,** *61*(14), 4625–4633.

[458] Amemiya, Y.; Arakaki, A.; Staniland, S.S.; Tanaka, T.; Matsunaga, T. Controlled formation of magnetite crystal by partial oxidation of ferrous hydroxide in the presence

of recombinant magnetotactic bacterial protein Mms6. *Biomaterials*, **2007,** *28*(35), 5381–5389.

[459] Vereda, F.; Rodríguez-González, B.; de Vicente, J.; Hidalgo-Álvarez, R. Evidence of direct crystal growth and presence of hollow microspheres in magnetite particles prepared by oxidation of Fe(OH)2. *J. Colloid Interface Sci.*, **2008,** *318*(2), 520–524.

[460] Wu, S.; Sun, A.; Zhai, F.; Wang, J.; Xu, W.; Zhang, Q.; Volinsky, A.A. Fe_3O_4 magnetic nanoparticles synthesis from tailings by ultrasonic chemical co-precipitation. *Mater. Lett.*, **2011,** *65*(12), 1882–1884.

[461] Salavati-Niasari, M.; Mahmoudi, T.; Amiri, O. Easy Synthesis of Magnetite Nanocrystals via Coprecipitation Method. *J. Clust. Sci.*, **2012,** *23*(2), 597–602.

[462] Suh, S.K.; Yuet, K.; Hwang, D.K.; Bong, K.W.; Doyle, P.S.; Hatton, T.A. Synthesis of nonspherical superparamagnetic particles: in situ coprecipitation of magnetic nanoparticles in microgels prepared by stop-flow lithography. *J. Am. Chem. Soc.*, **2012,** *134*(17), 7337–7343.

[463] Jolivet, J.-P.; Chanéac, C.; Tronc, E. Iron oxide chemistry. From molecular clusters to extended solid networks. *Chem. Commun.*, **2004,** , 481–487.

[464] Sugimoto, T. Formation of Monodispersed Nano- and Micro-Particles Controlled in Size, Shape, and Internal Structure. *Chem. Eng. Technol.*, **2003,** *26*(3), 313–321.

[465] Schwarzer, H.-C.; Peukert, W. Tailoring particle size through nanoparticle precipitation. *Chem. Eng. Commun.*, **2004,** *191*(4), 580–606.

[466] Itoh, H.; Sugimoto, T. Systematic control of size, shape, structure, and magnetic properties of uniform magnetite and maghemite particles. *J. Colloid Interface Sci.*, **2003,** *265*(2), 283–295.

[467] Thapa, D.; Palkar, V.; Kurup, M..; Malik, S.. Properties of magnetite nanoparticles synthesized through a novel chemical route. *Mater. Lett.*, **2004,** *58*(21), 2692–2694.

[468] Babes, L.; Denizot, B.; Tanguy, G.; Le Jeune, J.J.; Jallet, P. Synthesis of Iron Oxide Nanoparticles Used as MRI Contrast Agents: A Parametric Study. *J. Colloid Interface Sci.*, **1999,** *212*(2), 474–482.

[469] Pardoe, H.; Chua-anusorn, W.; St. Pierre, T.G.; Dobson, J. Structural and magnetic properties of nanoscale iron oxide particles synthesized in the presence of dextran or polyvinyl alcohol. *J. Magn. Magn. Mater.*, **2001,** *225*(1–2), 41–46.

[470] Massart, R. Preparation of aqueous magnetic liquids in alkaline and acidic media. *IEEE Trans. Magn.*, **1981,** *17*(2), 1247–1248.

[471] Gribanov, N.M.; Bibik, E.E.; Buzunov, O.V.; Naumov, V.N. Physico-chemical regularities of obtaining highly dispersed magnetite by the method of chemical condensation. *J. Magn. Magn. Mater.*, **1990,** *85*(1–3), 7–10.

[472] Pereira, C.; Pereira, A.M.; Fernandes, C.; Rocha, M.; Mendes, R.; Fernández-García, M.P.; Guedes, A.; Tavares, P.B.; Grenèche, J.-M.; Araújo, J.P.; Freire, C. Superparamagnetic MFe_2O_4 (M = Fe, Co, Mn) Nanoparticles: Tuning the Particle Size and Magnetic Properties through a Novel One-Step Coprecipitation Route. *Chem. Mater.*, **2012,** *24*(8), 1496–1504.

[473] Gilchrist, R.K.; Medal, R.; Shorey, W.D.; Hanselman, R.C.; Parrott, J.C.; Taylor, C.B. Selective inductive heating of lymph nodes. *Ann. Surg.*, **1957,** *146*(4), 596–606.

[474] Stauffer, P.R. Evolving technology for thermal therapy of cancer. *Int. J. Hyperthermia*, **2005,** *21*(8), 731–744.

[475] Diederich, C.J. Thermal ablation and high-temperature thermal therapy: overview of technology and clinical implementation. *Int. J. Hyperthermia*, **2005,** *21*(8), 745–753.

[476] Hilger, I.; Hergt, R.; Kaiser, W.A. Towards breast cancer treatment by magnetic heating. *J. Magn. Magn. Mater.*, **2005,** *293*(1), 314–319.

[477] Ryu, S.; Brown, S.L.; Kim, S.H.; Khil, M.S.; Kim, J.H. Preferential radiosensitization of human prostatic carcinoma cells by mild hyperthermia. *Int. J. Radiat. Oncol. Biol. Phys.*, **1996,** *34*(1), 133–138.

[478] Hilger, I.; Hiergeist, R.; Hergt, R.; Winnefeld, K.; Schubert, H.; Kaiser, W.A. Thermal ablation of tumors using magnetic nanoparticles: an in vivo feasibility study. *Invest. Radiol.*, **2002,** *37*(10), 580–586.

[479] Kohler, N.; Sun, C.; Fichtenholtz, A.; Gunn, J.; Fang, C.; Zhang, M. Methotrexate-Immobilized Poly(ethylene glycol) Magnetic Nanoparticles for MR Imaging and Drug Delivery. *Small*, **2006,** *2*(6), 785–792.

[480] Xu, Z.P.; Zeng, Q.H.; Lu, G.Q.; Yu, A.B. Inorganic nanoparticles as carriers for efficient cellular delivery. *Chem. Eng. Sci.*, **2006,** *61*(3), 1027–1040.

[481] Pankhurst, Q.A.; Connolly, J.; Jones, S.K.; Dobson, J. Applications of magnetic nanoparticles in biomedicine. *J. Phys. D. Appl. Phys.*, **2003,** *36*(13), R167.

[482] Kohler, N.; Fryxell, G.E.; Zhang, M. A Bifunctional Poly(ethylene glycol) Silane Immobilized on Metallic Oxide-Based Nanoparticles for Conjugation with Cell Targeting Agents. *J. Am. Chem. Soc.*, **2004,** *126*(23), 7206–7211.

[483] Kong, G.; Anyarambhatla, G.; Petros, W.P.; Braun, R.D.; Colvin, O.M.; Needham, D.; Dewhirst, M.W. Efficacy of liposomes and hyperthermia in a human tumor xenograft model: importance of triggered drug release. *Cancer Res.*, **2000,** *60*(24), 6950–7.

[484] Chang, Y.; Meng, X.; Zhao, Y.; Li, K.; Zhao, B.; Zhu, M.; Li, Y.; Chen, X.; Wang, J. Novel water-soluble and pH-responsive anticancer drug nanocarriers: Doxorubicin–PAMAM dendrimer conjugates attached to superparamagnetic iron oxide nanoparticles (IONPs). *J. Colloid Interface Sci.*, **2011,** *363*(1), 403–409.

[485] Marcu, A.; Pop, S.; Dumitrache, F.; Mocanu, M.; Niculite, C.M.; Gherghiceanu, M.; Lungu, C.P.; Fleaca, C.; Ianchis, R.; Barbut, A.; Grigoriu, C.; Morjan, I. Magnetic iron oxide nanoparticles as drug delivery system in breast cancer. *Appl. Surf. Sci.*, **2013,** *281*, 60–65.

[486] Rivera Gil, P.; Hühn, D.; del Mercato, L.L.; Sasse, D.; Parak, W.J. Nanopharmacy: Inorganic nanoscale devices as vectors and active compounds. *Pharmacol. Res.*, **2010,** *62*(2), 115–125.

[487] Bregoli, L.; Movia, D.; Gavigan-Imedio, J.D.; Lysaght, J.; Reynolds, J.; Prina-Mello, A. Nanomedicine applied to translational oncology: A future perspective on cancer treatment. *Nanomedicine*, **2016,** *12*(1), 81–103.

[488] Liu, Z.; Robinson, J.T.; Tabakman, S.M.; Yang, K.; Dai, H. Carbon materials for drug delivery & cancer therapy. *Mater. Today*, **2011,** *14*(7–8), 316–323.

[489] Kostarelos, K.; Bianco, A.; Prato, M. Promises, facts and challenges for carbon nanotubes in imaging and therapeutics. *Nat. Nanotechnol.*, **2009,** *4*(10), 627–633.

[490] Feng, L.; Liu, Z. Graphene in biomedicine: opportunities and challenges. *Nanomedicine*, **2011,** *6*(2), 317–324.

[491] Zeng, Q.; Shao, D.; He, X.; Ren, Z.; Ji, W.; Shan, C.; Qu, S.; Li, J.; Chen, L.; Li, Q. Carbon dots as a trackable drug delivery carrier for localized cancer therapy in vivo. *J. Mater. Chem. B*, **2016,** *4*(30), 5119–5126.

[492] Liu, Z.; Yang, K.; Lee, S.-T. Single-walled carbon nanotubes in biomedical imaging. *J. Mater. Chem.*, **2011,** *21*(3), 586–598.

[493] Sun, Y.-P.; Zhou, B.; Lin, Y.; Wang, W.; Fernando, K.A.S.; Pathak, P.; Meziani, M.J.; Harruff, B.A.; Wang, X.; Wang, H.; Luo, P.G.; Yang, H.; Kose, M.E.; Chen, B.; Veca, L.M.; Xie, S.-Y. Quantum-Sized Carbon Dots for Bright and Colorful Photoluminescence. *J. Am. Chem. Soc.*, **2006,** *128*(24), 7756–7757.

[494] Yu, S.-J.; Kang, M.-W.; Chang, H.-C.; Chen, K.-M.; Yu, Y.-C. Bright Fluorescent Nanodiamonds: No Photobleaching and Low Cytotoxicity. *J. Am. Chem. Soc.*, **2005,** *127*(50), 17604–17605.

[495] Loh, K.P.; Bao, Q.; Eda, G.; Chhowalla, M. Graphene oxide as a chemically tunable platform for optical applications. *Nat. Chem.*, **2010,** *2*(12), 1015–1024.

[496] Yang, W.; Ratinac, K.R.; Ringer, S.P.; Thordarson, P.; Gooding, J.J.; Braet, F. Carbon Nanomaterials in Biosensors: Should You Use Nanotubes or Graphene? *Angew. Chemie Int. Ed.*, **2010,** *49*(12), 2114–2138.

[497] Mohanty, N.; Berry, V. Graphene-Based Single-Bacterium Resolution Biodevice and DNA Transistor: Interfacing Graphene Derivatives with Nanoscale and Microscale Biocomponents. *Nano Lett.*, **2008,** *8*(12), 4469–4476.

[498] Sun, X.; Liu, Z.; Welsher, K.; Robinson, J.T.; Goodwin, A.; Zaric, S.; Dai, H. Nano-graphene oxide for cellular imaging and drug delivery. *Nano Res.*, **2008,** *1*(3), 203–212.

[499] Liu, Z.; Sun, X.; Nakayama-Ratchford, N.; Dai, H. Supramolecular Chemistry on Water-Soluble Carbon Nanotubes for Drug Loading and Delivery. *ACS Nano*, **2007,** *1*(1), 50–56.

[500] Liu, Z.; Robinson, J.T.; Sun, X.; Dai, H. PEGylated Nanographene Oxide for Delivery of Water-Insoluble Cancer Drugs. *J. Am. Chem. Soc.*, **2008,** *130*(33), 10876–10877.

[501] Liang, X.-J.; Meng, H.; Wang, Y.; He, H.; Meng, J.; Lu, J.; Wang, P.C.; Zhao, Y.; Gao, X.; Sun, B.; Chen, C.; Xing, G.; Shen, D.; Gottesman, M.M.; Wu, Y.; Yin, J. -j.; Jia, L. Metallofullerene nanoparticles circumvent tumor resistance to cisplatin by reactivating endocytosis. *Proc. Natl. Acad. Sci.*, **2010,** *107*(16), 7449–7454.

[502] Hong, S.Y.; Tobias, G.; Al-Jamal, K.T.; Ballesteros, B.; Ali-Boucetta, H.; Lozano-Perez, S.; Nellist, P.D.; Sim, R.B.; Finucane, C.; Mather, S.J.; Green, M.L.H.; Kostarelos, K.; Davis, B.G. Filled and glycosylated carbon nanotubes for in vivo radioemitter localization and imaging. *Nat. Mater.*, **2010,** *9*(6), 485–490.

[503] Yang, K.; Wan, J.; Zhang, S.; Tian, B.; Zhang, Y.; Liu, Z. The influence of surface chemistry and size of nanoscale graphene oxide on photothermal therapy of cancer using ultra-low laser power. *Biomaterials*, **2012,** *33*(7), 2206–2214.

[504] Yang, K.; Zhang, S.; Zhang, G.; Sun, X.; Lee, S.-T.; Liu, Z. Graphene in Mice: Ultrahigh In Vivo Tumor Uptake and Efficient Photothermal Therapy. *Nano Lett.*, **2010,** *10*(9), 3318–3323.

[505] Liu, X.; Tao, H.; Yang, K.; Zhang, S.; Lee, S.-T.; Liu, Z. Optimization of surface chemistry on single-walled carbon nanotubes for in vivo photothermal ablation of tumors. *Biomaterials*, **2011,** *32*(1), 144–151.

[506] Moon, H.K.; Lee, S.H.; Choi, H.C. In Vivo Near-Infrared Mediated Tumor Destruction by Photothermal Effect of Carbon Nanotubes. *ACS Nano*, **2009,** *3*(11), 3707–3713.

[507] Taylor, R.; Hare, J.P.; Abdul-Sada, A.K.; Kroto, H.W. Isolation, separation and characterisation of the fullerenes C60 and C70: the third form of carbon. *J. Chem. Soc. Chem. Commun.*, **1990,** (20), 1423.

[508] Prato, M. [60]Fullerene chemistry for materials science applications. *J. Mater. Chem.*, **1997,** *7*(7), 1097–1109.

[509] Samal, S.; Geckeler, K.E. Cyclodextrin–fullerenes: a new class of water-soluble fullerenes. *Chem. Commun.*, **2000,** (13), 1101–1102.

[510] Ikeda, A.; Nobukuni, S.; Udzu, H.; Zhong, Z.; Shinkai, S. A Novel [60]Fullerene-Calixarene Conjugate Which Facilitates Self-Inclusion of the [60]Fullerene Moiety into the Homooxacalix[3]arene Cavity. *European J. Org. Chem.*, **2000,** *2000*(19), 3287–3293.

[511] Atwood, J.L.; Koutsantonis, G.A.; Raston, C.L. Purification of C60 and C70 by selective complexation with calixarenes. *Nature*, **1994,** *368*(6468), 229–231.

[512] Ikeda, A.; Suzuki, Y.; Yoshimura, M.; Shinkai, S. On the prerequisites for the formation of solution complexes from [60]fullerene and calix[n]arenes: A novel allosteric effect between [60]fullerene and metal cations in calix[n]aryl ester complexes. *Tetrahedron*, **1998,** *54*(11), 2497–2508.

[513] Yamakoshi, Y.N.; Yagami, T.; Fukuhara, K.; Sueyoshi, S.; Miyata, N. Solubilization of fullerenes into water with polyvinylpyrrolidone applicable to biological tests. *J. Chem. Soc. Chem. Commun.*, **1994,** (4), 517.

[514] Bensasson, R. V.; Bienvenue, E.; Dellinger, M.; Leach, S.; Seta, P. C60 in Model Biological Systems. A Visible-UV Absorption Study of Solvent-Dependent Parameters and Solute Aggregation. *J. Phys. Chem.*, **1994,** *98*(13), 3492–3500.

[515] Hetzer, M.; Bayerl, S.; Camps, X.; Vostrowsky, O.; Hirsch, A.; Bayerl, T.M. Fullerenes in membranes: Structural and dynamic effects of lipophilic C60 derivatives in phospholipid bilayers. *Adv. Mater.*, **1997,** *9*(11), 913–917.

[516] Kato, H.; Kanazawa, Y.; Okumura, M.; Taninaka, A.; Yokawa, T.; Shinohara, H. Lanthanoid endohedral metallofullerenols for MRI contrast agents. *J. Am. Chem. Soc.*, **2003,** *125*(14), 4391–4397.

[517] Arbogast, J.W.; Darmanyan, A.P.; Foote, C.S.; Diederich, F.N.; Whetten, R.L.; Rubin,

Y.; Alvarez, M.M.; Anz, S.J. Photophysical properties of sixty atom carbon molecule (C60). *J. Phys. Chem.*, **1991,** *95*(1), 11–12.

[518] Mikawa, M.; Kato, H.; Okumura, M.; Narazaki, M.; Kanazawa, Y.; Miwa, N.; Shinohara, H. Paramagnetic Water-Soluble Metallofullerenes Having the Highest Relaxivity for MRI Contrast Agents. *Bioconjug. Chem.*, **2001,** *12*(4), 510–514.

[519] Bolskar, R.D.; Benedetto, A.F.; Husebo, L.O.; Price, R.E.; Jackson, E.F.; Wallace, S.; Wilson, L.J.; Alford, J.M. First Soluble M@C60 Derivatives Provide Enhanced Access to Metallofullerenes and Permit in Vivo Evaluation of $Gd@C_{60}[C(COOH)_2]_{10}$ as a MRI Contrast Agent. *J. Am. Chem. Soc.*, **2003,** *125*(18), 5471–5478.

[520] Shu, C.-Y.; Ma, X.-Y.; Zhang, J.-F.; Corwin, F.D.; Sim, J.H.; Zhang, E.-Y.; Dorn, H.C.; Gibson, H.W.; Fatouros, P.P.; Wang, C.-R.; Fang, X.-H. Conjugation of a Water-Soluble Gadolinium Endohedral Fulleride with an Antibody as a Magnetic Resonance Imaging Contrast Agent. *Bioconjug. Chem.*, **2008,** *19*(3), 651–655.

[521] Fillmore, H.L.; Shultz, M.D.; Henderson, S.C.; Cooper, P.; Broaddus, W.C.; Chen, Z.J.; Shu, C.-Y.; Zhang, J.; Ge, J.; Dorn, H.C.; Corwin, F.; Hirsch, J.I.; Wilson, J.; Fatouros, P.P. Conjugation of functionalized gadolinium metallofullerenes with IL-13 peptides for targeting and imaging glial tumors. *Nanomedicine*, **2011,** *6*(3), 449–458.

[522] Liu, J.; Tabata, Y. Photodynamic Antitumor Activity of Fullerene Modified with Poly(ethylene glycol) with Different Molecular Weights and Terminal Structures. *J. Biomater. Sci. Polym. Ed.*, **2011,** *22*(1–3), 297–312.

[523] Alvarez, M.G.; Prucca, C.; Milanesio, M.E.; Durantini, E.N.; Rivarola, V. Photodynamic activity of a new sensitizer derived from porphyrin-C_{60} dyad and its biological consequences in a human carcinoma cell line. *Int. J. Biochem. Cell Biol.*, **2006,** *38*(12), 2092–2101.

[524] Mroz, P.; Pawlak, A.; Satti, M.; Lee, H.; Wharton, T.; Gali, H.; Sarna, T.; Hamblin, M.R. Functionalized fullerenes mediate photodynamic killing of cancer cells: Type I versus Type II photochemical mechanism. *Free Radic. Biol. Med.*, **2007,** *43*(5), 711–719.

[525] Diener, M.D.; Alford, J.M.; Kennel, S.J.; Mirzadeh, S. $^{212}Pb@C60$ and Its Water-Soluble Derivatives: Synthesis, Stability, and Suitability for Radioimmunotherapy. *J. Am. Chem. Soc.*, **2007,** *129*(16), 5131–5138.

[526] Shultz, M.D.; Duchamp, J.C.; Wilson, J.D.; Shu, C.-Y.; Ge, J.; Zhang, J.; Gibson, H.W.; Fillmore, H.L.; Hirsch, J.I.; Dorn, H.C.; Fatouros, P.P. Encapsulation of a Radiolabeled Cluster Inside a Fullerene Cage, $^{177}Lu_xLu_{(3-x)}N@C_{80}$: An Interleukin-13-Conjugated Radiolabeled Metallofullerene Platform. *J. Am. Chem. Soc.*, **2010,** *132*(14), 4980–4981.

[527] Zhu, J.; Ji, Z.; Wang, J.; Sun, R.; Zhang, X.; Gao, Y.; Sun, H.; Liu, Y.; Wang, Z.; Li, A.; Ma, J.; Wang, T.; Jia, G.; Gu, Y. Tumor-Inhibitory Effect and Immunomodulatory Activity of Fullerol $C_{60}(OH)_x$. *Small*, **2008,** *4*(8), 1168–1175.

[528] Jiao, F.; Liu, Y.; Qu, Y.; Li, W.; Zhou, G.; Ge, C.; Li, Y.; Sun, B.; Chen, C. Studies on anti-tumor and antimetastatic activities of fullerenol in a mouse breast cancer model. *Carbon N. Y.*, **2010,** *48*(8), 2231–2243.

[529] Liu, Z.; Kiessling, F.; Gätjens, J. Advanced Nanomaterials in Multimodal Imaging:

Design, Functionalization, and Biomedical Applications. *J. Nanomater.*, **2010,** *2010*, 1–15.

[530] Mody, V. V.; Nounou, M.I.; Bikram, M. Novel nanomedicine-based MRI contrast agents for gynecological malignancies. *Adv. Drug Deliv. Rev.*, **2009,** *61*(10), 795–807.

[531] Sitharaman, B.; Bolskar, R.D.; Rusakova, I.; Wilson, L.J. $Gd@C_{60}[C(COOH)_2]_{10}$ and $Gd@C_{60}(OH)_x$: Nanoscale Aggregation Studies of Two Metallofullerene MRI Contrast Agents in Aqueous Solution. *Nano Lett.*, **2004,** *4*(12), 2373–2378.

[532] Liu, Y.; Jiao, F.; Qiu, Y.; Li, W.; Lao, F.; Zhou, G.; Sun, B.; Xing, G.; Dong, J.; Zhao, Y.; Chai, Z.; Chen, C. The effect of $Gd@C_{82}(OH)_{22}$ nanoparticles on the release of Th1/Th2 cytokines and induction of TNF-α mediated cellular immunity. *Biomaterials*, **2009,** *30*(23–24), 3934–3945.

[533] Shu, C.-Y.; Wang, C.-R.; Zhang, J.-F.; Gibson, H.W.; Dorn, H.C.; Corwin, F.D.; Fatouros, P.P.; Dennis, T.J.S. Organophosphonate Functionalized $Gd@C_{82}$ as a Magnetic Resonance Imaging Contrast Agent. *Chem. Mater.*, **2008,** *20*(6), 2106–2109.

[534] Satoh, M.; Takayanagi, I. Pharmacological Studies on Fullerene (C60), a Novel Carbon Allotrope, and Its Derivatives. *J. Pharmacol. Sci.*, **2006,** *100*(5), 513–518.

[535] Tabata, Y.; Ikada, Y. Biological functions of fullerene. *Pure Appl. Chem.*, **1999,** *71*(11).

[536] Nakajima, N.; Nishi, C.; Li, F.M.; Ikada, Y. Photo-Induced Cytotoxicity of Water-Soluble Fullerene. *Fuller. Sci. Technol.*, **1996,** *4*(1), 1–19.

[537] Liu, J.; Ohta, S.; Sonoda, A.; Yamada, M.; Yamamoto, M.; Nitta, N.; Murata, K.; Tabata, Y. Preparation of PEG-conjugated fullerene containing Gd^{3+} ions for photodynamic therapy. *J. Control. Release*, **2007,** *117*(1), 104–110.

[538] Ji, Z.Q.; Sun, H.; Wang, H.; Xie, Q.; Liu, Y.; Wang, Z. Biodistribution and tumor uptake of $C_{60}(OH)_x$ in mice. *J. Nanoparticle Res.*, **2006,** *8*(1), 53–63.

[539] Li, W.; Zhao, L.; Wei, T.; Zhao, Y.; Chen, C. The inhibition of death receptor mediated apoptosis through lysosome stabilization following internalization of carboxyfullerene nanoparticles. *Biomaterials*, **2011,** *32*(16), 4030–4041.

[540] Zakharian, T.Y.; Seryshev, A.; Sitharaman, B.; Gilbert, B.E.; Knight, V.; Wilson, L.J. A Fullerene−Paclitaxel Chemotherapeutic: Synthesis, Characterization, and Study of Biological Activity in Tissue Culture. *J. Am. Chem. Soc.*, **2005,** *127*(36), 12508–12509.

[541] Koshkina, N. V; Waldrep, J.C.; Roberts, L.E.; Golunski, E.; Melton, S.; Knight, V. Paclitaxel liposome aerosol treatment induces inhibition of pulmonary metastases in murine renal carcinoma model. *Clin. Cancer Res.*, **2001,** *7*(10), 3258–3262.

[542] Ryman-Rasmussen, J.P. Penetration of Intact Skin by Quantum Dots with Diverse Physicochemical Properties. *Toxicol. Sci.*, **2006,** *91*(1), 159–165.

[543] Wang, J. Carbon-Nanotube Based Electrochemical Biosensors: A Review. *Electroanalysis*, **2005,** *17*(1), 7–14.

[544] Fubini, B.; Ghiazza, M.; Fenoglio, I. Physico-chemical features of engineered nanoparticles relevant to their toxicity. *Nanotoxicology*, **2010,** *4*(4), 347–363.

[545] Porter, A.E.; Gass, M.; Muller, K.; Skepper, J.N.; Midgley, P.A.; Welland, M. Direct

imaging of single-walled carbon nanotubes in cells. *Nat. Nanotechnol.*, **2007,** *2*(11), 713–717.

[546] McDevitt, M.R.; Chattopadhyay, D.; Kappel, B.J.; Jaggi, J.S.; Schiffman, S.R.; Antczak, C.; Njardarson, J.T.; Brentjens, R.; Scheinberg, D.A. Tumor Targeting with Antibody-Functionalized, Radiolabeled Carbon Nanotubes. *J. Nucl. Med.*, **2007,** *48*(7), 1180–1189.

[547] Nerl, H.C.; Cheng, C.; Goode, A.E.; Bergin, S.D.; Lich, B.; Gass, M.; Porter, A.E. Imaging methods for determining uptake and toxicity of carbon nanotubes in vitro and in vivo. *Nanomedicine*, **2011,** *6*(5), 849–865.

[548] Boncel, S.; Müller, K.H.; Skepper, J.N.; Walczak, K.Z.; Koziol, K.K.K. Tunable chemistry and morphology of multi-wall carbon nanotubes as a route to non-toxic, theranostic systems. *Biomaterials*, **2011,** *32*(30), 7677–7686.

[549] Hiramatsu, M.; Hori, M. Aligned Growth of Single-Walled and Double-Walled Carbon Nanotube Films by Control of Catalyst Preparation. In *Carbon Nanotubes - Synthesis, Characterization, Applications*; InTech, **2011**.

[550] Bhirde, A.A.; Patel, S.; Sousa, A.A.; Patel, V.; Molinolo, A.A.; Ji, Y.; Leapman, R.D.; Gutkind, J.S.; Rusling, J.F. Distribution and clearance of PEG-single-walled carbon nanotube cancer drug delivery vehicles in mice. *Nanomedicine*, **2010,** *5*(10), 1535–1546.

[551] Vardharajula, S.; Ali, S.Z.; Tiwari, P.M.; Eroğlu, E.; Vig, K.; Dennis, V.A.; Singh, S.R. Functionalized carbon nanotubes: biomedical applications. *Int. J. Nanomedicine*, **2012,** *7*, 5361–5374.

[552] Tasis, D.; Tagmatarchis, N.; Bianco, A.; Prato, M. Chemistry of Carbon Nanotubes. *Chem. Rev.*, **2006,** *106*(3), 1105–1136.

[553] Yan, L.; Zhao, F.; Li, S.; Hu, Z.; Zhao, Y. Low-toxic and safe nanomaterials by surface-chemical design, carbon nanotubes, fullerenes, metallofullerenes, and graphenes. *Nanoscale*, **2011,** *3*(2), 362–382.

[554] Hirsch, A. Functionalization of Single-Walled Carbon Nanotubes. *Angew. Chem. Int. Ed. Engl.*, **2002,** *41*(11), 1853.

[555] Wu, W.; Wieckowski, S.; Pastorin, G.; Benincasa, M.; Klumpp, C.; Briand, J.-P.; Gennaro, R.; Prato, M.; Bianco, A. Targeted Delivery of Amphotericin B to Cells by Using Functionalized Carbon Nanotubes. *Angew. Chem. Int. Ed. Engl.*, **2005,** *44*(39), 6358–6362.

[556] Pastorin, G.; Wu, W.; Wieckowski, S.; Briand, J.-P.; Kostarelos, K.; Prato, M.; Bianco, A. Double functionalisation of carbon nanotubes for multimodal drug delivery. *Chem. Commun.*, **2006,** (11), 1182.

[557] Wong, B.S.; Yoong, S.L.; Jagusiak, A.; Panczyk, T.; Ho, H.K.; Ang, W.H.; Pastorin, G. Carbon nanotubes for delivery of small molecule drugs. *Adv. Drug Deliv. Rev.*, **2013,** *65*(15), 1964–2015.

[558] Zhang, X.; Meng, L.; Lu, Q.; Fei, Z.; Dyson, P.J. Targeted delivery and controlled release of doxorubicin to cancer cells using modified single wall carbon nanotubes. *Biomaterials*, **2009,** *30*(30), 6041–6047.

[559] Ji, Z.; Lin, G.; Lu, Q.; Meng, L.; Shen, X.; Dong, L.; Fu, C.; Zhang, X. Targeted therapy of SMMC-7721 liver cancer in vitro and in vivo with carbon nanotubes based drug delivery system. *J. Colloid Interface Sci.*, **2012,** *365*(1), 143–149.

[560] Huang, H.; Yuan, Q.; Shah, J.S.; Misra, R.D.K. A new family of folate-decorated and carbon nanotube-mediated drug delivery system: Synthesis and drug delivery response. *Adv. Drug Deliv. Rev.*, **2011,** *63*(14–15), 1332–1339.

[561] Liu, Z.; Sun, X.; Nakayama-Ratchford, N.; Dai, H. Supramolecular Chemistry on Water-Soluble Carbon Nanotubes for Drug Loading and Delivery. *ACS Nano*, **2007,** *1*(1), 50–56.

[562] Liu, Z.; Fan, A.C.; Rakhra, K.; Sherlock, S.; Goodwin, A.; Chen, X.; Yang, Q.; Felsher, D.W.; Dai, H. Supramolecular Stacking of Doxorubicin on Carbon Nanotubes for In Vivo Cancer Therapy. *Angew. Chem. Int. Ed. Engl.*, **2009,** *48*(41), 7668–7672.

[563] Ali-Boucetta, H.; Al-Jamal, K.T.; McCarthy, D.; Prato, M.; Bianco, A.; Kostarelos, K. Multiwalled carbon nanotube–doxorubicin supramolecular complexes for cancer therapeutics. *Chem. Commun.*, **2008,** (4), 459–461.

[564] Tian, Z.; Yin, M.; Ma, H.; Zhu, L.; Shen, H.; Jia, N. Supramolecular Assembly and Antitumor Activity of Multiwalled Carbon Nanotube–Camptothecin Complexes. *J. Nanosci. Nanotechnol.*, **2011,** *11*(2), 953–958.

[565] Tripisciano, C.; Rümmeli, M.H.; Chen, X.; Borowiak-Palen, E. Multi-wall carbon nanotubes - a vehicle for targeted Irinotecan drug delivery. *Phys. status solidi*, **2010,** *247*(11–12), 2673–2677.

[566] Klibanov, A.L.; Maruyama, K.; Torchilin, V.P.; Huang, L. Amphipathic polyethyleneglycols effectively prolong the circulation time of liposomes. *FEBS Lett.*, **1990,** *268*(1), 235–237.

[567] Allen, T.M.; Mehra, T.; Hansen, C.; Chin, Y.C. Stealth liposomes: an improved sustained release system for 1-beta-D-arabinofuranosylcytosine. *Cancer Res.*, **1992,** *52*(9), 2431–2439.

[568] Li, C.; Yu, D.; Inoue, T.; Yang, D.J.; Milas, L.; Hunter, N.R.; Kim, E.E.; Wallace, S. Synthesis and evaluation of water-soluble polyethylene glycol-paclitaxel conjugate as a paclitaxel prodrug. *Anticancer. Drugs*, **1996,** *7*(6), 642–648.

[569] Liu, Z.; Chen, K.; Davis, C.; Sherlock, S.; Cao, Q.; Chen, X.; Dai, H. Drug Delivery with Carbon Nanotubes for In vivo Cancer Treatment. *Cancer Res.*, **2008,** *68*(16), 6652–6660.

[570] Lay, C.L.; Liu, H.Q.; Tan, H.R.; Liu, Y. Delivery of paclitaxel by physically loading onto poly(ethylene glycol) (PEG)-graftcarbon nanotubes for potent cancer therapeutics. *Nanotechnology*, **2010,** *21*(6), 65101.

[571] Wheate, N.J.; Walker, S.; Craig, G.E.; Oun, R. The status of platinum anticancer drugs in the clinic and in clinical trials. *Dalt. Trans.*, **2010,** *39*(35), 8113.

[572] Wang, D.; Lippard, S.J. Cellular processing of platinum anticancer drugs. *Nat. Rev. Drug Discov.*, **2005,** *4*(4), 307–320.

[573] Chin, C.F.; Tian, Q.; Setyawati, M.I.; Fang, W.; Tan, E.S.Q.; Leong, D.T.; Ang, W.H.

Tuning the Activity of Platinum(IV) Anticancer Complexes through Asymmetric Acylation. *J. Med. Chem.*, **2012,** *55*(17), 7571–7582.

[574] Xu, P.; Van Kirk, E.A.; Murdoch, W.J.; Zhan, Y.; Isaak, D.D.; Radosz, M.; Shen, Y. Anticancer Efficacies of Cisplatin-Releasing pH-Responsive Nanoparticles. *Biomacromolecules*, **2006,** *7*(3), 829–835.

[575] Dhar, S.; Liu, Z.; Thomale, J.; Dai, H.; Lippard, S.J. Targeted Single-Wall Carbon Nanotube-Mediated Pt(IV) Prodrug Delivery Using Folate as a Homing Device. *J. Am. Chem. Soc.*, **2008,** *130*(34), 11467–11476.

[576] Yang, F.; Fu, D.L.; Long, J.; Ni, Q.X. Magnetic lymphatic targeting drug delivery system using carbon nanotubes. *Med. Hypotheses*, **2008,** *70*(4), 765–767.

[577] Guven, A.; Rusakova, I.A.; Lewis, M.T.; Wilson, L.J. Cisplatin@US-tube carbon nanocapsules for enhanced chemotherapeutic delivery. *Biomaterials*, **2012,** *33*(5), 1455–1461.

[578] Bhirde, A.A.; Sousa, A.A.; Patel, V.; Azari, A.A.; Gutkind, J.S.; Leapman, R.D.; Rusling, J.F. Imaging the distribution of individual platinum-based anticancer drug molecules attached to single-wall carbon nanotubes. *Nanomedicine*, **2009,** *4*(7), 763–772.

[579] Feazell, R.P.; Nakayama-Ratchford, N.; Dai, H.; Lippard, S.J. Soluble Single-Walled Carbon Nanotubes as Longboat Delivery Systems for Platinum(IV) Anticancer Drug Design. *J. Am. Chem. Soc.*, **2007,** *129*(27), 8438–8439.

[580] Antony, A.C. The biological chemistry of folate receptors. *Blood*, **1992,** *79*(11), 2807–2820.

[581] Bae, Y.; Jang, W.-D.; Nishiyama, N.; Fukushima, S.; Kataoka, K. Multifunctional polymeric micelles with folate-mediated cancer cell targeting and pH-triggered drug releasing properties for active intracellular drug delivery. *Mol. Biosyst.*, **2005,** *1*(3), 242.

[582] Zhang, Z.; Huey Lee, S.; Feng, S.-S. Folate-decorated poly(lactide-co-glycolide)-vitamin E TPGS nanoparticles for targeted drug delivery. *Biomaterials*, **2007,** *28*(10), 1889–1899.

[583] Yang, F.; Hu, J.; Yang, D.; Long, J.; Luo, G.; Jin, C.; Yu, X.; Xu, J.; Wang, C.; Ni, Q.; Fu, D. Pilot study of targeting magnetic carbon nanotubes to lymph nodes. *Nanomedicine*, **2009,** *4*(3), 317–330.

[584] Hampel, S.; Kunze, D.; Haase, D.; Krämer, K.; Rauschenbach, M.; Ritschel, M.; Leonhardt, A.; Thomas, J.; Oswald, S.; Hoffmann, V.; Büchner, B. Carbon nanotubes filled with a chemotherapeutic agent: a nanocarrier mediates inhibition of tumor cell growth. *Nanomedicine*, **2008,** *3*(2), 175–182.

[585] Khazaei, A.; Rad, M.N.S.; Borazjani, M.K. Organic functionalization of single-walled carbon nanotubes (SWCNTs) with some chemotherapeutic agents as a potential method for drug delivery. *Int. J. Nanomedicine*, **2010,** *5*, 639–645.

[586] Das, M.; Datir, S.R.; Singh, R.P.; Jain, S. Augmented Anticancer Activity of a Targeted, Intracellularly Activatable, Theranostic Nanomedicine Based on Fluorescent and Radiolabeled, Methotrexate-Folic Acid-Multiwalled Carbon Nanotube Conjugate. *Mol. Pharm.*, **2013,** *10*(7), 2543–2557.

[587] Li, Q.; Ruan, H.; Li, H. Nanocarbon Materials for Photodynamic Therapy and Photothermal Therapy. *Pharm. Nanotechnol.*, **2014,** *2*(2), 58–64.

[588] Brennan, M.E.; Coleman, J.N.; Drury, A.; Lahr, B.; Kobayashi, T.; Blau, W.J. Nonlinear photoluminescence from van Hove singularities in multiwalled carbon nanotubes. *Opt. Lett.*, **2003,** *28*(4), 266.

[589] Torti, S. V; Byrne, F.; Whelan, O.; Levi, N.; Ucer, B.; Schmid, M.; Torti, F.M.; Akman, S.; Liu, J.; Ajayan, P.M.; Nalamasu, O.; Carroll, D.L. Thermal ablation therapeutics based on CN(x) multi-walled nanotubes. *Int. J. Nanomedicine*, **2007,** *2*(4), 707–714.

[590] Zhou, F.; Xing, D.; Ou, Z.; Wu, B.; Resasco, D.E.; Chen, W.R. Cancer photothermal therapy in the near-infrared region by using single-walled carbon nanotubes. *J. Biomed. Opt.*, **2009,** *14*(2), 21009.

[591] Huang, N.; Wang, H.; Zhao, J.; Lui, H.; Korbelik, M.; Zeng, H. Single-wall carbon nanotubes assisted photothermal cancer therapy: Animal study with a murine model of squamous cell carcinoma. *Lasers Surg. Med.*, **2010,** *42*(9), 798–808.

[592] Ogbodu, R.O.; Limson, J.L.; Prinsloo, E.; Nyokong, T. Photophysical properties and photodynamic therapy effect of zinc phthalocyanine-spermine-single walled carbon nanotube conjugate on MCF-7 breast cancer cell line. *Synth. Met.*, **2015,** *204*, 122–132.

[593] Erbas, S.; Gorgulu, A.; Kocakusakogullari, M.; Akkaya, E.U. Non-covalent functionalized SWNTs as delivery agents for novel Bodipy-based potential PDT sensitizers. *Chem. Commun.*, **2009,** (33), 4956.

[594] Huang, P.; Lin, J.; Yang, D.; Zhang, C.; Li, Z.; Cui, D. Photosensitizer-loaded dendrimer-modified multi-walled carbon nanotubes for photodynamic therapy. *J. Control. Release*, **2011,** *152*, e33–e34.

[595] Wang, Y.; Hu, A. Carbon quantum dots: synthesis, properties and applications. *J. Mater. Chem. C*, **2014,** *2*(34), 6921.

[596] Demchenko, A.P.; Dekaliuk, M.O. Novel fluorescent carbonic nanomaterials for sensing and imaging. *Methods Appl. Fluoresc.*, **2013,** *1*(4), 42001.

[597] Yang, Y.; Cui, J.; Zheng, M.; Hu, C.; Tan, S.; Xiao, Y.; Yang, Q.; Liu, Y. One-step synthesis of amino-functionalized fluorescent carbon nanoparticles by hydrothermal carbonization of chitosan. *Chem. Commun.*, **2012,** *48*(3), 380–382.

[598] Bhunia, S.K.; Saha, A.; Maity, A.R.; Ray, S.C.; Jana, N.R. Carbon nanoparticle-based fluorescent bioimaging probes. *Sci. Rep.*, **2013,** *3*, 1473.

[599] Chen, B.; Li, F.; Li, S.; Weng, W.; Guo, H.; Guo, T.; Zhang, X.; Chen, Y.; Huang, T.; Hong, X.; You, S.; Lin, Y.; Zeng, K.; Chen, S. Large scale synthesis of photoluminescent carbon nanodots and their application for bioimaging. *Nanoscale*, **2013,** *5*(5), 1967.

[600] Cao, L.; Yang, S.-T.; Wang, X.; Luo, P.G.; Liu, J.-H.; Sahu, S.; Liu, Y.; Sun, Y.-P. Competitive performance of carbon “quantum” dots in optical bioimaging. *Theranostics*, **2012,** *2*(3), 295–301.

[601] Skrabalak, S.E. Ultrasound-assisted synthesis of carbon materials. *Phys. Chem. Chem. Phys.*, **2009,** *11*(25), 4930–42.

[602] Lee, H.U.; Park, S.Y.; Park, E.S.; Son, B.; Lee, S.C.; Lee, J.W.; Lee, Y.-C.; Kang, K.S.; Kim, M. Il; Park, H.G.; Choi, S.; Huh, Y.S.; Lee, S.-Y.; Lee, K.-B.; Oh, Y.-K.; Lee, J. Photoluminescent carbon nanotags from harmful cyanobacteria for drug delivery and imaging in cancer cells. *Sci. Rep.*, **2014,** *4*, 4665.

[603] Bechet, D.; Couleaud, P.; Frochot, C.; Viriot, M.-L.; Guillemin, F.; Barberi-Heyob, M. Nanoparticles as vehicles for delivery of photodynamic therapy agents. *Trends Biotechnol.*, **2008,** *26*(11), 612–621.

[604] Juzenas, P.; Kleinauskas, A.; George Luo, P.; Sun, Y.-P. Photoactivatable carbon nanodots for cancer therapy. *Appl. Phys. Lett.*, **2013,** *103*(6), 63701.

[605] Fowley, C.; Nomikou, N.; McHale, A.P.; McCaughan, B.; Callan, J.F. Extending the tissue penetration capability of conventional photosensitisers: a carbon quantum dot–protoporphyrin IX conjugate for use in two-photon excited photodynamic therapy. *Chem. Commun.*, **2013,** *49*(79), 8934.

[606] Zhang, Z.; Shi, Y.; Pan, Y.; Cheng, X.; Zhang, L.; Chen, J.; Li, M.-J.; Yi, C. Quinoline derivative-functionalized carbon dots as a fluorescent nanosensor for sensing and intracellular imaging of Zn^{2+}. *J. Mater. Chem. B*, **2014,** *2*(31), 5020.

[607] Qu, Q.; Zhu, A.; Shao, X.; Shi, G.; Tian, Y. Development of a carbon quantum dots-based fluorescent Cu^{2+} probe suitable for living cell imaging. *Chem. Commun.*, **2012,** *48*(44), 5473.

[608] Jiao, Y.; Zhu, B.; Chen, J.; Duan, X. Fluorescent sensing of fluoride in cellular system. *Theranostics*, **2015,** *5*(2), 173–187.

[609] Tang, L.; Ji, R.; Cao, X.; Lin, J.; Jiang, H.; Li, X.; Teng, K.S.; Luk, C.M.; Zeng, S.; Hao, J.; Lau, S.P. Deep Ultraviolet Photoluminescence of Water-Soluble Self-Passivated Graphene Quantum Dots. *ACS Nano*, **2012,** *6*(6), 5102–5110.

[610] Cao, L.; Sahu, S.; Anilkumar, P.; Bunker, C.E.; Xu, J.; Fernando, K.A.S.; Wang, P.; Guliants, E.A.; Tackett, K.N.; Sun, Y.-P. Carbon nanoparticles as visible-light photocatalysts for efficient CO_2 conversion and beyond. *J. Am. Chem. Soc.*, **2011,** *133*(13), 4754–4757.

[611] Li, H.; He, X.; Liu, Y.; Huang, H.; Lian, S.; Lee, S.T.; Kang, Z. One-step ultrasonic synthesis of water-soluble carbon nanoparticles with excellent photoluminescent properties. *Carbon*, **2011,** *49*(2), 605–609.

[612] Baker, S.N.; Baker, G.A. Luminescent carbon nanodots: emergent nanolights. *Angew. Chem. Int. Ed. Engl.*, **2010,** *49*(38), 6726–6744.

[613] Shen, J.; Zhu, Y.; Yang, X.; Li, C. Graphene quantum dots: emergent nanolights for bioimaging, sensors, catalysis and photovoltaic devices. *Chem. Commun. (Camb).*, **2012,** *48*(31), 3686–99.

[614] Hu, S.-L.; Niu, K.-Y.; Sun, J.; Yang, J.; Zhao, N.-Q.; Du, X.-W. One-step synthesis of fluorescent carbon nanoparticles by laser irradiation. *J. Mater. Chem.*, **2009,** *19*(4), 484–488.

[615] Lu, J.; Yang, J.; Wang, J.; Lim, A.; Wang, S.; Loh, K.P. One-Pot Synthesis of Fluorescent Carbon Nanoribbons, Nanoparticles, and Graphene by the Exfoliation of Graphite in Ionic Liquids. *ACS Nano*, **2009,** *3*(8), 2367–2375.

[616] Zhao, Q.-L.; Zhang, Z.-L.; Huang, B.-H.; Peng, J.; Zhang, M.; Pang, D.-W. Facile preparation of low cytotoxicity fluorescent carbon nanocrystals by electrooxidation of graphite. *Chem. Commun.*, **2008,** (41), 5116.

[617] Zheng, L.; Chi, Y.; Dong, Y.; Lin, J.; Wang, B. Electrochemiluminescence of Water-Soluble Carbon Nanocrystals Released Electrochemically from Graphite. *J. Am. Chem. Soc.*, **2009,** *131*(13), 4564–4565.

[618] Zhou, J.; Booker, C.; Li, R.; Zhou, X.; Sham, T.-K.; Sun, X.; Ding, Z. An Electrochemical Avenue to Blue Luminescent Nanocrystals from Multiwalled Carbon Nanotubes (MWCNTs). *J. Am. Chem. Soc.*, **2007,** *129*(4), 744–745.

[619] Bourlinos, A.B.; Stassinopoulos, A.; Anglos, D.; Zboril, R.; Georgakilas, V.; Giannelis, E.P. Photoluminescent Carbogenic Dots. *Chem. Mater.*, **2008,** *20*(14), 4539–4541.

[620] Bourlinos, A.B.; Stassinopoulos, A.; Anglos, D.; Zboril, R.; Karakassides, M.; Giannelis, E.P. Surface Functionalized Carbogenic Quantum Dots. *Small*, **2008,** *4*(4), 455–458.

[621] Liu, H.; Ye, T.; Mao, C. Fluorescent Carbon Nanoparticles Derived from Candle Soot. *Angew. Chem. Int. Ed. Engl.*, **2007,** *119*(34), 6593–6595.

[622] Ray, S.C.; Saha, A.; Jana, N.R.; Sarkar, R. Fluorescent Carbon Nanoparticles: Synthesis, Characterization, and Bioimaging Application. *J. Phys. Chem. C*, **2009,** *113*(43), 18546–18551.

[623] Tian, L.; Ghosh, D.; Chen, W.; Pradhan, S.; Chang, X.; Chen, S. Nanosized Carbon Particles From Natural Gas Soot. *Chem. Mater.*, **2009,** *21*(13), 2803–2809.

[624] Lu, S.; Guo, S.; Xu, P.; Li, X.; Zhao, Y.; Gu, W.; Xue, M. Hydrothermal synthesis of nitrogen-doped carbon dots with real-time live-cell imaging and blood–brain barrier penetration capabilities. *Int. J. Nanomedicine*, **2016,** *11*, 6325–6336.

[625] Zhu, H.; Wang, X.; Li, Y.; Wang, Z.; Yang, F.; Yang, X. Microwave synthesis of fluorescent carbon nanoparticles with electrochemiluminescence properties. *Chem. Commun. (Camb).*, **2009,** (34), 5118–20.

[626] Li, H.; He, X.; Liu, Y.; Yu, H.; Kang, Z.; Lee, S.T. Synthesis of fluorescent carbon nanoparticles directly from active carbon via a one-step ultrasonic treatment. *Mater. Res. Bull.*, **2011,** *46*(1), 147–151.

[627] Li, H.; He, X.; Kang, Z.; Huang, H.; Liu, Y.; Liu, J.; Lian, S.; Tsang, C.H.A.; Yang, X.; Lee, S.T. Water-soluble fluorescent carbon quantum dots and photocatalyst design. *Angew. Chemie - Int. Ed.*, **2010,** *49*(26), 4430–4434.

[628] Ming, H.; Ma, Z.; Liu, Y.; Pan, K.; Yu, H.; Wang, F.; Kang, Z. Large scale electrochemical synthesis of high quality carbon nanodots and their photocatalytic property. *Dalt. Trans.*, **2012,** *41*(31), 9526.

[629] Liu, H.; Ye, T.; Mao, C. Fluorescent carbon nanoparticles derived from candle soot. *Angew. Chem. Int. Ed. Engl.*, **2007,** *46*(34), 6473–5.

[630] Li, S.; Wang, L.; Chusuei, C.C.; Suarez, V.M.; Blackwelder, P.L.; Micic, M.; Orbulescu, J.; Leblanc, R.M. Nontoxic Carbon Dots Potently Inhibit Human Insulin Fibrillation. *Chem. Mater.*, **2015,** *27*(5), 1764–1771.

[631] Qian, Z.S.; Chai, L.J.; Huang, Y.Y.; Tang, C.; Jia Shen, J.; Chen, J.R.; Feng, H. A real-time fluorescent assay for the detection of alkaline phosphatase activity based on carbon quantum dots. *Biosens. Bioelectron.*, **2015,** *68*, 675–680.

[632] Wang, L.; Ruan, F.; Lv, T.; Liu, Y.; Deng, D.; Zhao, S.; Wang, H.; Xu, S. One step synthesis of Al/N co-doped carbon nanoparticles with enhanced photoluminescence. *J. Lumin.*, **2015,** *158*, 1–5.

[633] Wang, C.; Xu, Z.; Cheng, H.; Lin, H.; Humphrey, M.G.; Zhang, C. A hydrothermal route to water-stable luminescent carbon dots as nanosensors for pH and temperature. *Carbon*, **2015,** *82*, 87–95.

[634] Sadhanala, H.K.; Khatei, J.; Nanda, K.K. Facile hydrothermal synthesis of carbon nanoparticles and possible application as white light phosphors and catalysts for the reduction of nitrophenol. *RSC Adv.*, **2014,** *4*(22), 11481.

[635] Gao, X.; Lu, Y.; Zhang, R.; He, S.; Ju, J.; Liu, M.; Li, L.; Chen, W. One-pot synthesis of carbon nanodots for fluorescence turn-on detection of Ag^+ based on the Ag^+ -induced enhancement of fluorescence. *J. Mater. Chem. C*, **2015,** *3*(10), 2302–2309.

[636] Tong, G.; Wang, J.; Wang, R.; Guo, X.; He, L.; Qiu, F.; Wang, G.; Zhu, B.; Zhu, X.; Liu, T. Amorphous carbon dots with high two-photon fluorescence for cellular imaging passivated by hyperbranched poly(amino amine). *J. Mater. Chem. B*, **2015,** *3*(4), 700–706.

[637] Zhou, L.; He, B.; Huang, J. Amphibious fluorescent carbon dots: one-step green synthesis and application for light-emitting polymer nanocomposites. *Chem. Commun.*, **2013,** *49*(73), 8078.

[638] Pei, S.; Zhang, J.; Gao, M.; Wu, D.; Yang, Y.; Liu, R. A facile hydrothermal approach towards photoluminescent carbon dots from amino acids. *J. Colloid Interface Sci.*, **2015,** *439*, 129–133.

[639] Li, C.-L.; Huang, C.-C.; Periasamy, A.P.; Roy, P.; Wu, W.-C.; Hsu, C.-L.; Chang, H.-T. Synthesis of photoluminescent carbon dots for the detection of cobalt ions. *RSC Adv.*, **2015,** *5*(3), 2285–2291.

[640] Zhang, Z.; Sun, W.; Wu, P. Highly Photoluminescent Carbon Dots Derived from Egg White: Facile and Green Synthesis, Photoluminescence Properties, and Multiple Applications. *ACS Sustain. Chem. Eng.*, **2015,** *3*(7), 1412–1418.

[641] Wu, Z.L.; Zhang, P.; Gao, M.X.; Liu, C.F.; Wang, W.; Leng, F.; Huang, C.Z. One-pot hydrothermal synthesis of highly luminescent nitrogen-doped amphoteric carbon dots for bioimaging from Bombyx mori silk – natural proteins. *J. Mater. Chem. B*, **2013,** *1*(22), 2868.

[642] Mehta, V.N.; Jha, S.; Basu, H.; Singhal, R.K.; Kailasa, S.K. One-step hydrothermal approach to fabricate carbon dots from apple juice for imaging of mycobacterium and fungal cells. *Sensors Actuators B Chem.*, **2015,** *213*, 434–443.

[643] Xue, M.; Zou, M.; Zhao, J.; Zhan, Z.; Zhao, S. Green preparation of fluorescent carbon dots from lychee seeds and their application for the selective detection of methylene blue and imaging in living cells. *J. Mater. Chem. B*, **2015,** *3*(33), 6783–6789.

[644] Liu, S.; Tian, J.; Wang, L.; Zhang, Y.; Qin, X.; Luo, Y.; Asiri, A.M.; Al-Youbi, A.O.;

Sun, X. Hydrothermal Treatment of Grass: A Low-Cost, Green Route to Nitrogen-Doped, Carbon-Rich, Photoluminescent Polymer Nanodots as an Effective Fluorescent Sensing Platform for Label-Free Detection of Cu(II) Ions. *Adv. Mater.*, **2012,** *24*(15), 2037–2041.

[645] Wu, L.; Luderer, M.; Yang, X.; Swain, C.; Zhang, H.; Nelson, K.; Stacy, A.J.; Shen, B.; Lanza, G.M.; Pan, D. Surface passivation of carbon nanoparticles with branched macromolecules influences near infrared bioimaging. *Theranostics*, **2013,** *3*, 677–686.

[646] Park, S.Y.; Lee, H.U.; Park, E.S.; Lee, S.C.; Lee, J.-W.; Jeong, S.W.; Kim, C.H.; Lee, Y.-C.; Huh, Y.S.; Lee, J. Photoluminescent green carbon nanodots from food-waste-derived sources: large-scale synthesis, properties, and biomedical applications. *ACS Appl. Mater. Interfaces*, **2014,** *6*(5), 3365–3370.

[647] Sun, D.; Ban, R.; Zhang, P.-H.; Wu, G.-H.; Zhang, J.-R.; Zhu, J.-J. Hair fiber as a precursor for synthesizing of sulfur- and nitrogen-co-doped carbon dots with tunable luminescence properties. *Carbon*, **2013,** *64*, 424–434.

[648] Prasannan, A.; Imae, T. One-Pot Synthesis of Fluorescent Carbon Dots from Orange Waste Peels. *Ind. Eng. Chem. Res.*, **2013,** *52*(44), 15673–15678.

[649] Sahu, S.; Behera, B.; Maiti, T.K.; Mohapatra, S. Simple one-step synthesis of highly luminescent carbon dots from orange juice: application as excellent bio-imaging agents. *Chem. Commun. (Camb).*, **2012,** *48*(70), 8835–8837.

[650] Pan, D.; Zhang, J.; Li, Z.; Wu, M. Hydrothermal Route for Cutting Graphene Sheets into Blue-Luminescent Graphene Quantum Dots. *Adv. Mater.*, **2010,** *22*(6), 734–738.

[651] Zhang, B.; Liu, C.; Liu, Y. A Novel One-Step Approach to Synthesize Fluorescent Carbon Nanoparticles. *Eur. J. Inorg. Chem.*, **2010,** *2010*(28), 4411–4414.

[652] Pan, D.; Guo, L.; Zhang, J.; Xi, C.; Xue, Q.; Huang, H.; Li, J.; Zhang, Z.; Yu, W.; Chen, Z.; Li, Z.; Wu, M. Cutting sp^2 clusters in graphene sheets into colloidal graphene quantum dots with strong green fluorescence. *J. Mater. Chem.*, **2012,** *22*(8), 3314.

[653] Zhang, J.; Shen, W.; Pan, D.; Zhang, Z.; Fang, Y.; Wu, M. Controlled synthesis of green and blue luminescent carbon nanoparticles with high yields by the carbonization of sucrose. *New J. Chem.*, **2010,** *34*(4), 591.

[654] He, X.; Li, H.; Liu, Y.; Huang, H.; Kang, Z.; Lee, S.-T. Water soluble carbon nanoparticles: hydrothermal synthesis and excellent photoluminescence properties. *Colloids Surf B Biointerfaces.*, **2011,** *87*(2), 326–332.

[655] Guo, Y.; Wang, Z.; Shao, H.; Jiang, X. Hydrothermal synthesis of highly fluorescent carbon nanoparticles from sodium citrate and their use for the detection of mercury ions. *Carbon*, **2013,** *52*, 583–589.

[656] Zhou, J.; Sheng, Z.; Han, H.; Zou, M.; Li, C. Facile synthesis of fluorescent carbon dots using watermelon peel as a carbon source. *Mater. Lett.*, **2012,** *66*(1), 222–224.

[657] Ding, C.; Zhu, A.; Tian, Y. Functional surface engineering of C-dots for fluorescent biosensing and in vivo bioimaging. *Acc. Chem. Res.*, **2014,** *47*(1), 20–30.

[658] Zhu, S.; Meng, Q.; Wang, L.; Zhang, J.; Song, Y.; Jin, H.; Zhang, K.; Sun, H.; Wang, H.; Yang, B. Highly Photoluminescent Carbon Dots for Multicolor Patterning, Sensors,

and Bioimaging. *Angew. Chem. Int. Ed. Engl.*, **2013,** *125*(14), 4045–4049.

[659] Jiang, K.; Sun, S.; Zhang, L.; Lu, Y.; Wu, A.; Cai, C.; Lin, H. Red, Green, and Blue Luminescence by Carbon Dots: Full-Color Emission Tuning and Multicolor Cellular Imaging. *Angew. Chem. Int. Ed. Engl.*, **2015,** *54*(18), 5360–5363.

[660] Lee, C.H.; Rajendran, R.; Jeong, M.-S.; Ko, H.Y.; Joo, J.Y.; Cho, S.; Chang, Y.W.; Kim, S. Bioimaging of targeting cancers using aptamer-conjugated carbon nanodots. *Chem. Commun.*, **2013,** *49*(58), 6543.

[661] Chandra, S.; Patra, P.; Pathan, S.H.; Roy, S.; Mitra, S.; Layek, A.; Bhar, R.; Pramanik, P.; Goswami, A. Luminescent S-doped carbon dots: an emergent architecture for multimodal applications. *J. Mater. Chem. B*, **2013,** *1*(18), 2375.

[662] Dong, Y.; Pang, H.; Yang, H. Bin; Guo, C.; Shao, J.; Chi, Y.; Li, C.M.; Yu, T. Carbon-based dots co-doped with nitrogen and sulfur for high quantum yield and excitation-independent emission. *Angew. Chem. Int. Ed. Engl.*, **2013,** *52*(30), 7800–7804.

[663] Puvvada, N.; Kumar, B.N.P.; Konar, S.; Kalita, H.; Mandal, M.; Pathak, A. Synthesis of biocompatible multicolor luminescent carbon dots for bioimaging applications. *Sci. Technol. Adv. Mater.* **2012**, , *13*, 45008.

[664] Wang, W.; Li, Y.; Cheng, L.; Cao, Z.; Liu, W. Water-soluble and phosphorus-containing carbon dots with strong green fluorescence for cell labeling. *J. Mater. Chem. B*, **2014,** *2*(1), 46–48.

[665] Wang, X.; Qu, K.; Xu, B.; Ren, J.; Qu, X. Microwave assisted one-step green synthesis of cell-permeable multicolor photoluminescent carbon dots without surface passivation reagents. *J. Mater. Chem.*, **2011,** *21*(8), 2445.

[666] Jaiswal, A.; Ghosh, S.S.; Chattopadhyay, A. One step synthesis of C-dots by microwave mediated caramelization of poly(ethylene glycol). *Chem. Commun.*, **2012,** *48*(3), 407–409.

[667] Lai, C.-W.; Hsiao, Y.-H.; Peng, Y.-K.; Chou, P.-T. Facile synthesis of highly emissive carbon dots from pyrolysis of glycerol; gram scale production of carbon dots/mSiO_2 for cell imaging and drug release. *J. Mater. Chem.*, **2012,** *22*(29), 14403.

[668] Wei, W.; Xu, C.; Wu, L.; Wang, J.; Ren, J.; Qu, X. Non-enzymatic-browning-reaction: a versatile route for production of nitrogen-doped carbon dots with tunable multicolor luminescent display. *Sci. Rep.*, **2014,** *4*, 3564.

[669] Qian, Z.; Ma, J.; Shan, X.; Feng, H.; Shao, L.; Chen, J. Highly Luminescent N-Doped Carbon Quantum Dots as an Effective Multifunctional Fluorescence Sensing Platform. *Chem. - A Eur. J.*, **2014,** *20*(8), 2254–2263.

[670] Xu, Y.; Wu, M.; Liu, Y.; Feng, X.-Z.; Yin, X.-B.; He, X.-W.; Zhang, Y.-K. Nitrogen-Doped Carbon Dots: A Facile and General Preparation Method, Photoluminescence Investigation, and Imaging Applications. *Chem. - A Eur. J.*, **2013,** *19*(7), 2276–2283.

[671] Xu, Z.-Q.; Yang, L.-Y.; Fan, X.-Y.; Jin, J.-C.; Mei, J.; Peng, W.; Jiang, F.-L.; Xiao, Q.; Liu, Y. Low temperature synthesis of highly stable phosphate functionalized two color carbon nanodots and their application in cell imaging. *Carbon*, **2014,** *66*, 351–360.

[672] Chandra, S.; Das, P.; Bag, S.; Laha, D.; Pramanik, P. Synthesis, functionalization and

bioimaging applications of highly fluorescent carbon nanoparticles. *Nanoscale*, **2011,** *3*, 1533–1540.

[673] Jahan, S.; Mansoor, F.; Naz, S.; Lei, J.; Kanwal, S. Oxidative synthesis of highly fluorescent boron/nitrogen co-doped carbon nanodots enabling detection of photosensitizer and carcinogenic dye. *Anal. Chem.*, **2013,** *85*(21), 10232–10239.

[674] Hu, S.; Tian, R.; Dong, Y.; Yang, J.; Liu, J.; Chang, Q. Modulation and effects of surface groups on photoluminescence and photocatalytic activity of carbon dots. *Nanoscale*, **2013,** *5*(23), 11665.

[675] Hu, C.; Yu, C.; Li, M.; Wang, X.; Yang, J.; Zhao, Z.; Eychmüller, A.; Sun, Y.-P.; Qiu, J. Chemically Tailoring Coal to Fluorescent Carbon Dots with Tuned Size and Their Capacity for Cu(II) Detection. *Small*, **2014,** *10*(23), 4926–4933.

[676] Peng, H.; Travas-Sejdic, J. Simple Aqueous Solution Route to Luminescent Carbogenic Dots from Carbohydrates. *Chem. Mater.*, **2009,** *21*(23), 5563–5565.

[677] Shen, J.; Zhu, Y.; Chen, C.; Yang, X.; Li, C. Facile preparation and upconversion luminescence of graphene quantum dots. *Chem. Commun. (Camb).*, **2011,** *47*(9), 2580–2582.

[678] Qu, S.; Chen, H.; Zheng, X.; Cao, J.; Liu, X. Ratiometric fluorescent nanosensor based on water soluble carbon nanodots with multiple sensing capacities. *Nanoscale*, **2013,** *5*(12), 5514.

[679] Jia, X.; Li, J.; Wang, E. One-pot green synthesis of optically pH-sensitive carbon dots with upconversion luminescence. *Nanoscale*, **2012,** *4*(18), 5572.

[680] Jia, X.; Yang, X.; Li, J.; Li, D.; Wang, E. Stable Cu nanoclusters: from an aggregation-induced emission mechanism to biosensing and catalytic applications. *Chem. Commun.*, **2014,** *50*(2), 237–239.

[681] Chen, H.; Xie, Y.; Kirillov, A.M.; Liu, L.; Yu, M.; Liu, W.; Tang, Y. A ratiometric fluorescent nanoprobe based on terbium functionalized carbon dots for highly sensitive detection of an anthrax biomarker. *Chem. Commun.*, **2015,** *51*(24), 5036–5039.

[682] Ge, J.; Jia, Q.; Liu, W.; Guo, L.; Liu, Q.; Lan, M.; Zhang, H.; Meng, X.; Wang, P. Red-Emissive Carbon Dots for Fluorescent, Photoacoustic, and Thermal Theranostics in Living Mice. *Adv. Mater.*, **2015,** *27*(28), 4169–4177.

[683] Lim, S.Y.; Shen, W.; Gao, Z. Carbon quantum dots and their applications. *Chem. Soc. Rev.*, **2014,** *44*(1), 362–381.

[684] Wang, X.; Cao, L.; Yang, S.-T.; Lu, F.; Meziani, M.J.; Tian, L.; Sun, K.W.; Bloodgood, M. a; Sun, Y.-P. Bandgap-like strong fluorescence in functionalized carbon nanoparticles. *Angew. Chem. Int. Ed. Engl.*, **2010,** *49*(31), 5310–5314.

[685] Zheng, H.; Wang, Q.; Long, Y.; Zhang, H.; Huang, X.; Zhu, R. Enhancing the luminescence of carbon dots with a reduction pathway. *Chem. Commun.* **2011**, *47*, 10650.

[686] Wang, J.; Su, S.; Wei, J.; Bahgi, R.; Hope-Weeks, L.; Qiu, J.; Wang, S. Ratio-metric sensor to detect riboflavin via fluorescence resonance energy transfer with ultrahigh sensitivity. *Phys. E Low-dimensional Syst. Nanostructures*, **2015,** *72*, 17–24.

[687] Zhang, H.; Chen, Y.; Liang, M.; Xu, L.; Qi, S.; Chen, H.; Chen, X. Solid-Phase Synthesis of Highly Fluorescent Nitrogen-Doped Carbon Dots for Sensitive and Selective Probing Ferric Ions in Living Cells. *Anal. Chem.*, **2014,** *86*(19), 9846–9852.

[688] Jiang, J.; He, Y.; Li, S.; Cui, H. Amino acids as the source for producing carbon nanodots: microwave assisted one-step synthesis, intrinsic photoluminescence property and intense chemiluminescence enhancement. *Chem. Commun.*, **2012,** *48*(77), 9634.

[689] Xu, Q.; Pu, P.; Zhao, J.; Dong, C.; Gao, C.; Chen, Y.; Chen, J.; Liu, Y.; Zhou, H. Preparation of highly photoluminescent sulfur-doped carbon dots for Fe(III) detection. *J. Mater. Chem. A*, **2015,** *3*(2), 542–546.

[690] Sun, Y.; Wang, X.; Lu, F.; Cao, L.; Meziani, M.J.; Luo, P.G.; Gu, L.; Veca, L.M. Doped Carbon Nanoparticles as a New Platform for Highly Photoluminescent Dots. *J. Phys. Chem. C. Nanomater. Interfaces*, **2008,** *112*(47), 18295–18298.

[691] Stan, C.S.; Albu, C.; Coroaba, A.; Popa, M.; Sutiman, D. One step synthesis of fluorescent carbon dots through pyrolysis of N-hydroxysuccinimide. *J. Mater. Chem. C*, **2015,** *3*(4), 789–795.

[692] Shen, J.; Zhu, Y.; Yang, X.; Zong, J.; Zhang, J.; Li, C. One-pot hydrothermal synthesis of graphenequantum dots surface-passivated by polyethylene glycol and their photoelectric conversion under near-infrared light. *New J. Chem.*, **2012,** *36*(1), 97–101.

[693] Lin, Z.; Xue, W.; Chen, H.; Lin, J.-M. Classical oxidant induced chemiluminescence of fluorescent carbon dots. *Chem. Commun.*, **2012,** *48*(7), 1051–1053.

[694] Teng, P.; Xie, J.; Long, Y.; Huang, X.; Zhu, R.; Wang, X.; Liang, L.; Huang, Y.; Zheng, H. Chemiluminescence behavior of the carbon dots and the reduced state carbon dots. *J. Lumin.*, **2014,** *146*, 464–469.

[695] Zhao, L.; Di, F.; Wang, D.; Guo, L.-H.; Yang, Y.; Wan, B.; Zhang, H. Chemiluminescence of carbon dots under strong alkaline solutions: a novel insight into carbon dot optical properties. *Nanoscale*, **2013,** *5*(7), 2655.

[696] Zhu, H.; Wang, X.; Li, Y.; Wang, Z.; Yang, F.; Yang, X. Microwave synthesis of fluorescent carbon nanoparticles with electrochemiluminescence properties. *Chem. Commun. (Camb).*, **2009,** (34), 5118–5120.

[697] Kong, W.; Liu, J.; Liu, R.; Li, H.; Liu, Y.; Huang, H.; Li, K.; Liu, J.; Lee, S.-T.; Kang, Z. Quantitative and real-time effects of carbon quantum dots on single living HeLa cell membrane permeability. *Nanoscale*, **2014,** *6*(10), 5116.

[698] Shang, W.; Zhang, X.; Zhang, M.; Fan, Z.; Sun, Y.; Han, M.; Fan, L. The uptake mechanism and biocompatibility of graphene quantum dots with human neural stem cells. *Nanoscale*, **2014,** *6*(11), 5799.

[699] Huang, X.; Zhang, F.; Zhu, L.; Choi, K.Y.; Guo, N.; Guo, J.; Tackett, K.; Anilkumar, P.; Liu, G.; Quan, Q.; Choi, H.S.; Niu, G.; Sun, Y.-P.; Lee, S.; Chen, X. Effect of injection routes on the biodistribution, clearance, and tumor uptake of carbon dots. *ACS Nano*, **2013,** *7*(7), 5684–93.

[700] Wang, Y.; Anilkumar, P.; Cao, L.; Liu, J.-H.; Luo, P.G.; Tackett, K.N.; Sahu, S.; Wang, P.; Wang, X.; Sun, Y.-P. Carbon dots of different composition and surface functionalization: cytotoxicity issues relevant to fluorescence cell imaging. *Exp. Biol.*

Med., **2011,** *236*(11), 1231–1238.

[701] Li, N.; Liang, X.; Wang, L.; Li, Z.; Li, P.; Zhu, Y.; Song, J. Biodistribution study of carbogenic dots in cells and in vivo for optical imaging. *J. Nanoparticle Res.*, **2012,** *14*(10), 1177.

[702] Liu, J.-H.; Anilkumar, P.; Cao, L.; Wang, X.; Yang, S.-T.; Luo, P.G.; Wang, H.; Lu, F.; Meziani, M.J.; Liu, Y.; Korch, K.; Sun, Y.-P. Cytotoxicity Evaluations of Fluorescent Carbon Nanoparticles. *Nano Life*, **2010,** *1*(01n02), 153–161.

[703] Zhao, Q.-L.; Zhang, Z.-L.; Huang, B.-H.; Peng, J.; Zhang, M.; Pang, D.-W. Facile preparation of low cytotoxicity fluorescent carbon nanocrystals by electrooxidation of graphite. *Chem. Commun. (Camb).*, **2008,** (41), 5116–5118.

[704] Dong, Y.; Wang, R.; Li, G.; Chen, C.; Chi, Y.; Chen, G. Polyamine-Functionalized Carbon Quantum Dots as Fluorescent Probes for Selective and Sensitive Detection of Copper Ions. *Anal. Chem.*, **2012,** *84*(14), 6220–6224.

[705] Wang, Y.; Bao, L.; Liu, Z.; Pang, D.-W. Aptamer Biosensor Based on Fluorescence Resonance Energy Transfer from Upconverting Phosphors to Carbon Nanoparticles for Thrombin Detection in Human Plasma. *Anal. Chem.*, **2011,** *83*(21), 8130–8137.

[706] Wang, X.; Cao, L.; Yang, S.-T.; Lu, F.; Meziani, M.J.; Tian, L.; Sun, K.W.; Bloodgood, M.A.; Sun, Y.-P. Bandgap-Like Strong Fluorescence in Functionalized Carbon Nanoparticles. *Angew. Chem. Int. Ed. Engl.*, **2010,** *122*(31), 5438–5442.

[707] Yu, H.; Zhao, Y.; Zhou, C.; Shang, L.; Peng, Y.; Cao, Y.; Wu, L.-Z.; Tung, C.-H.; Zhang, T. Carbon quantum dots/TiO_2 composites for efficient photocatalytic hydrogen evolution. *J. Mater. Chem. A*, **2014,** *2*(10), 3344.

[708] Zhang, X.; Huang, H.; Liu, J.; Liu, Y.; Kang, Z. Carbon quantum dots serving as spectral converters through broadband upconversion of near-infrared photons for photoelectrochemical hydrogen generation. *J. Mater. Chem. A*, **2013,** *1*(38), 11529.

[709] Dey, D.; Bhattacharya, T.; Majumdar, B.; Mandani, S.; Sharma, B.; Sarma, T.K. Carbon dot reduced palladium nanoparticles as active catalysts for carbon–carbon bond formation. *Dalt. Trans.*, **2013,** *42*(38), 13821.

[710] Zhang, X.; Zhang, Y.; Wang, Y.; Kalytchuk, S.; Kershaw, S. V.; Wang, Y.; Wang, P.; Zhang, T.; Zhao, Y.; Zhang, H.; Cui, T.; Wang, Y.; Zhao, J.; Yu, W.W.; Rogach, A.L. Color-Switchable Electroluminescence of Carbon Dot Light-Emitting Diodes. *ACS Nano*, **2013,** *7*(12), 11234–11241.

[711] Chen, Q.-L.; Wang, C.-F.; Chen, S. One-step synthesis of yellow-emitting carbogenic dots toward white light-emitting diodes. *J. Mater. Sci.*, **2013,** *48*(6), 2352–2357.

[712] Sekiya, R.; Uemura, Y.; Murakami, H.; Haino, T. White-Light-Emitting Edge-Functionalized Graphene Quantum Dots. *Angew. Chem. Int. Ed. Engl.*, **2014,** *53*(22), 5619–5623.

[713] Li, M.; Ni, W.; Kan, B.; Wan, X.; Zhang, L.; Zhang, Q.; Long, G.; Zuo, Y.; Chen, Y. Graphene quantum dots as the hole transport layer material for high-performance organic solar cells. *Phys. Chem. Chem. Phys.*, **2013,** *15*(43), 18973.

[714] Huang, J.J.; Zhong, Z.F.; Rong, M.Z.; Zhou, X.; Chen, X.D.; Zhang, M.Q. An easy

approach of preparing strongly luminescent carbon dots and their polymer based composites for enhancing solar cell efficiency. *Carbon*, **2014,** *70*, 190–198.

[715] Zhang, Y.-Q.; Ma, D.-K.; Zhang, Y.-G.; Chen, W.; Huang, S.-M. N-doped carbon quantum dots for TiO_2-based photocatalysts and dye-sensitized solar cells. *Nano Energy*, **2013,** *2*(5), 545–552.

[716] Mirtchev, P.; Henderson, E.J.; Soheilnia, N.; Yip, C.M.; Ozin, G.A. Solution phase synthesis of carbon quantum dots as sensitizers for nanocrystalline TiO_2 solar cells. *J. Mater. Chem.*, **2012,** *22*(4), 1265–1269.

[717] Gupta, V.; Chaudhary, N.; Srivastava, R.; Sharma, G.D.; Bhardwaj, R.; Chand, S. Luminscent Graphene Quantum Dots for Organic Photovoltaic Devices. *J. Am. Chem. Soc.*, **2011,** *133*(26), 9960–9963.

[718] Kwon, W.; Lee, G.; Do, S.; Joo, T.; Rhee, S.-W. Size-Controlled Soft-Template Synthesis of Carbon Nanodots toward Versatile Photoactive Materials. *Small*, **2014,** *10*(3), 506–513.

[719] Qin, Y.; Cheng, Y.; Jiang, L.; Jin, X.; Li, M.; Luo, X.; Liao, G.; Wei, T.; Li, Q. Top-down Strategy toward Versatile Graphene Quantum Dots for Organic/Inorganic Hybrid Solar Cells. *ACS Sustain. Chem. Eng.*, **2015,** *3*(4), 637–644.

[720] Ma, Z.; Zhang, Y.-L.; Wang, L.; Ming, H.; Li, H.; Zhang, X.; Wang, F.; Liu, Y.; Kang, Z.; Lee, S.-T. Bioinspired Photoelectric Conversion System Based on Carbon-Quantum-Dot-Doped Dye–Semiconductor Complex. *ACS Appl. Mater. Interfaces*, **2013,** *5*(11), 5080–5084.

[721] Mehta, V.N.; Jha, S.; Singhal, R.K.; Kailasa, S.K. Preparation of multicolor emitting carbon dots for HeLa cell imaging. *New J. Chem.*, **2014,** *38*(12), 6152–6160.

[722] Liu, C.; Zhang, P.; Zhai, X.; Tian, F.; Li, W.; Yang, J.; Liu, Y.; Wang, H.; Wang, W.; Liu, W. Nano-carrier for gene delivery and bioimaging based on carbon dots with PEI-passivation enhanced fluorescence. *Biomaterials*, **2012,** *33*(13), 3604–3613.

[723] Zhai, X.; Zhang, P.; Liu, C.; Bai, T.; Li, W.; Dai, L.; Liu, W. Highly luminescent carbon nanodots by microwave-assisted pyrolysis. *Chem. Commun.*, **2012,** *48*(64), 7955.

[724] Li, H.; Zhang, Y.; Wang, L.; Tian, J.; Sun, X. Nucleic acid detection using carbon nanoparticles as a fluorescent sensing platform. *Chem. Commun.*, **2011,** *47*(3), 961–963.

[725] Zhao, H.X.; Liu, L.Q.; Liu, Z. De; Wang, Y.; Zhao, X.J.; Huang, C.Z. Highly selective detection of phosphate in very complicated matrixes with an off–on fluorescent probe of europium-adjusted carbon dots. *Chem. Commun.*, **2011,** *47*(9), 2604.

[726] Liu, J.; Li, J.; Jiang, Y.; Yang, S.; Tan, W.; Yang, R. Combination of π–π stacking and electrostatic repulsion between carboxylic carbon nanoparticles and fluorescent oligonucleotides for rapid and sensitive detection of thrombin. *Chem. Commun.*, **2011,** *47*(40), 11321.

[727] Lin, Z.; Xue, W.; Chen, H.; Lin, J.-M. Peroxynitrous-Acid-Induced Chemiluminescence of Fluorescent Carbon Dots for Nitrite Sensing. *Anal. Chem.*, **2011,** *83*(21), 8245–8251.

[728] Shi, W.; Wang, Q.; Long, Y.; Cheng, Z.; Chen, S.; Zheng, H.; Huang, Y. Carbon nanodots as peroxidase mimetics and their applications to glucose detection. *Chem. Commun.*, **2011,** *47*(23), 6695.

[729] Karfa, P.; Roy, E.; Patra, S.; Kumar, S.; Tarafdar, A.; Madhuri, R.; Sharma, P.K. Amino acid derived highly luminescent, heteroatom-doped carbon dots for label-free detection of Cd^{2+}/Fe^{3+}, cell imaging and enhanced antibacterial activity. *RSC Adv.*, **2015,** *5*(72), 58141–58153.

[730] Kong, B.; Zhu, A.; Ding, C.; Zhao, X.; Li, B.; Tian, Y. Carbon Dot-Based Inorganic-Organic Nanosystem for Two-Photon Imaging and Biosensing of pH Variation in Living Cells and Tissues. *Adv. Mater.*, **2012,** *24*(43), 5844–5848.

[731] Li, H.; Zhai, J.; Sun, X. Sensitive and Selective Detection of Silver(I) Ion in Aqueous Solution Using Carbon Nanoparticles as a Cheap, Effective Fluorescent Sensing Platform. *Langmuir*, **2011,** *27*(8), 4305–4308.

[732] Li, H.; Zhai, J.; Tian, J.; Luo, Y.; Sun, X. Carbon nanoparticle for highly sensitive and selective fluorescent detection of mercury(II) ion in aqueous solution. *Biosens. Bioelectron.*, **2011,** *26*(12), 4656–4660.

[733] Hou, Y.; Lu, Q.; Deng, J.; Li, H.; Zhang, Y. One-pot electrochemical synthesis of functionalized fluorescent carbon dots and their selective sensing for mercury ion. *Anal. Chim. Acta*, **2015,** *866*, 69–74.

[734] Huang, H.; Lv, J.-J.; Zhou, D.-L.; Bao, N.; Xu, Y.; Wang, A.-J.; Feng, J.-J. One-pot green synthesis of nitrogen-doped carbon nanoparticles as fluorescent probes for mercury ions. *RSC Adv.*, **2013,** *3*(44), 21691.

[735] Yan, F.; Zou, Y.; Wang, M.; Mu, X.; Yang, N.; Chen, L. Highly photoluminescent carbon dots-based fluorescent chemosensors for sensitive and selective detection of mercury ions and application of imaging in living cells. *Sensors Actuators B Chem.*, **2014,** *192*, 488–495.

[736] Qu, K.; Wang, J.; Ren, J.; Qu, X. Carbon Dots Prepared by Hydrothermal Treatment of Dopamine as an Effective Fluorescent Sensing Platform for the Label-Free Detection of Iron(III) Ions and Dopamine. *Chem. - A Eur. J.*, **2013,** *19*(22), 7243–7249.

[737] Shi, W.; Li, X.; Ma, H. A Tunable Ratiometric pH Sensor Based on Carbon Nanodots for the Quantitative Measurement of the Intracellular pH of Whole Cells. *Angew. Chem. Int. Ed. Engl.*, **2012,** *51*(26), 6432–6435.

[738] Zhu, A.; Qu, Q.; Shao, X.; Kong, B.; Tian, Y. Carbon-Dot-Based Dual-Emission Nanohybrid Produces a Ratiometric Fluorescent Sensor for In Vivo Imaging of Cellular Copper Ions. *Angew. Chem. Int. Ed. Engl.*, **2012,** *51*(29), 7185–7189.

[739] Shao, X.; Gu, H.; Wang, Z.; Chai, X.; Tian, Y.; Shi, G. Highly Selective Electrochemical Strategy for Monitoring of Cerebral Cu^{2+} Based on a Carbon Dot-TPEA Hybridized Surface. *Anal. Chem.*, **2013,** *85*(1), 418–425.

[740] Wang, Y.; Wang, S.; Ge, S.; Wang, S.; Yan, M.; Zang, D.; Yu, J. Facile and sensitive paper-based chemiluminescence DNA biosensor using carbon dots dotted nanoporous gold signal amplification label. *Anal. Methods*, **2013,** *5*(5), 1328.

[741] Wu, L.; Wang, J.; Ren, J.; Li, W.; Qu, X. Highly sensitive electrochemiluminescent

cytosensing using carbon nanodot@Ag hybrid material and graphene for dual signal amplification. *Chem. Commun.*, **2013,** *49*(50), 5675.

[742] Kumar, V.; Toffoli, G.; Rizzolio, F. Fluorescent carbon nanoparticles in medicine for cancer therapy. *ACS Med. Chem. Lett.*, **2013,** *4*(11), 1012–1013.

[743] Dulkeith, E.; Morteani, A.C.; Niedereichholz, T.; Klar, T.A.; Feldmann, J.; Levi, S.A.; van Veggel, F.C.J.M.; Reinhoudt, D.N.; Möller, M.; Gittins, D.I. Fluorescence Quenching of Dye Molecules near Gold Nanoparticles: Radiative and Nonradiative Effects. *Phys. Rev. Lett.*, **2002,** *89*(20), 203002.

[744] Tang, J.; Kong, B.; Wu, H.; Xu, M.; Wang, Y.; Wang, Y.; Zhao, D.; Zheng, G. Carbon Nanodots Featuring Efficient FRET for Real-Time Monitoring of Drug Delivery and Two-Photon Imaging. *Adv. Mater.*, **2013,** *25*(45), 6569–6574.

[745] Zheng, M.; Liu, S.; Li, J.; Qu, D.; Zhao, H.; Guan, X.; Hu, X.; Xie, Z.; Jing, X.; Sun, Z. Integrating oxaliplatin with highly luminescent carbon dots: an unprecedented theranostic agent for personalized medicine. *Adv. Mater.*, **2014,** *26*(21), 3554–3560.

[746] Mewada, A.; Pandey, S.; Thakur, M.; Jadhav, D.; Sharon, M. Swarming carbon dots for folic acid mediated delivery of doxorubicin and biological imaging. *J. Mater. Chem. B*, **2014,** *2*(6), 698–705.

[747] Wu, L.; Cai, X.; Nelson, K.; Xing, W.; Xia, J.; Zhang, R.; Stacy, A.J.; Luderer, M.; Lanza, G.M.; Wang, L. V; Shen, B.; Pan, D. A Green Synthesis of Carbon Nanoparticle from Honey for Real-Time Photoacoustic Imaging. *Nano Res.*, **2013,** *6*(5), 312–325.

[748] Huang, P.; Lin, J.; Wang, X.; Wang, Z.; Zhang, C.; He, M.; Wang, K.; Chen, F.; Li, Z.; Shen, G.; Cui, D.; Chen, X. Light-Triggered Theranostics Based on Photosensitizer-Conjugated Carbon Dots for Simultaneous Enhanced-Fluorescence Imaging and Photodynamic Therapy. *Adv. Mater.*, **2012,** *24*(37), 5104–5110.

[749] Kleinauskas, A.; Rocha, S.; Sahu, S.; Sun, Y.-P.; Juzenas, P. Carbon-core silver-shell nanodots as sensitizers for phototherapy and radiotherapy. *Nanotechnology*, **2013,** *24*(32), 325103.

[750] Wen, X.; Yu, P.; Toh, Y.-R.; Hao, X.; Tang, J. Intrinsic and Extrinsic Fluorescence in Carbon Nanodots: Ultrafast Time-Resolved Fluorescence and Carrier Dynamics. *Adv. Opt. Mater.*, **2013,** *1*(2), 173–178.

[751] Kumar, V.; Toffoli, G.; Rizzolio, F. Fluorescent carbon nanoparticles in medicine for cancer therapy. *ACS Med. Chem. Lett.*, **2013,** *4*(11), 1012–1013.

[752] Liu, S.; Tian, J.; Wang, L.; Luo, Y.; Zhai, J.; Sun, X. Preparation of photoluminescent carbon nitride dots from CCl_4 and 1,2-ethylenediamine: a heat-treatment-based strategy. *J. Mater. Chem.*, **2011,** *21*(32), 11726.

[753] Tan, M.; Li, X.; Wu, H.; Wang, B.; Wu, J. N-doped carbon dots derived from bovine serum albumin and formic acid with one- and two-photon fluorescence for live cell nuclear imaging. *Colloids Surf B Biointerfaces.*, **2015,** *136*, 141–149.

[754] Ray, S.C.; Saha, A.; Jana, N.R.; Sarkar, R. Fluorescent carbon nanoparticles: Synthesis, characterization, and bioimaging application. *J. Phys. Chem. C*, **2009,** *113*(43), 18546–18551.

[755] Salame, I.I.; Bandosz, T.J. Surface Chemistry of Activated Carbons: Combining the Results of Temperature-Programmed Desorption, Boehm, and Potentiometric Titrations. *J. Colloid Interface Sci.*, **2001,** *240*(1), 252–258.

[756] Melo, S.A.; Luecke, L.B.; Kahlert, C.; Fernandez, A.F.; Gammon, S.T.; Kaye, J.; LeBleu, V.S.; Mittendorf, E.A.; Weitz, J.; Rahbari, N.; Reissfelder, C.; Pilarsky, C.; Fraga, M.F.; Piwnica-Worms, D.; Kalluri, R. Glypican-1 identifies cancer exosomes and detects early pancreatic cancer. *Nature*, **2015,** *523*(7559), 177–182.

[757] Toffoli, G.; Hadla, M.; Corona, G.; Caligiuri, I.; Palazzolo, S.; Semeraro, S.; Gamini, A.; Canzonieri, V.; Rizzolio, F. Exosomal doxorubicin reduces the cardiac toxicity of doxorubicin. *Nanomedicine (Lond).*, **2015,** *10*(19), 2963–2971.

[758] Eskelinen, E.-L.; Saftig, P. Autophagy: A lysosomal degradation pathway with a central role in health and disease. *Biochim. Biophys. Acta - Mol. Cell Res.*, **2009,** *1793*(4), 664–673.

[759] Huang, D.; Zhou, H.; Gao, J. Nanoparticles modulate autophagic effect in a dispersity-dependent manner. *Sci. Rep.*, **2015,** *5*, 14361.

[760] Wolfram, J.; Shen, H.; Ferrari, M. Multistage vector (MSV) therapeutics. *J. Control. Release*, **2015,** *219*, 406–415.

[761] Blanco, E.; Shen, H.; Ferrari, M. Principles of nanoparticle design for overcoming biological barriers to drug delivery. *Nat. Biotechnol.*, **2015,** *33*(9), 941–951.

[762] Tehan, B.G.; Lloyd, E.J.; Wong, M.G.; Pitt, W.R.; Montana, J.G.; Manallack, D.T.; Gancia, E. Estimation of pKa Using Semiempirical Molecular Orbital Methods. Part 1: Application to Phenols and Carboxylic Acids. *Quant. Struct. Relationships*, **2002,** *21*(5), 457–472.

[763] Reijenga, J.; van Hoof, A.; van Loon, A.; Teunissen, B. Development of Methods for the Determination of pKa Values. *Anal. Chem. Insights*, **2013,** *8*, 53–71.

[764] Kato, Y.; Ozawa, S.; Miyamoto, C.; Maehata, Y.; Suzuki, A.; Maeda, T.; Baba, Y. Acidic extracellular microenvironment and cancer. *Cancer Cell Int.*, **2013,** *13*(1), 89.

[765] Vander Heiden, M.G.; Cantley, L.C.; Thompson, C.B. Understanding the Warburg Effect: The Metabolic Requirements of Cell Proliferation. *Science*, **2009,** *324*(5930), 1029–1033.

[766] Gatenby, R.A.; Gillies, R.J. Why do cancers have high aerobic glycolysis? *Nat. Rev. Cancer*, **2004,** *4*(11), 891–899.

[767] Warburg, O.; Wind, F.; Negelein, E. The Metabolism of Tumors in the Body. *J. Gen. Physiol.*, **1927,** *8*(6), 519–530.

[768] Gerweck, L.E.; Seetharaman, K. Cellular pH gradient in tumor versus normal tissue: potential exploitation for the treatment of cancer. *Cancer Res.*, **1996,** *56*(6), 1194–1198.

[769] Hulikova, A.; Harris, A.L.; Vaughan-Jones, R.D.; Swietach, P. Regulation of intracellular pH in cancer cell lines under normoxia and hypoxia. *J. Cell. Physiol.*, **2013,** *228*(4), 743–752.

[770] Hashim, A.I.; Zhang, X.; Wojtkowiak, J.W.; Martinez, G. V.; Gillies, R.J. Imaging pH

and metastasis. *NMR Biomed.*, **2011,** *24*(6), 582–591.

[771] Shirmanova, M. V.; Druzhkova, I.N.; Lukina, M.M.; Matlashov, M.E.; Belousov, V. V.; Snopova, L.B.; Prodanetz, N.N.; Dudenkova, V. V.; Lukyanov, S.A.; Zagaynova, E. V. Intracellular pH imaging in cancer cells in vitro and tumors in vivo using the new genetically encoded sensor SypHer2. *Biochim. Biophys. Acta - Gen. Subj.*, **2015,** *1850*(9), 1905–1911.

[772] Sorkin, A.; von Zastrow, M. Signal transduction and endocytosis: close encounters of many kinds. *Nat. Rev. Mol. Cell Biol.*, **2002,** *3*(8), 600–614.

[773] Wang, Z.; Xia, J.; Zhou, C.; Via, B.; Xia, Y.; Zhang, F.; Li, Y.; Xia, L.; Tang, J. Synthesis of strongly green-photoluminescent graphene quantum dots for drug carrier. *Colloids Surf B Biointerfaces.*, **2013,** *112*, 192–196.

[774] Chowdhuri, A.R.; Singh, T.; Ghosh, S.K.; Sahu, S.K. Carbon Dots Embedded Magnetic Nanoparticles @Chitosan @Metal Organic Framework as a Nanoprobe for pH Sensitive Targeted Anticancer Drug Delivery. *ACS Appl. Mater. Interfaces*, **2016,** *8*(26), 16573–16583.

[775] Horowitz, A.T.; Barenholz, Y.; Gabizon, A.A. In vitro cytotoxicity of liposome-encapsulated doxorubicin: dependence on liposome composition and drug release. *Biochim. Biophys. Acta - Biomembr.*, **1992,** *1109*(2), 203–209.

LIST OF PUBLICATIONS

- **Paper 1: "A Bottom-Up Synthesis of Carbon Nanoparticles with Higher Doxorubicin Efficacy".**

Samer Bayda, Mohamad Hadla, Stefano Palazzolo, Vinit Kumar, Isabella Caligiuri, Emmanuele Ambrosi, Enrico Pontoglio, Marco Agostini, Tiziano Tuccinardi, Alvise Benedetti, Pietro Riello, Vincenzo Canzonieri, Giuseppe Corona, Giuseppe Toffoli, and Flavio Rizzolio. *J. Control. Release,* 248, (**2017)**, 144-152. DOI: 10.1016/j.jconrel.2017.01.022 **(IF: 7.441)**

- **Paper 2: "DNA Nanotechnology for Cancer Therapy".**

Vinit Kumar*, Stefano Palazzolo*, Samer Bayda*, Giuseppe Corona, Giuseppe Toffoli, and Flavio Rizzolio. *Theranostics* **2016**; 6(5): 710-725. DOI: 10.7150/thno.14203 (* Authors equal contribution) **(IF: 8.854)**

- **Paper 3: "Enhanced Chemotherapeutic Behavior of Open-Caged DNA@Doxorubicin Nanostructures for Cancer Cells".**

Vinit Kumar, Samer Bayda, Mohamad Hadla, Isabella Caligiuri, Concetta Russo Spena, Stefano Palazzolo, Susanne Kempter, Giuseppe Corona, Giuseppe Toffoli and Flavio Rizzolio, *J. Cell. Physiol.* **(2016),** 231: 106–110. DOI: 10.1002/jcp.25057 **(IF: 4.155)**

- **Paper 4: "Synthesis and characterization of new chiral P,O ferrocenyl ligands and catalytic application to asymmetric Suzuki–Miyaura coupling".**

Samer Bayda, Audrey Cassen, Jean-Claude Daran, Catherine Audin, Rinaldo Poli, Eric Manoury, Eric Deydier, *J. Organomet. Chem.* 772-773, **(2014),** 258-264, DOI: 10.1016/j.jorganchem.2014.09.027 **(IF: 2.336)**